Abstract of "Mechanics of 1D continua with applications in bio-inspired engineering" by Wenqiang Fang, Ph.D., Brown University, May 2022.

Stiff biological materials (SBMs), such as nacre and bone, are composites that display remarkable toughness enhancements over their primary constituents, which are brittle minerals. The enhanced fracture toughness in those tough SBMs is known to be a direct consequence of their intricate internal architectures. By studying the connections between a biological material's microscale structures and mechanical properties, researchers can learn new mechanical design principles that can be used to improve the design of engineering composites. With this goal in mind, a special type of SBMs, called spicules, which are the skeletal elements from the marine sponge *Euplectella aspergillum*, draws our attention. Spicules are fiber-like structures that consist of a solid silica cylinder surrounded by concentric cylindrical silica layers. The curves from flexural tests carried out on spicules display sawtooth patterns, which are typically a signature of toughening mechanisms through crack arrest and reinitiation. Intriguingly, the spicules were recently found not to display any significant toughness enhancement. To resolve this apparent contradiction, I present a model for the spicule's flexural tests in which I allow for the slipping of the specimen on the test fixtures. By choosing experimentally reasonable values for the friction coefficient, I was able to get the model's predictions to match experimental measurements. The model predicts that the sawtooth patterns are due to the slipping instabilities of the spicules on the test fixtures, not from toughening mechanisms. With the demand of a new explanation for the beneficial properties of the spicules' internal architectures, I proposed a hypothesis that the internal architectures enhance the spicules' anchoring ability by reducing their effective bending stiffness. I calculated the effective bending stiffness of helical symmetric, cylindrical orthotropic multilayer composite cylinders using anisotropic elasticity theory and homogenization theory. This result provides theoretical support to our hypothesis that it is possible to design a composite beam with desired bending stiffness through lamellar architectures. In another hypothesis, with the aim to explore whether effective shear stiffness affects the spicules' anchoring ability, I developed a variationally consistent geometrically nonlinear shear deformable beam theory. Inspired by spicules, the works in this dissertation provide fundamental understanding in the mechanics of 1D continua.

Mechanics of 1D continua with applications in bio-inspired engineering

by
Wenqiang Fang
B.S., Engineering Mechanics, Tsinghua University, 2015

Submitted in partial fulfillment of the requirements
for the Degree of Doctor of Philosophy in
Solid Mechanics at Brown University

Providence, Rhode Island
May 2022

This dissertation by Wenqiang Fang is accepted in its present form by
the School of Engineering as satisfying the dissertation requirement
for the degree of Doctor of Philosophy.

Date _____ _____

Haneesh Kesari, Ph.D., Advisor

Recommended to the Graduate Council

Date _____ _____

Allan F. Bower, Ph.D., Reader

Date _____ _____

Vikas Srivastava, Ph.D., Reader

Approved by the Graduate Council

Date _____ _____

Andrew G. Campbell, Ph.D.
Dean of the Graduate School

Curriculum Vitæ

Wenqiang Fang was born in Qingzhou, Shandong, China. He attended Tsinghua University in 2011. Later he received his Bachelor of Science degree in Engineering Mechanics in 2015 and began his doctoral study in the Solid Mechanics program at Brown University in the fall of 2015.

Wenqiang received the Outstanding Teaching Assistant Award of the School of Engineering, Brown University in May, 2021.

Refereed Journal Publications

W. Fang, W. Deng, and H. Kesari. Effective bending stiffness of multilayered composite cylinders with cylindrical orthotropy. *International Journal of Solids and Structures*, In submission.

W. Fang, S. Kochiyama, and H. Kesari. Sawtooth patterns in flexural force curves of structural biological materials are not signatures of toughness enhancement: Part II. *Journal of the Mechanical Behavior of Biomedical Materials*, 124:104787, 2021.

S. Kochiyama, **W. Fang**, M. A. Monn, and H. Kesari. Sawtooth patterns in flexural force curves of structural biological materials are not signatures of toughness enhancement: Part I. *Journal of the Mechanical Behavior of Biomedical Materials*, 119:104362, 2021.

R.A. Gutierrez, **W. Fang**, H. Kesari, and E.M. Darling. Force sensors for measuring microenvironmental forces during mesenchymal condensation. *Biomaterials*, 270:120684, 2021.

M. M. Rahaman, **W. Fang**, A. L. Fawzi, Y. Wan, and H. Kesari. An accelerometer-only algorithm for determining the acceleration field of a rigid body, with application in studying the mechanics of mild traumatic brain injury. *Journal of the Mechanics and Physics of Solids*, 143:104014, 2020.

W. Fang, J. Mok, and H. Kesari. Effects of geometric nonlinearity in an adhered microbeam for measuring the work of adhesion. *Proceedings of the Royal Society A: Mathematical, Physical and Engineering Sciences*, 474:20170594, 2018.

Conference Proceedings

(1 = poster, 2 = talk)

W. Fang, S. Kochiyama, M. A. Monn, and H. Kesari, "Flexure of biological glass fibers leads to sawtooth force-displacement responses related to slip instabilities, not toughness enhancement," 25th International Congress of Theoretical and Applied Mechanics (ICTAM), Virtual, Aug., 2021.[1]

W. Fang and H. Kesari, "Asymptotic analysis of sponge spicules' sensitivity to geometric imperfection regarding buckling instability," ASME 2019 International Mechanical Engineering Congress and Exposition (IMECE), Salt Lake City, UT, USA. Nov., 2019.[2]

W. Fang and H. Kesari, "Optimal shape for buckling resistance and imperfection sensitivity: inspiration from sponge spicules," Society of Engineering Science 56th annual technical meeting (SES), St. Louis, MO, USA. Oct., 2019.[2]

W. Fang and H. Kesari, 'Asymptotic analysis of sponge spicules' sensitivity to geometric imperfection regarding buckling instability," ASME 2019 International Mechanical Engineering Congress and Exposition (IMECE), Pittsburgh, PA, USA. Nov., 2018.[2]

K. Vijaykumar, **W. Fang** and H. Kesari, "Effective toughness in materials with interfaces," Society of Engineering Science 55th annual technical meeting (SES), Leganeś, Madrid, Spain. Oct., 2018.[2]

W. Fang and H. Kesari, "Role of small scale geometric heterogeneity on effective interfacial toughness," 9th New England Workshop on Mechanics of Materials and Structures, Brown University, Providence, RI, Sep., 2018.[2]

Teaching Experience at Brown

Graduate

ENGN 2210 Continuum Mechanics, TA (Fall 2020)

Undergraduate

ENGN 1950 Advanced Engineering Optimization, TA (Fall 2017, Fall 2018)

ENGN 1370 Advanced Engineering Mechanics, TA (Spring 2019, Spring 2020)

Acknowledgements

I am eternally grateful to my advisor Haneesh Kesari, for his continuous support of my Ph.D. study and research over the last six years. Haneesh is a pure scientist, a great mentor and a warm friend. His pure enthusiasm for science and observant mind has been something I have admired over the years. From working with him, I have learnt a lot, not only about how to do great scientific research, but also about how to pursue what you really love. I was also deeply influenced by his optimism when situations were difficult. In my hardest time when research did not go smoothly, he was always supportive and encouraged me to try new ideas or think of the problem from a different perspective. In our numerous discussions, he was always patient, inspiring, and encouraging, ready to clarify any confusion that I may have had. I am so grateful for the opportunity to work with him. I could not have imagined having a better advisor and mentor for my Ph.D. study.

I am really grateful to have had the opportunity to pursue my graduate studies in Solid Mechanics at Brown University. I am honored to be part of the community and build up my understanding of solid mechanics through courses and discussions with all the faculty here. I would like to thank Prof. David Henann and Prof. Huajian Gao for their insights to my research projects. I am also grateful to Prof. Allan F. Bower for serving as committee member of my progress review and Prof. Pradeep Guduru for serving as the examiner of my preliminary exam.

I would like to specifically thank my dissertation committee members, Prof. Allan F. Bower and Prof. Vikas Srivastava for taking time to read my dissertation and give me constructive advice with their broad knowledge and critical insights.

I want to say thanks to the people I spent most of my time with at Brown—my colleagues in the Kesari lab. I am so lucky to work with this group of knowledgeable and reliable people. I am especially thankful to Max, Kaushik, and Weilin. They were always ready to put their own work aside when I need help. I cannot remember how many times they inspired me when we were having discussions together. I also want to thank Sayaka, Yang, Masiur, Jianzhe and Wenbo for all the moments we worked and had fun together. It is a pity that COVID took away a lot of "lab time" from us, but I appreciate every meeting on zoom whenever I need advice from you guys. I would like to gratefully acknowledge Corrie for helping me improve my thesis writing. Thank you for bringing the group together and hosting the Christmas dinner with your lovely family.

Besides my colleagues in the Kesari lab, I would like to thank my other collaborators during my Ph.D. study. I would like to thank Robert A. Gutierrez and Prof. Eric Darling for introducing me to the fascinating field of cell mechanics and providing me the great opportunity to make my contribution to the field. I want to acknowledge Prof. Christopher Larsen for his contribution to the proof of an important statement in this dissertation. Without his critical insights and generous guidance, I would not come up with this clear and rigorous proof. I would also like to thank Prof. Rika Wright Carlsen for collaborating on the brain strain project. Her deep knowledge and

understanding helped me get around many obstacles in this area.

During my years at Brown, I very much enjoyed my life and study because of my peers and friends who stood by me at all times. I will never forget the many fun activities we have done together and the wonderful moments we spent together. Whenever I am stressed or get stuck in research, you are the ones who keep me energized and remind me that I am not alone.

Special thanks to my girlfriend, Mona, for all her love and support. You helped me come through the most difficult and happiest times of my Ph.D. study. Every time I doubted myself or became exhausted, you always helped me out and made me become better and stronger. I cannot imagine my life without you. You became the biggest strength that guided me through all the struggles.

I am deeply grateful to my parents for their unconditional support and endless love to me. They raised me up, taught me how to be a good person, sent me to school, and then experienced farewells again and again. Thanks to them for giving me the freedom to find my own path and being proud of every small achievement I made. Without their support, I would not have made it here. I also thank my sisters for taking care of my parents when I was absent, and encouraging me when I was depressed.

Dedicated to my parents

Table of Contents

List of Tables

List of Illustrations

Chapter 1

Introduction

The mechanics of 3D continua is a huge success in describing the deformation and stress state for most solid bodies. However, the equations governing the deformation of 3D continua are relatively difficult to handle even if the object is composed of simple isotropic elastic materials. Researchers have developed many reduced-dimensional theories to model structures with specific geometric features. For structures with one dimension being much larger than the other two, the corresponding one-dimensional theory is called the mechanics of 1D continua. In the mechanics of 1D continua, when the object is primarily subjected to bending deformation, the theory is usually categorized as beam theory. When it is primarily subjected to axial loading, the corresponding theory is usually referred as column theory.

There are a plethora of beam theories available in literature [1]. The most elementary theory among them is Euler-Bernoulli beam theory, which is widely employed in civil engineering. It is known that the shear effect usually play an important role in composite beams since the material interfaces are typically weak in shear. Hence, shear deformable beam theories such as Timoshenko beam theory [2, 3] and some high-order shear deformable beam theories [4, 5] are established to model short beams and composite beams. For the study of the deformation of highly flexible structures, the most elementary theory is Euler's Elastica theory [6, 7], which is an extension of Euler-Bernoulli beam theory in the finite deformation regime. A more general finite deformation plane beam theory in which bending, transverse shearing and axial stretching are taken account was first presented by Reissner [8]. Later, Simo [9] extended Reissner's plane beam theory into a

three-dimensional dynamic theory, also known as geometrically-exact rod model.

As for columns, if the structure is relatively slender, it may deflect laterally and fail by bending rather than failing by direct compression of the material. The well-known Euler buckling theory [10] can be applied to determine the critical load for elastic buckling. If a column is of intermediate length, the stress in the column will reach the proportional limit before buckling begins. One will need a theory of inelastic buckling, such as tangent-modulus theory [11], the reduced-modulus theory [12], and the Shanley theory [13] to calculate the critical load.

The mechanics of 1D continua plays an important role in the modeling and analysis of many bio-inspired systems, such as plant stems [14], bones and spines [15], and marine sponge skeletons [16]. In this dissertation, I will discuss some biological systems in which I propose hypotheses and develop new theoretical models to explain the structure-function connections. Through the development of new models, we aim to better understand the evolution of biological systems and apply that knowledge to build stronger structures.

1.1 Structural biological materials serve as templates for bio-inspiration

Structural biological materials (SBMs), such as mother of pearl (nacre) [17], spicules [18], and bones [15] are of growing interest in material and mechanics communities. They are composites that mainly consist of a stiff mineral phase which is often in the form of platelets [19, 20, 21] or fibers [16, 22, 23], and contributes to 95% of the materials' volumes. The platelets and fibers are glued to the mineral phase by a compliant organic phase (see Figure 1.1). These natural composites are distinguished from their synthetic counterparts by the fact that their effective properties at the macro scale, such as strength and fracture toughness, are quite high despite the corresponding properties of their constituent phases being poor. With remarkable mechanical performances, structural biomaterials can serve as fascinating model material systems for the discovery of new mechanics of materials principles.

Among all structural biomaterials, we focus on the anchor spicules of the marine sponge *Euplectella aspergillum* (*Ea.*) (see Figure 1.1 (C)). While the *Ea.* anchor spicules are composed primarily of glass, they are surprisingly flexible and can even be tied in knots before

breaking. The spicules have been the subject of several previous structure-function investigations [24, 18, 25, 26, 27, 28, 29, 30, 31]. However, the functional implications of their internal architectures are still not fully understood.

Euplectella aspergillum is a species of "glass sponge" (class Hexactinellida) that lives in the deep waters of the Pacific Ocean [32, 33, 25]. Like most other sponges, they feed by filtering sea water to capture plankton. The anchor spicules of *Ea.* sponges are fiber-like glass skeletal elements. They are approximately 50 μm in diameter and up to 10 cm in length. They also have a lamellar architecture that resembles those in nacre and bone. The architecture consists of alternating layers of glass and organic phases laid out in a concentric manner, as shown in Figure 1.1(D). Specifically, when viewed in cross-section, an anchor spicule consists of a $\approx$10 μm silica core that is surrounded by a coaxial assembly of $\approx$25 cylindrical silica layers [18, 33, 25]. From the core to the periphery, the thicknesses of the silica layers are decreasing. A 5-10 nm thin proteinaceous interlayer is present in between adjacent silica layers [25]. Similar cylindrical lamellar architectures are also found in spicules of a number of related sponge species [34, 35, 32].

1.1.1 Does lamellar architecture in *Ea.* spicules contribute to toughness enhancement?

It is natural to hypothesize that, analogous to other SBMs, the spicules' architecture is closely related to their high toughness. However, the presupposition that the anchor spicules have high toughness may not be correct. To find out how much does a spicule's architecture enhance its toughness, Monn et al. have performed flexural tests on the anchor spicules to measure their crack growth resistance [30, 38]. They compared these toughness properties to the properties of spicules from a related sponge (*Tethya aurantia*) that has a similar chemical composition but lacks the lamellar architecture. Through this comparison they have found that:

1. The cylindrical lamellar architecture has little effect on the *Ea.* spicule's fracture initiation toughness.

2. The average crack growth resistance of the *Ea.* spicules was roughly 73 times larger than the average crack growth resistance of the monolithic spicules.

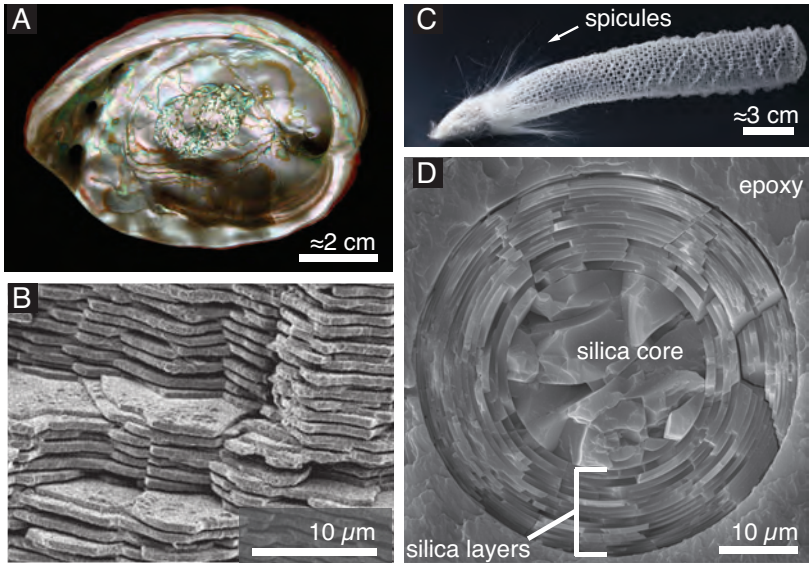

Figure 1.1: Lamellar architectures in biological materials. (A) The shell of *Haliotis rufescens*—the red abalone (image courtesy of John Varner). (B) The nacre from *H. rufescens* consists of aragonite tablets assembled in a brick-and-mortar manner, where thin protein layers (not identifiable in the image) in between the tablets function as the mortar (modified with permission from [36]; copyright 2012 the Royal Society of Chemistry). (C) The entire skeletal structure of a marine sponge *Euplectella aspergillum* is shown (modified from [18]; copyright 2015 National Academy of Sciences). The white arrow identifies the spicules, which are around 50 μm in diameter and can be several centimeters long. In some of our recent studies, we performed three-point bending tests on these spicules [29, 30]. (D) A scanning electron microscope (SEM) image of an *E. aspergillum* spicule's cross section shows lamellar architecture consisting of a cylindrical silica core surrounded by concentric silica layers (modified from [18]; copyright 2015 National Academy of Sciences). Each of these concentric silica layers are separated from their adjacent layers or the silica core by a compliant organic layer whose thickness is roughly in the 5–10 nm range (not identifiable in the SEM image) [25].

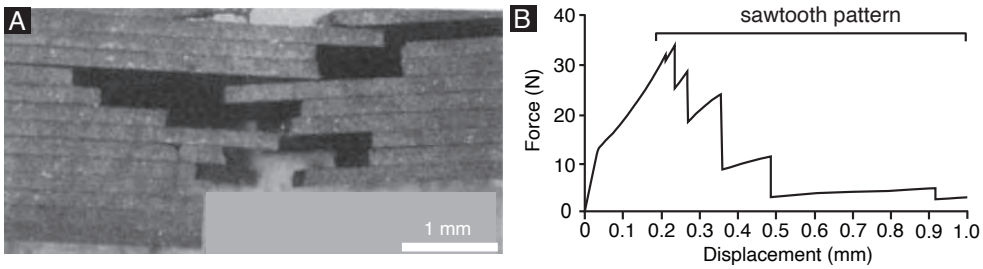

Figure 1.2: Sawtooth pattern in the flexural test curve of nacre-mimicking specimen. (A) nacre-mimicking specimen with layered architecture that consisted of a stack of silicon carbide layers coated with graphite. This nacre-mimicking specimen displayed fracture toughness enhancement, i.e. the fracture toughness of the nacre-mimicking specimen was higher than that of a homogenous silicon carbide specimen [37]. (B) A representative force-displacement curve from three-point bending tests of the specimen in (A). Both (A) and (B) are adapted from Clegg et al. [37].

3. The toughness enhancement provided by the spicule's lamellar architecture was much smaller than toughness enhancements observed in other structural biological materials like nacre and bone.

It is commonly accepted that a signature of the toughness enhancement mechanism in the SBMs with lamellar architectures is the sawtooth pattern in the flexural test curve (see Figure 1.2). The above results by Monn et al. imply that the *Ea.* spicules' lamellar architecture does not significantly contribute to their toughness enhancement. However, this conclusion appears to contradict the observations made in Monn and Kesari [29, 31], in which they observed sawtooth patterns in the force-displacement curves from flexural tests on *Ea.* spicules. For the detailed discussion of the observation and interpretation of sawtooth patterns, please see Kochiyama et al. [31].

In Chapter 2 of this dissertation, I aim to answer the question: what is the physical mechanism behind the sawtooth patterns in the force-displacement curves from flexural tests on *Ea.* spicules? I put forward the hypothesis that the sawtooth pattern was due to the spicules' slipping at the tests' supports. To illustrate my hypothesis, I present a model for the spicules' flexural tests in which I allow for the possibility for the specimen to slip at the tests' supports. I model the specimen using Euler's Elastica theory and the contact between the specimen and the tests' supports using the Coulomb's friction law. By choosing experimentally reasonable values for the friction coefficient, I was able to get the model's predictions to match experimental measurements remarkably well. Additionally, on incorporating the spicules' surface roughness into the model, which I did by varying the friction coefficient along the spicules' length, its predictions can also be made to match the measured sawtooth patterns. We find that the sawtooth pattern in the model are due to slip type instabilities, which further reinforces our hypothesis that sawtooth patterns in flexural force curves of structural biological materials are not signatures of toughness enhancement.

1.1.2 New hypothesis about the beneficial properties of the lamellar architectures in *Ea.* anchor spicules

Now that it has been shown that the *Ea.* spicules' lamellar architecture does not significantly contribute to their toughness enhancement, we demand a new hypothesis to explain the beneficial

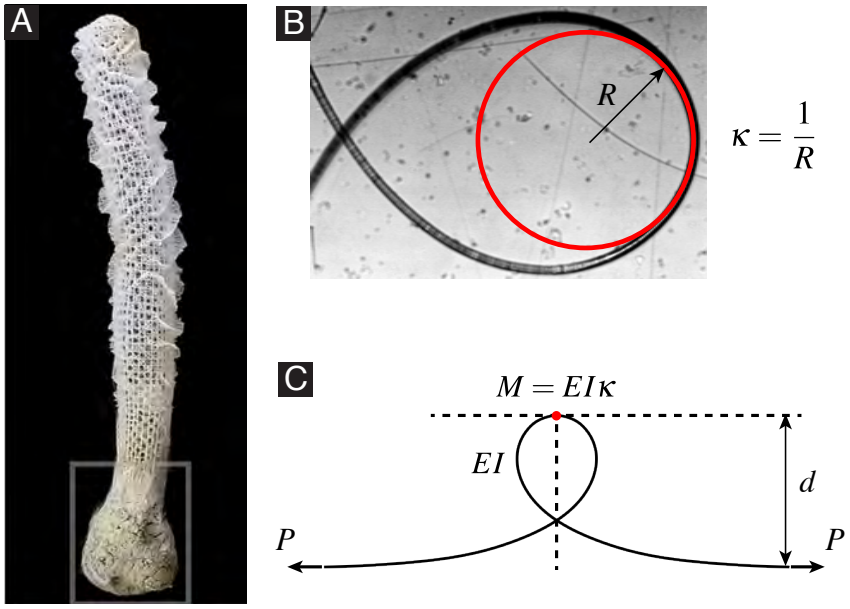

Figure 1.3: (A) An *Euplectella aspergillum* sponge with mud on its root (image courtesy of Swee Cheng Lim). (B) An *Ea.* anchor spicule bent into a loop. The radius of curvature at the symmetric point of the loop is R while the curvature at that point is κ. (C) A schematic of a beam bent into a loop by force P applied on the two ends. As per Euler-Bernoulli beam theory, the critical point (marked in red) on the beam undergoes bending moment $M = EI\kappa$ where E is the Young's modulus and I is the second moment of area of the beam's cross section. From the rigid body diagram, we also have $M = Pd$ where d is the size of the loop.

properties of the lamellar architecture. Recall that the primary mechanical function of the spicules is to secure the sponge into the soft sediments of the sea floor [39]. Since some spicules will tangle with small rocks in the mud and form knots (see Figure 1.3), which helps the sponge anchor tightly to the sea floor, the spicule's anchoring capacity is mainly determined by the maximum end force P it can transmit without breaking. If the deformation of the spicules is governed mainly by bending, assuming that the normal stress is distributed in a linear way over the cross section of the spicules, the maximum tensile stress will appear at the top edge of the symmetric point of the loop. We refer to the symmetric point of the loop as the critical point (marked by red dot in Figure 1.3 (C)). An estimation of the maximum tensile stress at the the critical point is

$$\sigma_m = \frac{M}{I} r, \tag{1.1}$$

where M is bending moment at the critical point, I is the second moment of area of the beam's cross section, and r is the radius of beam's cross section. From rigid body diagram, we have,

$$M = Pd, \tag{1.2}$$

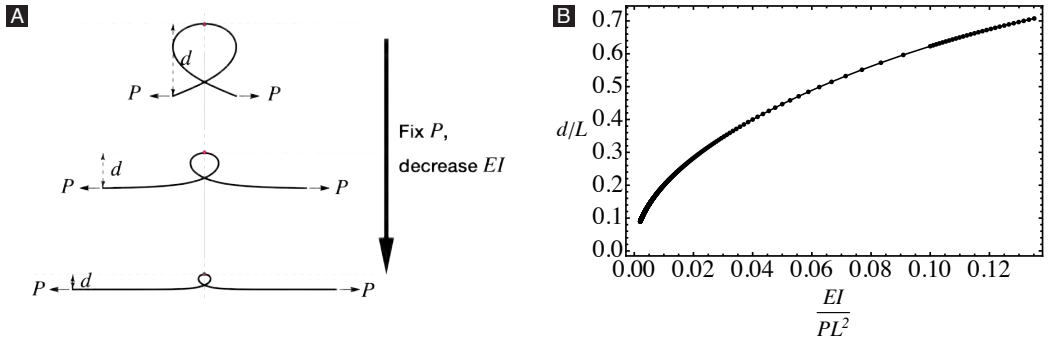

Figure 1.4: (A) Schematics of beams with different bending stiffness forming loops with different size (B) The relation between the normalized loop size and the normalized bending stiffness for the problem given in (A) using Euler's Elastica theory.

where d is the projection of the distance between the critical point and the tail of the loop in the direction perpendicular to the end force P. For simplicity, we refer to the size of the loop as d.

Inserting (1.2) to (1.2), we arrive at

$$\sigma_m = \frac{Pd}{I} r. \tag{1.3}$$

Considering the spicules is composed of brittle ceramic material, we assume the spicule fails when the maximum tensile stress exceeds a critical failure value σ_f. We denote the maximum end force just before the spicule fails as P_f, which is a measure of the spicule's anchoring ability. By taking σ_m to be the failure curvature σ_f, we have

$$P_f = \frac{\sigma_f I}{d\, r}. \tag{1.4}$$

Using Euler's Elastica theory, when a beam is bent into a loop, the loop size d will decrease if the bending stiffness is reduced while all other parameters are fixed (see Figure 1.4). From (1.4), we identify the dependence of the beam's maximum end force on the loop size d. Taking all of the above information together, it can be deduced that the spicule's anchoring ability is negatively correlated with the effective bending stiffness, EI, of the spicule. However, how to make connections between the spicule's lamellar architecture and its effective bending stiffness?

In Chapter 3, we present our exploration on how lamellar architectures enhance the spicules' anchoring ability by reducing their effective bending stiffness. This is based on our observation that

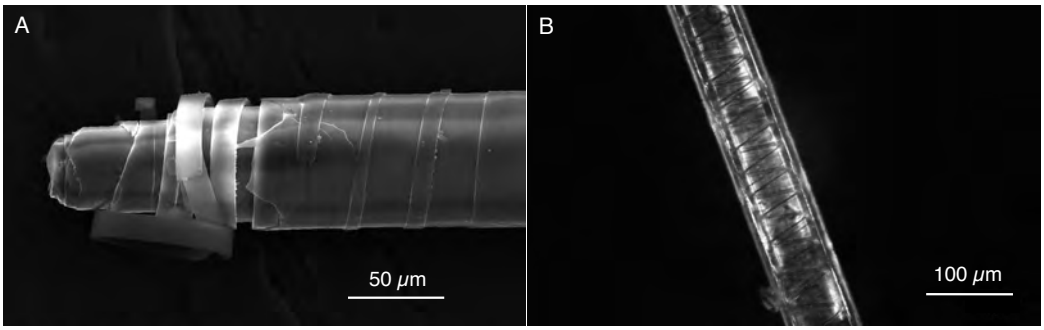

Figure 1.5: Helical structure developed under tensile stress in *Ea.* anchor spicules.

the spicules are essentially multilayered composite cylinders with cylindrical orthotropy. Through tensile tests on the *Ea.* anchor spicules, we surprisingly observed helical structures in the spicules (see Figure 1.5). The observation implies that the *Ea.* spicules are essentially anisotropic and heterogeneous. Moreover, the helical symmetric layers of the spicules are cylindrical orthotropic. The effective bending stiffness of such structures can be obtained through the anisotropic elasticity theory and homogenization theory. Based on the formulae obtained by Jolicoeur and Cardou [40], we derived analytical expressions for the asymptotic bending stiffness of multilayered composite cylinders with cylindrical orthotropy. For the particular case that a hollow cylinder cut into multiple concentric tubes and assuming no friction between adjacent layers, it is found the effective bending stiffness of the multilayered hollow cylinder is reduced. This result provides theoretical support to our hypothesis that the spicules' lamellar architectures help to enhance their anchoring ability by reducing their effective bending stiffness.

1.1.3 Exploring the shear effect of the lamellar architectures in *Ea.* anchor spicules

When a spicule forms a loop, we expect not only bending deformation but also shearing deformation along the spicule. The proteinaceous interlayers between adjacent concentric silica layers are known to be highly compliant. When the spicules are under shear traction, shear strain localization is expected to form in the organic phase, which results in smaller apparent shear stiffness than a monolithic counterpart without any organic phase. Therefore, it is reasonable to assume that the *Ea.* spicules with layered architecture appear to be softer in shear deformation than monolithic spicules.

In Chapter 4, I try to explore whether the lamellar architecture in *Ea.* anchor spicules affects the

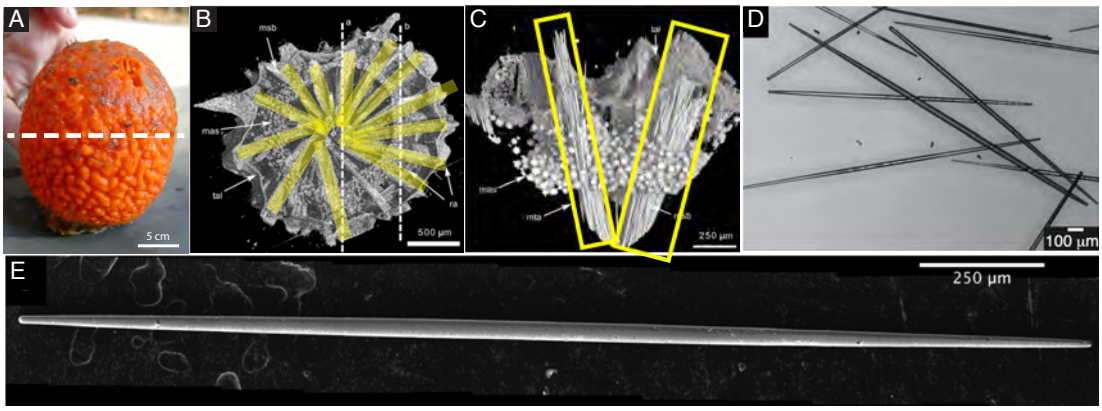

Figure 1.6: Skeletal anatomy of *Tethya aurantia* (*Ta.*) sponge and strongyloxea spicules. (A) *Tethya aurantia* sponge, also known as the orange puffball sponge (image courtesy Karakal). (B) The skeletal morphology of a similar specie called *Tethya minuta* (modified with permission from [41]). The radially arranged bundle structures are marked in yellow. (C) A 3D-visualization of a part of the cortical region of *T. minuta* (modified with permission from [41]). The bundles which containing a bunch of spicules are marked by yellow boxes. (D) A micrograph of several strongyloxea spicules. (E) An SEM image of a single spicule.

spicules' anchor ability through shear effect. I addressed this problem by developing a variationally consistent geometrically nonlinear shear deformable beam theory. I solved for the deformed configurations and calculated the maximum moment of beams with different effective shearing stiffness when the beams form loops. Unfortunately, I was not able to draw any constructive conclusion from these results. Although the results from my exploration could not prove my hypothesis, the development of the geometrically nonlinear shear deformable beam theory itself is of significant importance. The beam theory derivation follows the general three-dimensional continuum theory and Hellinger-Reissner variational principle. On top of this beam theory, we have provided a proof of existence of the solutions and a scheme for computing numerical solutions.

1.2 Theoretical analysis of Clausen column's buckling behavior inspired by tapered spicules in *Tethya aurantia*

During the investigation of the structure-property connections of the *Ea.* spicules, we identified a different type of spicules, which has similar chemical composition but lacks the lamellar architecture, as a reference group. The reference spicules are skeletal components of marine sponge *Tethya aurantia* (*Ta.*, see Figure 1.6 (A)). The *Ta.* sponge's body consists of a dense, spherical core (choanosome) surrounded by a thick, fibrous shell (cortex) [42] (see Figure 1.6 (B) and (C)). The

choanosome and cortex are critical for metabolic processes in *Ta.* However, they are too soft to provide necessary mechanical integrity to the sponge. It is found that several types of spicules are produced to stiffen the choanosome and cortex. The specific type of *Ta.* spicules that draws our attention is known as strongyloxea spicules, which are around 2 mm long and 35 μm in diameter (see Figure 1.6 (D)). The *Ta.* spicules are tapered along their length (see Figure 1.6 (E)). And the tapered shape is remarkably uniform across different *Ta.* spicules.

According to the theory of Euler buckling, the buckling resistance of a slender structure can be increased by tapering it [43]. Therefore, Monn and Kesari proposed the hypothesis that the tapered shape of *Ta.* spicules will enhance their buckling resistance to better support the sponge. They verified their hypothesis through the resemblance of the spicules' shape to the Clausen column, which is the optimal axisymmetric column with maximum buckling strength for given length and volume. A more detailed narrative of Monn and Kesari's hypothesis and results can be found in Section 5.1.1.

Since the tapered shape of *Ta.* spicules formed in sponge always deviate from the mathematically precise Clausen profile, it is important that the small deviation does not cause significant reduction to the buckling strength of the *Ta.* spicules. Therefore, in Chapter 5, I studied the Clausen column's sensitivity to shape variations. To get a theoretical formula of the column's sensitivity, I assume that the shape perturbations are axisymmetric and asymptotically small. I also performed Rayleigh-Ritz based numerical experiments to validate the theoretical formula. The result shows that Clausen column is not only the strongest column against buckling, but also the most tolerant column to shape variations. Both features of the Clausen profile make the structure-property connection between the spicules' shape and its ability to guard buckling instability more substantial .

Finally, in Chapter 6 we conclude the dissertation with a discussion of the main findings of my works and a outlook of related future directions.

The main objectives of this dissertation are to develop analytical models for 1D continua to explore our hypotheses when trying to understand the structure-function connections in biological systems. The research carried out in this dissertation aims to provide fundamental understanding of the mechanics of 1D continua, including the coupling of bending and slipping instabilities, bending stiffness homogenization, shear effects in geometrically nonlinear beam, and geometric effects on

buckling instability. Although we put all of our results in the background of structural biological materials, the results of this dissertation have direct applications in various fields including micro-electromechanical system (MEMS) devices, soft electronics, and bionic robot, etc.

Chapter 2

Sawtooth patterns in flexural force curves of structural biological materials are not signatures of toughness enhancement

Note: A version of this chapter is published in *Journal of the Mechanical Behavior of Biomedical Materials*. Data and figures have been used with all co-authors' consent.

W. Fang, S. Kochiyama, and H. Kesari. Sawtooth patterns in flexural force curves of structural biological materials are not signatures of toughness enhancement: Part II. Journal of the Mechanical Behavior of Biomedical Materials, 124:104787, 2021.

2.1 Introduction

Stiff biological materials (SBMs), such as nacre and bone, are natural layered composites that are known for having remarkable fracture toughness that can be orders of magnitude higher than that of the brittle ceramics that dominates their composition [17, 19, 44, 45, 46, 15]. The key to such enhancement in fracture toughness lies in their lamellar architectures, which are the intricate

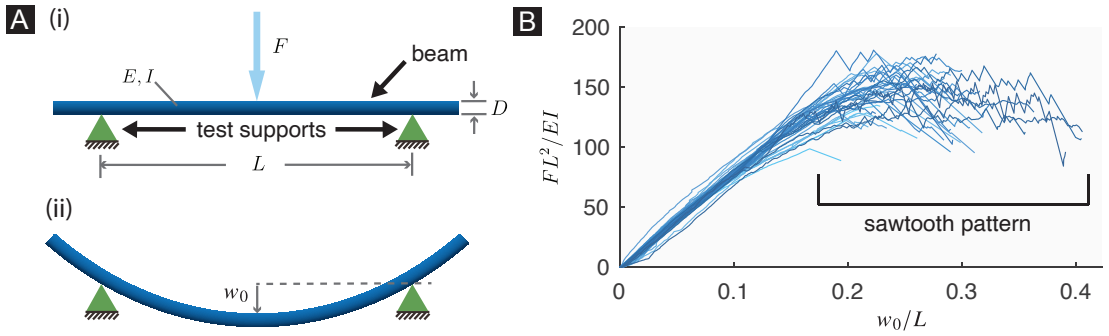

Figure 2.1: (A) (i) Typical schematic of a three-point bending test in its reference configuration and (ii) the deformed beam with midpoint displacement w_0 under the action of some midpoint force F. The support span is L, and D, E, and $I = \pi D^4/64$ are the diameter, Young's modulus, and the bending moment of inertia of the beam, respectively. (B) Thirty eight scaled force-displacement curves from three-point bending tests carried out on *E. aspergillum* spicules and previously presented in [29, 31]. The spicules respond linearly until a certain point, and then, in most cases, start displaying the sawtooth pattern.

arrangements of ceramic and organic phases at the sub-micron scales (see Figure 1.1(A)&(B)). One way in which the lamellar architecture contributes to the toughness enhancement is by supporting the operation of the Cook-Gordon mechanism [47] (crack-arrest-and-reinitiation mechanism). In this mechanism, when a crack initiates in and propagates through the ceramic phase, the organic phase, which separates one region of the ceramic phase from another, can effectively act as a "trap" and arrest the crack [48, 47]. In flexural tests, the operation of the Cook-Gordon mechanism reflects as a drop in the measured force as the crack advances, and then as the end of that force drop as the crack gets arrested [37]. As such, when the Cook-Gordon mechanism operates in layered materials, the measured force-displacement curve can have the appearance of a sawtooth pattern (see Figure 2.1(B)).

Monn et al. recently showed that the presence of lamellar architectures by itself does not necessarily guarantee the operation of the Cook-Gordon mechanism [30]. They performed notched three-point bending tests on the spicules and directly measured their fracture toughness in terms of the initiation fracture toughness and the average crack growth resistance, and found that the fracture toughness enhancement in them was negligible [30]. This implied that the Cook-Gordon mechanism either operated to a negligible level or was absent in the spicules.

However, the implication that the Cook-Gordon mechanism operates to an insignificant level during the failure of *Ea.* spicules in flexural tests appears to contradict the observations made in

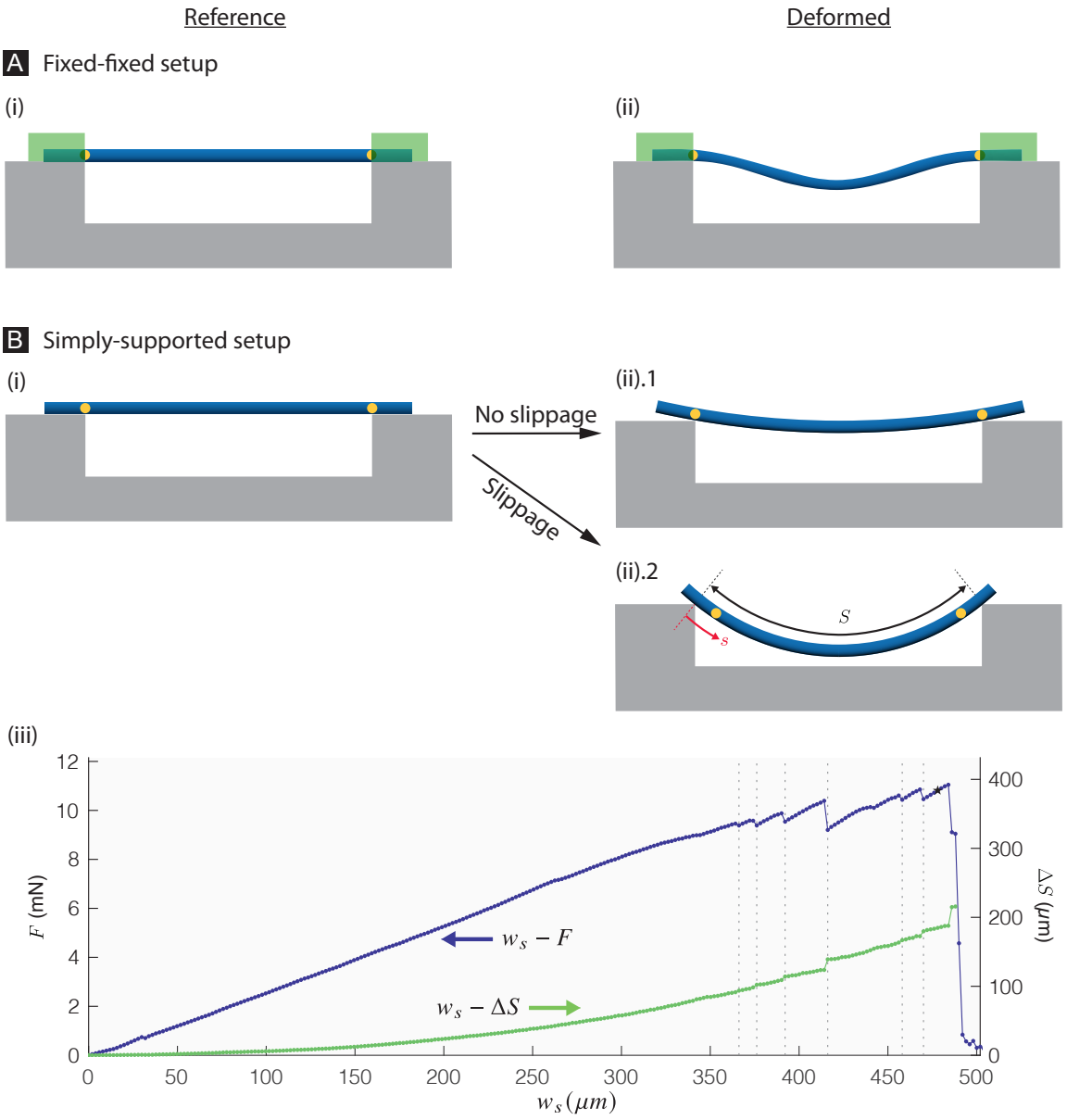

Figure 2.2: Fixed-fixed setup and spicule slippage in simply-supported setup. (A) (i) shows the reference configuration of a spicule set up for a flexural test in a fixed-fixed setup; the spicule ends are glued onto the test's supports (adhesive shown in green). The yellow circles mark two spicule material particles that sit at the test's supports in this configuration. (A) (ii) shows the spicule in its deformed configuration as it is being tested with its ends glued to the test's supports. The material particles that were at the test's supports in the reference configuration (yellow circles) are still at the test's supports. (B) (i) shows a spicule in its reference configuration in the simply-supported setup. The yellow circles mark two spicule material particles that sit at the test's supports in this configuration. (B) (ii) .1 shows a deformed spicule configuration in which the spicule has not undergone any slipping at the supports; the material particles that were at the test's supports in the reference configuration (yellow circles) are still at the test's supports in this configuration as well. This is the assumption made in standard beam theories, such as the Euler-Bernoulli beam theory, when they are used to model three point bending tests. (Caption continued on next page)

Figure 2.2: (continued from previous page) (B) (ii) .2 shows a deformed configuration of the spicule in which the spicule has undergone slippage at the test's supports. The material particles denoted by the yellow circles are no longer at the test's supports, but have slipped down into the trench. The parameter S denotes the spicule's total length, which is the length of the section of the spicule specimen lying between the test's supports. (B) (iii) shows the measured force F (left axis) (for details of force, F, see §2.3) and the change in the total length, ΔS (right axis), from a representative three point bending test carried out in the simply supported setup as a function of stage displacement, w_s, in blue and green, respectively. The vertical dashed lines indicate the instances at which the drops in the force take place. As can be noted from the graphs, the jumps in the spicule's total length take place at those very same instances (modified from [31]).

Monn and Kesari [34, 35, 29]. To be specific, in [29] Monn and Kesari carried out three-point bending tests on *Ea.* spicules. They observed sawtooth patterns in the force-displacement curves from their tests, in which the spicules were being loaded all the way until failure (see Figure 2.1). As intimated previously, sawtooth-patterns in layered materials are usually a signature of the operation of the Cook-Gordon mechanism [37]. Therefore, if the Cook-Gordon mechanism is indeed irrelevant during the spicule's failure as argued in Monn et al., there must be alternative explanations for the appearance of the sawtooth patterns observed in the force-displacements curves of Monn and Kesari.

The paper by Kochiyama et al. [31] attempts to resolve the apparent contradiction by hypothesizing that the sawtooth patterns, at least in the case of *Ea.* spicules, are solely the consequence of the spicules slipping (see Figure 2.2(B)) at the test's supports, rather than of the operation of the Cook-Gordon mechanism. I summarize the arguments from the paper by Kochiyama et al. [31] in the following few paragraphs.

In [31], we reported force-displacement measurements from three-point bending tests that were carried out on *Ea.* spicules in the simply-supported (SS) setup (see Figure 2.1). Micrographs of the spicules were taken *in-situ* via a microscope during the tests. By conducting image analysis on those micrographs, it was demonstrated that in the tests in which the force-displacement curve displayed a sawtooth pattern, there were sudden jumps in the total length of the spicule section lying between the test's supports. This total length is shown marked as S in Figure 2.2(B) (ii) .2. The jumps appear, e.g., as the discontinuities in the green curve shown in Figure 2.2(B) (iii). It was further shown that the jumps and the force-drop events (which appear, e.g., as the discontinuities in the blue curve in Figure 2.2(B) (iii)) took place at the exact same time instances. These observations imply one of the following three scenarios: (i) the force-drop events are solely due to the layer-fracture events associated with the Cook-Gordon mechanism, (ii) they are due to a combination of layer-fracture events and slip-events, or (iii) they are entirely due to the slip-events.

To determine which of the three scenarios is likely true, three-point bending tests were carried out on the spicules again in the fixed-fixed (FF) setup (see Figure 2.2(A)). In the FF setup, the spicule's ends are glued to the test's supports, which prevents the occurrence of any slip-events at the test's supports. None of the force-displacement curves from the FF tests displayed a sawtooth pattern. Although this observation points to scenario (iii) as being true, it is with the implicit assumption that the operation of the Cook-Gordon mechanism would be unaffected regardless of whether or not the spicule ends are free to slide and rotate. Since such an assumption is not explicitly validated, additional experiments were performed to gauge the likelihood of each of the three scenarios in an alternative manner. To be specific, the three-point bending tests were carried out on the spicules again in the SS setup, but the spicules were only loaded until a few force drops that are characteristic of the sawtooth-pattern were observed instead of until complete failure. The specimens were then unloaded until they regained their straight shape and the force on them almost vanished. Finally, the spicules were loaded for the second time (re-loaded) until a few force drops were again observed. If the sawtooth pattern observed during the loading phase was due to the Cook-Gordon mechanism, then the spicule's stiffness (slope of the initial linear portion of the force-displacement curve before the appearance of the force drops) from the re-loading (second loading) phase should be different from that in the loading (first loading) phase. However, the spicules' stiffnesses in the loading and the re-loading phases were found to be almost the same. This observation implies that the force-drops in the loading phases are not due to the Cook-Gordon mechanism, which leads us to conclude that scenario (iii) is the one that is true.

In this chapter, with the goal of further investigating our hypothesis, we develop and study a mechanics model for the spicule's SS bending tests. A distinguishing feature of our model is that the test specimen is allowed to slide at the test's supports. In contrast, in the standard Euler-Bernoulli (EB) model of the three point bending test, the specimen is not allowed to slide at the test's supports.

Considering the geometry in the SS experiments (e.g., see Figure 2.1), in our model, the spicule's displacements are taken to be two dimensional in nature. The spicules are modeled as 1D continua considering their high aspect ratios (length:diameter) of ≈ 25, and their bending behavior is modeled using Euler's elastica theory since they undergo large displacements in the experiments. Any stretching behavior along their axes are ignored. The contact at the test's supports is modeled

using the Coulomb friction model. Scanning electron microscopy (SEM) revealed that the spicules' surfaces could have both smooth and rough regions. By roughness, we are referring to the different types of imperfections, including debris, scrapes and outer layer damage, that were observed on the spicules' surfaces (Figure 2.3). We incorporate the spicules' surface roughness in our model by assuming that the coefficient of friction between the spicule and the test's supports varies depending on which particular spicule cross-section is in contact with the supports. Specifically, in the model it is assumed that the coefficient of friction varies along the spicule's length as

$$\mu_0 \left(1 + A \cos\left(\frac{2\pi s}{\lambda} - \phi\right)\right), \tag{2.1}$$

where s is the arc-length coordinate along the spicule's axis (see Figure 2.2(B) (ii) .2), and we refer to the parameters μ_0, A, λ, and ϕ as the average value of coefficient of friction, the amplitude, the wavelength, and the phase, respectively. In our problem, the static and kinetic coefficients of friction are taken to have the same value. In §2.4.1, we present the governing equations of our model. In §2.4.2, we semi-analytically solve the governing equations to derive what we call our model's equilibrium force-displacement curve. Each point on that curve corresponds to a static equilibrium configuration. Our model predicts that any measured force-displacement point will lie on the equilibrium curve. However, due to the finite stiffness of the loading apparatus, not all the points on the equilibrium curve will be measured in an experiment. Taking into account the stability of the equilibrium points in §2.4.3, we provide an algorithm for numerically determining our model's prediction for the force-displacement curve that will be measured in an SS experiment.

In §2.5, we compare the force-displacement curves predicted by our models with the ones that were experimentally measured in [29, 31]. We find that not only do the predicted force-displacement curves capture the sawtooth pattern, but they can also be made to quantitatively match the measured force-displacement remarkably well by appropriately choosing the value of μ_0, A, λ, and ϕ. The sawtooth pattern in our model is a direct consequence of the slip events at the supports. We find that the values of μ_0, which were chosen to match our model's prediction with the experimental measurements as closely as possible, is quite consistent with the values reported in literature for the coefficient of friction between glass and steel (note that the contact in the spicule SS experiments is between silica (spicule) and stainless steel (test's supports)).

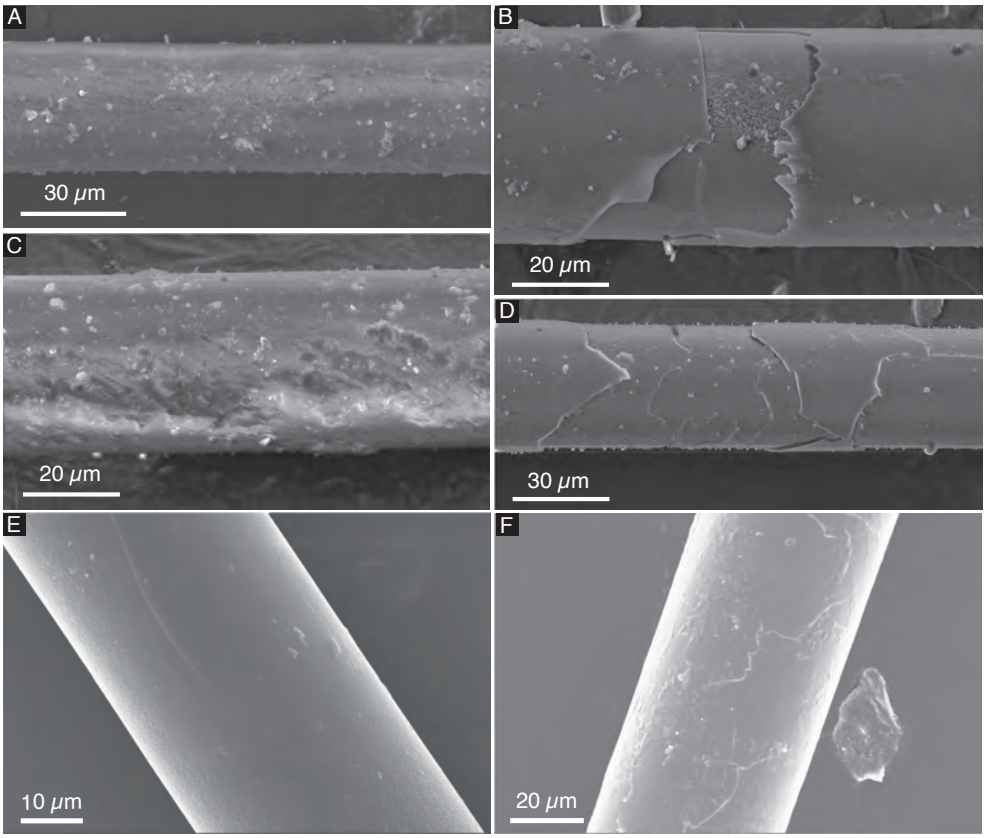

Figure 2.3: Representative SEM images of a few randomly selected *E. aspergillum* spicules that were taken after the spicules had been flexurally tested in a simply-supported setup. Each spicule is identified by the label given to the flexural test in which it was used (see Tables S1–S2 of [31] for detailed information pertaining to a given test). (A) and (B) are two different images of the spicule from the test SS4. (C)–(F) are images of the spicules from the tests SS7, SS24, SS32, and SS34, respectively. The imaged region in each spicule was chosen randomly. These images demonstrate how the spicules can have rough surfaces, as shown in (A)–(D), or relatively smooth surfaces, as shown in (E)–(F).

Since the sawtooth pattern in our model is a direct consequence of slip events, the good match between our model's predictions and the experimental measurements supports our hypothesis that the sawtooth patterns in the experiments of Monn and Kesari are solely a consequence of the slip instabilities that take place at the trench's edges. However, the modeling results we put forward in this chapter do not conclusively prove our hypothesis. This is because we were unable to check the reasonableness of the values we chose for the parameters A and λ while we were comparing our model to the experiments. We discuss this limitation of our current work in the concluding section of this chapter, §2.6. We also discuss a potential future direction for addressing this limitation in §6.

We begin by discussing some mathematical notions that are needed for the development of our model. Following that we recapitulate the experimental setup of the SS bending tests in §2.3 before presenting our model in §2.4.

2.2 Mathematical preliminaries

The mathematical notions that we use in this chapter are discussed in Section 2.1 of [31]. However, for the readers' convenience, I briefly review some of those notions in this section.

We assume that our experiments take place in the three dimensional physical point space $\mathcal{E}$, and take $\mathbb{E}$ to be a three dimensional, oriented, Hilbert space, such that $\mathcal{E}$ is $\mathbb{E}$'s principle homogenous space. We introduce vectors $\hat{e}_1$, $\hat{e}_2$,and $\hat{e}_3$, as shown in Figure 2.4(A), to form a basis for $\mathbb{E}$. We denote the dot product between any two vectors $\boldsymbol{u}$ and $\boldsymbol{v}$ as $\boldsymbol{u} \cdot \boldsymbol{v}$, where by definition $\boldsymbol{u} \cdot \boldsymbol{v} \in \mathbb{R}$, and $\mathbb{R}$ is the set of all real numbers. The vectors $\hat{e}_1$, $\hat{e}_2$, and $\hat{e}_3$ are orthonormal. This can be expressed by stating that $\hat{e}_i \cdot \hat{e}_j = \delta_{ij}$, where $i,j \in (1,2,3)$, and the Kronecker delta symbol δ_{ij} is defined as having a value of unity if $i = j$ and zero otherwise.

Following [49], we consider vectors to carry units with them if they belong to a physical vector space. For instance, we take that $\hat{e}_i$, $i \in (1,2,3)$, carry the units of μm (micrometers). The magnitude/norm of the vector $\boldsymbol{u}$ is denoted as $\|\boldsymbol{u}\| = (\boldsymbol{u} \cdot \boldsymbol{u})^{1/2}$. The norm $\|\boldsymbol{u}\|$ is non-dimensional, or to be more precise, $\|\boldsymbol{u}\| \in \mathbb{R}_{\geq 0}$, where $\mathbb{R}_{\geq 0}$ is the set of non-negative real numbers.

Following [49] and [50], we model force as a linear map from $\mathbb{E}$ into the one dimensional

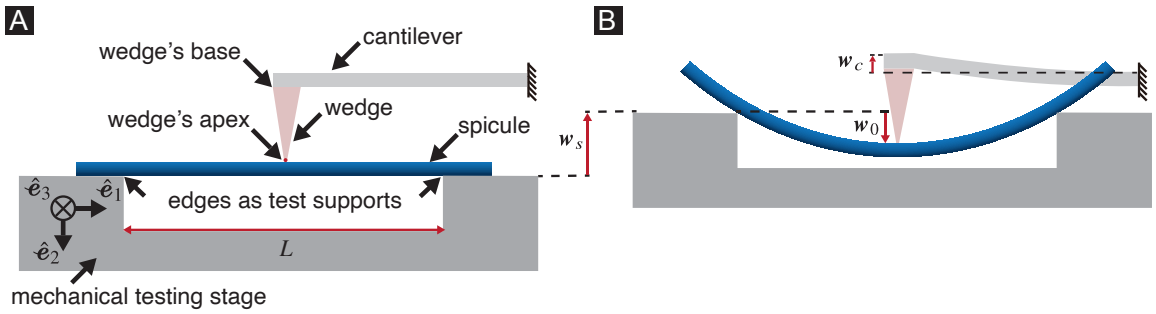

Figure 2.4: An illustration of the simply-supported setup. (A) Schematic of the experimental setup used in our recent study [31] for testing spicules in a simply-supported setup. The mechanical testing stage consisted of a stainless steel plate with a L μm wide trench, where the trench edges served as the test's supports. The loading device consisted of a wedge attached to a cantilever; to ensure that the cantilever's right end remained fixed in space during the experiment, the right end was encastered into a rigid aluminum frame (not shown in the schematic) that was independent of all the other testing structures. (B) Schematic of a simply-supported spicule in our experiment, which is being deformed under some applied load. The loading of the spicules was achieved by displacing the mechanical testing stage by w_s μm ($\boldsymbol{w}_s = -w_s\hat{e}_2$) as shown, where the mechanical testing stage was mounted onto a three-axis motorized translation stage (not shown in the schematic) to enable precise control of its motion. As a result, the midpoint of the spicule is deflected by w_0 μm ($\boldsymbol{w}_0 = w_0\hat{e}_2$) and the free end of the cantilever is deflected by w_c μm ($\boldsymbol{w}_c = -w_c\hat{e}_2$). For more details on the experiments see §2.3.

vector space whose elements carry units of energy. Let the forces $\hat{\mathbf{f}}_i$, $i \in (1,2,3)$, be defined such that $\hat{\mathbf{f}}_i\left(\hat{e}_j\right) = \delta_{ij}$ nJ $\left(10^{-9}\text{ Joules}\right)$, where $\hat{\mathbf{f}}_i$ is a milli-newton of force acting in the $\hat{e}_i$ direction. The set of all forces can be made into a vector space $\mathbb{F}$ by defining the addition between two forces $\mathfrak{u}$ and $\mathfrak{v}$ to be the force $\mathfrak{w}$ such that $\mathfrak{w}(\boldsymbol{x}) = \mathfrak{u}(\boldsymbol{x}) + \mathfrak{v}(\boldsymbol{x})$ for all $\boldsymbol{x} \in \mathbb{E}$. Let $\mathfrak{F}$ be the linear map from $\mathbb{E}$ to $\mathbb{F}$ such that $\mathfrak{F}\left(\hat{e}_i\right) = \hat{\mathbf{f}}_i$. Then, defining the dot product between forces $\mathfrak{u}$ and $\mathfrak{v}$ to be the dot product in $\mathbb{E}$ between the vectors $\mathfrak{F}^{-1}(\mathfrak{u})$ and $\mathfrak{F}^{-1}(\mathfrak{v})$, where $\mathfrak{F}^{-1}$ is the inverse of $\mathfrak{F}$, the space $\mathbb{F}$ can be made into a Hilbert space. It can be shown that $\left(\hat{\mathbf{f}}_i\right)_{i\in(1,2,3)}$ provides an orthonormal basis for $\mathbb{F}$.

2.3 A brief review of the simply supported, three-point bending experiments

In this section we briefly recall the set-up of the simply-supported (SS) experiments mentioned in §2.1. A trench of width L μm was cut into a stainless steel mechanical testing stage (MTS) (see Figure 2.4(A)). The non-dimensional trench width L was 1278 ± 3 (mean ± standard deviation) in the experiments. Spicules were placed across the trench with their lengths parallel to the $\hat{e}_1$ direction so that initially, the spicule's cross-sections were normal to $\hat{e}_1$. The trench's edges, which

run parallel to the $\hat{e}_3$ direction, served as the test's supports. A cantilever with a wedge attached to it was positioned over the spicule. The wedge's triangular faces were normal to the $\hat{e}_3$ direction with the triangle's base normal to the $-\hat{e}_2$ direction and facing away from the spicule, and the triangle's apex facing the spicule. At the beginning of the experiment, the wedge's apex (shown marked in Figure 2.4(A)) was just above the spicule's midpoint, i.e., over the spicule cross-section that lay midway across the trench. The cantilever and the wedge were made of either steel or aluminum.

The loading phase of the tests were conducted by moving the MTS in the $-\hat{e}_2$ direction at a rate of 1 μm/sec. The MTS was driven by a DC servo motor, whose motion was controlled through a PID algorithm. The stage was moved in 2 μm increments. During the increment, the stage's velocity was maintained between 50 and 200 μm/sec. Thus, each stage increment took anywhere between 10 and 40 ms. After each increment, the stage was held motionless so that there was a 2100 ms time interval between the starting points of any two consecutive increments. Each data point that we report was calculated using the average value of the sensor readings collected over the last 100 ms of each of those time intervals.

We denote an arbitrary time instance during the experiment as τ ms, where $\tau \in [0, \tau^*]$. The time $\tau = 0$ corresponds to the instance at which the spicule first makes contact with the wedge's apex, and the time $\tau = \tau^* > 0$ corresponds to the instance when the spicule fails. We express the MTS's displacement as $-w_s(\tau)\hat{e}_2$. Here, $w_s(\tau) \in \mathbb{R}$ is a known non-dimensional quantity since the stage's displacement was an input in our experiment.

As the stage moved upwards ($-\hat{e}_2$ direction) the spicule made contact with the wedge's apex and got deflected into the trench, while the cantilever got deflected away from the trench. We express the cantilever's wedge's motion as $-w_c(\tau)\hat{e}_2$ (compare Figures 2.4(A) and (B)). Here, $w_c(\tau)$ is the non-dimensional cantilever displacement, which is defined as the dot product between $-\hat{e}_2$ and the wedge's displacement vector at the time instance τ. We denote the spicule's midpoint deflection, or simply displacement, as $w_0(\tau)\hat{e}_2$, where $w_0(\tau) \in \mathbb{R}$ is the dot product between $\hat{e}_2$ and the displacement vector of the centroid of the spicule's cross-section that is directly underneath the wedge's apex. It can be shown that the quantities $w_s(\tau)$, $w_c(\tau)$, and $w_0(\tau)$ are related as

$$w_s(\tau) = w_c(\tau) + w_0(\tau). \tag{2.2}$$

$$\hat{w}_s(\tau) := \frac{w_s(\tau)}{L}, \tag{2.3a}$$

$$\hat{w}_c(\tau) := \frac{w_c(\tau)}{L}, \tag{2.3b}$$

In terms of

$$\hat{w}_0(\tau) := \frac{w_0(\tau)}{L}, \tag{2.3c}$$

equation (2.2) reads

$$\hat{w}_s(\tau) = \hat{w}_c(\tau) + \hat{w}_0(\tau). \tag{2.4}$$

Let $\boldsymbol{F}(\tau)$ be the force acting on the spicule's midpoint. We assume that the wedge's apex only applies force in the $\pm\hat{e}_2$ directions. This allows us to express

$$\boldsymbol{F}(\tau) = F(\tau)\hat{\mathbf{f}}_2, \tag{2.5}$$

where $F(\tau) \in \mathbb{R}$ is a non-dimensional quantity. We model the cantilever as a linear spring that is oriented in the $\hat{e}_2$ direction and having a stiffness of $\mathscr{k}_\mathrm{c} = k_\mathrm{c}$ mN/μm. From this model, it follows that

$$F(\tau) = k_c w_c(\tau). \tag{2.6a}$$

We measured k_c independently, using a procedure unrelated to the SS experiments, and found it to vary from 86.4 to 90.1 (see Tables S1–S2 of [31]). The constitutive law expressed by (2.6a) can alternately be written as

$$\hat{F}(\tau) = \hat{k}_c \hat{w}_c(\tau), \tag{2.6b}$$

where

$$\hat{F}(\tau) := \frac{F(\tau)L^2}{EI}, \tag{2.7a}$$

$$\hat{k}_c := \frac{k_c L^3}{EI}, \tag{2.7b}$$

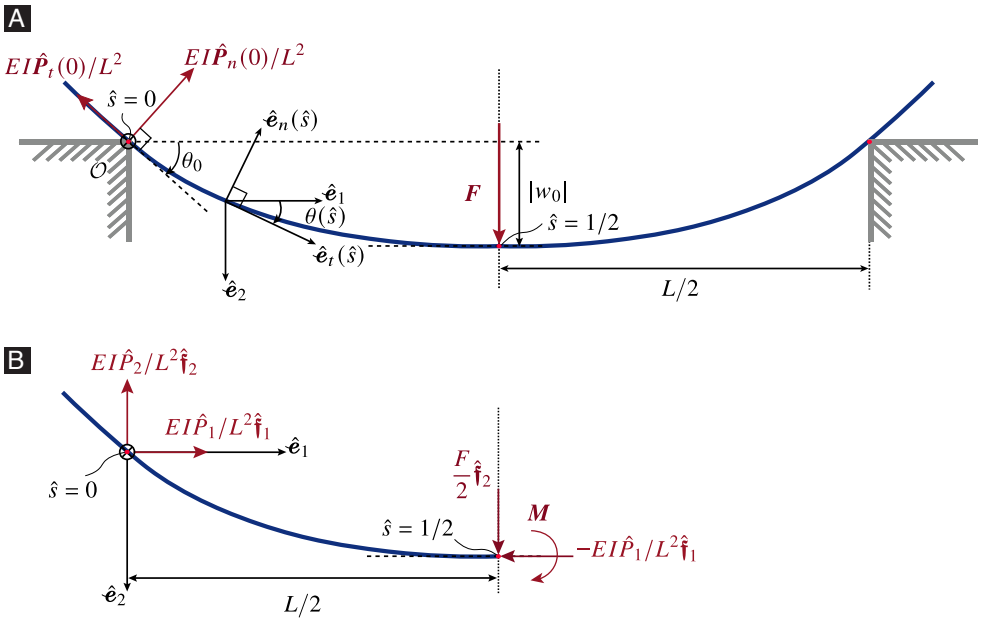

Figure 2.5: Geometry in our mechanics model. (A) A schematic of a beam (blue) suspended over a trench (gray). At $\hat{s}=0$ the beam experiences the normal reaction force $EI\hat{\boldsymbol{P}}_n(0)/L^2$ and the frictional reaction force $EI\hat{\boldsymbol{P}}_t(0)/L^2$. The force $\boldsymbol{F}$ acts at the spicule midpoint. The magnitude of the beam's midpoint's deflection is $|w_0|$. The angle between $\hat{e}_1$ and $\hat{e}_t$ $(\hat{s})$ is $\theta(\hat{s})$, and $\theta_0 := \theta(0)$. (B) A free body diagram of the left half of the beam (blue). The beam is subject to the forces $EI\hat{P}_1/L^2\hat{\mathbf{f}}_1$, and $EI\hat{P}_2/L^2\hat{\mathbf{f}}_2$ at $\hat{s}=0$, and the forces $-EI\hat{P}_1/L^2\hat{\mathbf{f}}_1$, and $F/2\hat{\mathbf{f}}_2$ at $\hat{s}=1/2$. At $\hat{s}=1/2$ the beam is also subject to a moment $\boldsymbol{M}$.

E mN/μm^2 is the spicule specimen's Young's modulus, and I μm^4 is the spicule specimen's bending moment of inertia.

In each experiment, we measured the function $\mathbb{R}_{\geq 0} \ni \tau \mapsto w_c(\tau) \in \mathbb{R}$. Since we knew k_c, on account of (2.3b) and (2.6b), this was tantamount to measuring the function $\tau \mapsto \hat{F}(\tau)$. Additionally, since we know $w_s(\cdot)$, using the measured $w_c(\cdot)$ along with (2.3a), (2.3b), and (2.4), we can construct $\tau \mapsto \hat{w}_0(\tau)$. We call the map

$$\tau \overset{\gamma_{\mathrm{m}}}{\mapsto} \left(\hat{w}_0(\tau), \hat{F}(\tau)\right), \tag{2.8}$$

the measured force-displacement curve.

2.4 Theory

The goal of the model we develop in this section is to provide a prediction for the measured force-displacement curves in the loading phase of the SS experiments.

2.4.1 Equations governing the spicule's equilibrium configurations

We denote the total length of the spicule specimen lying between the supports in the deformed configuration S μm (see Figure 2.2(B) (ii) .1). We take our problem to be completely symmetric about the trench's mid-plane. For a given total spicule length, S, we define a spicule's equilibrium configuration to be a kinematically admissible spicule deformation map and a spicule-trench edge contact force. The map should be such that the net force and the moment vanish on every one of the spicule's material regions; the contact force should be such that it satisfies the prescribed contact constitutive law between the spicule and the trench.

Euler's elastica theory

We assume the spicule to be inextensible. Thus, S denotes the total length of the spicule specimen lying between the supports in its reference configuration as well. We call the length of the spicule-section lying between a spicule material particle on the spicule's central axis and the spicule cross-section contacting the trench's left edge the particle's arc-length coordinate $s \in (0, S)$ (see Figure 2.2(B) (ii) .2). When there is no risk of confusion, we will henceforth be referring to a spicule material particle lying on the spicule's central axis simply as a spicule material particle. We call

$$\hat{s} := s/S, \tag{2.9}$$

the particle's scaled arc-length coordinate. We identify a spicule material particle with either its arc-length or scaled arc-length coordinate.

As mentioned before, we assume that our problem is completely symmetric about the trench's mid-plane, i.e., the plane perpendicular to $\hat{e}_1$ and containing the point $(L/2, 0, 0)$. Therefore, the spicule's deformed shape can be described using the (scaled) deformation mapping

$$\hat{\boldsymbol{\alpha}}(\cdot) : (0, 1/2) \to \mathbb{E}, \tag{2.10a}$$

where

$$\hat{\boldsymbol{\alpha}}(\cdot) = \frac{\boldsymbol{\alpha}(\cdot)}{L}, \tag{2.10b}$$

and $\boldsymbol{\alpha}(\xi)$ is the position vector of the spicule material particle whose arc-length coordinate is ξS.

We can define a Frenet–Serret frame [51] corresponding to the curve $\hat{\boldsymbol{\alpha}}(\cdot)$ at each spicule material particle. The unit tangent and normal vectors in that frame at the material particle $\hat{s}$ can be computed as

$$\hat{e}_t(\hat{s}) = \hat{\boldsymbol{\alpha}}'(\hat{s}) / \|\hat{\boldsymbol{\alpha}}'(\hat{s})\|, \tag{2.11a}$$

$$\hat{e}_n(\hat{s}) = \hat{e}_t'(\hat{s}) / \|\hat{e}_t'(\hat{s})\|, \tag{2.11b}$$

respectively, where $\hat{\boldsymbol{\alpha}}'(\cdot)$ is the derivative of $\hat{\boldsymbol{\alpha}}(\cdot)$, and $\hat{e}_t'(\cdot)$ is the derivative of $\hat{e}_t(\cdot)$. Using the definition of s, the equations (2.9), and (2.10), it can be shown that $\|\hat{\boldsymbol{\alpha}}'(\hat{s})\| = \hat{S}$, where

$$\hat{S} = \frac{S}{L}. \tag{2.12}$$

Let $\theta(\cdot) : (0, 1/2) \to (-\pi, \pi]$ be defined such that $\theta(\hat{s})$ is the angle between $\hat{e}_1$ and $\hat{e}_t(\hat{s})$ [1] (see Figure 2.5(A)). We can express $\hat{e}_t(\hat{s})$, $\hat{e}_n(\hat{s})$ using $\theta(\hat{s})$ as

$$\hat{e}_t(\hat{s}) = \cos(\theta(\hat{s}))\hat{e}_1 + \sin(\theta(\hat{s}))\hat{e}_2, \tag{2.13a}$$

$$\hat{e}_n(\hat{s}) = \sin(\theta(\hat{s}))\hat{e}_1 - \cos(\theta(\hat{s}))\hat{e}_2, \tag{2.13b}$$

respectively. Let $EI\hat{\boldsymbol{P}}(\hat{s})/L^2 \in \mathbb{F}$ be the force acting on the spicule cross-section containing the spicule material particle $\hat{s}$. Specifically, $EI\hat{\boldsymbol{P}}(0)/L^2$ is the force acting on the spicule due to its contact with the trench's left edge. The vector $\hat{\boldsymbol{P}}(0)$ can be expressed as

$$\hat{\boldsymbol{P}}(0) = \hat{P}_1\hat{\mathbf{f}}_1 + \hat{P}_2\hat{\mathbf{f}}_2, \tag{2.14}$$

where $\hat{P}_1,\ \hat{P}_2 \in \mathbb{R}$.

The spicule's high aspect ratio and the observation of large displacements in our SS experiments motivates us to use the Euler's elastica theory [52, 7] to model the spicule's deformation. The elastica theory is an extension of the EB theory to the regime of large displacements and rotations.

[1] To be clear, considering two vectors of unit magnitude $\boldsymbol{a} := a_1\hat{e}_1 + a_2\hat{e}_2$ and $\boldsymbol{b} := b_1\hat{e}_1 + b_2\hat{e}_2$, the angle between them is the real number θ in $(-\pi, \pi]$ such that $a_1\cos(\theta) - a_2\sin(\theta) = b_1$ and $a_2\cos(\theta) + a_1\sin(\theta) = b_2$.

As per the elastica theory, the spicule's cross-sectional rotation $\theta(\cdot)$ needs to satisfy the non-linear differential equation

$$\theta''(\hat{s})/\hat{S}^2 + \hat{P}_1 \sin(\theta(\hat{s})) - \hat{P}_2 \cos(\theta(\hat{s})) = 0, \tag{2.15a}$$

over the domain $(0, 1/2)$ and satisfy the boundary conditions

$$\theta'(\hat{s})|_{\hat{s}=0} = 0, \tag{2.15b}$$

$$\theta(\hat{s})|_{\hat{s}=1/2} = 0. \tag{2.15c}$$

In (2.15), $\theta'(\cdot)$ and $\theta''(\cdot)$ denote $\theta(\cdot)$'s first and second derivatives, respectively. The boundary condition (2.15b) follows from the fact that there is no bending moment acting on the spicule at $\hat{s} = 0$, and the boundary condition (2.15c) follows from the problem's symmetry about the trench's mid plane.

Coulomb friction model

Let

$$\hat{\mathbf{f}}_t(\hat{s}) := \mathfrak{F}\left(\hat{e}_t(\hat{s})\right) = \cos(\theta(\hat{s}))\hat{\mathbf{f}}_1 + \sin(\theta(\hat{s}))\hat{\mathbf{f}}_2, \tag{2.16a}$$

$$\hat{\mathbf{f}}_n(\hat{s}) := \mathfrak{F}\left(\hat{e}_n(\hat{s})\right) = \sin(\theta(\hat{s}))\hat{\mathbf{f}}_1 - \cos(\theta(\hat{s}))\hat{\mathbf{f}}_2. \tag{2.16b}$$

The linear map $\mathfrak{F}$ appearing in (2.16) has been defined in §2.2. Using $\hat{\mathbf{f}}_t(\hat{s})$, $\hat{\mathbf{f}}_n(\hat{s})$, we can express $\hat{\boldsymbol{P}}(\hat{s})$ as the sum of $\hat{\boldsymbol{P}}_t(\hat{s})$ and $\hat{\boldsymbol{P}}_n(\hat{s})$, where $\hat{\boldsymbol{P}}_t(\hat{s}) = \hat{P}_t(\hat{s})\hat{\mathbf{f}}_t(\hat{s})$, $\hat{\boldsymbol{P}}_n(\hat{s}) = \hat{P}_n(\hat{s})\hat{\mathbf{f}}_n(\hat{s})$, and $\hat{P}_t(\cdot)$, $\hat{P}_n(\cdot) : (0, 1/2) \to \mathbb{R}$. We refer to $\hat{\boldsymbol{P}}_t(\hat{s})$ and $\hat{\boldsymbol{P}}_n(\hat{s})$ as, respectively, the (scaled) tangential and normal forces at the material particle $\hat{s}$. We call $\hat{\boldsymbol{P}}_t(0)$ and $\hat{\boldsymbol{P}}_n(0)$ the (scaled) tangential and normal contact forces (at the left trench edge), respectively, and for brevity, denote their magnitudes, i.e., $\hat{P}_t(0)$ and $\hat{P}_n(0)$, as $\hat{P}_t$ and $\hat{P}_n$, respectively.

We define the angle $\beta_0 \in (0, \pi)$ such that

$$\cot(\beta_0) = \frac{\hat{P}_t}{\hat{P}_n}. \tag{2.17}$$

It follows from equations (2.14), (2.16), and (2.17), and the definitions of $\hat{P}_t$ and $\hat{P}_n$ that

$$\hat{P}_1 = \hat{P}_n \csc(\beta_0) \cos(\theta_0 - \beta_0), \tag{2.18a}$$

$$\hat{P}_2 = \hat{P}_n \csc(\beta_0) \sin(\theta_0 - \beta_0), \tag{2.18b}$$

where

$$\theta_0 := \theta(0). \tag{2.18c}$$

Substituting $\hat{P}_1$, $\hat{P}_2$ from (2.18) into (2.15a) and simplifying, we get that

$$\theta''(\hat{s}) + \hat{S}^2 \hat{P}_n \csc(\beta_0) \sin(\theta(\hat{s}) - \theta_0 + \beta_0) = 0. \tag{2.19}$$

We model contact between the spicule and the trench edges using the Coulomb's law of friction [53]. As per the Coulomb's law, when $\hat{P}_n \geq 0$, $\left|\hat{P}_t\right| \leq \mu \hat{P}_n$, which in terms of β_0 reads

$$-\mu \leq \cot(\beta_0) \leq \mu, \tag{2.20}$$

where μ is the coefficient of friction. (As we mentioned in §2.1, in our problem we take the static and kinetic coefficients of friction to have the same value).

2.4.2 Equilibrium force-displacement curves

Solution to the boundary value problem (2.15) using the solution to the nonlinear pendulum problem

Following Blasius (see, e.g., [54, 55] for accessible references), we construct the solution to our boundary value problem (BVP) (2.15) using the solution of an auxiliary initial value problem (IVP).

The IVP we consider is as follows. The function $\beta : (0, 1/2) \to (-\pi, \pi]$ satisfies the nonlinear

ordinary differential equation (ODE)

$$\beta''(\hat{s}) + \omega^2 \sin(\beta(\hat{s})) = 0, \tag{2.21a}$$

and the initial conditions

$$\beta(\hat{s})|_{\hat{s}=0} = \beta_0, \tag{2.21b}$$

$$\beta'(\hat{s})|_{\hat{s}=0} = 0, \tag{2.21c}$$

where $\omega > 0$ and $\beta_0 \in (0, \pi)$. The IVP (2.21) is related to the problem of a simple pendulum executing finite angle motions in a plane. The complete solution to the IVP (2.21) is commonly attributed to Euler [56]. For more modern references of the solution, see, e.g., [57, 58]. In order to explicitly note the dependence of the solution to the IVP (2.21), i.e., $\beta(\cdot)$, on the parameters ω and β_0, we denote $\beta(\cdot)$ in the remainder of this chapter as $\beta(\cdot; \omega, \beta_0)$ and express it as

$$\beta\left(\hat{s}; \omega, \beta_0\right) = 2 \arcsin\left(\sin\frac{\beta_0}{2} \operatorname{cd}\left(\omega\, \hat{s}; \sin^2\frac{\beta_0}{2}\right)\right), \tag{2.22}$$

where $\operatorname{cd}(u; m) := \cos(\psi(u; m)) \left(1 - m \sin^2(\psi(u; m))\right)^{-1/2}$ is the Jacobi elliptic function. Here, $\psi(u; m)$ is the Jacobi amplitude, which is the inverse of the elliptic integral of the first kind, i.e., ψ, u, m satisfy the equation $u = \int_0^{\psi} \left(1 - m^2 \sin(\zeta)^2\right)^{-1/2} d\zeta$.

It can be shown that the solution to our BVP, $\theta(\cdot)$, can be constructed using $\beta\left(\cdot; \omega, \beta_0\right)$ as

$$\theta(\hat{s}) = \beta\left(\hat{s}; \omega\left(\hat{S}, \hat{P}_n, \beta_0\right), \beta_0\right) - \beta\left(\frac{1}{2}; \omega\left(\hat{S}, \hat{P}_n, \beta_0\right), \beta_0\right), \tag{2.23a}$$

where

$$\omega\left(\hat{S}, \hat{P}_n, \beta_0\right) := \hat{S}\left(\hat{P}_n \csc\left(\beta_0\right)\right)^{1/2}. \tag{2.23b}$$

It can be deduced from (2.23) that $\theta(\cdot)$ depends on the independent parameters $\hat{S}$, $\hat{P}_n$, and β_0. We will explicitly note this dependence by denoting $\theta(\cdot)$ as $\theta(\cdot; \hat{S}, \hat{P}_n, \beta_0)$. In order to make our

results look less cumbersome, we will denote the sequence of independent parameters $\hat{S}$, $\hat{P}_n$, and β_0 simply as p. In terms of p, the solution $\theta(\cdot; \hat{S}, \hat{P}_n, \beta_0)$ will appear as $\theta(\cdot; \mathsf{p})$, and the result (2.23) will read

$$\theta(\hat{s}; \mathsf{p}) = \beta\left(\hat{s}; \omega\left(\mathsf{p}\right), \beta_0\right) - \beta\left(\frac{1}{2}; \omega\left(\mathsf{p}\right), \beta_0\right), \tag{2.24a}$$

where

$$\omega\left(\mathsf{p}\right) := \hat{S}\left(\hat{P}_n \csc\left(\beta_0\right)\right)^{1/2}. \tag{2.24b}$$

Midpoint deflection and force

In this section, we present formulae for calculating the midpoint deflection $\hat{w}_0$ and force $\hat{F}$. As we did with $\theta(\cdot)$, when we want to note the dependence of $\hat{w}_0$, $\hat{F}$, θ_0, and $\hat{\boldsymbol{\alpha}}\left(\cdot\right)$ on the independent parameters $\hat{S}$, $\hat{P}_n$, and β_0 explicitly, we will denote them as $\hat{w}_0\left(\mathsf{p}\right)$, $\hat{F}(\mathsf{p})$, $\theta_0(\mathsf{p})$ and $\hat{\boldsymbol{\alpha}}\left(\cdot; \mathsf{p}\right)$, respectively.

We can express $\hat{\boldsymbol{\alpha}}(\hat{s}; \mathsf{p})$ as $\hat{x}_1(\hat{s}; \mathsf{p})\hat{e}_1 + \hat{x}_2(\hat{s}; \mathsf{p})\hat{e}_2$, where $\hat{x}_1(\cdot; \mathsf{p})$, $\hat{x}_2(\cdot; \mathsf{p})$ are smooth real valued functions on $(0, 1/2)$. It follows from (2.11a) and (2.13a) that

$$\hat{x}_1'(\hat{s}; \mathsf{p}) = \hat{S}\cos(\theta(\hat{s}; \mathsf{p})), \tag{2.25a}$$

$$\hat{x}_2'(\hat{s}; \mathsf{p}) = \hat{S}\sin(\theta(\hat{s}; \mathsf{p})). \tag{2.25b}$$

Midpoint deflection Integrating (2.25b) from $\hat{s} = 0$ to $\hat{s} = 1/2$, simplifying the expression $\int_0^{1/2} \hat{x}_2'(\hat{s}; \mathsf{p})\, d\hat{s}$ that appears on the left hand side (LHS) of the resulting equation as $\hat{x}_2(1/2; \mathsf{p}) - \hat{x}_2(0; \mathsf{p})$, and then noting that $\hat{x}_2(1/2; \mathsf{p}) = \hat{w}_0(\mathsf{p})$ and $\hat{x}_2(0; \mathsf{p}) = 0$, we get that

$$\hat{w}_0\left(\mathsf{p}\right) = \hat{S}\int_0^{1/2} \sin\left(\theta\left(\hat{s}; \mathsf{p}\right)\right)\, d\hat{s}. \tag{2.26}$$

Midpoint force From the balance of external forces acting on the left half of the spicule specimen (Figure 2.5(B)) in the $\hat{\mathbf{f}}_2$ direction, we get that

$$\hat{F} + 2\hat{P}_2 = 0. \tag{2.27}$$

Substituting $\hat{P}_2$ in (2.27) from (2.18b) and then using (2.24b) and substituting the factor $\hat{P}_n \csc(\beta_0)$ as $\omega(\mathsf{p})^2/\hat{S}^2$, we get

$$\hat{F}(\mathsf{p}) = -2\omega(\mathsf{p})^2 \sin(\theta_0(\mathsf{p}) - \beta_0) \frac{1}{\hat{S}^2}. \tag{2.28}$$

Integrating (2.25a) from $\hat{s} = 0$ to $\hat{s} = 1/2$, simplifying the expression $\int_0^{1/2} \hat{x}_1'(\hat{s};\mathsf{p})\, d\hat{s}$ that appears on the LHS as $\hat{x}_1(1/2;\mathsf{p}) - \hat{x}_1(0;\mathsf{p})$, noting that $\hat{x}_1(1/2;\mathsf{p}) = 1/2$ and $\hat{x}_1(0;\mathsf{p}) = 0$, multiplying the resulting equation with $2/\hat{S}$, and then squaring the result, we get that

$$\frac{1}{\hat{S}^2} = 4\left(\int_0^{1/2} \cos(\theta(\hat{s};\mathsf{p}))\, d\hat{s}\right)^2. \tag{2.29}$$

Substituting the factor $1/\hat{S}^2$ in (2.28) from (2.29) and simplifying, we get that

$$\hat{F}(\mathsf{p}) = 8\omega(\mathsf{p})^2 \left(\int_0^{1/2} \cos(\theta(\hat{s};\mathsf{p}))\, d\hat{s}\right)^2 \sin(\beta_0 - \theta_0(\mathsf{p})). \tag{2.30}$$

Compatibility

Substituting $\theta(\cdot;\mathsf{p})$ in (2.29) from (2.24) and rearranging, we get

$$\hat{S} = \frac{1}{2}\left(\int_0^{1/2} \cos\left(\beta(\hat{s};\omega(\mathsf{p}),\beta_0) - \beta\left(\frac{1}{2};\omega(\mathsf{p}),\beta_0\right)\right) d\hat{s}\right)^{-1}. \tag{2.31}$$

Upper envelope of the equilibrium region and the closing equation

In order to derive our model's predictions for the force-displacement curves measured by the SS experiments in the loading phase, the spicule-specimen's equilibrium configurations first need to be extracted. We define what we physically mean by the spicule specimen's equilibrium configuration at the beginning of §2.4.1 (when the spicule specimen is in one of its equilibrium configurations,

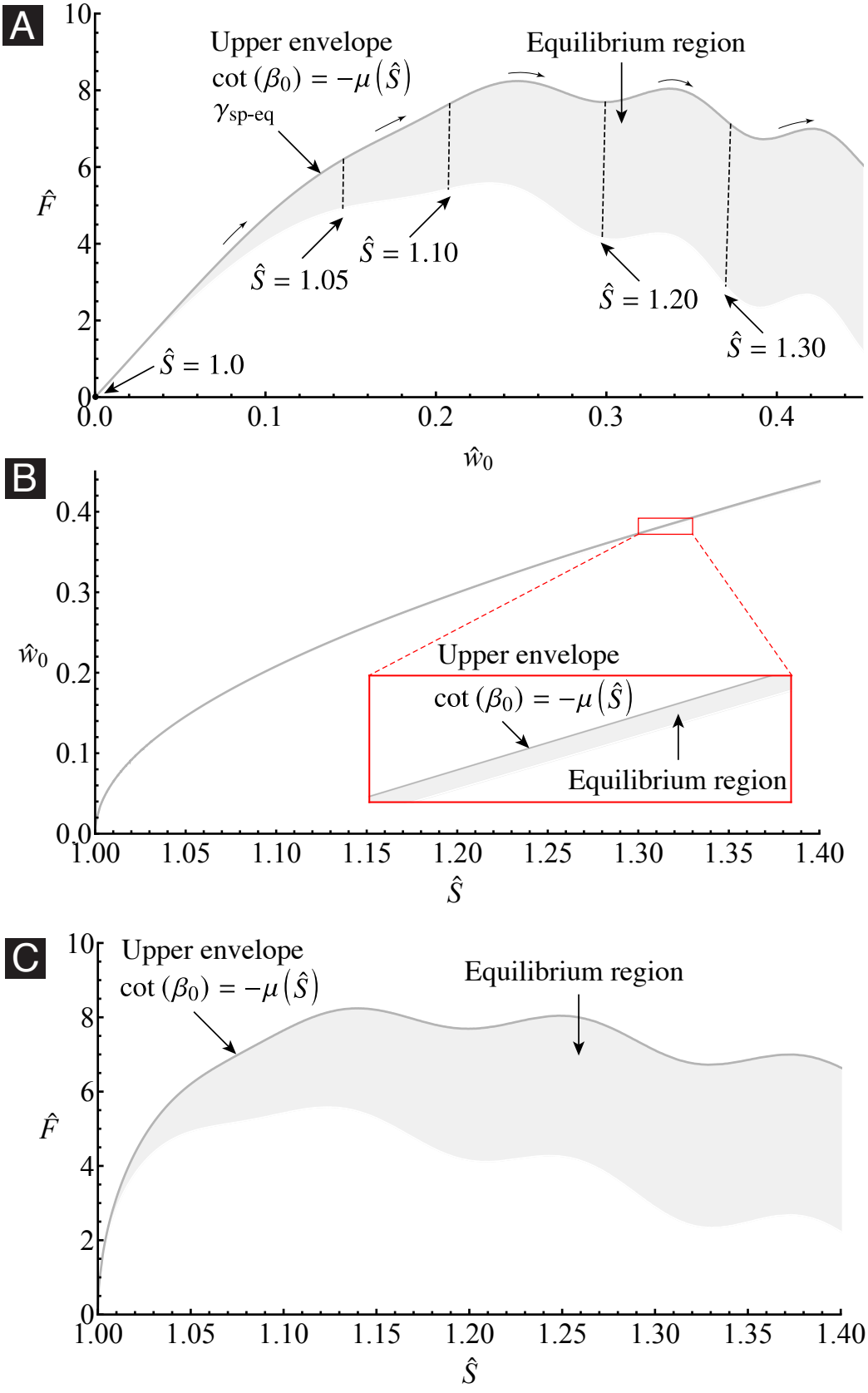

Figure 2.6: (Caption continued on next page)

Figure 2.6: The equilibrium region in the $\hat{w}_0$-$\hat{F}$, $\hat{S}$-$\hat{w}_0$, and $\hat{S}$-$\hat{F}$ space for a representative case. We consider the case in which the coefficient of friction varies as in (2.33) with $\mu_0 = 0.3$, $A = 0.2$, $\hat{\lambda} = 0.02\pi$, and $\phi = 0$, i.e., in which $\mu(\hat{S}) = 0.3\left(1 + 0.2\cos\left(\hat{S}/0.02\right)\right)$. For this case we computed the equilibrium regions using the procedure detailed in Algorithm 1. Subfigures (A), (B), and (C) show the equilibrium region in the $\hat{w}_0$-$\hat{F}$, $\hat{S}$-$\hat{w}_0$, and $\hat{S}$-$\hat{F}$ space, respectively. In each of the subfigures the equilibrium region is shown in light gray, while the upper envelope of the equilibrium region (i.e., the equilibrium curve) is shown as a dark gray curve. In (A) we mark a locus of configurations in which $\hat{S}$ is constant using a dashed black curve. The solid arrows above the equilibrium curve indicate that $\hat{S}$ strictly increases as we travel along the curve starting from the origin.

that does not necessarily mean that the MTS's cantilever wedge is also in one of its equilibrium configurations, i.e., that our entire mechanical system is in equilibrium. See §2.4.3 for further discussion of this issue). Mathematically, a spicule's equilibrium configuration can be described as an ordered set $\left(\hat{S}, \hat{P}_n, \beta_0\right)$ that satisfies the contact constitutive law (2.20) and the compatibility condition (2.31). We mark the equilibrium configurations, which were determined numerically using Algorithm 1, in the $\hat{w}_0$-$\hat{F}$, $\hat{S}$-$\hat{w}_0$, and $\hat{S}$-$\hat{F}$ spaces for a representative case in Figures 2.6(A), (B), and (C), respectively. For a given $\hat{S}$, there can exist more than one equilibrium configuration. This is partly because as can be seen from (2.17) and (2.20), the number $\cot(\beta_0)$ only needs to lie between certain bounds, specifically between $\pm\mu$. Therefore, in general, the sets of equilibrium states have non-zero measures in the $\hat{w}_0$-$\hat{F}$, $\hat{S}$-$\hat{w}_0$ or $\hat{S}$-$\hat{F}$ spaces.

However, it can be argued that in the loading portion of the SS experiments, $\hat{P}_n \geq 0$. Under some mild assumptions on the loading rate, it can be further argued[2] that $\cot(\beta_0)$ in fact achieves its lower bound, i.e., that

$$\cot(\beta_0) = -\mu. \tag{2.32}$$

As discussed in §2.1, it is reasonable to assume that μ varies along the spicule's length so that the value of μ depends on the contact position between the spicule and the trench's left edge, which depends on $\hat{S}$. We assume that the dependence of μ on $\hat{S}$ can be expressed as

$$\mu\left(\hat{S}\right) = \mu_0\left(1 + A\cos\left(\frac{\pi\hat{S}}{\hat{\lambda}} + \phi\right)\right), \tag{2.33}$$

where $\hat{\lambda} := \lambda/L$, $\lambda \in \mathbb{R}_{\geq 0}$. Here, λ μm is the wavelength of the assumed periodic variation of the coefficient of friction. Note that the value of the phase ϕ, depending on the positions of contacting points between the spicule specimens and the trench edges at the beginning of the experiments, may

[2]The mathematical analysis underlying this assertion is quite involved and therefore we plan on publishing it elsewhere.

not be the same as the value of ϕ in (2.1).

Therefore, in an equilibrium state, the value of β_0 is fully determined by the value of $\hat{S}$ in that state. More specifically, it follows from (2.32) that β_0 is equal to the value of $\beta_0\left(\hat{S}\right)$, where the function $\beta_0(\cdot) : [1, \infty) \to (0, \pi)$ is defined by equations

$$\sin\left(\beta_0\left(\hat{S}\right)\right) = \frac{1}{\sqrt{1+\mu\left(\hat{S}\right)^2}}, \tag{2.34a}$$

$$\cos\left(\beta_0\left(\hat{S}\right)\right) = \frac{-\mu\left(\hat{S}\right)}{\sqrt{1+\mu\left(\hat{S}\right)^2}}. \tag{2.34b}$$

As mentioned in §2.1, for simplicity, we take $\mu(\cdot)$ to be of the form given by (2.33).

It now follows from (2.31) that in the state mentioned above, the value of $\hat{P}_n$ is also fully determined by the value of $\hat{S}$; the value of $\hat{P}_n$ has to be a root of $f\left(\cdot; \hat{S}, \beta_0\left(\hat{S}\right)\right)$, and the function $f\left(\cdot; \hat{S}, \beta_0\right) : \mathbb{R}_{\geq 0} \to \mathbb{R}$ is defined by equation

$$f\left(\cdot; \hat{S}, \beta_0\right) = 1 - 2\hat{S}\int_0^{1/2} \cos\left(\beta\left(\hat{s}; \omega(\hat{S}, \cdot, \beta_0), \beta_0\right) - \beta\left(\frac{1}{2}; \omega(\hat{S}, \cdot, \beta_0), \beta_0\right)\right) d\hat{s}. \tag{2.35}$$

In general, $f\left(\cdot; \hat{S}, \beta_0\left(\hat{S}\right)\right)$ will have multiple roots. However, using practical considerations, it can be deduced that only the smallest of $f\left(\cdot; \hat{S}, \beta_0\left(\hat{S}\right)\right)$'s roots is relevant in the context of the SS experiments. We denote the value of that smallest root as $\hat{P}_n\left(\hat{S}\right)$, which can be computed using the Newton-Raphson method.

The results put forward in the last three paragraphs can be summarized by stating that, during the loading portion of the SS experiments, the equilibrium states have the form $\left(\hat{S}, \hat{P}_n\left(\hat{S}\right), \hat{\beta}_0\left(\hat{S}\right)\right)$. We call the set of the equilibrium states having this form the upper envelope of the equilibrium region (shown as gray curves in Figure 2.6). The upper envelope of the equilibrium region in the $\hat{w}_0$-$\hat{F}$ space can be expressed as the parametric curve

$$\gamma_{\text{sp-eq}} := \left\{\left(w_0^+\left(\hat{S}\right), \hat{F}^+\left(\hat{S}\right)\right) \mid \hat{S} \geq 1\right\}, \tag{2.36a}$$

where $\hat{w}_0^+(\cdot) : [1, \infty) \to \mathbb{R}_{\geq 0}$ is defined by the equation

$$\hat{w}_0^+\left(\hat{S}\right) = \hat{w}_0\left(\hat{S}, \hat{P}_n\left(\hat{S}\right), \hat{\beta}_0\left(\hat{S}\right)\right), \tag{2.36b}$$

and $\hat{F}^+ : [1, \infty) \to \mathbb{R}_{\geq 0}$ is defined by the equation

$$\hat{F}^+\left(\hat{S}\right) = \hat{F}\left(\hat{S}, \hat{P}_n\left(\hat{S}\right), \hat{\beta}_0\left(\hat{S}\right)\right). \tag{2.36c}$$

We will be referring to $\gamma_{\text{sp-eq}}$ simply as the spicule equilibrium curve. The equilibrium curve can be numerically constructed using Algorithm 1 after changing line number 5 in it to "Compute $\beta_0^+ \leftarrow \operatorname{arccot}\left(-\mu\left(\hat{S}\right)\right)$, then $\beta_0^- \leftarrow \beta_0^+$".

Algorithm 1 Procedure for computing the equilibrium region

1: **Input:** $\mu_0, A, \hat{\lambda}, \phi, \hat{S}^*$[a], and natural numbers $n_{\hat{S}}$, and n_{β_0}[b]
2: **Initialization:** $\hat{S} = 1$, $\hat{P}_n = 0$, $\hat{w}_0 = 0$, $\hat{F} = 0$, $\Delta\hat{S} = \hat{S}^*/n_{\hat{S}}$
3: **for** $\hat{S} = 1, 1 + \Delta\hat{S}, 1 + 2\Delta\hat{S}, \ldots, \hat{S}^*$ **do**
4: Compute $\mu\left(\hat{S}\right) \leftarrow \mu_0\left(1 + A\cos\left(\pi\hat{S}/\hat{\lambda} + \phi\right)\right)$
5: Compute $\beta_0^+ \leftarrow \operatorname{arccot}\left(-\mu\left(\hat{S}\right)\right)$ and $\beta_0^- \leftarrow \operatorname{arccot}\left(\mu\left(\hat{S}\right)\right)$
6: Compute $\Delta\beta_0 \leftarrow \left(\beta_0^+ - \beta_0^-\right)/n_{\beta_0}$
7: **for** $\beta_0 = \beta_0^-, \beta_0^- + \Delta\beta_0, \beta_0^- + 2\Delta\beta_0, \ldots \beta_0^+$ **do**
8: Solve for $\hat{P}_n$ as the smallest root of $f(\cdot; \hat{S}, \beta_0)$[c]
9: Construct $\theta(\cdot; \mathsf{p})$ from (2.24) using $\hat{S}$, $\hat{P}_n$,and β_0
10: Determine $\hat{w}_0(\mathsf{p})$ and $\hat{F}(\mathsf{p})$ from (2.26), (2.30), (2.24b) and (2.18c)
11: Save the points $(\hat{S}, \hat{w}_0(\mathsf{p}))$, $(\hat{S}, \hat{F}(\mathsf{p}))$, and $(\hat{w}_0(\mathsf{p}), \hat{F}(\mathsf{p}))$ as respective members of the equilibrium regions in the $\hat{S}$-$\hat{w}_0$, $\hat{S}$-$\hat{F}$, and $\hat{w}_0$-$\hat{F}$ spaces
12: **end for**
13: **end for**
14: **Output:** A collection of $n_{\hat{S}} \times n_{\beta_0}$ equilibrium points in each of the $\hat{S}$-$\hat{w}_0$, $\hat{S}$-$\hat{F}$, and $\hat{w}_0$-$\hat{F}$ spaces

[a] The parameter $\hat{S}^* > 1$ specifies the maximum value of $\hat{S}$ among all the computed equilibrium configurations.
[b] The parameters $n_{\hat{S}}$ and n_{β_0}, respectively, specify the number of different $\hat{S}$ and β_0 values among the computed equilibrium configurations.
[c] defined in (2.35)

Remarks

1. As can be noted from (2.36), the curve $\gamma_{\text{sp-eq}}$ is parameterized by the total length $\hat{S}$. The left end of the curve, i.e., the point $(0, 0)$, corresponds to $\hat{S} = 1$ (see Figure 2.6(A)). Thus, the value of $\hat{S}$ strictly increases as we travel along the curve starting from the origin.

2. The equilibrium curves from our model for the cases in which $\mu_0 = 0.0$ or 0.6 and $A = 0.0$ or 0.4 are shown in Figure 2.7(A). In all cases, as expected, the equilibrium curves predicted by our model asymptote to the one predicted by the EB theory (see equation (5) in [31]) as the midpoint deflection becomes small.

3. When $A = 0.0$, the most noticeable aspect of the equilibrium curves from our model is that the force initially increases and later decreases with the midpoint deflection. In contrast, in the equilibrium curve predicted by the EB theory (see Figure 2.7(A)), the force always increases with the deflection.

4. When $A \neq 0.0$, the equilibrium curves from our model have an undulatory nature. The sawtooth pattern in our model is a consequence of these undulations. The undulations appear to become more pronounced as the values of $\hat{S}$ and $\hat{w}_0$ increase, starting from when $\hat{F}$ is about to reach its maximum value. As noted from Figure 2.1 in the SS experiments, the sawtooth-pattern is pronounced in this very same region.

2.4.3 Force-displacement curves that will be measured in the simply-supported experiments

In §2.4.2, we discussed that only a subset (specifically, the upper envelope) of the spicule's equilibrium configurations is relevant in the loading phase of the SS experiments. In the $\hat{w}_0$-$\hat{F}$ space, we termed that upper envelope (2.36) the spicule-equilibrium curve, $\gamma_{\text{sp-eq}}$. The spicule configurations sampled by the experiment have to necessarily lie on $\gamma_{\text{sp-eq}}$. However, not all the configurations in $\gamma_{\text{sp-eq}}$ will be sampled during the loading portion of the SS experiment. This is because the spicule being in equilibrium does not necessarily mean that the MTS's wedge is in one of its equilibrium configurations. The force acting on the spicule's midpoint has to be provided by the wedge's apex (shown marked in Figure 2.4(A)). However, that force may not necessarily be balanced by the force acting on the wedge's base due to the MTS's cantilever's deformation.

To be more precise, we analyze the force balance on the wedge of the MTS. We assume that in the SS experiments, the total length $\hat{S}$ evolves in the manner dictated by the function $\hat{S} : [0, \tau^*] \to [1, \infty)$. As mentioned previously, the experiment will only sample configurations on $\gamma_{\text{sp-eq}}$. At the time

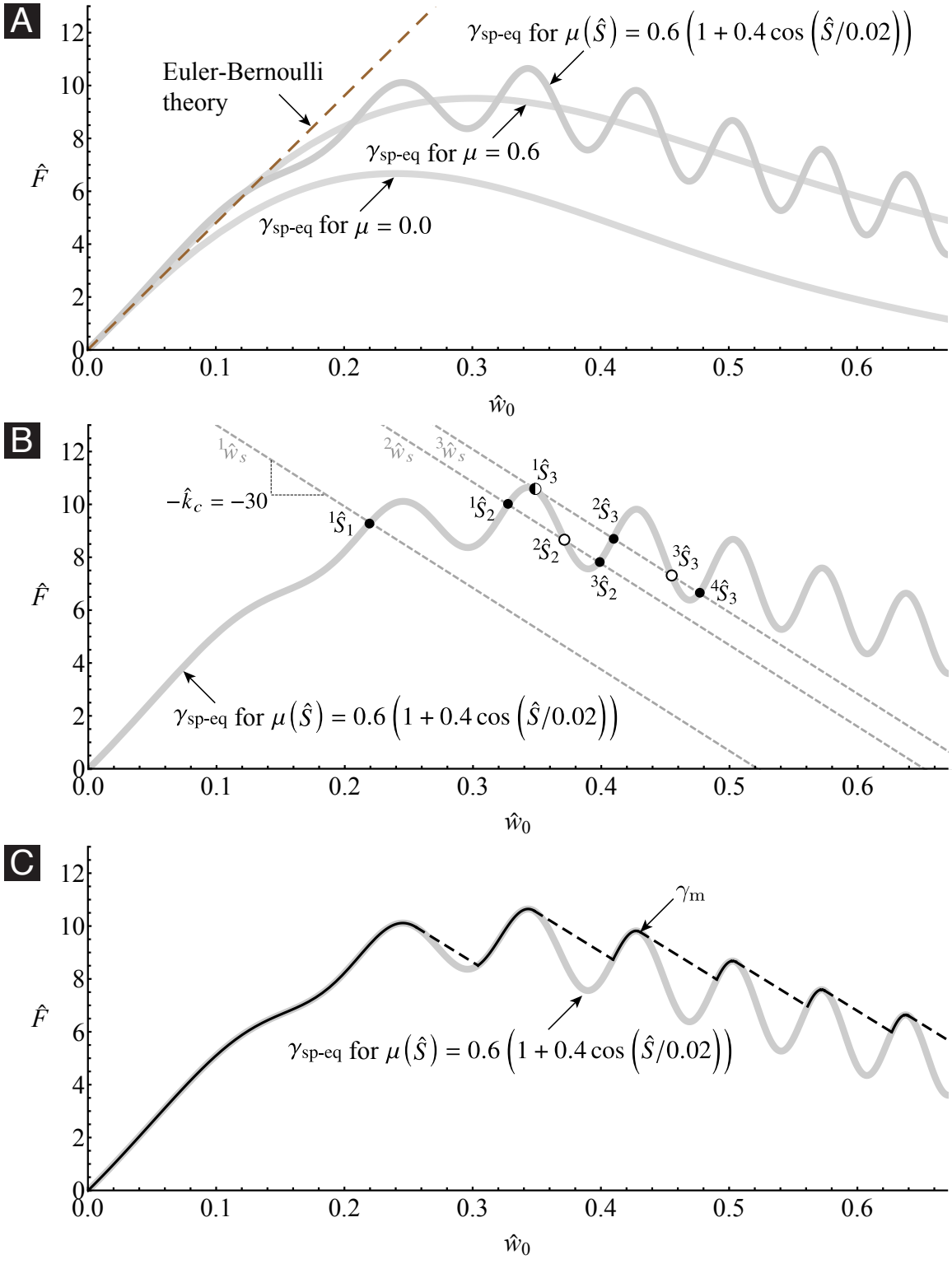

Figure 2.7: (Caption continued on next page)

Figure 2.7: Equilibrium and measured force-displacement curves. (A) shows the equilibrium curves, $\gamma_{\text{sp-eq}}$, for the cases $\mu\left(\hat{S}\right) = 0.6\left(1 + 0.4\cos\left(\hat{S}/0.02\right)\right)$, $\mu\left(\hat{S}\right) = 0.6$, and $\mu\left(\hat{S}\right) = 0.0$, using gray lines. The equilibrium curve predicted by the Euler-Bernoulli theory is also shown for reference, using dashed brown lines. (B) and (C) again show the equilibrium curve corresponding to $\mu\left(\hat{S}\right) = 0.6\left(1 + 0.4\cos\left(\hat{S}/0.02\right)\right)$. They only consider this equilibrium curve and a cantilever stiffness of $\hat{k}_c = 30$ and show the measured curves for two different $\hat{w}_s(\cdot)$. (B) considers the $\hat{w}_s(\cdot)$ given in (2.38) for ${}^1w_s$, ${}^2w_s$, and ${}^3w_s$ equal to 0.52, 0.65, and 0.69, respectively. In (B), on the equilibrium curve, we mark the overall-equilibrium configurations at some three time instances that, respectively, belong to the intervals $(0, \tau_1]$, $(\tau_1, \tau_2]$, and $(\tau_2, \tau_3]$, which appear in (2.38). The stable overall-equilibrium configurations are shown as filled circles; the unstable configurations as open circles; and the partially-stable configurations as semi-filled circles. All overall-equilibrium configurations corresponding to the same time instance are connected using a dashed gray line. The three dashed gray lines are the graphs of the function (2.37b) at the three previously mentioned time instances. The graph of the measured curve in this case consists of just the three points that are shown as ${}^1\hat{S}_1$, ${}^1\hat{S}_2$, and ${}^2\hat{S}_3$. (C) shows the measured curve γ_m for the case in which $\hat{w}_s(\cdot)$ is some continuous, monotonically increasing function of time. The measured curve in this case is the discontinuous curve that is shown using thin black lines. The straight line segments that span the discontinuities of this curve signify the slip instabilities occurring at the trench edges.

instance τ, the measured midpoint deflection will be $\hat{w}_0^+\left(\hat{S}\left(\tau\right)\right)$, i.e., $\hat{w}_0(\tau) = \hat{w}_0^+\left(\hat{S}\left(\tau\right)\right)$, and the measured force acting on the spicule's midpoint will be $\hat{F}^+\left(\hat{S}(\tau)\right)\hat{\mathbf{f}}_2$, i.e., $\hat{F}(\tau) = \hat{F}^+\left(\hat{S}(\tau)\right)$. This force needs to be provided by the wedge's apex. Therefore, the force acting on the wedge's apex will be $-\hat{F}^+\left(\hat{S}(\tau)\right)\hat{\mathbf{f}}_2$. It follows from (2.4) and (2.2) that the force acting on the wedge's base is $\hat{k}_c\left(\hat{w}_s(\tau) - \hat{w}_0^+\left(\hat{S}\left(\tau\right)\right)\right)\hat{\mathbf{f}}_2$, where $\hat{w}_s(\cdot)$ prescribes how the stage-displacement evolves with time during the experiment. Therefore, the equilibrium condition for the wedge gives that $\hat{S}(\tau)$ be a root of the function $R(\cdot;\tau) : [1,\infty) \to \mathbb{R}$,

$$R\left(\hat{S};\tau\right) := \hat{F}_{\text{cant}}(\hat{w}_0^+\left(\hat{S}\right);\tau) - \hat{F}^+\left(\hat{S}\right), \tag{2.37a}$$

where

$$\hat{F}_{\text{cant}}(\hat{w}_0;\tau) := \hat{k}_c(\hat{w}_s(\tau) - \hat{w}_0). \tag{2.37b}$$

We will be referring to the point $\left(\hat{w}_0^+\left(\hat{S}\left(\tau\right)\right), \hat{F}^+\left(\hat{S}\left(\tau\right)\right)\right)$, where $\hat{S}\left(\tau\right)$ is a root of $R(\cdot;\tau)$, an overall-equilibrium configuration at the time instance τ. The overall-equilibrium configurations at the time instance τ can be visualized in the $\hat{w}_0$-$\hat{F}$ space (see, e.g., Figure 2.7(B)) as the intersection points between $\gamma_{\text{sp-eq}}$ and the graph of $\hat{F}_{\text{cant}}(\cdot;\tau)$.

Evolution postulate and our model's prediction for the measured force-displacement curves

In order to derive our model's prediction for the measured force-displacement curve, we consider a thought experiment in which

$$\hat{w}_s(\tau) = \begin{cases} {}^1\hat{w}_s, & \tau \in (0, \tau_1], \\ {}^2\hat{w}_s, & \tau \in (\tau_1, \tau_2], \\ {}^3\hat{w}_s, & \tau \in (\tau_2, \tau_3]. \end{cases} \tag{2.38}$$

In Figure 2.7(B), considering a representative $\hat{k}_c$, we mark and label the overall-equilibrium configurations at the three different stage displacements ${}^1\hat{w}_s$, ${}^2\hat{w}_s$, and ${}^3\hat{w}_s$. As noted from the figure, there can exist more than one overall-equilibrium configurations at a given stage displacement. At the stage displacement ${}^1\hat{w}_s$, there exists only one overall-equilibrium configuration. We denote the total length in that configuration as ${}^1\hat{S}_1$ and label the configuration as ${}^1\hat{S}_1$ in Figure 2.7(B). However, at ${}^2\hat{w}_s$, there exist three overall-equilibrium configurations. As before, we label these configurations in Figure 2.7(B) using their total lengths, i.e., as ${}^1\hat{S}_2$, ${}^2\hat{S}_2$, and ${}^3\hat{S}_2$. At ${}^1\hat{w}_s$, it is clear that the experiment will measure the total length ${}^1\hat{S}_1$, i.e., $\hat{S}(\tau) = {}^1\hat{S}_1$ for all $\tau \in (0, \tau_1]$. However, at ${}^2\hat{w}_s$, which one of the three total lengths will the experiment measure? From a theoretical mechanics perspective, the question just posed is the same as the one analyzed in [59, 60, 50], though the mechanical system investigated in [59, 60, 50] is different from the one studied in this chapter. Following the analysis presented in [59, 60, 50], a prerequisite for an overall-equilibrium configuration to be measurable is that it is *stable*. The overall equilibrium state with total length ${}^j\hat{S}_i$ is stable, iff

$$R'\left({}^j\hat{S}_i; \tau\right) = -\hat{k}_c\ \hat{w}_0^{+\prime}\left({}^j\hat{S}_i\right) - \hat{F}^{+\prime}\left({}^j\hat{S}_i\right) < 0. \tag{2.39}$$

Using (2.39), it can be deduced from Figure 2.7(B) that ${}^1\hat{S}_2$ and ${}^3\hat{S}_2$ are stable, while ${}^2\hat{S}_2$ is unstable. However, the question still remains as to which of ${}^1\hat{S}_2$ and ${}^3\hat{S}_2$ will be measured. To answer this question, as done in [60], we postulate that among the different measurable configurations, the system will evolve into the one that is closest to the last measured configuration. In the current case, this evolution postulate implies that the configuration that the system will chose among the measurable configurations will be the one whose total length is closest to the one in the last measured

configuration. The last measured configuration in our thought experiment is ${}^{1}\hat{S}_1$. Therefore, when the stage displacement is ${}^{2}\hat{w}_s$, amongst ${}^{1}\hat{S}_2$ and ${}^{3}\hat{S}_2$, the experiment will measure the one that is closer to ${}^{1}\hat{S}_1$. It follows from remark 1 in §2.4.2 and Figure 2.7(B) that ${}^{1}\hat{S}_1 < {}^{1}\hat{S}_2 < {}^{3}\hat{S}_2$. Therefore, at ${}^{2}\hat{w}_s$, the experiment will measure the configuration ${}^{1}\hat{S}_2$, i.e., $\hat{S}(\tau) = {}^{1}\hat{S}_2$ for all $\tau \in (\tau_1, \tau_2]$. When the stage displacement is ${}^{3}\hat{w}_s$, there are four overall equilibrium configurations. We label those as ${}^{j}\hat{S}_3$, $j = 1, .., 4$, in Figure 2.7(B). Through similar analysis, it can be deduced that the system will measure ${}^{2}\hat{S}_3$ at ${}^{3}\hat{w}_s$, implying that $\hat{S}(\tau_3) = {}^{2}\hat{S}_3$ for all $\tau \in (\tau_2, \tau_3]$.

Now we consider the measured force-displacement curve for arbitrary $\gamma_{\text{sp-eq}}$, $\hat{w}_s(\cdot)$, and $\hat{k}_c$. The given $\hat{w}_s(\cdot)$ can be approximated using a function of the form (2.38). For example, we consider a large number of equally spaced time instances in $[0, \tau^*]$, say τ_0, τ_1, τ_2, etc., and define the value of the approximate-$\hat{w}_s(\cdot)$ for any time instance in $(\tau_i, \tau_{i+1}]$ to be the constant value ${}^{i+1}\hat{w}_s := \hat{w}_s(\tau_{i+1})$. We can construct the evolution of the measured approximate-$\hat{S}(\cdot)$ by carrying out analysis similar to the one presented in the previous paragraph. By increasing the number of time instances, $\hat{S}(\cdot)$ can be approximated to any desired degree.

After determining the evolution of the measured configuration, i.e., $\hat{S}(\cdot)$, the measured force-displacement curve can be constructed as

$$\gamma_{\text{m}} = \left\{ \left(\hat{w}_0^+ \left(\hat{S}(\tau) \right), \hat{F}^+ \left(\hat{S}(\tau) \right) \right) \mid \tau \in [0, \tau^*) \right\}. \tag{2.40}$$

We provide a systematic procedure for numerically constructing γ_{m} in Algorithm 2. In Figure 2.7(C), we show a representative γ_{m} (black) by considering a continuous, monotonically increasing $\hat{w}_s(\tau)$. The corresponding spicule equilibrium curve $\gamma_{\text{sp-eq}}$ (gray) and cantilever stiffness $\hat{k}_c$ are the same as those in Figure 2.7(B). As can be seen in (C), the curve γ_{m} is discontinuous, i.e., it is a union of non-intersecting smooth curves. We connect the nearest terminal ends of adjoining smooth curve segments in γ_{m} using dashed line segments. The dashed line segments physically denote mechanical instabilities. The quantities $\hat{w}_0$, $\hat{F}$, and $\hat{S}$ all change by a finite amount during the occurrence of those instabilities. With its discontinuities, γ_{m}, at least qualitatively, captures the sawtooth pattern observed in the SS experiments.

Algorithm 2 Procedure for computing the measured force-displacement curve

Input: $\gamma_{\text{sp-eq}}$, $\hat{w}_s(\cdot)$, $\hat{k}_c$, τ^*, and a natural number n[a]
Initialization: $\tau_0 = 0$, $\hat{S}_0 = 1$, $\Delta\tau = \tau^*/n$
for $i = 0, 1, 2, \ldots, n$ **do**
    Compute $\tau_{i+1} \leftarrow \tau_i + \Delta\tau$
    Construct $R(\cdot; \tau_{i+1})$ from (2.37) using $\gamma_{\text{sp-eq}}$, $\hat{w}_s(\cdot)$, and $\hat{k}_c$
    Solve for the roots of $R(\cdot; \tau_{i+1})$. We denote those roots as ${}^j\hat{S}_{i+1}$, where $j \in \mathcal{J} := \{1, 2, \ldots, n_{i+1}\}$
    Set $\hat{S}_{i+1} \leftarrow {}^{k^*}\hat{S}_{i+1}$, where $k^* = \arg\min_{k\in\mathcal{K}} \left|{}^k\hat{S}_{i+1} - \hat{S}_i\right|, \mathcal{K} := \left\{p \in \mathcal{J} \mid R'({}^p\hat{S}_{i+1}; \tau_{i+1}) < 0\right\}$[b]
    Save $\left(\hat{w}_0^+\left(\hat{S}_{i+1}\right), \hat{F}^+\left(\hat{S}_{i+1}\right)\right)$ as a point belonging to the measured force-displacement curve
end for
Output: A collection of n points that belong to the measured force-displacement curve

[a] The parameter n specifies the number of computed points on the measured force-displacement curve.
[b] $R'(\cdot; \tau)$ is defined in (2.39).

2.5 Comparing theoretical predictions for the force-displacement curves with their experimental measurements

In §2.4.3, we discussed how the force-displacement curves predicted by our model qualitatively capture the sawtooth pattern (see Figure 2.7(C)). In this section, we discuss how the predictions from our model for the force-displacement curves compare with their measurements reported in [31].

Kochiyama et al. [31] reported measurements of force-displacement curves from 38 SS experiments. We place those curves in the following three categories based on the nature of the sawtooth pattern observed in them.

C.1 Curves displaying a clear sawtooth pattern.

C.2 Curves displaying a nominal sawtooth pattern.

C.3 Curves displaying almost no sawtooth pattern.

Category *C.1* This category consists of curves from the SS experiments which Kochiyama et al. labeled as SS4, SS8, SS11, SS12, SS14, SS16, SS18, SS20, SS25, SS30, SS32, SS33, SS35, and SS38 (see Figure 2.9). There are 14 curves in total in this category.

Category *C.2* This category consists of curves from the SS experiments which Kochiyama et al. labeled as SS5, SS7, SS17, SS19, SS22, SS24, SS26, and SS29 (see Figure 2.10). There are eight curves in total in this category.

Category *C.3* This category consists of curves from the SS experiments which Kochiyama et al. labeled as SS1, SS2, SS3, SS6, SS9, SS10, SS13, SS15, SS21, SS23, SS27, SS28, SS31, SS34, SS36, and SS37 (see Figure 2.11). These are 16 curves in total.

We compare our model's predictions with each of the measured curves in Figures 2.9 (Category *C.1*), 2.10 (Category *C.2*), and 2.11 (Category *C.3*). The values of the parameters μ_0, A, λ, and ϕ were manually adjusted so that our model's predictions matched the measured curves as closely as possible. These manually chosen values are shown alongside each comparison (see top right hand corner of each subfigure in Figures 2.9–2.11). In each of the subfigures of Figures 2.9–2.11, our model's prediction for the measured curve is shown in black (consisting of solid and dashed segments). The measured curve is shown in blue. For reference, we also include the prediction from the EB theory, as well as from our model for the case $\mu_0 = 0$. The prediction from the EB theory (brown dashed) appears as a straight line, while that from our model for the case $\mu_0 = 0$ (brown solid) appears as a section of an upside down parabola.

When comparing our model to the curves from *C.1* and *C.2*, the values of μ_0, A, λ, and ϕ were adjusted, whereas when comparing to the curves from *C.3*, only the value of μ_0 was adjusted. We will explain this difference shortly after we discuss the former. The values chosen for ϕ do not have much experimental significance, since they primarily correlate with the position of contacting points between the spicule specimens and the trench edges at the beginning of the experiments. The values of A and λ do have experimental significance, as we expect their values to correlate with the variation in spicules' surface friction. The mean-range of the values chosen for λ when comparing to curves from *C.1* and *C.2* are, in the format of mean-(minimum, maximum), 10.883-(5.498, 25.133) and 44.670-(23.562,58.905), respectively (see Figure 2.8(A)). The mean-range of the values chosen for A when comparing to curves from *C.1* and *C.2* are 0.145-(0.030, 0.333) and 0.074-(0.040, 0.135), respectively. A graphical representation of the distribution of the values chosen for A is shown as error bars in Figure 2.8(B). We would consider the chosen values for A and λ to be reasonable if

they were, respectively, close to other estimates of A and λ that were arrived at independently. For ascertaining how reasonable the values chosen for A and λ are, it would be ideal if we could directly measure the variation of the coefficient of friction along the spicules' lengths, perhaps using an Atomic Force Microscope (AFM). Unfortunately, we currently do not have such AFM data available to us (see §2.6 for further discussion).

We considered the possibility of evaluating the values chosen for A and λ using the spicules' SEM images, such as those shown in Figure 2.3. Though we believe that the parameter A depends on the spicules' surface topography, we do not currently have an insight into the mathematical nature of that dependence. Consequently, we are unable to gauge the reasonableness of the values chosen for A from the spicules' SEM images. We are more confident of evaluating λ's chosen values using the SEM images. We denote the projected thickness of a spicule on an image as z, and define the topography map: $s \mapsto z(s)$. If we calculate the Fourier spectrum of $z(s)$, we expect the dominant angular frequency in that spectrum to be a good estimate for $2\pi/\lambda$. However, we were unable to successfully carry out such an evaluation. The reason behind this can be explained through a rough estimation as follows. As mentioned previously, the means of the values chosen for λ when comparing to the curves from *C.1* and *C.2* are ≈ 11 and 45 μm, respectively. In order to evaluate the soundness of these values using the aforementioned Fourier analysis, SEM images with a horizontal field width (HFW) of ideally 10 times the expected wavelength (around 450 μm) would be needed. The resolution in our SEM images with such HFW would be limited to around 0.29 μm. Considering that the outer-layer thickness of a spicule is typically 0.4 μm [18] and assuming that at least 10 pixels are needed on an image for describing the undulation in a spicule's lateral surface, a resolution of ideally 0.04 μm is required. Therefore, the competition between the HFW and the resolution of SEM images prevents us from evaluating the reasonableness of the values chosen for λ from the spicules' SEM images.

When comparing to the curves from category *C.3*, we only adjusted the value of μ_0. Our model predicts the lack of any sawtooth pattern when $A = 0$, i.e., when the coefficient of friction is constant along the spicule's length. Since the curves in *C.3* displayed almost no sawtooth-pattern, we took $A = 0$ when comparing to the curves from this category. Due to the form of $\mu(\cdot)$ given in (2.33), with $A = 0$, the values of λ and ϕ become irrelevant.

We show the values we chose for μ_0 when comparing to the curves from *C.1*–*C.3* in Figure 2.8(B). The mean-range of the values chosen for μ_0 when comparing our model's predictions to the curves from *C.1*, *C.2*, and *C.3* are 0.656-(0.284, 1.3), 0.688-(0.52, 1.07), and 0.520-(0.0,1.0), respectively. We consider a final category of curves, *C.4*, which consists of the curves SS8 and SS32 from *C.1*, SS24 from *C.2*, and SS13 and SS36 from *C.3*. We believe that the curves from *C.4* are suspect. Within the context of beam models, the EB theory provides an upper bound for the force, while our model for the case $\mu_0 = 0$ provides a lower bound. As can be seen from Figure 2.12, the forces in the curves from *C.4* sometimes exceed the force predicted by the EB theory. We speculate that the spicules in the experiments related to *C.4* were unable to slide due to some reason, perhaps due to a protrusion on the spicule's surface getting stuck at the trench's edge. On excluding the curves from *C.4*, we get the mean-range of the values chosen for μ_0 to be 0.584-(0.284,0.93), 0.633-(0.52, 0.77), and 0.457-(0.0, 0.7) for *C.1*, *C.2*, and *C.3*, respectively. The mean-range considering all curves except those from *C.4* is 0.541-(0.0, 0.93).

As mentioned previously, we were unable to directly characterize the $\mu(\cdot)$ in our experiments. Note that the contact in our experiments is between silica (spicule) and stainless steel (trench edge). Therefore, as an alternative, we compare the values we chose for μ_0 to the values reported in literature for the coefficient of friction between glass and different types of steel, see Table 2.1. We mark the minimum and the maximum of the values shown in Table 2.1, which are respectively 0.5 and 0.721, as green dashed lines in Figure 2.8(B).

As can be noted from Figure 2.8(B), the values we chose for μ_0 are quite reasonable.

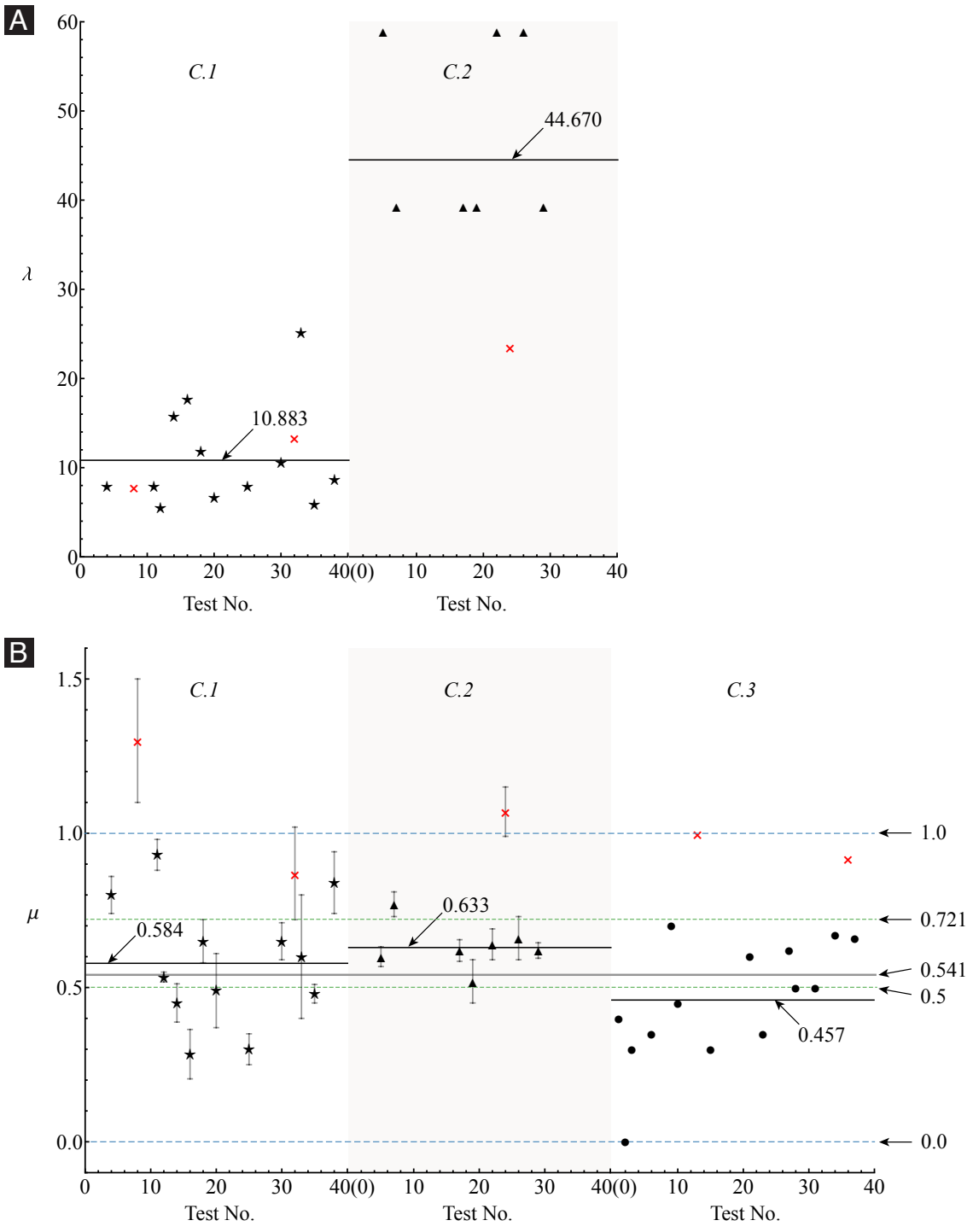

Figure 2.8: (Caption continued on next page)

Figure 2.8: Distribution of the values we chose for λ and μ_0 to get the predictions from our model for the force-displacement curves to compare favorably with their experimental measurements. Subfigure (A) consists of two plots, which show the chosen values for λ that we arrived at when comparing to curves from *C.1* and *C.2*, respectively. Subfigure (B) consists of three plots, which show the chosen values for μ_0 that we arrived at when comparing to curves from *C.1*, *C.2*, and *C.3*, respectively. All plots belonging to either (A) or (B) share the same y-axis. The x-axis in all plots in both (A) and (B) gives the test number, which ranges from 0 to 40. We use black five-pointed star, black up-pointing triangle, and black circle to mark the values we chose when comparing, respectively, to curves from *C.1*, *C.2*, and *C.3*. However, if the curve corresponding to a chosen value also belonged to *C.4* then we show that chosen value using a red cross. In each plot a black horizontal line is used to mark the mean of the chosen values in that plot. In computing the means, we excluded a chosen value if the curve that it corresponds to also belonged to *C.4*. The remainder of the statements in this caption pertain only to (B). The gray horizontal line (labeled as 0.541) that runs across all plots in (B) marks the mean of values we chose for μ_0 when comparing to all curves not from *C.4*. We mark the maximum (labeled as 0.721) and the minimum (labeled as 0.5) of the measured values for the coefficient of friction between glass and steels that are shown in Table 2.1. In general, the coefficient of friction is expected to lie between 0 and 1. These two values are shown marked using blue dashed lines. The size of the error bar around each value chosen for μ_0 when comparing to a curve from either *C.1* or *C.2* is proportional to the value chosen for A in that comparison. Note that there are no error bars in the plot corresponding to *C.3*, since when comparing to curves from that category we took $A = 0$ (see §2.5 for details).

Materials	Geometry	Surface condition	Coefficient of friction
Glass–Hard steel [61]	plane–spherical end of a rod (of diameter 2.54mm)	polished, clean, dry	0.605
Glass–Mild steel [61]	plane–spherical end of a rod (of diameter 2.54mm)	polished, clean, dry	0.721
Glass–Mild steel [62]	plane–sphere (of diameter 5 mm)	polished, clean, dry	0.51-0.61
Glass–Stainless steel [63]	—	polished, in vacuum	0.5
Stainless steel (with silica coating)–Stainless steel [64]	plane–sphere (of diameter 10 mm)	in air	0.7

Table 2.1: Estimates for the coefficient of friction between glass and steel from literature

2.6 Concluding remarks

1. As can be noted from Table 2.1 and Figure 2.8(B), the values of μ_0, which were chosen to match our model's predictions as closely as possible with the measurements of [31] are quite consistent with the values reported in literature for the coefficient of friction between glass and steel (note that the contact in our experiments is between silica (spicule) and stainless steel (trench edge)). This consistency supports the view that it is valid to use the developed model to interpret Kochiyama et al.'s SS experiments.

2. It is unlikely that the friction coefficient varies in a sinusoidal fashion along the spicule's length. It is even more unlikely that the coefficient of friction varies in the exact same manner

at both the left and the right trench edges during the experiment, as assumed in our model. The goal of assuming that the variation of the coefficient of friction along the spicule's length was symmetric about the spicule's midpoint was to make the problem tractable. However, the decision to model the variation of the coefficient of friction using a single sinusoid was more deliberate. We have compared the predictions from other versions of our model that incorporate more realistic variations for the friction coefficient with the experimental curves. These more realistic variations involved superposition of multiples sinusoids, and consequently involved a larger number of free parameters than the presented single sinusoidal variation, which contains four free parameters, namely μ_0, A, λ, and ϕ. Unsurprisingly, the predictions from those other versions of our model match the experimental curves better than those from the presented version of the model. Despite the above fact, we chose to focus this chapter on the version based on the single sinusoidal variation, since our primary goal was to present insight into the potential mechanism(s) underlying the sawtooth pattern, rather than to analytically reproduce the measured curves. And among the different versions of our model that we studied, we believe that the one based on the single sinusoidal variation illustrates the sawtooth mechanism captured by our model in the clearest manner.

3. The mechanism underlying the sawtooth patterns in our experiments is similar to the surface topography (roughness) based mechanism put forward for explaining the stick-slip phenomenon [65, 66, 67]. The controlling factors in the surface topography mechanism of stick-slip are the surface's roughness and the stiffness of the loading system, which are the same as the ones in our model's mechanism for the sawtooth pattern if we assume that the friction variation in our work is primarily due to the spicule's surface roughness. One difference in the mechanics of the SS experiments and the stick-slip phenomenon is that in the SS experiments, the spicule is slipping both before and after the occurrence of an instability, while in the stick-slip phenomenon, the specimen is stationary before the occurrence of an instability, and is sliding afterwards.

4. Our preliminary research suggests that there can exist an alternative model for the SS experiments, which is also capable of capturing the sawtooth patterns in the measured force-displacement curves. Interestingly, in that model, it is not required to assume that the coefficient

of friction varies along the spicule's length. Since we were unable to experimentally ascertain that the coefficient of friction indeed varied along the spicule's length, a model that does not require the assumption of a varying friction coefficient may seem preferable to the one that does. However, this alternative model also contains assumptions that cannot be readily justified through experiments. Furthermore, we were unable to derive any quantitative predictions from that different model for the measured force-displacement curves. For these reasons, we gave preference to the variable friction based model that we presented in this chapter.

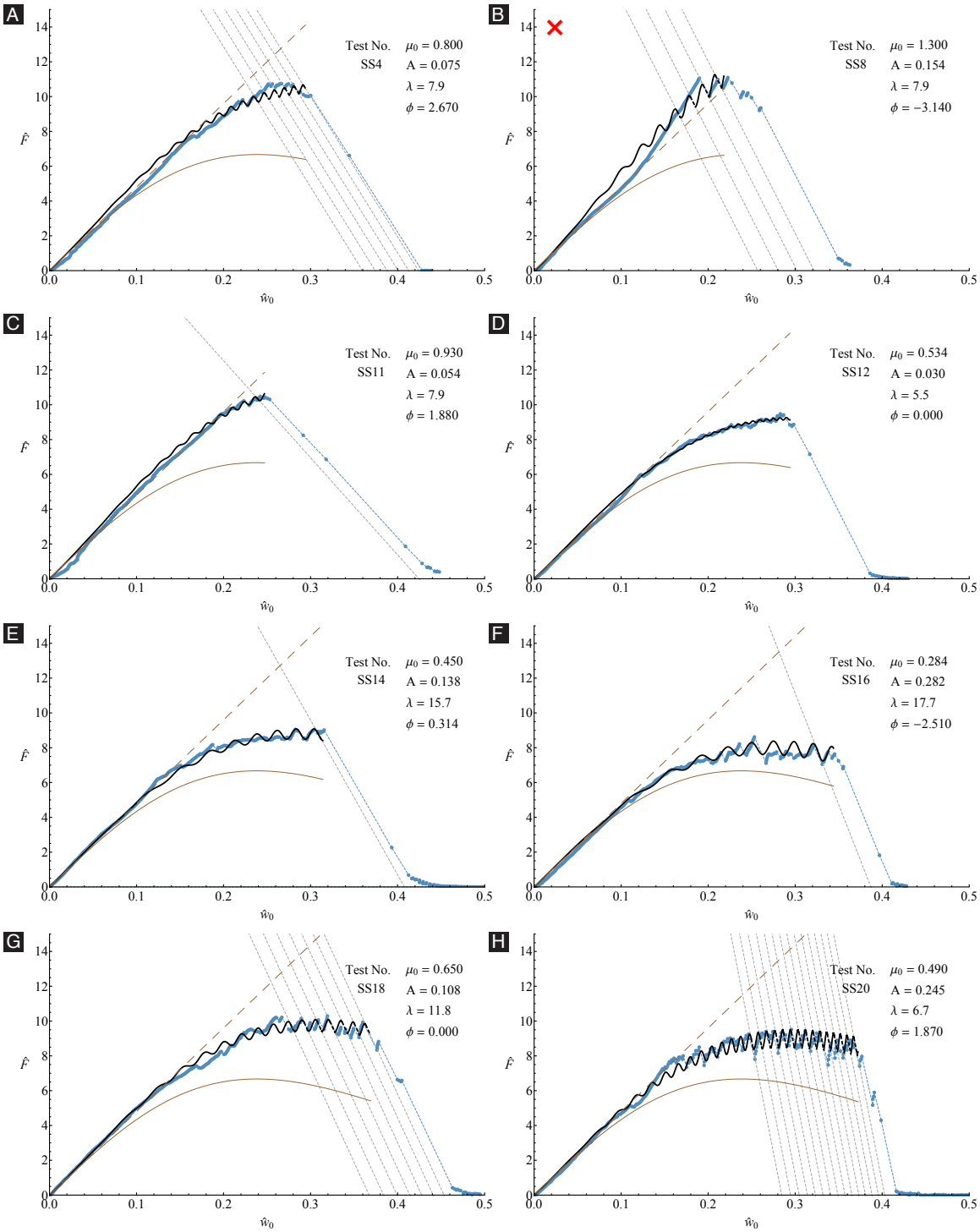
A
Test No. SS4
$\mu_0 = 0.800$
A = 0.075
$\lambda = 7.9$
$\phi = 2.670$
B
Test No. SS8
$\mu_0 = 1.300$
A = 0.154
$\lambda = 7.9$
$\phi = -3.140$
C
Test No. SS11
$\mu_0 = 0.930$
A = 0.054
$\lambda = 7.9$
$\phi = 1.880$
D
Test No. SS12
$\mu_0 = 0.534$
A = 0.030
$\lambda = 5.5$
$\phi = 0.000$
E
Test No. SS14
$\mu_0 = 0.450$
A = 0.138
$\lambda = 15.7$
$\phi = 0.314$
F
Test No. SS16
$\mu_0 = 0.284$
A = 0.282
$\lambda = 17.7$
$\phi = -2.510$
G
Test No. SS18
$\mu_0 = 0.650$
A = 0.108
$\lambda = 11.8$
$\phi = 0.000$
H
Test No. SS20
$\mu_0 = 0.490$
A = 0.245
$\lambda = 6.7$
$\phi = 1.870$
$\hat{F}$
$\hat{w}_0$

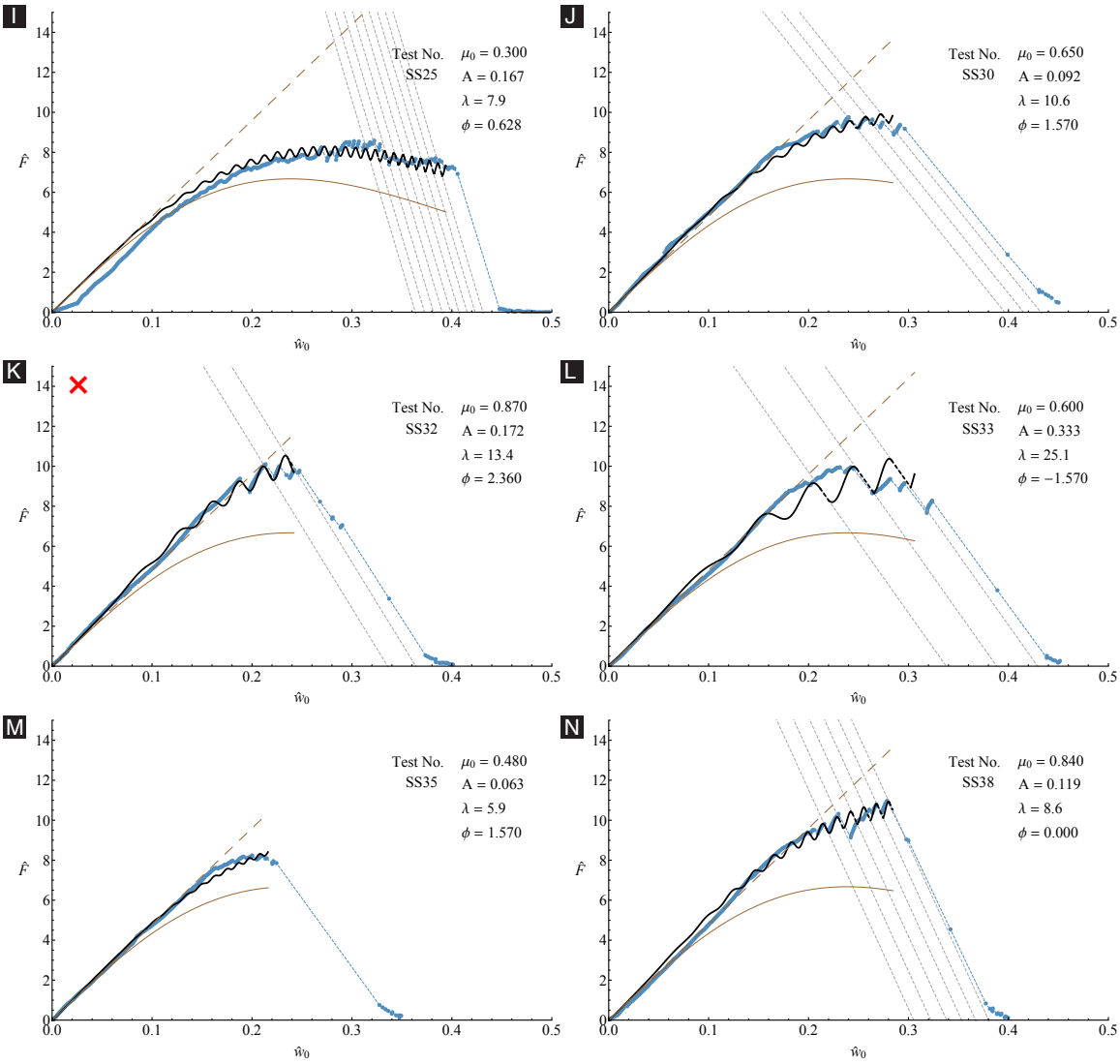

Figure 2.9: Comparing measured force-displacement curves from the SS tests belonging to category *C.1* with their theoretical predictions. Each subfigure corresponds to a different test. The subfigures with a red cross mark at their top left corners correspond to tests that also belong to category *C.4*. The following statements apply to each subfigure separately. The experimentally measured force-displacement curve is shown in blue. The prediction from our model for that curve is shown in black. The values we chose for the parameters μ_0, A, λ, and ϕ in our model for generating that prediction are shown at the top right corner. The predictions from the Euler-Bernoulli theory and from our model for the case $\mu_0 = 0$ are shown using brown dashed and brown solid lines, respectively. The gray dashed oblique lines are the graphs of the function (2.37b) at the time instances at which we noted a sudden drop in the measured force. In generating these graphs, in the function (2.37b) we used the $\hat{k}_c$ and $\hat{w}_s(\cdot)$ that we constructed using the experimental details of the test.

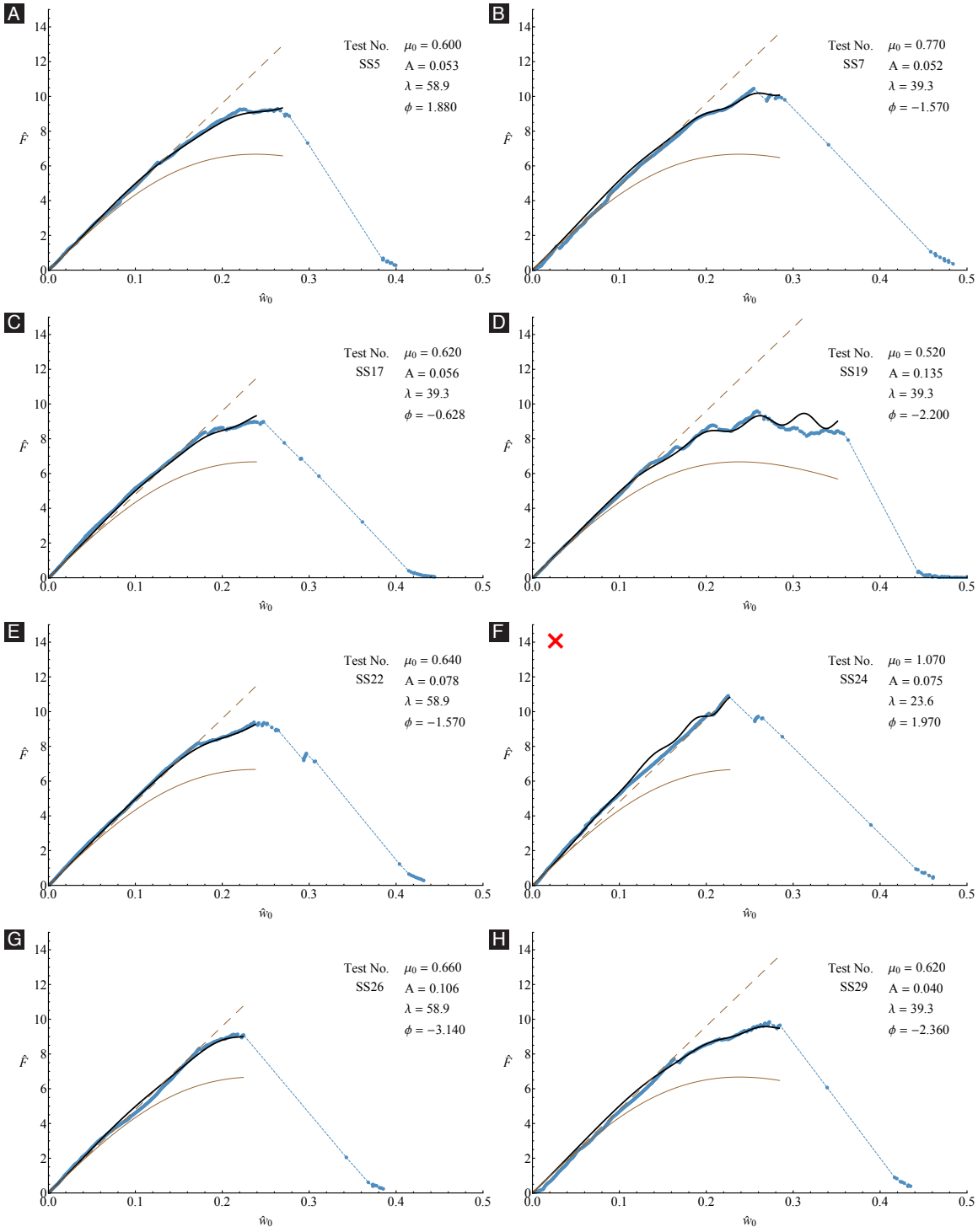

Figure 2.10: Comparing measured force-displacement curves from the SS tests belonging to category *C.2* with their theoretical predictions. Each subfigure corresponds to a different test. The subfigures with a red cross mark at their top left corners correspond to tests that also belong to category *C.4*. The statements made in the caption of Figure 2.9 that apply to its subfigures individually apply to the subfigures of this figure individually as well.

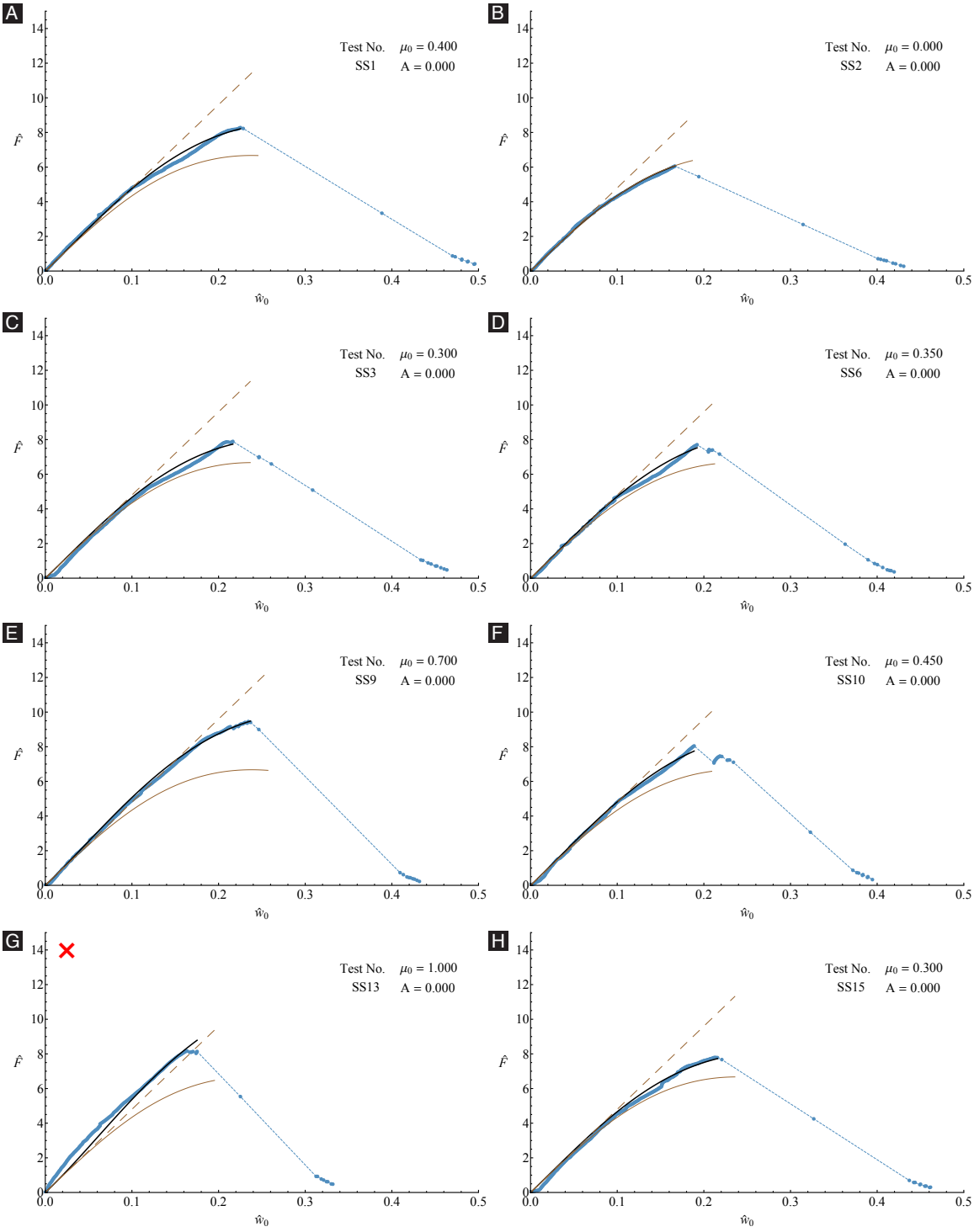
A
Test No. $\mu_0 = 0.400$
SS1 A = 0.000
B
Test No. $\mu_0 = 0.000$
SS2 A = 0.000
C
Test No. $\mu_0 = 0.300$
SS3 A = 0.000
D
Test No. $\mu_0 = 0.350$
SS6 A = 0.000
E
Test No. $\mu_0 = 0.700$
SS9 A = 0.000
F
Test No. $\mu_0 = 0.450$
SS10 A = 0.000
G
Test No. $\mu_0 = 1.000$
SS13 A = 0.000
H
Test No. $\mu_0 = 0.300$
SS15 A = 0.000
$\hat{F}$
$\hat{w}_0$

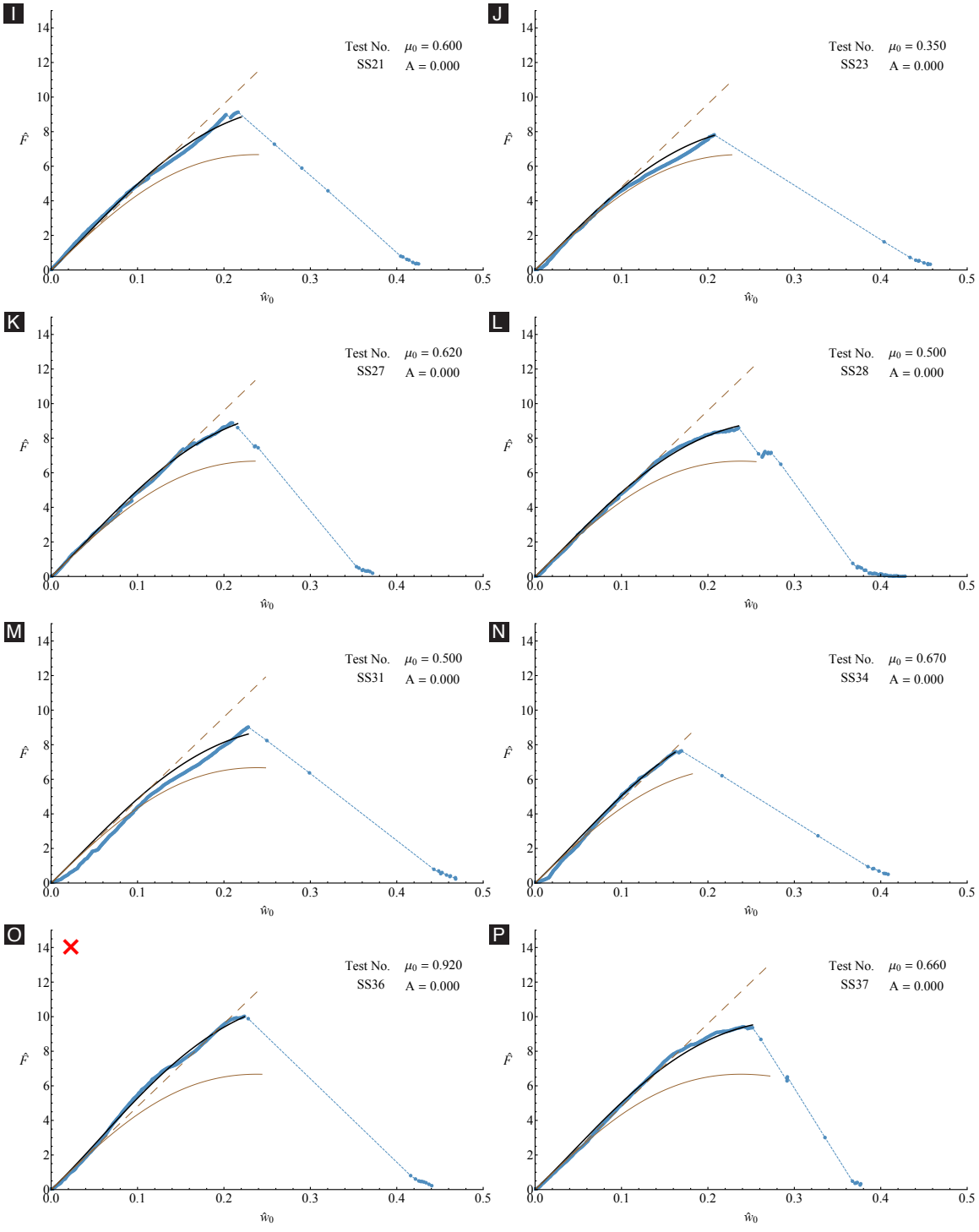

Figure 2.11: Comparing measured force-displacement curves from the SS tests belonging to category *C.3* with their theoretical predictions. Each subfigure corresponds to a different test. The subfigures with a red cross mark at their top left corners correspond to tests that also belong to category *C.4*. The statements made in the caption of Figure 2.9 that apply to its subfigures individually apply to the subfigures of this figure individually as well.

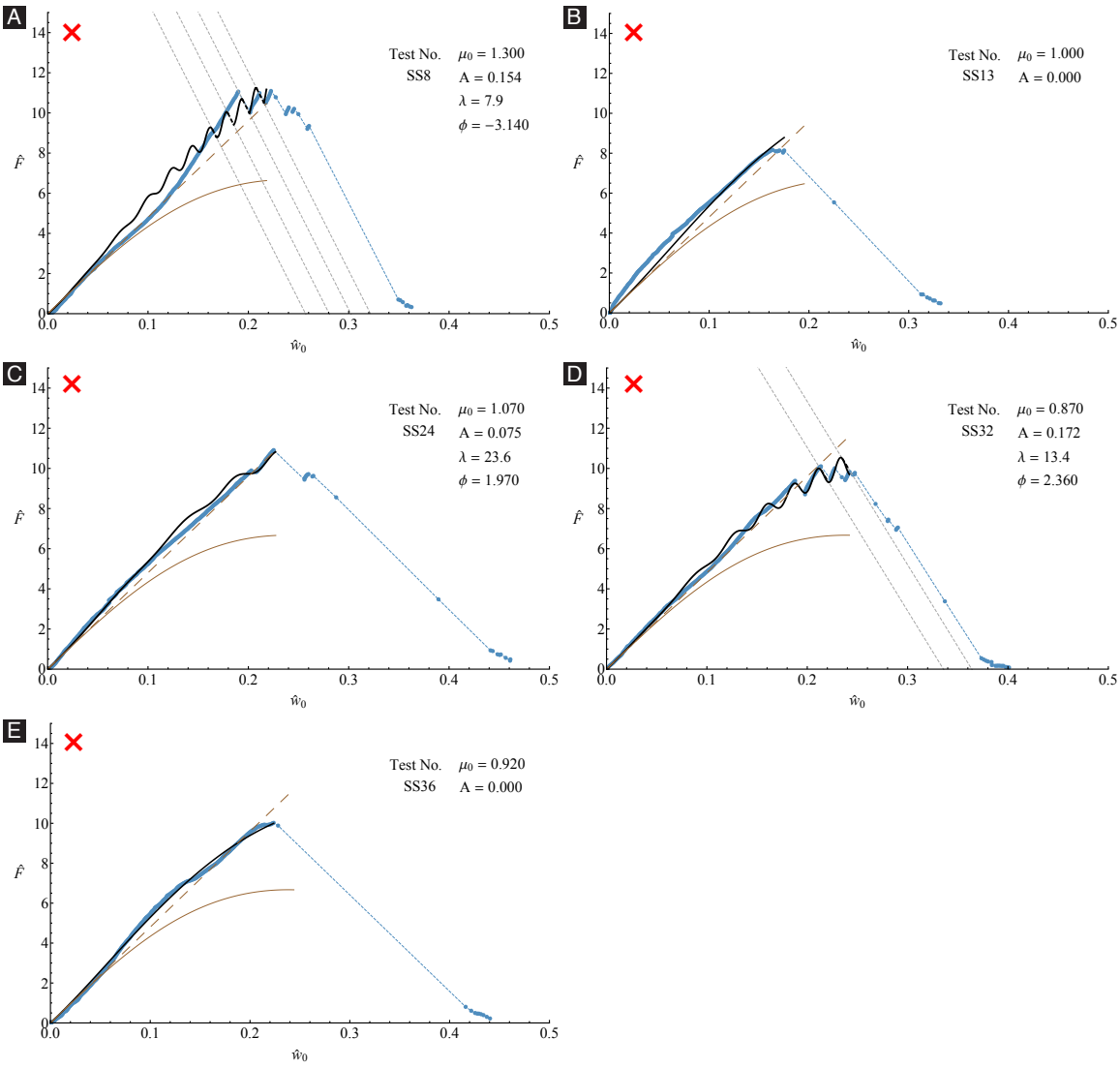

Figure 2.12: Comparing measured force-displacement curves from the SS tests belonging to category *C.4* with their theoretical predictions. Each subfigure corresponds to a different test. The statements made in the caption of Figure 2.9 that apply to its subfigures individually apply to the subfigures of this figure individually as well.

Chapter 3

Effective bending stiffness of multilayered composite cylinders with cylindrical orthotropy

Note: A version of this chapter is in submission to *International Journal of Solids and Structures*. Data and figures have been used with all co-authors' consent.

W. Fang, W. Deng, and H. Kesari. Effective bending stiffness of multilayered composite cylinders with cylindrical orthotropy. International Journal of Solids and Structures, In submission.

3.1 Introduction

Structural biomaterials are fascinating model material systems for the discovery of new mechanics of materials principles. The remarkable enhancement in the structural biomaterials' macro-scale properties in comparison to their micro-scale properties is believed to be due to the highly organized and quite elaborate architecture in which the mineral phases is interlaid with the organic phase. A number of studies have been performed to delineate the mechanical principles that quantitatively capture the relationship between large-scale mechanical properties and small-scale architecture. In most of those studies the focus has been on the brick-mortar architecture which can be described

as a ordered stacking of thin flat platelets. For example, Gao and co-workers [68, 69] developed a multi-level staggered mechanical (tension-shear chain) model for a self-similar bone to understand the role of hierarchical structures of bone. Bertoldi et al. [70] derived the effective stiffness tensor of nacre based on the tension-shear chain model through the homogenization technique and showed that nacre was orthotropic and had different Young's modulus when in tension and compression. Rim et al. [71] performed a parametric analysis to investigate the effect of the microstructure geometry on the nacre-inspired composite's strength and toughness. Begley et al. [72] developed a micromechanical model to evaluate the effective properties of the brick-mortar composite, such as elastic modulus, strength and work-to-failure. Shao et al. [73] presented a microstructure-based fracture mechanics model to study the toughening effect due to the crack-bridging mechanism of platelets in nacre.

However, there exist a large number of structural biomaterials with cylindrical structures and displaying a helical symmetry. Representative examples include the Ponderosa pine [14], the sea sponge skeletons [16], and the tusk of the narwhal [74], as shown in Figure 3.1 (A-C). Furthermore, some other helical structural biomaterials are often found to have the architecture consisting of a co-axial array of thin annular layers, which is referred to multilayered composite structure. This multilayered helical structure is observed in the osteon of bone [15], the artery wall [75], and the wood's cell wall [76] etc. (see Figure 3.1 (D-F)). Some engineering materials such as multi-walled carbon nanotube (see Figure 3.1(G)) and filament-wound composite pipes have multilayered helical structure as well. Although the property-structure connection of biomaterials with brick-mortar architecture has been extensively studied, the relationship between the effective mechanical properties and the small-scale architectures for structural biomaterials consisting of cylindrical layers with helical symmetries is much elusive.

Most of the multilayered structural biological and engineering composite materials are essentially anisotropic and heterogeneous. Moreover, the helical symmetric layers of the structures are cylindrical orthotropic. Understanding and analyzing the overall deformation of such materials with multilayered anisotropic cylindrical microstructures requires the knowledge of their effective (i.e., homogenized) elastic properties, which can be obtained through the anisotropic elasticity theory and homogenization theory. The theory of anisotropic elasticity in the cylindrical coordinates system is developed and summarized in monographs by [79, 80]. Analytical solutions for displacement

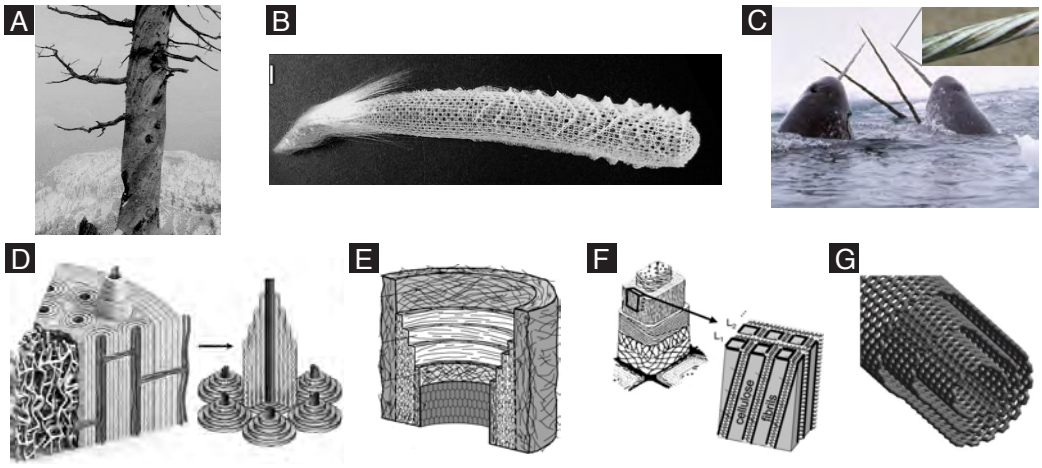

Figure 3.1: Representative examples of structures displaying a helical symmetry. (A) Ponderosa pine (modified with permission from [14]), (B) the sea sponge skeletons (reprinted from [18]), (C) the tusk of the narwhal (image courtesy Glenn Williams), (D) the osteon microstructure of bone (modified with permission from [77]), (E) the artery wall (modified with permission from [75]), (F) the wood's cell wall (modified with permission from [76]), and (G) multiwalled carbon nanotube (modified with permission from [78]).

and stress analysis of anisotropic composite cylinders subjected to typical loading conditions such as tension, shear, torsion, pressuring, thermal deformation and bending are extensively studied, for example, see [81, 82, 40, 83, 84, 85, 86, 87, 88, 89] etc. Inspired by those analytical solutions, a recent study by Gnoli et al. [90] compared the stiffness of the fiber-reinforced cylinder composite beams with various lamination schemes. One interesting observation is that all stiffness constants seem to become stable when three or four layers are considered in the composite beams.

Regarding the homogenization of multilayered cylindrical structures, Chatzigeorgiou et al. [91] studied the homogenized elastic coefficients of an anisotropic hollow layered tube with discontinuous elastic constants under axisymmetric loading condition. They [92] also proposed a modified asymptotic expansion homogenization method to compute effective thermomechanical properties of composites with periodicity in cylindrical coordinates. By taking into account the discontinuous stress and strain distributions in each layer, Sun et al. [93, 94] proposed a force-displacement equivalence method to determine the homogenized elastic constants of general multilayered composite cylindrical structures with curvilinear orthotropy. However, the lack of asymptotic analysis makes their method too complicated to apply in practice.

In this chapter, we derive analytical expressions for the asymptotic bending stiffness of multilayered composite cylinders with cylindrical orthotropy by performing asymptotic analysis on the

bending stiffness formula obtained by Jolicoeur and Cardou [40]. While Jolicoeur and Cardou studied cylinders, with or without a core, with both no-slip and no-friction interfacial conditions between adjacent layers, we focus on hollow multilayered cylindrical structures in particular. It is found that the asymptotic bending stiffness of perfectly bonded multilayered cylindrical structures consisting of two alternatively arranged orthotropic materials is higher than that of structures made of either constituent material. The calculation of the asymptotic bending stiffness, unlike Jolicoeur and Cardou's formula, does not involve the inversion of a large-size matrix, therefore is much more computational efficient.

The chapter is organized as follows: §3.2 describes the model problem of pure bending of multilayered cylindrical structures and summarizes the results obtained by Jolicoeur and Cardou; §3.3 presents the asymptotic analysis procedures of bending stiffness of the structure. The expressions of asymptotic bending stiffness for different interfacial conditions and lamination schemes are derived; §3.4 illustrates the numerical examples and discussions of the results; The final section includes the major conclusions and discussions.

3.2 Pure bending of multilayered composite cylinders with cylindrical orthotropy

We consider a hollow composite cylinder consisting of N co-axial cylindrical layers without a solid core and each layer is cylindrical orthotropic with different principal material property orientations (see Figure 3.2). The inner and outer radius of the cylinder is ${}^{0}r$ and ${}^{N}r$, respectively, where $0 < {}^{0}r < {}^{N}r$.

We take $\mathbb{E}$ to be a three dimensional, oriented, Hilbert space and introduce vectors $(\hat{e}_1, \hat{e}_2, \hat{e}_3)$ to form a basis for $\mathbb{E}$. We also define an Euclidean point space $\mathcal{E}$ as $\mathbb{E}$'s principle homogeneous space. The vectors $\hat{e}_1$, $\hat{e}_2$, and $\hat{e}_3$ are orthonormal, that is, $\hat{e}_i \cdot \hat{e}_j = \delta_{ij}$, for $i, j \in (1, 2, 3)$, where the Kronecker delta symbol δ_{ij} is defined as unity if $i = j$ and zero otherwise. Following the conventions in [95, 96], we define the vectors in $\mathbb{E}$ to have units of length, say meters, and refer to $\mathbb{E}$ as the physical-space. The units are carried by the basis vectors $(\hat{e}_1, \hat{e}_2, \hat{e}_3)$ (see Figure 3.3(A)).

We place the cylinder in $\mathcal{E}$ so that the axis of the cylinder is aligned with $\hat{e}_3$ and cross sections are in $(\hat{e}_1, \hat{e}_2)$ plane (see Figure 3.3(A)).

We also introduce a set of orthonormal vectors $(\hat{e}_r(\theta), \hat{e}_\theta(\theta), \hat{e}_z(\theta))$ as basis for a global cylindrical coordinate system in $\mathbb{E}$. The dependence of $(\hat{e}_r(\theta), \hat{e}_\theta(\theta), \hat{e}_z(\theta))$ on $(\hat{e}_1, \hat{e}_2, \hat{e}_3)$ is given by

$$\hat{e}_r(\theta) = \cos(\theta)\hat{e}_1 + \sin(\theta)\hat{e}_2, \tag{3.1a}$$

$$\hat{e}_\theta(\theta) = -\sin(\theta)\hat{e}_1 + \cos(\theta)\hat{e}_2, \tag{3.1b}$$

$$\hat{e}_z(\theta) = \hat{e}_3. \tag{3.1c}$$

For an individual layer of material, we construct a local cylindrical coordinate system according to the principal material property orientation of the layer. We refer to the local cylindrical coordinate system as the material coordinate system. It is a rotation of the global cylindrical coordinate system through an angle φ, in clockwise direction with respect to the axis $\hat{e}_r(\theta)$ (see Figure 3.3). We denote the basis of the material coordinate system as $\left(\hat{\mathbf{f}}_r(\theta;\varphi), \hat{\mathbf{f}}_\theta(\theta;\varphi), \hat{\mathbf{f}}_z(\theta;\varphi)\right)$, and the transformation matrix from $(\hat{e}_r(\theta), \hat{e}_\theta(\theta), \hat{e}_z(\theta))$ to $\left(\hat{\mathbf{f}}_r(\theta;\varphi), \hat{\mathbf{f}}_\theta(\theta;\varphi), \hat{\mathbf{f}}_z(\theta;\varphi)\right)$ as $\mathbf{Q}(\varphi)$, which can be expressed as

$$\mathbf{Q}(\varphi) = \begin{bmatrix} 1 & 0 & 0 \\ 0 & \cos(\varphi) & -\sin(\varphi) \\ 0 & \sin(\varphi) & \cos(\varphi) \end{bmatrix}. \tag{3.2}$$

In terms of $\mathbf{Q}(\varphi)$, we have the transformation relation between $(\hat{e}_r(\theta), \hat{e}_\theta(\theta), \hat{e}_z(\theta))$ and $\left(\hat{\mathbf{f}}_r(\theta;\varphi), \hat{\mathbf{f}}_\theta(\theta;\varphi), \hat{\mathbf{f}}_z(\theta;\right.$ as

$$\hat{\mathbf{f}}_i(\theta;\varphi) = \sum_{j\in\mathcal{I}} Q_{ij}(\varphi)\hat{e}_j(\theta), \quad \text{for } i \in \mathcal{I}, \tag{3.3}$$

where $\mathcal{I} := (r, \theta, z)$, $Q_{ij}(\varphi) = (\mathbf{Q}(\varphi))_{ij}$ are elements of the matrix $\mathbf{Q}(\varphi)$.

It turns out that the basis $\left(\hat{\mathbf{f}}_r(\theta;\varphi), \hat{\mathbf{f}}_\theta(\theta;\varphi), \hat{\mathbf{f}}_z(\theta;\varphi)\right)$ are closely related to the Frenet–Serret frame [51], which describes a local coordinate system on a particle moving along a continuous, differentiable curve in $\mathcal{E}$. In this case, we imagine a helix tightly wound on the cylinder and the

tangent unit vector of the helix is along the principle direction of the orthotropic material $\hat{\mathbf{f}}_z(\theta;\varphi)$ (see Figure 3.3). Then, as per the definition of Frenet–Serret frame, $\hat{\mathbf{f}}_r(\theta;\varphi)$ is negative to the normal unit vector and $\hat{\mathbf{f}}_\theta(\theta;\varphi)$ is negative to the binormal unit vector of the helix. The helical angle is the complement of φ and the pitch size, p, is related to φ by

$$\tan(\varphi) = 2\pi r/p. \tag{3.4}$$

It should be noted that when two layers of different radii share the same helical angle, the pitch sizes of the two layers are not the same. According to the relation (3.4), for inner layer with smaller radius than that of the outer layer, p is smaller. In this chapter, we deal with the case in which φ are constant or alternatively arranged throughout the radial direction of the cylinder. The given formulae do not apply to the case in which pitch sizes are constant throughout the radial direction of the cylinder (e.g., helices on helicoid are of constant pitch). It is not clear whether the pitch size of cylindrical layers in osteons, cell-walls or spicules, changes from the outside to the inside. However, we highlight this fact since it might be critical to be cognizant of this fact when applying the presented theory to experiments.

The solution of a single cylinder with cylindrical orthotropy subjected to pure bending was obtained by Lekhnitskii [79]. Jolicoeur and Cardou extended this method to a more general bending problem of a co-axial array of N cylindrical layers with cylindrical orthotropy. Each cylindrical layers have different helical angles. The cylinder can be either hollow or with a solid core. The interfaces between adjacent layers could be either perfectly bonded or frictionless. The elastic problem is solved by using stress function method with assumptions that the elastic cylinder is under small strains, the loads along z-axis are constant, no shear load resultant, and stresses and strains only depend on r and θ, which implies constant curvature of the bent cylinder. In the following, we describe the generalized Hooke's law of cylindrical orthotropy in §3.2.1. The results obtained by Jolicoeur and Cardou and relevant to the pure bending problem are summarized in §3.2.2.

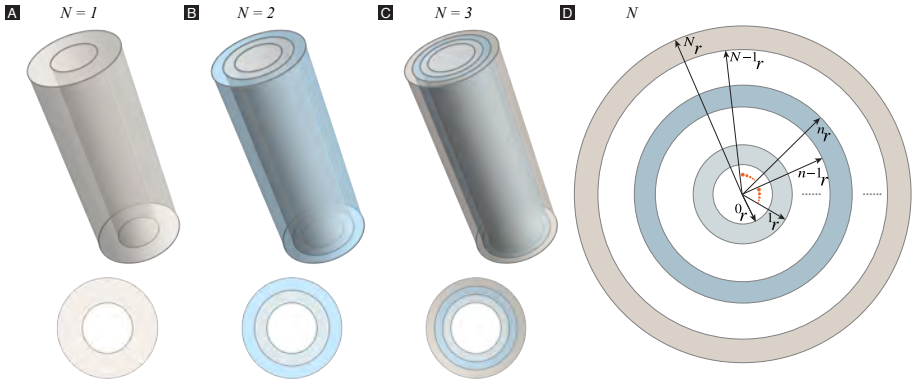

Figure 3.2: Three-dimensional schematics of N-layer cylindrical structure. (A) General view and cross section view for $N = 1$. (B) General view and cross section view for $N = 2$. (C) General view and cross section view for $N = 3$. (D) Cross-section view of an arbitrary N-layer cylindrical structure. Inner and outer radii for the 1^{st} layer, n^{th} layer and N^{th} layer are marked in the figure.

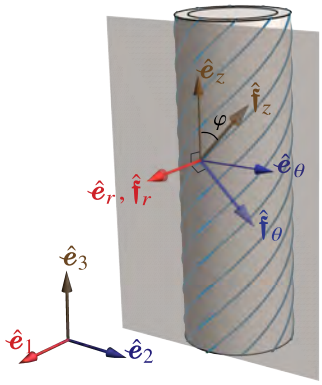

Figure 3.3: A single-layer cylindrical structure with cylindrical orthotropy. The set of vectors $(\hat{e}_1, \hat{e}_2, \hat{e}_3)$ are the basis vectors of the global Cartesian coordinate system, while $(\hat{e}_r(\theta), \hat{e}_\theta(\theta), \hat{e}_z(\theta))$ are the basis of a global cylindrical coordinate system. The vector set $\left(\hat{\mathbf{f}}_r(\theta;\varphi), \hat{\mathbf{f}}_\theta(\theta;\varphi), \hat{\mathbf{f}}_z(\theta;\varphi)\right)$ is used to denote the basis of the material coordinate system, where φ is the helical angle.

3.2.1 Transformation of constitutive law

The generalized Hooke's law is

$$\boldsymbol{\sigma} = \mathbb{C}\,\boldsymbol{\epsilon}, \tag{3.5}$$

where $\boldsymbol{\sigma}$, $\boldsymbol{\epsilon}$, and $\mathbb{C}$ are the Cauchy stress tensor, infinitesimal strain tensor[1] and elastic stiffness tensor, respectively. Eqn. (3.5) can be inverted as

$$\boldsymbol{\epsilon} = \mathbb{S}\,\boldsymbol{\sigma}, \tag{3.6}$$

[1]Here we replace the shear strain in the infinitesimal strain tensor by "engineering shear strains" which are related to the formal definition by a factor of 2.

where $\mathbb{S} = \text{Inv}\,(\mathbb{C})$ is the elastic compliance tensor, $\text{Inv}\,(\cdot)$ is the inverse operation.

In the material coordinate system whose basis is $\left(\hat{\mathbf{f}}_r(\theta;\varphi), \hat{\mathbf{f}}_\theta(\theta;\varphi), \hat{\mathbf{f}}_z(\theta;\varphi)\right)$, we rewrite Eqn. (3.6) with index notation as

$$\epsilon_{ij}^{(\hat{\mathbf{f}})} = \sum_{k,l\in\mathcal{I}} S_{ijkl}^{(\hat{\mathbf{f}})}\sigma_{kl}^{(\hat{\mathbf{f}})}, \quad \text{for}\, i,j \in \mathcal{I} = (r,\theta,z)\,, \tag{3.7}$$

where $\epsilon_{ij}^{(\hat{\mathbf{f}})}$, $S_{ijkl}^{(\hat{\mathbf{f}})}$, and $\sigma_{kl}^{(\hat{\mathbf{f}})}$ are the components of $\boldsymbol{\epsilon}$, $\mathbb{S}$, and $\boldsymbol{\sigma}$, respectively, with respect to the basis $\left(\hat{\mathbf{f}}_r(\theta;\varphi), \hat{\mathbf{f}}_\theta(\theta;\varphi), \hat{\mathbf{f}}_z(\theta;\varphi)\right)$. For helical fibers with cylindrical orthotropy, the elastic compliance components in its material coordinate system, $S_{ijkl}^{(\hat{\mathbf{f}})}$, are constant from point to point.

It is desirable to carry out the analysis in the global cylindrical coordinate system of the structure. Therefore we need to transform the constitutive equation from the material coordinate system to the global cylindrical coordinate system. As discussed in § 3.2, The material coordinates are related to the global cylindrical coordinates by a rotation transformation $\mathbf{Q}(\varphi)$ (see Eqn. (3.3)). Thus, through change of basis, the compliance form of the generalized Hooke's law in the global cylindrical coordinate system becomes

$$\epsilon_{ij}^{(\hat{e})} = \sum_{k,l\in\mathcal{I}} S_{ijkl}^{(\hat{e})}\sigma_{kl}^{(\hat{e})}, \quad \text{for}\, i,j \in \mathcal{I}, \tag{3.8}$$

where $\epsilon_{ij}^{(\hat{e})}$, $S_{ijkl}^{(\hat{e})}$, and $\sigma_{kl}^{(\hat{e})}$ are the components of $\boldsymbol{\epsilon}$, $\mathbb{S}$, and $\boldsymbol{\sigma}$, respectively, with respect to the basis $(\hat{e}_r(\theta), \hat{e}_\theta(\theta), \hat{e}_z(\theta))$. The relations between two sets of components w.r.t different bases are given by

$$\epsilon_{ij}^{(\hat{e})} = \sum_{k,l\in\mathcal{I}} Q_{ik}^{\mathsf{T}}(\varphi)Q_{jl}^{\mathsf{T}}(\varphi)\epsilon_{kl}^{(\hat{\mathbf{f}})}, \tag{3.9}$$

$$\sigma_{ij}^{(\hat{e})} = \sum_{k,l\in\mathcal{I}} Q_{ik}^{\mathsf{T}}(\varphi)Q_{jl}^{\mathsf{T}}(\varphi)\sigma_{kl}^{(\hat{\mathbf{f}})}, \tag{3.10}$$

$$S_{ijkl}^{(\hat{e})} = \sum_{p,q,r,s\in\mathcal{I}} Q_{ip}^{\mathsf{T}}(\varphi)Q_{jq}^{\mathsf{T}}(\varphi)Q_{kr}^{\mathsf{T}}(\varphi)Q_{ls}^{\mathsf{T}}(\varphi)S_{pqrs}^{(\hat{\mathbf{f}})}, \tag{3.11}$$

where $(\cdot)^{\mathsf{T}}$ is the transpose operation.

Therefore, $S_{ijkl}^{(\hat{e})}$ can be obtained from $S_{ijkl}^{(\hat{\mathbf{f}})}$ and the helical angle φ through relation (3.11). It

should be noted that due to symmetry, the 81 components in neither $S^{(\hat{\mathfrak{f}})}_{ijkl}$ nor $S^{(\hat{e})}_{ijkl}$ are independent. For a general orthotropic material in its material coordinate system, the number of independent compliance constants in $S^{(\hat{\mathfrak{f}})}_{ijkl}$ is nine. With the additional variable φ, there should be ten independent constants in $S^{(\hat{e})}_{ijkl}$.

3.2.2 Bending stiffness formula by Jolicoeur and Cardou

The bending stiffness of the N-layer cylindrical composite is obtained by Jolicoeur and Cardou as

$$EI = \sum_{n=1}^{N} \left[\sum_{i \in \mathcal{L}} {}^{n}\alpha_i \, {}^{n}K_i \left(\mathsf{p}\left({}^{n-1}r, {}^{n}m_i + 2 \right) - \mathsf{p}\left({}^{n}r, {}^{n}m_i + 2 \right) \right) + {}^{n}\gamma \left(\mathsf{p}\left({}^{n-1}r, 4 \right) - \mathsf{p}\left({}^{n}r, 4 \right) \right) \right], \tag{3.12a}$$

with

$${}^{n}\alpha_i := \frac{\pi}{{}^{n}s^{(\hat{e})}_{33}} \frac{{}^{n}s^{(\hat{e})}_{13} + {}^{n}s^{(\hat{e})}_{23}({}^{n}m_i + 1) - {}^{n}s^{(\hat{e})}_{34} \, {}^{n}g_i \, {}^{n}m_i}{{}^{n}m_i + 2}, \tag{3.12b}$$

$${}^{n}\gamma := \frac{\pi}{{}^{n}s^{(\hat{e})}_{33}} \frac{{}^{n}\mu_1({}^{n}s^{(\hat{e})}_{13} + 3\,{}^{n}s^{(\hat{e})}_{23}) - 2\,{}^{n}\mu_2 \, {}^{n}s^{(\hat{e})}_{34} - 1}{4}, \tag{3.12c}$$

where N denotes the total number of layers, $\mathcal{L} := (1, 2, 3, 4)$, ${}^{n-1}r$ and ${}^{n}r$ the internal and external radii of the n^{th} layer, ${}^{n}m_i$, ${}^{n}g_i$, ${}^{n}\mu_1$, and ${}^{n}\mu_2$ are material constants related with elastic constants of the n^{th} layer (see Appendix A.1). We use $\mathsf{p}\,(x, y)$ to denote the power operation where x is the base and y is the exponent. We also employed Voigt notation. That is, we introduce elastic compliance constants s_{ij}, $i, j \in (1, \ldots, 6)$. According to the convention of Voigt notation, the non-zero elements of s_{ij} are defined as

$$\begin{aligned}
&s_{11} := S_{rrrr}, \quad s_{12} := S_{rr\theta\theta}, \quad s_{13} := S_{rrzz}, \quad s_{14} := S_{rr\theta z}, \\
&s_{22} := S_{\theta\theta\theta\theta}, \quad s_{23} := S_{\theta\theta zz}, \quad s_{24} := S_{\theta\theta\theta z}, \quad s_{33} := S_{zzzz}, \\
&s_{34} := S_{zz\theta z}, \quad s_{44} := 2S_{\theta z\theta z}, \quad s_{55} := 2S_{rzrz}, \quad s_{66} := 2S_{r\theta r\theta}.
\end{aligned}$$

The coefficients ${}^{n}K_i$ are determined by the boundary conditions and continuity conditions of displacement and stress at the interface.

Boundary condition. The traction free boundaries at innermost radius ${}^{0}r$ and outermost radius ${}^{N}r$ require

$$\sum_{i\in\mathcal{L}} {}^{1}K_i \,\mathsf{p}\left({}^{0}r, {}^{1}m_i - 2\right) = -{}^{1}\mu_1, \quad \sum_{i\in\mathcal{L}} {}^{1}K_i\, {}^{1}g_i \,\mathsf{p}\left({}^{0}r, {}^{1}m_i - 2\right) = -{}^{1}\mu_2, \tag{3.13a}$$

$$\sum_{i\in\mathcal{L}} {}^{N}K_i \,\mathsf{p}\left({}^{N}r, {}^{N}m_i - 2\right) = -{}^{N}\mu_1, \quad \sum_{i\in\mathcal{L}} {}^{N}K_i\, {}^{N}g_i \,\mathsf{p}\left({}^{N}r, {}^{N}m_i - 2\right) = -{}^{N}\mu_2. \tag{3.13b}$$

Interfacial condition: no friction. In the case of no friction interface, u_r and σ_{rr} are continuous, $\tau_{r\theta}$ and τ_{rz} are zero at the interface. Therefore ${}^{n}K_i$ satisfy following equations

$$\sum_{i\in\mathcal{L}} {}^{n}K_i \,\mathsf{p}\left({}^{n}r, {}^{n}m_i - 2\right) = -{}^{n}\mu_1, \quad \sum_{i\in\mathcal{L}} {}^{n}K_i\, {}^{n}g_i \,\mathsf{p}\left({}^{n}r, {}^{n}m_i - 2\right) = -{}^{n}\mu_2, \tag{3.14a}$$

$$\sum_{i\in\mathcal{L}} {}^{n}K_i \,\mathsf{p}\left({}^{n-1}r, {}^{n}m_i - 2\right) = -{}^{n}\mu_1, \quad \sum_{i\in\mathcal{L}} {}^{n}K_i\, {}^{n}g_i \,\mathsf{p}\left({}^{n-1}r, {}^{n}m_i - 2\right) = -{}^{n}\mu_2, \tag{3.14b}$$

for $n = 1, 2, \ldots, N$, where $\mathcal{L} = (1, 2, 3, 4)$.

Interfacial condition: no slip. In the case of perfect bonding (no slip) interface between layers, the continuity conditions of stresses $\sigma_{rr}, \tau_{r\theta}, \tau_{rz}$ and displacements u_r, u_θ, u_z at the interface yields

$$\sum_{i\in\mathcal{L}} \left({}^{n}K_i \,\mathsf{p}\left(r, {}^{n}m_i - 2\right) - {}^{n+1}K_i \,\mathsf{p}\left(r, {}^{n+1}m_i - 2\right)\right) = {}^{n+1}\mu_1 - {}^{n}\mu_1, \tag{3.15a}$$

$$\sum_{i\in\mathcal{L}} \left({}^{n}K_i\, {}^{n}g_i \,\mathsf{p}\left(r, {}^{n}m_i - 2\right) - {}^{n+1}K_i\, {}^{n+1}g_i \,\mathsf{p}\left(r, {}^{n+1}m_i - 2\right)\right) = {}^{n+1}\mu_2 - {}^{n}\mu_2, \tag{3.15b}$$

$$\sum_{i\in\mathcal{L}} \left({}^{n}K_i\, {}^{n}Q_i \,\mathsf{p}\left(r, {}^{n}m_i - 2\right) - {}^{n+1}K_i\, {}^{n+1}Q_i \,\mathsf{p}\left(r, {}^{n+1}m_i - 2\right)\right) = {}^{n+1}Q_5 - {}^{n}Q_5, \tag{3.15c}$$

$$\sum_{i\in\mathcal{L}} \left({}^{n}K_i\, {}^{n}W_i \,\mathsf{p}\left(r, {}^{n}m_i - 2\right) - {}^{n+1}K_i\, {}^{n+1}W_i \,\mathsf{p}\left(r, {}^{n+1}m_i - 2\right)\right) = {}^{n+1}W_5 - {}^{n}W_5, \tag{3.15d}$$

for $n = 1, 2, \ldots, N-1$, where Q_i and $W_i, i \in (1, 2, 3, 4, 5)$ are material constants (see Appendix A.1).

3.3 Effective bending stiffness

In this section, we derive the asymptotic bending stiffness of multilayer cylindrical structure. Specifically, for a given lamination scheme, we analyze the asymptotic behavior of Eqn. (3.12a) by limiting the total number of layers, N, to infinity. The asymptotic expansion is performed under the following assumptions: (i) We assume that the cross-section area of the structure is constant and the thickness of each layer is equal and vanishing as N goes to infinity. (ii) We also assume that the constitutive properties of all layers are the same in their own material coordinate system. But the principal material property orientations, i.e. helical angles, of the layers may be different.

We use the stacking-sequence notation to describe the spatial arrangement of layers' helical angles. As per stacking-sequence notation, we use $[{}^{0}\varphi]_N$ to denote a lamination scheme consisting of N layers and all layers have same helical angle, ${}^{0}\varphi$. For this lamination scheme, the material property of a material point does not change with its position in the cylinder. Thus the material is essentially homogeneous.

We also consider cases where the helical angles are not uniform and the composed material becomes heterogeneous. We use $[{}^{I}\varphi/{}^{II}\varphi]_{N/2}$ to denote a lamination scheme consisting of N layers where layers with helical angles ${}^{I}\varphi$ and ${}^{II}\varphi$ are alternatively arranged.

Based on the lamination schemes and interfacial conditions, we consider three different scenarios here. (i) Homogeneous material, no friction: the lamination scheme is $[{}^{0}\varphi]_N$ and no friction exists between layers. (ii) Heterogeneous material, no friction: the lamination scheme is $[{}^{I}\varphi/{}^{II}\varphi]_{N/2}$ and the interfaces between layers is frictionless. (iii) Heterogeneous material, no slip: the lamination scheme is $[{}^{I}\varphi/{}^{II}\varphi]_{N/2}$ as well, but there is no slip between the adjacent layers.

3.3.1 Homogeneous material and freely slipping interface

First we consider that the elastic property for each layer is the same. The interfaces between layers are frictionless. This is equivalent to the scenario where a homogeneous cylinder is cut into layers with uniform thickness and there is no friction between the layers. In this case, we drop the subscript n of the material constants for the sake of simplicity. We solve for the coefficients ${}^{n}K_i$ for $n = 1, 2, \ldots, N$ from Eqns. (3.13) and (3.14). Let layer thickness $\Delta r := \left({}^{N}r - {}^{0}r\right)/N$, radius sequence ${}^{n}r := {}^{0}r + n \cdot \Delta r$.

Applying Taylor series expansion on the inverse of the coefficient matrix of ${}^{n}K_i$ around ${}^{n}r$, we have

$$ {}^{n}K_i = P_i \cdot \mathsf{p}\left({}^{n}r, -m_i + 2\right) + O(\Delta r), \quad \text{for } i \in \mathcal{L} = (1,2,3,4)\,,\ n = 1,2,\ldots,N, \tag{3.16} $$

where P_i are material constants given in Appendix A.2. Substituting Eqn. (3.16) into Eqn. (3.12a), we have

$$ EI = \sum_{n=1}^{N}\left[\sum_{i\in\mathcal{L}} \alpha_i \left(P_i\, \mathsf{p}\left({}^{n}r, -m_i + 2\right) + O(\Delta r)\right)\left(\mathsf{p}\left({}^{n-1}r, m_i + 2\right) - \mathsf{p}\left({}^{n}r, m_i + 2\right)\right)\right] + \gamma\left(\mathsf{p}\left({}^{0}r, 4\right) - \mathsf{p}\left({}^{N}r, 4\right)\right). $$

Applying Taylor series expansion and simplifying the above equation, we have

$$ EI = -\sum_{n=1}^{N}\left[\sum_{i\in\mathcal{L}} \left(\alpha_i P_i (m_i + 2)\, \mathsf{p}\left({}^{n}r, 3\right)\cdot \Delta r\right)\right] + \gamma\left(\mathsf{p}\left({}^{0}r, 4\right) - \mathsf{p}\left({}^{N}r, 4\right)\right) + O\left(\mathsf{p}\left(\Delta r, 2\right)\right). \tag{3.17} $$

Taking the limit $N \to \infty$, according to the definition of Riemann integral, we convert the sum of series in Eqn. (3.17) into integral as

$$ (EI)_{\infty} = -\sum_{i\in\mathcal{L}}\left(\int_{{}^{0}r}^{{}^{N}r} \alpha_i P_i (m_i + 2)\, \mathsf{p}\left(r, 3\right)\, dr\right) + \gamma\left(\mathsf{p}\left({}^{0}r, 4\right) - \mathsf{p}\left({}^{N}r, 4\right)\right). $$

Finally, we obtain the asymptotic bending stiffness as

$$ (EI)_{\infty} = -\frac{\mathsf{p}\left({}^{N}r, 4\right) - \mathsf{p}\left({}^{0}r, 4\right)}{4}\left(\sum_{i\in\mathcal{L}} \alpha_i P_i (m_i + 2) + 4\gamma\right). \tag{3.18} $$

3.3.2 Heterogeneous material and freely slipping interface

We consider the lamination scheme of the multilayered cylindrical composite as $[{}^{I}\varphi/{}^{II}\varphi]_{N/2}$. That is, layers with helical angles ${}^{I}\varphi$ and ${}^{II}\varphi$ are alternatively arranged from the core to the periphery of the cylinder. We use I and II as subscripts to denote material constants of layers with odd and even layer numbers. Under no friction interfacial condition (3.14) and considering boundary condition (3.13), the ${}^{n}K_i$ for $n = 1,2,\ldots,N$ can be solved from a linear system.

In this case, ${}^{n}K_i$ of adjacent layers are not coupled with each other and thus can be obtained by using the similar technique being used in the homogeneous material case. Applying Taylor series

expansion on the inverse of the coefficient matrix of ${}^{n}K_i$ around ${}^{n}r$ gives

$$ {}^{n}K_i = {}^{n}P_i \cdot \mathsf{p}\,({}^{n}r, -{}^{n}m_i + 2) + O(\Delta r), \quad \text{for } i \in \mathcal{L},\ n = 1, 2, \ldots, N, \tag{3.19} $$

where ${}^{n}P_i$ are material constants of the n^{th} layer (see Appendix A.2). Substituting Eqn. (3.19) into Eqn. (3.12a), we have

$$ \begin{aligned} EI = \sum_{n=1}^{N} \Bigg[\sum_{i \in \mathcal{L}} {}^{n}\alpha_i \left({}^{n}P_i\, \mathsf{p}\,({}^{n}r, -{}^{n}m_i + 2) + O(\Delta r) \right) \cdot \\ \left(-\mathsf{p}\,({}^{n}r, {}^{n}m_i + 1)\,({}^{n}m_i + 2)\Delta r + O(\mathsf{p}\,(\Delta r, 2)) \right) + {}^{n}\gamma(-4\,\mathsf{p}\,({}^{n}r, 3)\,\Delta r + O(\mathsf{p}\,(\Delta r, 2))) \Bigg]. \end{aligned} $$

Applying Taylor series expansion and simplifying the above equation, we have

$$ EI = -\sum_{n=1}^{N} \left[\sum_{i \in \mathcal{L}} {}^{n}\alpha_i {}^{n}P_i ({}^{n}m_i + 2) + 4^{n}\gamma \right] \mathsf{p}\,({}^{n}r, 3) \cdot \Delta r + O(\mathsf{p}\,(\Delta r, 2)). \tag{3.20} $$

Since the arrangement of material property is periodic, the odd layers share the same material constants ${}^{I}\alpha_i$, ${}^{I}P_i$, ${}^{I}m_i$, and ${}^{I}\gamma$ while the even layers share the same material constants ${}^{II}\alpha_i$, ${}^{II}P_i$, ${}^{II}m_i$, and ${}^{II}\gamma$. We rewrite Eqn. (3.20) as

$$ \begin{aligned} EI = &- \sum_{\text{odd layers}} \left[\sum_{i \in \mathcal{L}} {}^{I}\alpha_i {}^{I}P_i ({}^{I}m_i + 2) + 4^{I}\gamma \right] \mathsf{p}\,({}^{n}r, 3) \cdot \Delta r \\ &- \sum_{\text{even layers}} \left[\sum_{i \in \mathcal{L}} {}^{II}\alpha_i {}^{II}P_i ({}^{II}m_i + 2) + 4^{II}\gamma \right] \mathsf{p}\,({}^{n}r, 3) \cdot \Delta r + O(\mathsf{p}\,(\Delta r, 2)). \end{aligned} \tag{3.21} $$

Taking the limit $N \to \infty$, according to the definition of Riemann integral, the Eqn. (3.21) becomes

$$ \begin{aligned} (EI)_\infty = \frac{1}{2} \Bigg\{ &- \left[\sum_{i \in \mathcal{L}} {}^{I}\alpha_i {}^{I}P_i ({}^{I}m_i + 2) + 4^{I}\gamma \right] \int_{0_r}^{N_r} \mathsf{p}\,(r, 3)\ dr \\ &- \left[\sum_{i \in \mathcal{L}} {}^{II}\alpha_i {}^{II}P_i ({}^{II}m_i + 2) + 4^{II}\gamma \right] \int_{0_r}^{N_r} \mathsf{p}\,(r, 3)\ dr \Bigg\}. \end{aligned} $$

Finally, we obtain the asymptotic bending stiffness as

$$ (EI)_\infty = \frac{1}{2} \left[{}^{I}(EI)_\infty + {}^{II}(EI)_\infty \right], \tag{3.22a} $$

where

$$ {}^{j}(EI)_{\infty} = -\frac{\mathsf{p}\left({}^{N}r, 4\right) - \mathsf{p}\left({}^{0}r, 4\right)}{4}\left[\sum_{i\in\mathcal{L}} {}^{j}\alpha_i\, {}^{j}P_i({}^{j}m_i + 2) + 4^{j}\gamma\right], \quad \text{for } j = I, II. \tag{3.22b} $$

3.3.3 Heterogeneous material and no slipping interface

For the case that the lamination scheme of the multilayered cylindrical composite is $[{}^{I}\varphi/{}^{II}\varphi]_{N/2}$ under no slip interfacial condition, the $4N$ unknowns ${}^{n}K_i$ can be solved from the boundary conditions by Eqn. (3.13) and the interfacial conditions by Eqn. (3.15).

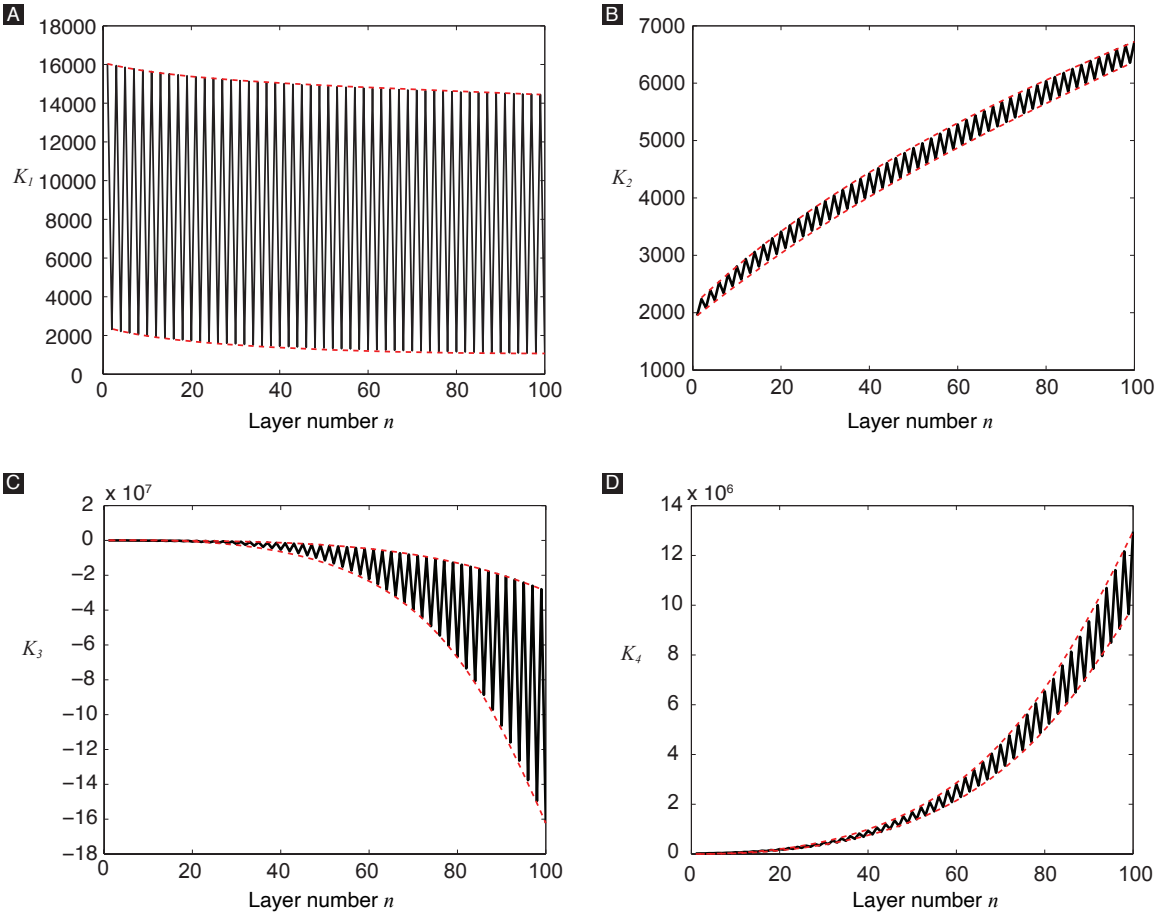

Figure 3.4: A set of representative plots of K_i with layer number n for a cylindrical composite with lamination scheme $[-15°/25°]_{50}$ under no slip interfacial condition. The dimensions and material properties of the cylindrical structure is given in Section 3.4

Using bold san-serif font symbol to denote matrices, we rewrite Eqns. (3.13) and (3.15) as

$$ {}^{n}\mathbf{B}\,{}^{n-1}\mathbf{K} = {}^{n}\mathbf{A}\,{}^{n}\mathbf{K} - {}^{n}\mathbf{D}, \quad \text{for } n = 2, 3, \ldots, N, \tag{3.23a} $$

where

$$
{}^{n}\mathbf{B} = \begin{bmatrix}
\mathsf{p}\left({}^{n-1}r, {}^{n-1}m_1\right) & \mathsf{p}\left({}^{n-1}r, {}^{n-1}m_2\right) & \mathsf{p}\left({}^{n-1}r, {}^{n-1}m_3\right) & \mathsf{p}\left({}^{n-1}r, {}^{n-1}m_4\right) \\
{}^{n-1}g_1\,\mathsf{p}\left({}^{n-1}r, {}^{n-1}m_1\right) & {}^{n-1}g_2\,\mathsf{p}\left({}^{n-1}r, {}^{n-1}m_2\right) & {}^{n-1}g_3\,\mathsf{p}\left({}^{n-1}r, {}^{n-1}m_3\right) & {}^{n-1}g_4\,\mathsf{p}\left({}^{n-1}r, {}^{n-1}m_4\right) \\
{}^{n-1}Q_1\,\mathsf{p}\left({}^{n-1}r, {}^{n-1}m_1\right) & {}^{n-1}Q_2\,\mathsf{p}\left({}^{n-1}r, {}^{n-1}m_2\right) & {}^{n-1}Q_3\,\mathsf{p}\left({}^{n-1}r, {}^{n-1}m_3\right) & {}^{n-1}Q_4\,\mathsf{p}\left({}^{n-1}r, {}^{n-1}m_4\right) \\
{}^{n-1}W_1\,\mathsf{p}\left({}^{n-1}r, {}^{n-1}m_1\right) & {}^{n-1}W_2\,\mathsf{p}\left({}^{n-1}r, {}^{n-1}m_2\right) & {}^{n-1}W_3\,\mathsf{p}\left({}^{n-1}r, {}^{n-1}m_3\right) & {}^{n-1}W_4\,\mathsf{p}\left({}^{n-1}r, {}^{n-1}m_4\right)
\end{bmatrix}, \tag{3.23b}
$$

$$
{}^{n}\mathbf{K} = \begin{bmatrix}
{}^{n}K_1 \\
{}^{n}K_2 \\
{}^{n}K_3 \\
{}^{n}K_4
\end{bmatrix}, \tag{3.23c}
$$

$$
{}^{n}\mathbf{A} = \begin{bmatrix}
\mathsf{p}\left({}^{n-1}r, {}^{n}m_1\right) & \mathsf{p}\left({}^{n-1}r, {}^{n}m_2\right) & \mathsf{p}\left({}^{n-1}r, {}^{n}m_3\right) & \mathsf{p}\left({}^{n-1}r, {}^{n}m_4\right) \\
{}^{n}g_1\,\mathsf{p}\left({}^{n-1}r, {}^{n}m_1\right) & {}^{n}g_2\,\mathsf{p}\left({}^{n-1}r, {}^{n}m_2\right) & {}^{n}g_3\,\mathsf{p}\left({}^{n-1}r, {}^{n}m_3\right) & {}^{n}g_4\,\mathsf{p}\left({}^{n-1}r, {}^{n}m_4\right) \\
{}^{n}Q_1\,\mathsf{p}\left({}^{n-1}r, {}^{n}m_1\right) & {}^{n}Q_2\,\mathsf{p}\left({}^{n-1}r, {}^{n}m_2\right) & {}^{n}Q_3\,\mathsf{p}\left({}^{n-1}r, {}^{n}m_3\right) & {}^{n}Q_4\,\mathsf{p}\left({}^{n-1}r, {}^{n}m_4\right) \\
{}^{n}W_1\,\mathsf{p}\left({}^{n-1}r, {}^{n}m_1\right) & {}^{n}W_2\,\mathsf{p}\left({}^{n-1}r, {}^{n}m_2\right) & {}^{n}W_3\,\mathsf{p}\left({}^{n-1}r, {}^{n}m_3\right) & {}^{n}W_4\,\mathsf{p}\left({}^{n-1}r, {}^{n}m_4\right)
\end{bmatrix}, \tag{3.23d}
$$

$$
{}^{n}\mathbf{D} = -\,\mathsf{p}\left({}^{n-1}r, 2\right) \begin{bmatrix}
{}^{n}\mu_1 - {}^{n-1}\mu_1 \\
{}^{n}\mu_2 - {}^{n-1}\mu_2 \\
{}^{n}Q_5 - {}^{n-1}Q_5 \\
{}^{n}W_5 - {}^{n-1}W_5
\end{bmatrix}. \tag{3.23e}
$$

The matrices ${}^{n-1}\mathbf{K}$ and ${}^{n}\mathbf{K}$ are coupled with each other in this case. Therefore, each ${}^{n}\mathbf{K}$ cannot be solved individually. The computational complexity of solving linear equation of size n is $O(n^3)$. Therefore, the computational time for solving a linear system of size $4N$ is growing up very quickly when N is increasing.

To overcome this difficulty, we come up with a differential equation based asymptotic analysis method to estimate ${}^{n}\mathbf{K}$ as N approaches infinity. Since the matrices ${}^{n}\mathbf{K}$ are decoupled for different layers, each ${}^{n}\mathbf{K}$ can be solved individually, which greatly improves the computational efficiency. For the sake of clarity, we only post essential steps of the derivation in this section. For the details of the complete derivation, we ask the readers to refer to Appendix A.3.

We first substitute n as $n-1$ into Eqn. (3.23a) and combine the resulting equation with Eqn. (3.23a) to find out the relation between ${}^{n}\mathbf{K}$ and ${}^{n-2}\mathbf{K}$ as

$$ {}^{n}\mathbf{A}\ {}^{n}\mathbf{K} = {}^{n}\mathbf{B}\ \mathrm{Inv}\left({}^{n-1}\mathbf{A}\right)\ {}^{n-1}\mathbf{B}\ {}^{n-2}\mathbf{K} + {}^{n}\mathbf{B}\ \mathrm{Inv}\left({}^{n-1}\mathbf{A}\right)\ {}^{n-1}\mathbf{D} + {}^{n}\mathbf{D}. \tag{3.24} $$

In Eqn. (3.24), we take Taylor series expansion on $\mathrm{Inv}\left({}^{n-1}\mathbf{A}\right)$ and ${}^{n-1}\mathbf{B}$ around ${}^{n-1}r$ to obtain (see Appendix A.3.1 for details)

$$ {}^{n}\mathbf{B}\ \mathrm{Inv}\left({}^{n-1}\mathbf{A}\right)\ {}^{n-1}\mathbf{B} = {}^{n}\mathbf{A} + \frac{\Delta r}{{}^{n-1}r}\left({}^{n}\mathbf{B}\ {}^{n-1}\tilde{\mathbf{m}}\ \mathrm{Inv}\left({}^{n}\mathbf{B}\right)\ {}^{n}\mathbf{A} - {}^{n}\mathbf{A}\ {}^{n}\tilde{\mathbf{m}}\right) + O(\mathrm{p}(\Delta r, 2)), \tag{3.25a} $$

$$ {}^{n}\mathbf{B}\ \mathrm{Inv}\left({}^{n-1}\mathbf{A}\right)\ {}^{n-1}\mathbf{D} + {}^{n}\mathbf{D} = \frac{\Delta r}{{}^{n-1}r}\left(2\,{}^{n}\mathbf{D} + {}^{n}\mathbf{B}\ {}^{n-1}\tilde{\mathbf{m}}\ \mathrm{Inv}\left({}^{n}\mathbf{B}\right)\ {}^{n-1}\mathbf{D}\right) + O(\mathrm{p}(\Delta r, 2)). \tag{3.25b} $$

Then by substituting Eqn. (3.25) into Eqn. (3.24), we obtain

$$ \begin{aligned} {}^{n}\mathbf{A}\ {}^{n}\mathbf{K} = {} & \left[{}^{n}\mathbf{A} + \frac{\Delta r}{{}^{n-1}r}\left({}^{n}\mathbf{B}\ {}^{n-1}\tilde{\mathbf{m}}\ \mathrm{Inv}\left({}^{n}\mathbf{B}\right)\ {}^{n}\mathbf{A} - {}^{n}\mathbf{A}\ {}^{n}\tilde{\mathbf{m}}\right) + O(\mathrm{p}(\Delta r, 2))\right]\ {}^{n-2}\mathbf{K} \\ & + \frac{\Delta r}{{}^{n-1}r}\left(2\,{}^{n}\mathbf{D} + {}^{n}\mathbf{B}\ {}^{n-1}\tilde{\mathbf{m}}\ \mathrm{Inv}\left({}^{n}\mathbf{B}\right)\ {}^{n-1}\mathbf{D}\right) + O(\mathrm{p}(\Delta r, 2)), \end{aligned} \tag{3.26} $$

which gives the asymptotic relation between ${}^{n-2}\mathbf{K}$ and ${}^{n}\mathbf{K}$. From a set of representative plots for K_i versus n of a 100-layered structure (see Figure 3.4), we deduce that the K_i of odd and even layer numbers are continuous in the asymptotic sense (for $N \to \infty$), which are indicated by red dashed lines. We use ${}^{n}\bar{\mathbf{K}}(r)$ to denote the continuous representation of ${}^{n}\mathbf{K}$ as a function of radius r. Hence, we approximate ${}^{n-2}\mathbf{K}$ to the first order of Δr as

$$ {}^{n-2}\bar{\mathbf{K}}(r) = {}^{n}\bar{\mathbf{K}}(r) - 2\frac{d\,{}^{n}\bar{\mathbf{K}}(r)}{dr}\Delta r + O(\mathrm{p}(\Delta r, 2)). \tag{3.27} $$

For the odd and even layer numbers, ${}^{n}\bar{\mathbf{K}}(r)$ are written as ${}^{\mathrm{odd}}\bar{\mathbf{K}}(r)$ and ${}^{\mathrm{even}}\bar{\mathbf{K}}(r)$. For simplicity, we drop the left superscript "odd" and "even" in the derivation of the governing equations for ${}^{\mathrm{odd}}\bar{\mathbf{K}}(r)$ and ${}^{\mathrm{even}}\bar{\mathbf{K}}(r)$ since both of them satisfy the same set of differential equations for $\bar{\mathbf{K}}(r)$. We also drop the left superscript for other variables in the following derivations when there is no confusion.

Substituting Eqn. (3.27) into Eqn. (3.26) and making simplification (see Appendix A.3.2 for

details), we obtain a linear ODE system of $\bar{\mathbf{K}}(r)$

$$2r\frac{d\left(\mathbf{f}(r)\bar{\mathbf{K}}(r)\right)}{dr} = \left(\tilde{\mathbf{M}}+\tilde{\mathbf{m}}\right)\left(\mathbf{f}(r)\bar{\mathbf{K}}(r)\right) + \mathsf{p}\,(r,2)\,\tilde{\mathbf{F}}, \tag{3.28}$$

with boundary conditions given by Eqn. (3.13). Solving this linear ODE system (see Appendix A.3.3 for the details of the solution procedures), we obtain

$${}^{n}K_i = \mathsf{p}\,({}^{n}r,-{}^{n}m_i)\left({}^{n}G_{i0}\,\mathsf{p}\,({}^{n}r,2) + \sum_{j\in\mathcal{L}}{}^{n}G_{ij}\,\mathsf{p}\left({}^{n}r,{}^{n}\lambda_j\right)\right), \quad \text{for } i\in\mathcal{L},\ n=1,2,3,...,N, \tag{3.29}$$

where ${}^{n}G_{ij}$ ($j=0$ to 4) and ${}^{n}\lambda_j$ ($j\in\mathcal{L}=(1,2,3,4)$) given by Eqn. (A.28) are constants related to material constants of the n^{th} layer. Substituting Eqn. (3.29) into Eqn. (3.12a), we obtain the bending stiffness as

$$EI = -\sum_{n=1}^{N}\left\{\sum_{i\in\mathcal{L}}{}^{n}\hat{\alpha}_i\left({}^{n}G_{i0}\,\mathsf{p}\,({}^{n}r,2) + \sum_{j\in\mathcal{L}}{}^{n}G_{ij}\,\mathsf{p}\left({}^{n}r,{}^{n}\lambda_j\right)\right){}^{n}r + 4\,{}^{n}\gamma\ \mathsf{p}\,({}^{n}r,3)\right\} + O(\Delta r), \tag{3.30}$$

where ${}^{n}\hat{\alpha}_i := {}^{n}\alpha_i\,({}^{n}m_i+2)$.

Since the material properties of the layers of the structure are alternately arranged, the odd layers share the same material constants ${}^{I}\alpha_i$, ${}^{I}\gamma$, ${}^{I}m_i$, ${}^{I}G_{ij}$, and ${}^{I}\lambda_j$, and the even layers have the same constants ${}^{II}\alpha_i$, ${}^{II}\gamma$, ${}^{II}m_i$, ${}^{II}G_{ij}$, and ${}^{II}\lambda_j$. Therefore,

$$\begin{aligned} EI = &-\frac{1}{2}\sum_{\text{odd layers}}\left[\left(\sum_{i\in\mathcal{L}}{}^{I}\hat{\alpha}_i{}^{I}G_{i0}+4{}^{I}\gamma\right)\mathsf{p}\,({}^{n}r,3) + \sum_{i\in\mathcal{L}}\sum_{j\in\mathcal{L}}{}^{I}\hat{\alpha}_i{}^{I}G_{ij}\,\mathsf{p}\left({}^{n}r,1+{}^{I}\lambda_j\right)\right] \\ &-\frac{1}{2}\sum_{\text{even layers}}\left[\left(\sum_{i\in\mathcal{L}}{}^{II}\hat{\alpha}_i{}^{II}G_{i0}+4{}^{II}\gamma\right)\mathsf{p}\,({}^{n}r,3)\right. \\ &\qquad\left.+\sum_{i\in\mathcal{L}}\sum_{j\in\mathcal{L}}{}^{II}\hat{\alpha}_i{}^{II}G_{ij}\,\mathsf{p}\left({}^{n}r,1+{}^{II}\lambda_j\right)\right] + O(\Delta r). \end{aligned} \tag{3.31}$$

As $N\to\infty$, according to the definition of Riemann integral, the Eqn. (3.31) becomes

$$\begin{aligned} (EI)_\infty = &-\frac{1}{2}\left[\sum_{i\in\mathcal{L}}\left({}^{I}\hat{\alpha}_i{}^{I}G_{i0}+{}^{II}\hat{\alpha}_i{}^{II}G_{i0}\right)+4\left({}^{I}\gamma+{}^{II}\gamma\right)\right]\int_{0_r}^{N_r}\mathsf{p}\,(r,3)\ dr \\ &-\frac{1}{2}\sum_{i\in\mathcal{L}}\sum_{j\in\mathcal{L}}\left[\int_{0_r}^{N_r}\left({}^{I}\hat{\alpha}_i{}^{I}G_{ij}\,\mathsf{p}\left(r,1+{}^{I}\lambda_j\right)+{}^{II}\hat{\alpha}_i{}^{II}G_{ij}\,\mathsf{p}\left(r,1+{}^{II}\lambda_j\right)\right)\ dr\right]. \end{aligned}$$

Finally, we obtain the asymptotic bending stiffness as

$$
\begin{aligned}
(EI)_{\infty} = -\frac{1}{8}\left[\sum_{i\in\mathcal{L}}\left({}^{I}\hat{\alpha}_i\,{}^{I}G_{i0} + {}^{II}\hat{\alpha}_i\,{}^{II}G_{i0}\right) + 4\left({}^{I}\gamma + {}^{II}\gamma\right)\right]\left(\mathsf{p}\left({}^{N}r, 4\right) - \mathsf{p}\left({}^{0}r, 4\right)\right) \\
- \frac{1}{2}\sum_{i\in\mathcal{L}}\sum_{j\in\mathcal{L}}\left[\frac{{}^{I}\hat{\alpha}_i\,{}^{I}G_{ij}}{2+{}^{I}\lambda_j}\left(\mathsf{p}\left({}^{N}r, 2+{}^{I}\lambda_j\right) - \mathsf{p}\left({}^{0}r, 2+{}^{I}\lambda_j\right)\right)\right. \\
\left. + \frac{{}^{II}\hat{\alpha}_i\,{}^{II}G_{ij}}{2+{}^{II}\lambda_j}\left(\mathsf{p}\left({}^{N}r, 2+{}^{II}\lambda_j\right) - \mathsf{p}\left({}^{0}r, 2+{}^{II}\lambda_j\right)\right)\right].
\end{aligned}
\tag{3.32}
$$

3.4 Numerical examples and discussions

In this section, the bending stiffness of multilayered cylindrical structures with different lamination schemes and interfacial conditions are numerically studied and the asymptotic bending stiffness formulae derived in §3.3 are validated.

The cylindrical composite is divided into N co-axial layers with constant thickness. The innermost and outermost radii of the cylindrical structure are taken to be ${}^{0}r = 2$ mm and ${}^{N}r = 14$ mm, respectively. Three different combinations of lamination schemes and interfacial conditions are considered: (i) $[-15^{\circ}]_N$ and $[25^{\circ}]_N$ with no friction interfacial condition, (ii) $[-15^{\circ}/25^{\circ}]_{N/2}$ with no friction interfacial condition, (iii) $[-15^{\circ}/25^{\circ}]_{N/2}$ with no slip interfacial condition. In all three scenarios, the non-zero elastic compliance components of cylindrically orthotropic material in each layer's in material coordinate system are the same and provided in Tab. 3.1.

Table 3.1: Elastic compliance components of cylindrically orthotropic material in material coordinate system (10^{-10} m^2/N)

$s_{11}^{(\hat{\mathfrak{f}})}$	$s_{12}^{(\hat{\mathfrak{f}})}$	$s_{13}^{(\hat{\mathfrak{f}})}$	$s_{22}^{(\hat{\mathfrak{f}})}$	$s_{23}^{(\hat{\mathfrak{f}})}$	$s_{33}^{(\hat{\mathfrak{f}})}$	$s_{44}^{(\hat{\mathfrak{f}})}$	$s_{55}^{(\hat{\mathfrak{f}})}$	$s_{66}^{(\hat{\mathfrak{f}})}$
1.05	-0.0632	-0.0842	1.18	-0.0941	0.20	4.00	5.00	2.50

The relations between bending stiffness and total layer number N for the structures consisting of homogeneous materials with no friction interface are shown as solid lines in Figure 3.5. The bending stiffness of one-layer cylinders is 881.47 N·m^2 and 528.11 N·m^2 for the materials with -15° and 25° helical angles, respectively. As we increase the total layer number, for both materials, the bending stiffness first decreases rapidly then becomes stable after N is greater than five. When the layer

thickness approaches to zero as $N \to \infty$, the bending stiffness converges to a non-zero constant, which is given by Eqn. (3.18). The asymptotic bending stiffness of composite with lamination scheme $[-15°]_\infty$ and $[25°]_\infty$ are 722.15 N·m^2 and 412.13 N·m^2, respectively (see Figure 3.5).

The relation between bending stiffness and total layer number for the heterogeneous layer properties with no friction interface is plotted as solid line in Figure 3.6. The lamination scheme for this case is $[-15°/25°]_{N/2}$. The bending stiffness oscillates as the total layer number increases due to the alternated arrangement of the layer properties. Eventually, it approaches to a non-zero constant as $N \to \infty$, which is the asymptotic bending stiffness given by Eqn. (3.22a). The asymptotic homogenized bending stiffness of the heterogeneous structure is 567.14 N·m^2 (see Figure 3.6), which is equal to the average of those of two homogeneous materials.

The plot of bending stiffness for the heterogeneous material and no slip interface case, in which the lamination scheme is $[-15°/25°]_{N/2}$, is shown as solid line in Figure 3.7. The bending stiffness oscillates as the total layer number increases and approaches to a non-zero constant, which is the asymptotic bending stiffness given by Eqn. (3.32). Furthermore, it is interesting to note that the asymptotic bending stiffness of heterogeneous structures exceeds the bending stiffness of both homogeneous structures. The maximum bending stiffness, 1093.12 N·m^2, is achieved when the total layer number is five. The asymptotic bending stiffness, 1046.94 N·m^2, is higher than those of the structures consisting of homogeneous materials, which are 881.47 N·m^2 and 528.11 N·m^2. This implies that we could build up stiffer composite from compliant materials by designing the spatial arrangements of laminae.

3.5 Conclusions

In this chapter, we present an asymptotic analysis of bending stiffness of multilayered composite cylindrical structures with cylindrical orthotropy. Specifically, we consider hollow cylinders composed of infinite number of layers with uniform thickness and alternatively arranged material orientations. The interfacial conditions between adjacent layers can be no slip or no friction. By taking the asymptotic limit of the result given by Jolicoeur and Cardou [40], we derived the analytical expressions for the asymptotic bending stiffness of multilayered composite cylindrical structures.

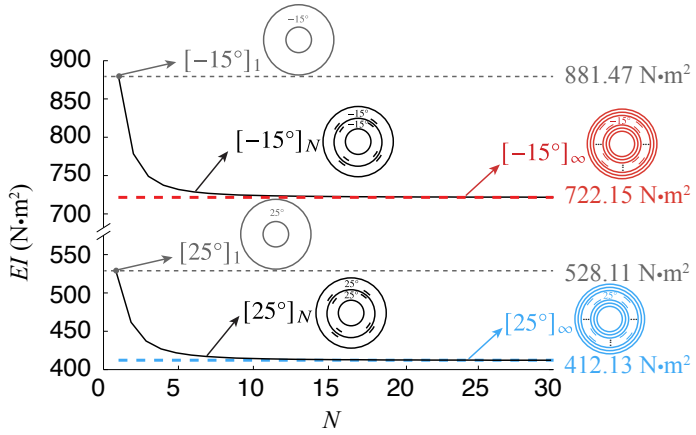

Figure 3.5: The variations of effective bending stiffness as the number of layers increases (solid lines) and their asymptotic limits as the number of layers approach infinity (dashed lines) for composite cylinders with lamination schemes $[-15°]_N$ and $[25°]_N$ with no friction interfacial condition.

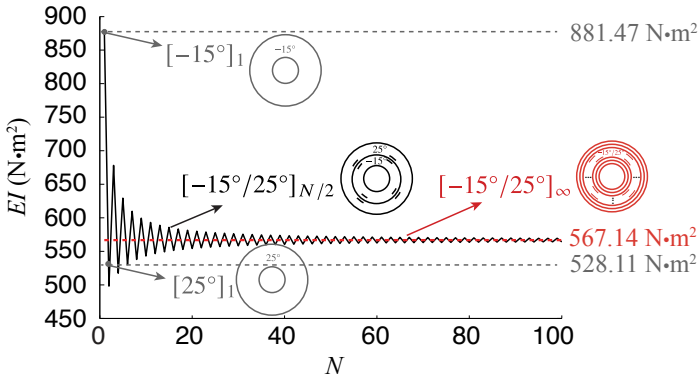

Figure 3.6: The variations of effective bending stiffness as the number of layers increases (solid lines) and their asymptotic limits as the number of layers approach infinity (dashed lines) for composite cylinders with lamination schemes $[-15°/25°]_{N/2}$ with no friction interfacial condition.

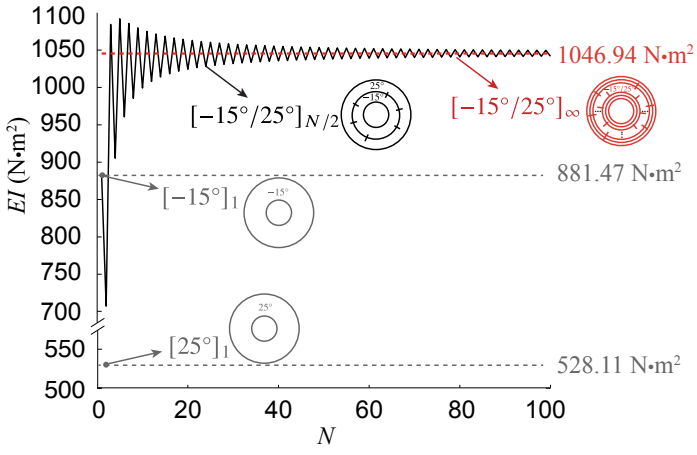

Figure 3.7: The variations of effective bending stiffness as the number of layers increases (solid lines) and their asymptotic limits as the number of layers approach infinity (dashed lines) for composite cylinders with lamination schemes $[-15°/25°]_{N/2}$ with no slip interfacial condition.

It can be noted from Figure 3.5, 3.6, and 3.7 that the effective bending stiffness converges to the asymptotic result rather fast as the number of layers increases. The asymptotic bending stiffness can be considered as an approximation to the effective bending stiffness of an actual N-layer composite cylinder when N is larger than 20. For the non-slip interface scenario, the boundary conditions (3.15) of adjacent layers are coupled. To solve for ${}^{n}K_i$ ($n = 1, 2, \ldots, N$, $i = 1, 2, 3, 4$), one needs to solve a $4N \times 4N$ linear system, which is substantially computational expensive when N is a large number. However, with the asymptotic expression given by (3.32), the computational cost becomes trivial, so as the loss in accuracy. Therefore, the asymptotic expressions of bending stiffness greatly accelerate the design process of the multilayered composite cylinders. Although we only consider two material orientations for the heterogeneous structure, we believe that the method used in this work can be extended to multiple material orientations with similar analysis procedures. It is also extensible to the scenario of non-hollow cylindrical structures, i.e. cylinders with solid cores, which brings in more applicability to the presented method.

More importantly, it can be shown in Figure 3.7 that it is possible to design a composite beam with higher bending stiffness using intrinsic compliant materials through lamellar architectures and appropriate geometric arrangement. In addition, from Figure 3.5 and Figure 3.6, the rational arrangement of material orientations and control of interfacial properties can be useful to design composite cylinders with desired bulk mechanical properties. The results shed light on the structure-property connections of a number of helical symmetric structural biological materials, such as *Ea.* anchor spicules, ponderosa pine and the artery wall, etc. The discovery also provides insights in the design of stiffer composite cylinders with applications in aerospace and building industries.

Taking the *Ea.* anchor spicules for example, the results shown in Figure 3.5 indicates that by cutting a hollow cylinder into multiple concentric tubes and assuming no friction between adjacent layers, the effective bending stiffness of the multilayered cylinder is reduced. This result is quite generous for structures made with orthotropic materials of different helical angles. Because of the high compliance property of the spicules under bending, the spicules are able to provide better anchorage to secure the glass sponge on the bottom sea floor.

It should be noted that, although the results presented in this chapter are very encouraging, they are far from a complete proof that the primary mechanical benefit of the lamellar architectures in

the *Ea.* anchor spicule is to increase its bending stiffness. To complete the proof, the following experiments are required:

1. Characterization of the *Ea.* spicule's material properties. In the numerical example in §3.4, we use a dummy material to illustrate our design idea to achieve desired bending stiffness for composite cylindrical structure. However, to determine whether the idea is also applicable in *Ea.* anchor spicules, we have to measure the orthotropic material properties of the actual *Ea.* spicules. Material characterization of orthotropic material is a difficult task, especially when the material is forming in cylindrical shape with multiple layers. Many material characterization methods involve inverse engineering, which is to deduce the material properties from the structure's bulk properties. These methods rely on the correctness of the assumptions on the material type and the homogenization theory. We will look for more independent method to characterize the *Ea.* spicule's material properties. One possible solution is to extract the solid silica core of the *Ea.* spicule and measure the core's material properties as the material properties of the genetic silica in the spicules.

2. Characterization of the interfacial property of the adjacent silica layers. We assume that the interfacial property to be no friction for the silica layers in *Ea.* anchor spicules. However, there exist thin proteinaceous interfaces between adjacent silica layers in *Ea.* anchor spicules. The interfacial condition should lay between no slip and no fraction.

3. Measurement of thickness and helical angles of each silica layers. The thickness of each cylindrical silica layers can be measured using high magnification images. The helical angles can be measured through images of spicule specimen after tensile test (see Figure 1.5). However, more efforts are required to correlate the helical angles with the right layer numbers.

4. Characterization of the *Ea.* spicule's bulk property. This is straightforward and can be performed on our customized mechanical test stage [38, 29].

Chapter 4

A geometrically nonlinear shear deformable beam theory

4.1 Introduction

With the rapid development of soft electronics and bionic robot, the study on deformation of highly flexible structures has raised a lot of interest. Furthermore, in the field of aircraft design, slender structures that can undergo large elastic deformations are widely used as construction components. Therefore, a practical and precise geometrically nonlinear beam theory is highly demanded.

In addition, slender composite structures undergoing large elastic deformation also exist in biological structural materials. For example, the *Ea.* anchor spicules (long, hair-like skeletal elements) play an important role in securing the sponge into the soft sediments of the sea floor [39]. Some spicules will tangle with small rocks in the mud and form knots, which helps the sponge anchor tightly to the sea floor. When a spicule forms a knot, we expect not only bending deformation but also shearing deformation along the spicule. As in artificial lamellar composite beams, the shearing effect can be critical in the deformation of spicules because of the layered internal architectures in spicules. To investigate the structure-function relationships in these finite deformable laminated structures, we demand a geometrically nonlinear beam theory incorporating shear deformation.

Among all geometrically nonlinear beam theories, the most elementary one is the Elastica

theory [6, 7], which is an extension of Euler-Bernoulli beam theory in finite deformation regime. A more general geometrically nonlinear plane beam theory where bending, transverse shearing and axial stretching are taken account of was first presented by Reissner [8]. In this theory, Reissner applied the principle of virtual work to determine the relations between physical strains and displacements. The balance laws of resultant forces and moments are derived by free-body-diagram analysis. He suggested that an associated system of constitutive equations can be deduced from experimental measurements. Later, Simo [9] extended Reissner's plane beam theory into a three-dimensional dynamic theory, also known as geometrically-exact rod model.

Due to the high nonlinearity of the governing equations of these beam theories, researchers usually solve them by numerical methods based on finite element approximation [97, 98]. However, for plane beam theory with simple constitutive relations, the problem can be solved analytically. For example, Goto *et al.* [99] presented elliptic integral solutions of geometrically nonlinear plane beam problem with axial and shear deformation.

In this chapter, we propose a variationally consistent shear deformable beam theory, which is a finite deformation generalization of Timoshenko beam theory. Taking advantage of the slender geometrical feature of beams, we propose a set of kinematic assumptions allowing for arbitrarily large bending and shearing deformation. Following the general three-dimensional continuum theory and employing the Hellinger-Reissner variational principle, we develop a shear deformable beam theory in a systematic way.

Here is a brief outline of this chapter. In section 4.2, we illustrate the kinematic assumptions and the derivations of the shear deformable beam theory in the context of continuum mechanics. Then in section 4.3, we discuss the well-posedness of the proposed beam theory by comparing this model with Reissner's finite strain beam theory [8]. In section 4.4, we briefly present the procedures of finite element formulation of the proposed beam theory. In section 4.5, we present a series of numerical examples to demonstrate the capacity of the proposed theory. Finally, in section 4.6, we make a conclusion of this work.

4.2 A variationally consistent formulation of shear deformable beams

We consider an initially straight slender structure of length L with constant cross-section $\Omega \in \mathbb{R}^2$. An orthonormal set of Cartesian basis vectors $\{\hat{\mathbf{E}}_1, \hat{\mathbf{E}}_2, \hat{\mathbf{E}}_3\}$ spans $\mathbb{R}^3$, with $\{X_1, X_2, X_3\}$ being its corresponding set of Cartesian coordinates. The origin of the coordinate system, marked as O, is located at one end of the centroidal axis of the beam. In its undeformed configuration, which we denote as $\mathcal{B}_0$, the beam is stress free. The axial direction of the beam is collinear with $\hat{\mathbf{E}}_1$ and the principal axes of inertia of Ω are collinear with $\{\hat{\mathbf{E}}_2, \hat{\mathbf{E}}_3\}$. Thus the centroidal axis of the beam can be described as $\{X_1 \in [0, L] \mid X_2 = 0, X_3 = 0\}$.

The deformation map is denoted by $\boldsymbol{\phi} : \mathcal{B}_0 \subset \mathbb{R}^3 \to \mathbb{R}^3$. The material points in the deformed configuration $\boldsymbol{\phi}(\mathbf{X})$ are designated by $\mathbf{x}$, with associated basis vectors $\{\hat{\mathbf{e}}_1, \hat{\mathbf{e}}_2, \hat{\mathbf{e}}_3\}$.

4.2.1 Kinematics

We consider the following four assumptions to the beam's kinematics: (i) Plane sections normal to the centroidal line remain plane after deformation. (ii) The centroidal line does not undergo any length change. (iii) The material of the beam is incompressible. (iv) We ignore the deformation in $\hat{\mathbf{E}}_3$ direction caused by Poisson's effect. The assumption (i) is a classical kinematic hypothesis that widely used in many beam models such as Euler-Bernoulli beam theory and Timoshenko beam theory [1]. The assumptions (ii-iv) are intended to simplify the model so that the resulting formulas are more tractable.

Based on these assumptions, we propose the following kinematics:

$$x_1 = X_1 + u(X_1) - \alpha(X_1) X_2 \sin(\theta(X_1)), \tag{4.1a}$$

$$x_2 = w(X_1) + \alpha(X_1) X_2 \cos(\theta(X_1)), \tag{4.1b}$$

$$x_3 = X_3. \tag{4.1c}$$

where $u(X_1)$ and $w(X_1)$ are the displacements of the material points on centroidal line in $\hat{\mathbf{E}}_1$ and $\hat{\mathbf{E}}_2$ directions, respectively (see Figure 4.1). The angle between the normal direction of deformed cross section and $\hat{\mathbf{E}}_1$ is designated by $\theta(X_1)$. The expansion factor $\alpha(X_1)$ allows the cross-section

area to change during the deformation and will be determined through assumption (iii). It should be noted that the incorporation of $\alpha(X_1)$ in the kinematics is important in stabilizing the system under high-shear deformation. We will elaborate this argument in Section 4.3.

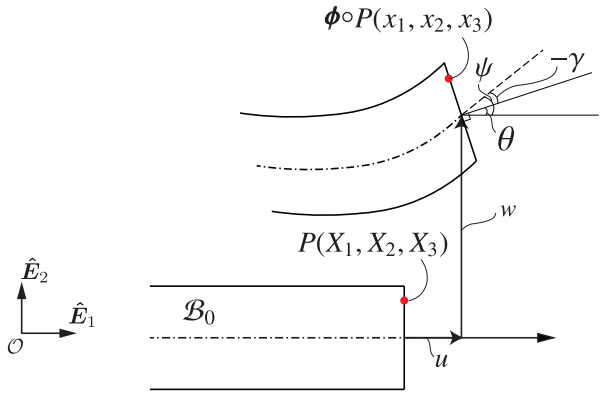

Figure 4.1: The schematic of the kinematics for a plane beam.

By imposing $X_2 = X_3 = 0$, we have $\boldsymbol{\phi}_0 = \boldsymbol{\phi}(\mathbf{X})|_{X_2=X_3=0}$, the deformation map of the centroidal line. An infinitesimal element of the centroidal line $\mathbf{dX} = dX_1\hat{\mathbf{E}}_1$ in undeformed configuration is mapped to $\mathbf{dx} = (dX_1 + du)\hat{\mathbf{E}}_1 + dw\hat{\mathbf{E}}_2$ in deformed configuration. The assumption (ii) implies that $|\mathbf{dx}| = |\mathbf{dX}| = dX_1$, that is, $\sqrt{(1+u')^2 + w'^2} = 1$, where $(\cdot)'$ indicates $d(\cdot)/dX_1$. We designate the tangent angle of the deformed centroidal line by $\psi(X_1)$. It follows that $\sin(\psi) = dw/|\mathbf{dx}| = w'$ and $\cos(\psi) = (dX_1 + du)/|\mathbf{dx}| = u' + 1$.

Following the standard continuum mechanics definition, we calculate the deformation gradient tensor as $\mathbf{F} = \partial\mathbf{x}/\partial\mathbf{X}$. The Jacobian $J = \det(\mathbf{F})$ is computed as $J = \alpha(X_1)\cos(\theta(X_1) - \psi(X_1)) - X_2\alpha(X_1)^2\theta'(X_1)$. We enforce J to be unit in average over the cross section, which gives the expansion factor $\alpha(X_1)$ as

$$\alpha(X_1) = \frac{1}{\cos(\theta(X_1) - \psi(X_1))} = \frac{1}{\cos(\gamma(X_1))}, \tag{4.2}$$

where shear angle $\gamma(X_1) = \theta(X_1) - \psi(X_1)$ is the difference angle between the normal direction of the cross section and the tangent direction of the centroidal line at position X_1. In Timoshenko beam theory, γ is independent of X_1 while in Euler-Bernoulli beam theory $\gamma = 0$ since shear deformation is ignored.

We now proceed to calculate the components of Green-Lagrangian strain tensor $\mathbf{E} = (\mathbf{F}^T\mathbf{F} - \mathbf{I})/2$

as

$$E_{11} = -X_2\left(\psi' + \gamma' \sec^2(\gamma)\right) + \frac{X_2^2}{2}\sec^2(\gamma)\left(\theta'^2 + \gamma'^2 \tan^2(\gamma)\right), \tag{4.3a}$$

$$E_{12} = E_{21} = -\frac{1}{2}\tan(\gamma) + \frac{X_2}{2}\gamma' \sec^2(\gamma)\tan(\gamma), \tag{4.3b}$$

$$E_{22} = \frac{1}{2}\tan^2(\gamma), \tag{4.3c}$$

$$E_{13} = E_{31} = E_{23} = E_{32} = E_{33} = 0. \tag{4.3d}$$

4.2.2 Hellinger-Reissner variational principle

In the previous section, we discussed about the kinematic hypotheses. In order to build a close-formed beam model, we also need equilibrium equations of motion and constitutive relations as well.

Generally, there are two paths one can follow to achieve this goal. They are theoretically equivalent but involve different experimental consideration. One path is to focus on the concepts of resultants forces/moments and physical strains (such as shear angles, curvatures of the centroidal line, etc.) [8, 100, 101, 102]. In this path, equilibrium equations of motion provide the relations between the internal resultant forces/moments and the external applied forces/moments. Physical constitutive relations between the resultants forces and physical strains are usually deduced from experimental measurements [8, 100].

In another path, the close-formed governing equations are derived from calculus of variations [103]. An energy functional is constructed following the theory of continuum mechanics. Among all kinds of energy functionals, the most commonly used one is the total potential energy of the system. By the principle of minimum total potential energy, the governing equations follows as the Euler-Lagrange equations. In this path, the material constitutive relations that connect the stress and strain of the beam's material are required. Such relations, analogous to the physical constitutive relations, are typically measured from experiments. However, due to the wide availability of material databases, the material constitutive relations are more accessible than the physical constitutive relations for beams.

In this model, we follow the second path. Thus our derivations circumvent the problem of

needing to determine constitutive relations between stress resultants and generalized strains by physical experiments. Instead, existing material constitutive relations, e.g. Saint Venant-Kirchhoff law, at the stress-strain level can be utilized.

The minimum total potential energy principle is commonly used to derive the governing equations of beam models [103]. According to this principle, the energy functional Π is defined as the combination of elastic strain energy U and external potential energy V, that is, $\Pi = U + V$. By minimizing Π over the space of kinematically admissible displacement field, one will obtain a set of governing equations and boundary conditions. However, even in the classic Euler-Bernoulli beam theory, the implementation of the minimum total potential energy principle causes inconsistency [104]. We will elaborate the inconsistency as follows.

In the derivation of pure bending Euler-Bernoulli beam theory, the only non-zero component of the linearized infinitesimal strain is $\epsilon_{11} = -X_2 w''$. Cauchy stress $\boldsymbol{\sigma}$ is calculated through the linear elastic constitutive law

$$\boldsymbol{\sigma} = 2\mu\boldsymbol{\epsilon} + \lambda \operatorname{tr}(\boldsymbol{\epsilon})\mathbf{I}, \tag{4.4}$$

where μ and λ are Lamé coefficients, $\mathbf{I}$ is the second order identity tensor and $\operatorname{tr}(\cdot)$ is trace operation. Lamé coefficients are related to Poisson's ratio ν and Young's modulus E by $\mu = E/(2+2\nu)$ and $\lambda = \nu E/((1+\nu)(1-2\nu))$.

It's easy to check that the lateral normal Cauchy stress components σ_{22} and σ_{33} are non-zero, which violates the stress-free boundary conditions on the beam's lateral surfaces. Furthermore, the total strain energy of Euler-Bernoulli beam $U_{\mathrm{EB}} = \int_{\mathcal{B}} \boldsymbol{\sigma} : \boldsymbol{\epsilon}/2 \, dV$ is given by

$$U_{\mathrm{EB}} = \frac{E^* I}{2} \int_0^L w''^2 \, dX_1, \tag{4.5}$$

where $E^* = E(1-\nu)/((1+\nu)(1-2\nu))$ is the effective Young's modulus, which is larger than E if $\nu \neq 0$. To resolve the problem of incorrect effective Young's modulus, one needs to artificially modify either the strain tensor or stress tensor. The artificially modified strain and stress will inevitably violate the constitutive law and boundary condition.

To avoid the inconsistency, we choose to apply the Hellinger-Reissner variational principle

instead of the minimum total potential energy principle for deriving the geometrically nonlinear shear deformable beam theory. The Hellinger-Reissner variational principle [105] allows displacements and stresses to be assumed and varied separately. As a result, the strains recovered from displacements and strains computed from stresses will not generally be the same. This expands the solution space and looses the constitutive constraint so that it is possible to further reduce functional value of total energy of the system.

The Hellinger-Reissner functional Π_{HR} for a general three-dimensional finite deformation problems is expressed as

$$\Pi_{\text{HR}}\left[\mathbf{u}, \mathbf{S}\right] = \int_V \left(\mathbf{S} : \mathbf{E}^{\mathbf{u}} - \frac{1}{2}\mathbf{S} : \mathbb{S} : \mathbf{S} - \mathbf{b} \cdot \mathbf{u} \right) dV - \int_{S_t} \hat{\mathbf{t}} \cdot \mathbf{u} \, dS, \tag{4.6}$$

where $\mathbf{b}$, $\hat{\mathbf{t}}$ and $\mathbb{S}$ are the body force vector, specified surface traction and compliance tensor, respectively. The first integral is over the whole beam and the second integral is over the traction boundary S_t. The kinematically admissible displacement field $\mathbf{u}$ only needs to satisfy the displacement boundary conditions and $\mathbf{E}^{\mathbf{u}}$ is the Green-Lagrangian strain tensor calculated from $\mathbf{u}$. The second Piola-Kirchhoff stress $\mathbf{S}$ may also come from assumptions.

In our geometrically nonlinear shear deformable beam model, we assume that S_{11} and $S_{12} = S_{21}$ distribute linearly and uniformly over cross sections, respectively:

$$S_{11} = -\frac{M(X_1)}{I} X_2, \tag{4.7a}$$

$$S_{12} = S_{21} = \frac{V(X_1)}{A}, \tag{4.7b}$$

where M and V are unknown functions of X_1, the second moment of inertia is $I = \int_\Omega X_2^2 \, d\Omega$ and the cross-section area is $A = \int_\Omega d\Omega$. We ignore all other components in $\mathbf{S}$ considering the relatively small magnitudes of those stress components. As for the constitutive law, we employ Saint Venant-Kirchhoff constitutive law [106] to model the stress-strain relation of the beam:

$$\mathbf{S} = 2\mu\mathbf{E} + \lambda \, \text{tr}(\mathbf{E})\mathbf{I}. \tag{4.8}$$

The corresponding compliance tensor in component form is

$$\mathbb{S}_{IJKL} = \frac{1+\nu}{2E}(\delta_{IL}\delta_{JK} + \delta_{IK}\delta_{JL}) - \frac{\nu}{E}\delta_{IJ}\delta_{KL}. \tag{4.9}$$

We choose to employ Saint Venant-Kirchhoff constitutive law because it is the simplest among all nonlinear constitutive models. As similar to other hyperelastic constitutive models, it reduces to linear elastic constitutive law in the limit of infinitesimal deformation. Although this constitutive model has a few drawbacks, e.g. the stored energy function is not polyconvex, the lack of any term preventing the Jacobian to approach zero [106], it is quite popular in numerical computations due to its relative simplicity in implementation. It is often used in modeling structures undergoing large deformation within the framework of finite element methods (FEM) and adopted by many commercial FEM software such as ABAQUS and ANSYS.

Due to the assumption (ii) that the centroidal line of the beam is inextensible, we are able to describe the material point position along the beam's centroidal line by arc-length coordinate $s = X_1 \in [0, L]$. For the boundary conditions, we assume that the left end ($s = 0$) of the beam is encastered while the right end ($s = L$) of the beam is under a moment $\mathbf{M} = M_0\hat{\mathbf{E}}_3$. In addition, there is distributed force $\mathbf{P}(s) = P_1(s)\hat{\mathbf{E}}_1 + P_2(s)\hat{\mathbf{E}}_2$ applied along the beam. We substitute the assumed deformation mapping (4.1a)-(4.1c), Green-Lagrangian strain components (4.3a)-(4.3d), the assumed stress components (4.7a), (4.7b) and the compliance tensor (4.9) into the Hellinger-Reissner functional (4.6):

$$\begin{aligned}\Pi_{\text{HR}}\left[M(s), V(s), \theta(s), \psi(s)\right] = &\int_V \left(\frac{MX_2^2}{I}\left(\gamma' \sec^2(\gamma) + \psi'\right) - \frac{V}{A}\tan(\gamma) - \frac{M^2X_2^2}{2EI^2} - \frac{V^2}{2\mu A^2}\right) dV \\ &- \int_0^L \left(P_u(s)\cos(\psi) - P_u(s) + P_w(s)\sin(\psi)\right)\, ds - M_0\theta|_{s=L}.\end{aligned} \tag{4.10}$$

where $P_u(s) = \int_s^L P_1(\xi)\, d\xi$, $P_w(s) = \int_s^L P_2(\xi)\, d\xi$, and the shear angle $\gamma(s) = \theta(s) - \psi(s)$. If the external force only involves concentrative force at the right end, that is $\mathbf{P} = P_0\delta(s-L)\hat{\mathbf{E}}_1 + V_0\delta(s-L)\hat{\mathbf{E}}_2$ where $\delta(x)$ is Dirac delta function, we will obtain $P_u(s) = P_0$ and $P_w(s) = V_0$.

Through variations with respect to $M(s)$, $V(s)$, $\theta(s)$ and $\psi(s)$, we obtain a set of governing

equations

$$M = EI\left(\gamma' \sec^2(\gamma) + \psi'\right), \tag{4.11a}$$

$$V = -\mu A \tan(\gamma), \tag{4.11b}$$

$$M' = P_u \sin(\psi) - P_w \cos(\psi), \tag{4.11c}$$

$$V = -P_u \sin(\psi) + P_w \cos(\psi). \tag{4.11d}$$

with boundary conditions

$$\theta = 0, \text{ at } s = 0, \tag{4.12a}$$

$$\gamma = 0, \text{ at } s = 0, \tag{4.12b}$$

$$\gamma = 0, \text{ at } s = L, \tag{4.12c}$$

$$M = M_0, \text{ at } s = L. \tag{4.12d}$$

4.2.3 Reduction to Elastica theory and Timoshenko beam theory

As a geometrically nonlinear shear deformable beam model, the closed-form system of first-order ODE (4.11a)-(4.12d) should reduce to the Elastica theory when the shear deformation is negligible. On the other hand, it should reduce to Timoshenko beam theory when restricted to small deformation. The rigorous way to show the reduction should start from the functional level. That is, we first make proper approximations of functional Π_{HR} (4.10), then derive the governing equations for the reduced theory through variations.

When the shear deformation is negligible, we expect the shear angle $\gamma = 0$ and the shear stiffness $\mu A \to \infty$, which implies $\psi = \theta$. Assuming concentrative force $\mathbf{P} = P_0\hat{\mathbf{E}}_1 + V_0\hat{\mathbf{E}}_2$ and moment $\mathbf{M} = M_0\hat{\mathbf{E}}_3$ are applied on the right end ($s = L$) of a cantilever beam, the Hellinger-Reissner functional as per Elastica theory becomes

$$\Pi_{\text{E}}\left[M(s), \theta(s)\right] = \int_V \left(\frac{MX_2^2}{I}\theta' - \frac{M^2X_2^2}{2EI^2}\right) dV - \int_0^L \left(P_0\left(\cos(\theta) - 1\right) + V_0 \sin(\theta)\right) ds - M_0\theta|_{s=L}. \tag{4.13}$$

Through variations with respect to $M(s)$, $\theta(s)$ and eliminating $M(s)$, we obtain the governing

equation of Elastica theory [104] as

$$(EI\theta')' - P_0 \sin(\theta) + V_0 \cos(\theta) = 0, \tag{4.14}$$

with boundary conditions

$$\theta = 0, \text{ at } s = 0, \tag{4.15a}$$

$$EI\theta' = M_0, \text{ at } s = L. \tag{4.15b}$$

On the other hand, if the deformation is restricted to be infinitesimally small, we can linearize the functional Π_{HR} (4.10) and reproduce the Timoshenko beam theory. Assuming concentrative force $\mathbf{P} = P_0\hat{\mathbf{E}}_1 + V_0\hat{\mathbf{E}}_2$ and moment $\mathbf{M} = M_0\hat{\mathbf{E}}_3$ are applied on the right end ($s = L$) of a cantilever beam, we substitute the expansions $\sin(\psi) = \psi + O(\psi^3)$, $\cos(\psi) = 1 + O(\psi^2)$, $\tan(\gamma) = \gamma + O(\gamma^3)$ and $\sec(\gamma) = 1 + O(\gamma^2)$ into functional (4.10)

$$\begin{aligned}\Pi_{\text{T}}\left[M(s), V(s), \theta(s), \gamma(s)\right] = &\int_V \left(\frac{MX_2^2}{I}\left(\theta' + O(\gamma^2)\gamma'\right) - \frac{V}{A}\left(\gamma + O(\gamma^3)\right) - \frac{M^2X_2^2}{2EI^2} - \frac{V^2}{2\mu A^2} \right) dV \\ &- \int_0^L \left(O(\psi^2)P_0 + V_0\left(\theta - \gamma + O(\psi^3)\right)\right) ds - M_0\theta|_{s=L},\end{aligned} \tag{4.16}$$

where the symbol $O(p^q)$ denotes all terms in the expression that vanish at a rate that is faster than or equal to p^q as $p \to 0$. As γ and ψ approach infinitesimal small, we take the first order approximation of Π_{T} (4.16). Through variations with respect to $M(s)$, $V(s)$, $\theta(s)$ and $\gamma(s)$, we obtain a set of governing equations

$$M = EI\theta', \tag{4.17a}$$

$$V = -\mu A\gamma, \tag{4.17b}$$

$$M' = -V_0, \tag{4.17c}$$

$$V = V_0, \tag{4.17d}$$

with boundary conditions

$$\theta = 0, \text{ at } s = 0, \tag{4.18a}$$

$$M = M_0, \text{ at } s = L. \tag{4.18b}$$

Recall that $w' = \sin(\psi) = \psi + O(\psi^3)$. Under first order approximation, we have $\psi = w'$. With an additional boundary condition $w(0) = w_0$, where w_0 is the deflection of the beam at position $s = 0$, the equations (4.17a)-(4.18b) are indeed the governing equations of Timoshenko beam theory [2].

4.3 Comparison with Reissner's theory in conjunction with Saint Venant-Kirchhoff constitutive model

Among the different versions of geometrically nonlinear shear deformable beam theories, the most prominent one is proposed by Reissner [8] in 1972 as mentioned in Section 4.1. The main differences between Reissner's theory and the proposed theory lie in the assumption of kinematics. As we described in Section 4.2.1, we proposed four assumptions to the beam's kinematics. The plane cross-section assumption (i) and no Poisson's effect assumption (iv) are shared by Reissner's theory as well. Other researchers, such as Iwakuma and Kuranishi [101], Chaisomphob *et al.* [102] and Simo [9], adopted the equivalent kinematics in their study. The in-extensibility assumption (ii) does not have fundamental effect to the model, as we include this assumption only for simplicity of the model since it suppresses one degree of freedom. It is the assumption (iii) and its implication that makes the proposed theory quite different from the existing models. In the kinematics (4.1a)-(4.1c) of the proposed theory, we introduce an extra expansion factor $\alpha(X_1)$ over the cross section of the beam while Reissner's theory does not have this degree of freedom. The ignorance of changes in the cross-sectional area in kinematic assumption also exists in Simo's geometrically nonlinear beam theory [9].

In this section, we are going to discuss the different characteristics between Reissner's theory and the proposed beam model under compressive axial loading. We show that Reissner's theory in conjunction with Saint Venant-Kirchhoff constitutive model is ill-posed, in the sense that the

existence of minimizers to the functional is not guaranteed, while the existence of minimizers to the proposed beam model is proved. The nonlinear FEM computation results are consistent with our analysis.

4.3.1 Ill-posedness of Reissner's theory in conjunction with Saint Venant-Kirchhoff constitutive model

To compare our model with Reissner's finite strain beam theory, we need to simplify Reissner's theory and make these two models comparable. Since Reissner's theory takes account of stretching, bending and shearing deformation of the beam, we would like to restrict the stretching deformation in his theory according to assumption (ii). Due to the fact that Reissner did not stipulate any constitutive relations for his model, we choose to employ Saint Venant-Kirchhoff constitutive law, the most fundamental nonlinear constitutive relation for finite deformation, as we did for our model. Stipulating the expansion factor $\alpha(X_1) \equiv 1$ and following the same procedures as in Section 4.2, we obtain a set of governing equations

$$M = EI\theta' \cos(\gamma), \tag{4.19a}$$

$$V = -\mu A \sin(\gamma), \tag{4.19b}$$

$$M\psi' = -(M' + V)\cot(\gamma), \tag{4.19c}$$

$$(M\cos(\gamma))' = P_u \sin(\psi) - P_w \cos(\psi). \tag{4.19d}$$

with boundary conditions

$$\theta = 0, \text{ at } s = 0, \tag{4.20a}$$

$$M\cos(\gamma) = M_0, \text{ at } s = L. \tag{4.20b}$$

We formulate the dimensionless Hellinger-Reissner functional $\hat{\Pi}_{\mathrm{HR}} = \Pi_{\mathrm{HR}} L/(EI)$ for the compressive buckling problem ($P_u(s) = P_0 < 0$, $P_w(s) = M_0 = 0$) as

$$\hat{\Pi}_{\mathrm{HR}}[\hat{M}(\hat{s}), \hat{V}(\hat{s}), \theta(\hat{s}), \gamma(\hat{s})] = \int_0^1 \left(\frac{1}{2}\hat{M}^2 + \frac{k}{2}\hat{V}^2 - \hat{P}_0(\cos(\theta - \gamma) - 1) \right) d\hat{s}, \tag{4.21}$$

where $\hat{s} = s/L$, $k = \mu AL^2/(EI)$, $\hat{M} = ML/(EI)$, $\hat{V} = V/(\mu A)$, $\hat{P}_0 = P_0L^2/(EI)$ are dimensionless variables.

For Reissner's finite strain beam theory, we non-dimensionalize equations (4.19a) and (4.19b) then substitute them into $\hat{\Pi}_{\mathrm{HR}}$ (4.21). In this way, we eliminate the dependence of the functional on $\hat{M}$ and $\hat{V}$. Only kinematic variables θ and γ remain in the functional, which is convenient for theoretical analysis and numerical calculation later (see Section 4.4). For Reissner's theory, it follows that

$$\hat{\Pi}^{\mathrm{R}}[\theta(\hat{s}), \gamma(\hat{s})] = \int_0^1 \left[\frac{1}{2}(\theta')^2\cos^2(\gamma) + \frac{k}{2}\sin^2(\gamma) - \hat{P}_0(\cos(\theta-\gamma)-1)\right] d\hat{s}. \tag{4.22}$$

The admissible space for θ and γ is

$$\mathcal{K} = \left\{\theta(\hat{s}) \in H^1_\gamma(0,1),\ \gamma(\hat{s}) \in L^\infty\left((0,1);[-\pi,\pi]\right) \,|\, \theta(0) = 0, \cos(\gamma) > 0\right\},$$

where $H^1_\gamma(0,1)$ is a weighted Sobolev space, with the norm

$$\left(\int_0^1 \left(\theta'(\hat{s})^2\cos^2(\gamma(\hat{s})) + \theta(\hat{s})^2\right) d\hat{s}\right)^{1/2} < \infty.$$

The constraint $\cos(\gamma) > 0$ comes from the compatibility condition of the beam's deformation, $\langle \det(\mathbf{F})\rangle = \cos(\gamma) > 0$, where $\langle\cdot\rangle$ indicates taking average over the cross section. In the following, we show that the functional $\hat{\Pi}^{\mathrm{R}}$ has no minimizer in the admissible space $\mathcal{K}$ through proof by contradiction.

We denote m as the infimum of $\hat{\Pi}^{\mathrm{R}}$ for any $(\theta(\hat{s}), \gamma(\hat{s})) \in \mathcal{K}$ and start by observing that $m \geq 2\hat{P}_0$ since

$$\begin{aligned}
\hat{\Pi}^{\mathrm{R}}[\theta(\hat{s}), \gamma(\hat{s})] &\geq \int_0^1 -\hat{P}_0(\cos(\theta-\gamma)-1)\, d\hat{s} \\
&\geq \int_0^1 -2|\hat{P}_0|\, d\hat{s} \\
&= 2\hat{P}_0.
\end{aligned}$$

We then show that $m = 2\hat{P}_0$ by constructing a minimizing sequence. Let $n \in \mathbb{N}$ and consider two sequences of piecewise functions

$$\theta_n(\hat{s}) := \begin{cases} -\pi n \hat{s}, & 0 \le \hat{s} \le \frac{1}{n}, \\ -\pi, & \frac{1}{n} \le \hat{s} \le 1. \end{cases} \tag{4.23a}$$

$$\gamma_n(\hat{s}) := \begin{cases} \frac{\pi}{2}\left(1 - \frac{1}{n}\right), & 0 \le \hat{s} \le \frac{1}{n}, \\ 0, & \frac{1}{n} \le \hat{s} \le 1. \end{cases} \tag{4.23b}$$

We substitute $\theta_n(\hat{s})$ and $\gamma_n(\hat{s})$ into functional $\hat{\Pi}^{\mathrm{R}}$ (4.22) and obtain a sequence of $\hat{\Pi}^{\mathrm{R}}_n$ as

$$\hat{\Pi}^{\mathrm{R}}_n = \frac{k - 4\hat{P}_0 + k\cos\left(\frac{\pi}{n}\right)}{4n} + \frac{2\hat{P}_0 \cos\left(\frac{\pi}{2n}\right)}{\pi n} + \frac{n\pi^2}{4}\left(1 - \cos\frac{\pi}{n}\right) + 2\hat{P}_0 \tag{4.24}$$

As $n \to \infty$, we have $\hat{\Pi}^{\mathrm{R}}_n \to 2\hat{P}_0$, which implies that $m = 2\hat{P}_0$.

For the sake of contradiction, we assume that there exists a minimizer $(\bar{\theta}(\hat{s}), \bar{\gamma}(\hat{s})) \in \mathcal{K}$. Then we should have $\hat{\Pi}^{\mathrm{R}}[\bar{\theta}(\hat{s}), \bar{\gamma}(\hat{s})] = 2\hat{P}_0$. We deduce that $\sin^2(\bar{\gamma}) = (\bar{\theta}')^2 = 0$ and $\cos(\bar{\theta} - \bar{\gamma}) = -1$ have to be true a.e. (almost everywhere) in $(0, 1)$. Since $\bar{\theta}(\hat{s}) \in H^1(0, 1)$ is continuous and $\bar{\theta}(0) = 0$, the only possible solution for $\bar{\theta}(\hat{s})$ is that $\bar{\theta} \equiv 0$. Thus we are left with that $\cos(\bar{\gamma}) = -1$ has to be true a.e. in $(0, 1)$. Obviously, $\cos(\bar{\gamma}) = -1$ contradicts the compatibility condition. Thus our assumption that there exists a minimizer for $\hat{\Pi}^{\mathrm{R}}$ leads to a contradiction. Therefore, at least for the compressive buckling problem, Reissner's theory is ill-posed.

4.3.2 Proof of the existence of solutions for the proposed beam model

In this subsection, we provide a proof to show the conditional existence of solutions for the proposed geometrically nonlinear shear deformable beam model. A sufficient existence condition is $k \ge \sqrt{\hat{P}_u(\hat{s})^2 + \hat{P}_w(\hat{s})^2}$ for a cantilever under distributed loading, where $\hat{P}_u(\hat{s}) = P_u(\hat{s})L^2/(EI)$ and $\hat{P}_w(\hat{s}) = P_w(\hat{s})L^2/(EI)$. Specifically, for the compressive buckling problem, a sufficient existence condition is $k + \hat{P}_0 > 0$. The general method to show existence of minimizers for minimization problems in the Calculus of Variations is the Direct Method [107]. For the proposed beam theory, not all conditions in the Direct Method are satisfied. Thus, the Direct Method is not applicable in this case. Although the Direct Method fails, existence of solutions might still be possible, as we

demonstrate in the following proof.

To obtain the dimensionless Hellinger-Reissner functional for a geometrically nonlinear shear deformable beam under distributed loading, we non-dimensionalize equations (4.11a) and (4.11b), then substitute them into $\hat{\Pi}_{\mathrm{HR}}$ (4.21). The functional for this model follows as

$$\hat{\Pi}^{\mathrm{F}}[\theta(\hat{s}), \gamma(\hat{s})] = \int_0^1 \left[\frac{1}{2}(\theta' + \gamma' \tan^2(\gamma))^2 + \frac{k}{2}\tan^2(\gamma) - \hat{P}_u(\cos(\theta - \gamma) - 1) - \hat{P}_w \sin(\theta - \gamma) \right] d\hat{s}, \tag{4.25}$$

with essential boundary condition $\theta(0) = 0$.

We introduce new variables $p(\hat{s}) = \theta(\hat{s}) - \gamma(\hat{s}) + \tan(\gamma(\hat{s}))$ and $q(\hat{s}) = \tan(\gamma(\hat{s}))$, so that $p'(\hat{s}) = \theta'(\hat{s}) + \gamma'(\hat{s})\tan^2(\gamma(\hat{s}))$ and $p(\hat{s}) - q(\hat{s}) = \theta(\hat{s}) - \gamma(\hat{s})$. Substituting these transformations into the functional $\hat{\Pi}^{\mathrm{F}}$ (4.25), we obtain a transformed functional of $p(\hat{s})$ and $q(\hat{s})$ as

$$\hat{\Pi}^{\mathrm{FT}}[p(\hat{s}), q(\hat{s})] = \int_0^1 \left[\frac{1}{2}(p')^2 + \frac{k}{2}q^2 + f(p - q) \right] d\hat{s}, \tag{4.26}$$

where $f(p-q) = -\hat{P}_u(\cos(p-q) - 1) - \hat{P}_w \sin(p-q)$. The essential boundary condition $\theta(0) = 0$ comes out to be a constraint

$$q(0) = \tan\left(q(0) - p(0)\right). \tag{4.27}$$

The constraint (4.27) can not be implemented directly since $q(\hat{s}) \in L^\infty((0,1);[-\pi,\pi])$ can take arbitrary value at $\hat{s} = 0$ without affecting the value of the functional 4.26. Considering that $p(\hat{s}) \in H^1((0,1);[-\pi,\pi])$, $p(\hat{s})$ has to be continuous on $(0,1)$. Therefore, it is reasonable to put constraints on $p(0)$. Based on the above discussion, the admissible space for $p(\hat{s}), q(\hat{s})$ comes out to be

$$\mathcal{K} = \left\{ p(\hat{s}) \in H^1((0,1);[-\pi,\pi]), q(\hat{s}) \in L^\infty((0,1);[-\pi,\pi]) \mid p(0) \in \mathcal{A} \right\},$$

where the set

$$\mathcal{A} = \left\{ y \in \mathbb{R} \mid \bar{x} := \arg\min x \mapsto kx^2/2 + f(y - x), \bar{x} = \tan(\bar{x} - y) \right\},$$

accounts for both the minimality of $q(0)$ and constraint (4.27). We present the proof of the existence of minimizers for functional $\hat{\Pi}^{\mathrm{FT}}$ (4.26) as follows. By introducing set $\mathcal{A}$ for $p(0)$, the

constraint (4.27) is compatibly incorporated into the proof.

Let $\{p_n, q_n\}$ be a minimizing sequence for $\hat{\Pi}^{\mathrm{FT}}$ (4.26). Then, since $\{p_n\}$ must be bounded in $H^1(0,1)$, for a subsequence and a $p_\infty \in H^1(0,1)$, $p_n \rightharpoonup p_\infty$ weakly in $H^1(0,1)$. As for boundary condition, we have $p_\infty(0) = 0$ by weak continuity of trace in $H^1(0,1)$.

Now we choose a sequence $\{g_n\} \subset L^\infty(0,1)$ of piecewise constant functions such that $g_n \to p_\infty$ strongly in $L^2(0,1)$. We further choose a subsequence, not relabeled, so that $g_n(\hat{s}) \to p_\infty(\hat{s})$ for a.e. $\hat{s}$, and call the set of all $\hat{s}$ for which we have this convergence $\mathcal{S}$. For each $n \in \mathbb{N}$ and $\hat{s} \in (0,1)$, we solve for $h_n(\hat{s})$ that minimizes

$$x \mapsto \frac{k}{2}x^2 + f(g_n(\hat{s}) - x).$$

This minimizer exists because the map is continuous on $[-\pi, \pi]$. Note that we can choose the h_n so that they are piecewise constant functions as well. Then we define $q_\infty := \limsup_{n\to\infty} h_n$. Now that we have defined p_∞ and q_∞, we will prove that they are minimizers of the functional $\hat{\Pi}^{\mathrm{FT}}$ through the following two claims.

Claim 1. *$q_\infty(\hat{s})$ minimizes*

$$x \mapsto \frac{k}{2}x^2 + f(p_\infty(\hat{s}) - x), \tag{4.28}$$

for all $\hat{s} \in \mathcal{S}$.

Proof of Claim 1. We prove this claim for any fixed $\hat{s} \in S$. By definition of $q_\infty(\hat{s})$, we can choose a sequence $\{n_l\}$ such that $h_{n_l}(\hat{s}) \to q_\infty(\hat{s})$. By continuity of $F(x,y) := \frac{k}{2}y^2 + f(x-y)$ in both x and y

$$\frac{k}{2}h_{n_l}(\hat{s})^2 + f(g_{n_l}(\hat{s}) - h_{n_l}(\hat{s})) \to \frac{k}{2}q_\infty(\hat{s})^2 + f(p_\infty(\hat{s}) - q_\infty(\hat{s})) =: \beta.$$

Suppose for some $\bar{y} \in [-\pi, \pi]$,

$$\frac{k}{2}\bar{y}^2 + f(p_\infty(\hat{s}) - \bar{y}) =: \alpha < \beta.$$

Then

$$\frac{k}{2}\bar{y}^2 + f(g_{n_l}(\hat{s}) - \bar{y}) \to \alpha < \beta.$$

So, for l large enough,

$$\frac{k}{2}\bar{y}^2 + f(g_{n_l}(\hat{s}) - \bar{y}) < \frac{k}{2}h_{n_l}(\hat{s})^2 + f(g_{n_l}(\hat{s}) - h_{n_l}(\hat{s})),$$

which is contradicting the minimality of $h_{n_l}(\hat{s})$. So the claim is true.

Note that it follows immediately that $\hat{\Pi}^{\mathrm{FT}}[p_\infty, q_\infty] \le \hat{\Pi}^{\mathrm{FT}}[p_\infty, q]$ for all $q \in L^\infty((0,1);[-\pi,\pi])$.

Claim 2. (p_∞, q_∞) *minimizes* $\hat{\Pi}^{FT}$.

Proof of Claim 2. As $\{p_n, q_n\}$ being minimizing sequence for $\hat{\Pi}^{\mathrm{FT}}$ (4.26), we know that $\hat{\Pi}^{\mathrm{FT}}[p_n, q_n] \to \inf \hat{\Pi}^{\mathrm{FT}}$. So it is enough to show $\hat{\Pi}^{\mathrm{FT}}[p_n, q_n] \to \hat{\Pi}^{\mathrm{FT}}[p_\infty, q_\infty]$.

Regarding the first term of $\hat{\Pi}^{\mathrm{FT}}$, we know from weak convergence [107, 108] that

$$\int_0^1 \frac{1}{2}(p_\infty')^2 d\hat{s} \le \liminf_{n\to\infty} \int_0^1 \frac{1}{2}(p_n')^2 d\hat{s}. \tag{4.29}$$

We also know from **claim 1** that $\hat{\Pi}^{\mathrm{FT}}[p_\infty, q_\infty] = \min \hat{\Pi}^{\mathrm{FT}}[p_\infty, \cdot]$. We then choose a subsequence, not relabeled, so that we have a.e. convergence of p_n to p_∞. Now set $F(x,y) := \frac{k}{2}y^2 + f(x-y)$, where $x, y \in [-\pi, \pi]$. Note that there exists $C > 0$ such that

$$|F(x,y) - F(u,v)| \le C(|x-u| + |y-v|).$$

It follows that if $x_n \to x$, then $\min F(x_n, \cdot) \to \min F(x, \cdot)$. In particular, by the a.e. convergence of p_n to p_∞ and the minimality of q_∞ on $F(x_n, \cdot)$, we have $\min F(p_n, \cdot) \to F(p_\infty, q_\infty)$ a.e., and therefore

$$\liminf_{n\to\infty} \int_0^1 F(p_n, q_n) d\hat{s} \ge \liminf_{n\to\infty} \int_0^1 \min F(p_n, \cdot) d\hat{s} = \int_0^1 F(p_\infty, q_\infty) d\hat{s}. \tag{4.30}$$

Combining (4.29) and (4.30), we have

$$\liminf_{n\to\infty} \hat{\Pi}^{\mathrm{FT}}[p_n, q_n] \ge \hat{\Pi}^{\mathrm{FT}}[p_\infty, q_\infty].$$

Since $\liminf_{n\to\infty} \hat{\Pi}^{\mathrm{FT}}[p_n, q_n] \le \hat{\Pi}^{\mathrm{FT}}[p_\infty, q_\infty]$ is always true, we obtain $\liminf_{n\to\infty} \hat{\Pi}^{\mathrm{FT}}[p_n, q_n] = \hat{\Pi}^{\mathrm{FT}}[p_\infty, q_\infty]$,

and (p_∞, q_∞) minimizes $\hat{\Pi}^{\mathrm{FT}}$.

Therefore, we proved the existence of solutions for the proposed beam model. The sufficient existence condition results from the boundary condition $p(0) \in \mathcal{A}$, where the non-emptiness of $\mathcal{A}$ requires $k \geq \sqrt{\hat{P}_u(\hat{s})^2 + \hat{P}_w(\hat{s})^2}$.

4.4 Finite element formulation

Due to the nonlinearity of the ODE system (4.11a)-(4.12d), analytical solutions are not available most of the time. Consequently, we derive a numerical formulation which can be solved using finite element method (FEM). We are going to present the derivation of the weak form, discretization and linearization in this section. The Newton-Raphson update procedure is examined subsequently.

4.4.1 Weak form

We take advantage of the Hellinger-Reissner functional we have built up in Section 4.3. The weak form can be derived directly by taking variations to the dimensionless functional $\hat{\Pi}^{\mathrm{FT}}$ (4.26):

$$\int_0^1 \left[p' \delta p' + \left(\hat{P}_u \sin(p-q) - \hat{P}_w \cos(p-q) \right) \delta p + \left(kq - \hat{P}_u \sin(p-q) + \hat{P}_w \cos(p-q) \right) \delta q \right] \, d\hat{s} = 0. \tag{4.31}$$

The admissible spaces for variations are $\delta p(\hat{s}) \in W^{1,2}(0,1)$ and $\delta q(\hat{s}) \in L^2(0,1)$. We will address the constraint equation (4.27) by eliminating the corresponding degree of freedom (DOF) in the discretized form.

4.4.2 Discretization

We introduce a standard finite element discretization $[0,1] = \bigcup_{e=1}^{n_{\mathrm{el}}} I_e^h$, where I_e^h is a typical element with length $h > 0$ and n_{el} is the total number of elements. As usual, the calculations are performed on an element basis. We interpolate the elemental trial solutions and weighting functions in terms

of shape functions $N_i(\hat{s})$ according to

$$p_e^h(\hat{s}) = \sum_{i=1}^{n_{\text{en}}} N_i(\hat{s}) p_i^e, \quad \delta p_e^h(\hat{s}) = \sum_{i=1}^{n_{\text{en}}} N_i(\hat{s}) \delta p_i^e, \tag{4.32a}$$

$$q_e^h(\hat{s}) = \sum_{i=1}^{n_{\text{en}}} N_i(\hat{s}) q_i^e, \quad \delta q_e^h(\hat{s}) = \sum_{i=1}^{n_{\text{en}}} N_i(\hat{s}) \delta q_i^e. \tag{4.32b}$$

where n_{en} is the number of nodes in element I_e^h, $N_i(\hat{s})$ the elemental shape function associated with node i, and p_i^e, δp_i^e, q_i^e, δq_i^e are the nodal values of corresponding solution functions of element I_e^h at node i.

We calculate the elemental contribution to the residual vector by substituting the discretization (4.32a) and (4.32b) into weak form (4.31). For each element I_e^h, we define residual vectors $\mathbf{F}^e(\mathbf{p}^e) = (F_i^{ep}, F_i^{er})_{i=(1,2,\ldots,n_{\text{en}})}^T$, where $\mathbf{p}^e = (p_i^e, q_i^e)_{i=(1,2,\ldots,n_{\text{en}})}^T$. We calculate F_i^{ep}, F_i^{er} as

$$F_i^{ep}(\mathbf{p}^e) = \int_{I_e^h} \left[\left(\sum_{j=1}^{n_{\text{en}}} N_j' p_j^e \right) N_i' + \hat{P}_u \sin\left(\sum_{j=1}^{n_{\text{en}}} N_j (p_j^e - q_j^e) \right) N_i - \hat{P}_w \cos\left(\sum_{j=1}^{n_{\text{en}}} N_j (p_j^e - q_j^e) \right) N_i \right] d\hat{s}, \tag{4.33a}$$

$$F_i^{er}(\mathbf{p}^e) = \int_{I_e^h} \left[k \left(\sum_{j=1}^{n_{\text{en}}} N_j q_j^e \right) - \hat{P}_u \sin\left(\sum_{j=1}^{n_{\text{en}}} N_j (p_j^e - q_j^e) \right) + \hat{P}_w \cos\left(\sum_{j=1}^{n_{\text{en}}} N_j (p_j^e - q_j^e) \right) \right] N_i \, d\hat{s}. \tag{4.33b}$$

We assemble all $\mathbf{F}^e$ together and obtain a global residual vector $\mathbf{F} = \mathcal{A}_{e=1}^{n_{\text{el}}} \mathbf{F}^e$, where $\mathcal{A}$ is the finite element assembly operator [109]. However, owing to the existence of a constraint equation (4.27), special treatment on $\mathbf{F}$ is required. Before discussing the modification on $\mathbf{F}$, we first define the global solution vector as $\mathbf{p} = (p_1, q_1, p_2, q_2, \ldots, p_{n_{\text{np}}}, q_{n_{\text{np}}})^T$ where p_I, q_I are global DOFs, n_{np} is the total number of nodes in finite element mesh. We arrange the ordering of nodes and elements in such a way that position $\hat{s} = 0$ corresponds to local node number $i = 1$ of element I_1^h and global node number $I = 1$ as well. It follows that the finite-dimensional solutions $p^h(\hat{s}), q^h(\hat{s})$ have boundary values $p^h(0) = p_1$ and $q^h(0) = q_1$. The constraint (4.27) becomes $q_1 = \tan(q_1 - p_1)$.

Now we proceed to discuss the modification on $\mathbf{F}$ after assembly $\mathbf{F} = \mathcal{A}_{e=1}^{n_{\text{el}}} \mathbf{F}^e$. To account for the constraint $q_1 = \tan(q_1 - p_1)$, we solve for p_1 as $p_1 = q_1 - \arctan(q_1)$. We substitute this

relation to the residual vector $\mathbf{F}$ to eliminate its dependence on p_1. Furthermore, we superpose $(\partial\hat{\Pi}^{\mathrm{FT}}/\partial p_1)(dp_1/dq_1)$ on the second element of $\mathbf{F}$ and remove the first element. In the meantime, we remove the DOF p_1 from the global solution vector $\mathbf{p}$. Therefore, the length of the modified residual vector $\mathbf{F}$ becomes $2n_{\mathrm{np}} - 1$, which is same as the modified total number of DOFs. In next subsection, we introduce the linearization and solving method for the nonlinear system $\mathbf{F}(\mathbf{p}) = \mathbf{0}$.

4.4.3 Linearization and modified Newton-Raphson method

We apply Newton-Raphson method [110] to solve the nonlinear system $\mathbf{F}(\mathbf{p}) = \mathbf{0}$. In the k^{th} iteration, the $(k+1)^{\mathrm{th}}$ solution vector is computed as

$$\mathbf{p}_{k+1} = \mathbf{p}_k - \alpha_k \mathbf{H}_k(\mathbf{p}_k)^{-1}\mathbf{F}_k(\mathbf{p}_k), \tag{4.34}$$

where $\mathbf{H}_k(\mathbf{p}_k) = \nabla_{\mathbf{p}_k}\mathbf{F}_k$ is a $(2n_{\mathrm{np}} - 1) \times (2n_{\mathrm{np}} - 1)$ Jacobian matrix, and α_k is the step length in the k^{th} iteration. We define the incremental search direction $\Delta\mathbf{p}_k$ as in $\mathbf{p}_{k+1} - \mathbf{p}_k = \alpha_k\Delta\mathbf{p}_k$ and rewrite the iteration equation (4.34) in form of a linear system

$$\mathbf{H}_k(\mathbf{p}_k)\Delta\mathbf{p}_k = -\mathbf{F}_k(\mathbf{p}_k). \tag{4.35}$$

In finite element implementation, similar to the assembly of $\mathbf{F}_k$, $\mathbf{H}_k$ is assembled following $\mathbf{H}_k = \mathcal{A}_{e=1}^{n_{\mathrm{el}}}\mathbf{H}_k^e$, where $\mathbf{H}_k^e(\mathbf{p}_k^e) = \nabla_{\mathbf{p}_k^e}\mathbf{F}_k^e$ is an $n_{\mathrm{en}} \times n_{\mathrm{en}}$ matrix in which the (i, j) element is calculated as $\partial[\mathbf{F}_k^e]_i/\partial[\mathbf{p}_k^e]_j$.

During the iteration, when $\mathbf{p}_k$ is far away from the solution, the Hessian matrix $\mathbf{H}_k(\mathbf{p}_k)$ may not be positive definite, so the search direction $\Delta\mathbf{p}_k$ may not be a descent direction. We use modified Cholesky factorization [111] to make sure that $\mathbf{p}_k$ solved from (4.35) is always a descent direction by replacing $\mathbf{H}_k(\mathbf{p}_k)$ with a positive definite approximation. In addition, we apply backtracking approach [112] to search for an appropriate step length α_k. The backtracking approach will select a short enough α_k to ensure that $\hat{\Pi}^{\mathrm{FT}}(\mathbf{p}_k + \alpha_k\Delta\mathbf{p}_k)$ achieves adequate reductions at modest cost. On the other hand, the step length α_k is not too short to make reasonable progress along the given search direction.

We use quadratic 1D elements to divide the domain. Three Gauss quadrature points are adopted for numerical integration. To initiate the Newton-Raphson procedure, an initial guess of the solution vector $\mathbf{p}_0$ is required. We calculate the error of convergence as $\|\Delta\mathbf{p}_k\|$ in each step. The iterative loop stops whenever the error of convergence drops below a threshold value $\varepsilon = 10^{-6}$.

4.5 Numerical Examples

In this section, we present a series of numerical examples using the FEM formulations derived in the above section. We obtain quadratic rate of convergence for these examples.

4.5.1 Compressive buckling problem

In the first subsection, we focus our attention on the compressive buckling problem, in which a cantilever is encastered at one end $\hat{s} = 0$ and loaded at the other end $\hat{s} = 1$ by a concentrated force $\hat{\mathbf{P}} = P_0\hat{\mathbf{E}}_1$ where $P_0 < 0$. As the magnitude of P_0 exceeds a certain critical value, the cantilever will buckle suddenly and deform continuously hereafter. We solve this problem using both the proposed theory and Reissner's theory.

Based on the proposed geometrically nonlinear shear deformable beam model, we solved for the deformed shapes of beams for $k = 1000, 200, 150, 110, 100$ under compressive force $\hat{\mathbf{P}} = -100\hat{\mathbf{E}}_1$. The centroidal lines of deformed beams are shown in Figure 4.2 (A)–(B). Although the deformed shapes are various for different k, the dimensionless displacements in $\hat{\mathbf{E}}_2$ direction at the right end $\hat{w}(\hat{s} = 1)$ are pretty consistent across all solutions.

We also employed Reissner's theory in conjunction with Saint Venant-Kirchhoff constitutive model to solve for the compressive buckling problem where $\hat{P}_0 = -100$. The nonlinear FEM calculation failed to converge for $k = 200, 150, 110, 100$ except for the case $k = 1000$. We plot the converged solution for $k = 1000$ and some representative unconverged solutions for $k = 200, 150, 110, 100$ in Figure 4.2 (C)–(D). The unconverged solutions depend on the choice of initial guess and number of Newton-Raphson iterations. For the unconverged deformed beam shapes shown in Figure 4.2 (C)–(D), we took the solutions in Figure 4.2 (A) as initial guess and ran 5 iterations. More iterations

cause both the error of convergence and the dimensionless Hellinger-Reissner energy $\hat{\Pi}^{\mathrm{R}}$ going to infinity.

As per our analysis in section 4.3.1, there is no global minimizer to functional (4.22). Thus we suspect that the converged solution for $k = 1000$ is not a global minimizer. By substituting the converged solution into (4.22), we obtain the dimensionless Hellinger-Reissner energy $\hat{\Pi}^{\mathrm{R}}$ as -160.811. While by substituting one set of admissible solutions taken from the minimizing sequences (4.23a) and (4.23b) (for example, taking $n = 200$) into (4.22), we obtain $\hat{\Pi}^{\mathrm{R}}$ to be -195.827, which is smaller than the energy from the numerical solution. Clearly, the numerical solution for $k = 1000$ shown in Figure 4.2 (C) is not a global minimizer to functional $\hat{\Pi}^{\mathrm{R}}$. Furthermore, we tried to use the aforementioned minimizing sequences solution as an initial guess to start the Newton-Raphson procedure. In this case, the error of convergence blew up after a few iterations. The failure of nonlinear FEM on the compressive buckling problem based on Reissner's theory in conjunction with Saint Venant-Kirchhoff constitutive model, is consistent with our analysis in section 4.3.1 that Reissner's theory is ill-posed in this loading scenario.

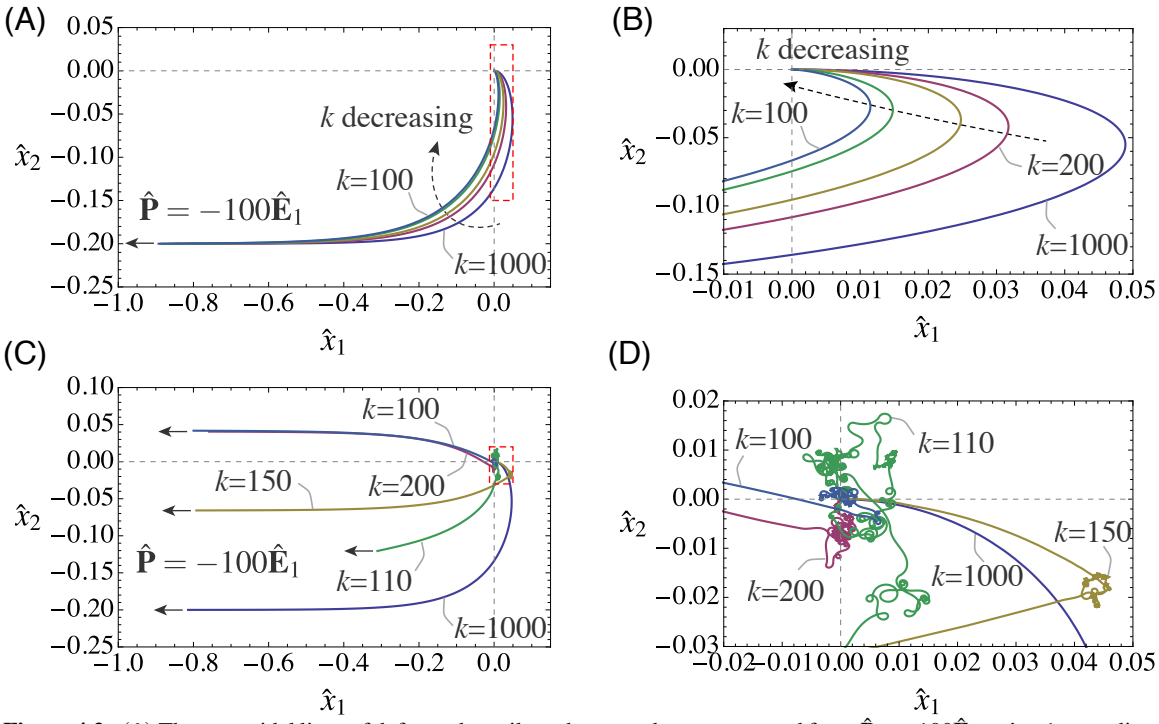

Figure 4.2: (A) The centroidal lines of deformed cantilever beam under concentrated force $\hat{\mathbf{P}} = -100\hat{\mathbf{E}}_1$ at $\hat{s} = 1$ according to the proposed beam theory. From bottom to top, k is decreasing as $1000, 200, 150, 110, 100$. (B) The zoomed figure of the region is surrounded by a red box in (A). Note that the aspect ratio has been adjusted. (C) The centroidal lines of a deformed cantilever beam under concentrated force $\hat{\mathbf{P}} = -100\hat{\mathbf{E}}_1$ at $\hat{s} = 1$ according to Reissner's beam theory. The corresponding k value for each curve is marked in the figure. (D) The zoomed figure of the region is surrounded by a red box in (C). Note that the aspect ratio has been adjusted.

4.5.2 Multiple loops example

In this subsection, we show a more complicated numerical example to illustrate the capacity of the proposed beam model. In the example shown in Figure 4.3, an initially straight beam, whose dimensionless arc length coordinate is $\hat{s} \in [0, 1]$, is under multiple concentrative forces and moments. We solved for the deformed shape through nonlinear FEM (see section. 4.4) based on the proposed shear deformable large deformation beam theory. We also plotted the variation of dimensionless shear force $\hat{V} = VL^2/(EI)$, axial force $\hat{P} = PL^2/(EI)$, moment $\hat{M} = ML/(EI)$, shear angle γ, cross-section rotation angle θ, and tangent angle of the centroidal line ψ along the beam.

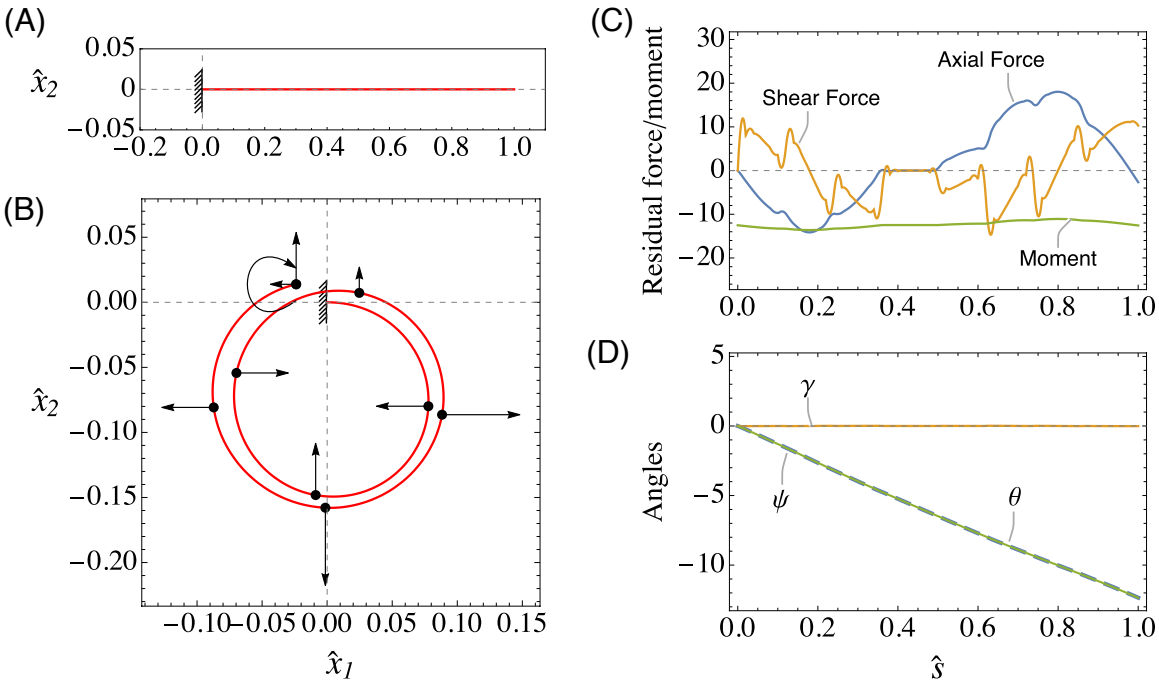

Figure 4.3: (A) Reference configuration of a straight cantilever beam fixed on the left end. (B) The deformed shape of the cantilever beam. The straight and curved arrows denote the concentrative forces and moment applied on the beam, respectively. Note that the direction of the concentrative forces does not change during the deformation process. (C) The variation of dimensionless shear force $\hat{V} = VL^2/(EI)$, axial force $\hat{P} = PL^2/(EI)$, and moment $\hat{M} = ML/(EI)$ along the beam. (D) The variation of shear angle γ, cross-section rotation angle θ, and tangent angle of the centroidal line ψ along the beam.

4.6 Discussion and conclusion

As discussed in Section 1, we are interested in exploring the effect of shear stiffness on the anchoring capacity of *Ea.* spicules. The layered structure of *Ea.* spicules does provide more degrees of freedom to their deformation, for example, interlayer slippage and delamination. For simplification, we model the multilayered composite beam as monolithic beam with various shear stiffness. Similar to the effective bending stiffness discussed in Chapter 3, the effective shear stiffness of the multilayered beam can be greater or smaller than the homogenized monolithic one depending on the interfacial properties. However, we do not put our focus on the computation of the effective shear stiffness. Instead, we assume that the multilayered beam has different effective shear stiffness and directly study the effect of various shear stiffness on the deformation of the beam.

Because we are interested in the anchoring ability of *Ea.* spicules, we deliberately bend the beam into a loop in our numerical example (see Section 4.5.1). This loading condition simulates the

actual behavior of spicules when they are wound around rocks or sands to prevent the sponge from being pulled away by underwater current. In Section 4.5.1, we vary the shear stiffness by choosing different values of k for the beam. As shown in Figure 4.2 (A) and (B), the shear stiffness does make a difference to the deformed shape of the beams. However, the maximum deflections in $\hat{\mathbf{e}}_2$ direction remain the same for all five numerical cases. That is, the resulting bending moment at the symmetric point of the beam does not depend on the effective shear stiffness of the beam. The maximum normal stress along the beam is mainly determined by the bending moment at the symmetric point of the beam. And the spicules' anchoring ability depends on how much end force they can transmit without failure through normal stress. Therefore, we can draw the conclusion that the shear effect from the multilayered architectures of *Ea.* spicules does not contribute to the spicules' anchoring ability. The internal architectures of the spicules help secure the sponge on the sea floor through mechanisms other than varying the spicules' shear stiffness.

Although we arrived at negative results in our exploration on the effect of shear for *Ea.* spicules, the development of the geometrically nonlinear shear deformable beam theory itself is of significant importance. We list the importance of the presented beam theory as follows

1. The presented beam theory is a finite deformation generalization of Timoshenko beam theory. It is the simplest geometrically nonlinear theory that is capable to deal with shear deformation of a beam. Unlike Simo's geometrically-exact rod model [9], which is more complicated to understand and utilize, the presented theory is lightweight and easy to use.

2. The development of the beam theory follows classical kinematic hypothesis for beams and general three-dimensional continuum theory. We develop this beam theory in a rigorous and systematic way. The procedure can be reused in the development of other reduced-order theories, such as plate theory and shell theory, with customized complexities.

3. The development of the beam theory provides a valuable example of the application of Hellinger-Reissner variational principle. As opposed to the commonly used minimum total potential energy principle, the Hellinger-Reissner variational principle looses the constitutive constraint and expands the solution space.

4. In this work, we provide a rigorous proof that the well-known Reissner's theory [8] can be

problematic if being used without extreme caution. On the other hand, we also provide a proof of the existence of solutions for the proposed beam model so that the audience know under what conditions the proposed theory is working. This is particularly useful in numerical computation to avoid non-physical numerical solutions.

The development of the geometrically nonlinear shear deformable beam theory is just a first step of our exploration. On top of this beam theory, we have provided a solution existence proof and a numerical scheme for computing numerical solutions. In future, we will seek for more potentials of the proposed theory and the development framework as well. For examples, we will try to loose some of the kinematic restrictions or expands the constitutive law to elasto-plastic constitutive relations. Potential applications of the expanded beam theory could be the design of guide wires for endoscopy, the mechanical analysis of power cords and data transmission cables, to name a few.

Chapter 5

Asymptotic analysis of sponge spicules' tolerance to geometric variations regarding buckling instability

5.1 Introduction

We have been concentrating on *Euplectella aspergillum* spicules in the previous chapters. In this chapter, we switch our focus to a related but different marine sponge, *Tethya aurantia* (*Ta.*), and its skeletal element. The sponge *Ta.* is a sessile animal that grows on rocky surfaces in the Mediterranean [113] (see Figure 1.6 (A)). The skeletal elements that we investigate are needle-shaped structures called strongyloxea spicules (see Figure 1.6 (E)).

In this chapter, we refer to strongyloxea spicules from *Ta.* as "*Ta.* spicules", or simply "spicules" when there is no ambiguity. The *Ta.* spicules are axially symmetric, silica rods. They are roughly 35 μm thick, 2 mm long, Unlike *Ea.* spicules, the *Ta.* spicules monolithic rods without any internal architectures. Besides, the *Ta.* spicules are tapered along their length. We found that the tapered shape is remarkably uniform across different *Ta.* spicules.

In previous study, Monn and Kesari have identified a new connection between the mechanical design and buckling resistance in *Ta.* spicules [114]. Although most research about stiff, mineralized

biomaterials, such as nacre and bone, focus on the material's toughness properties [115, 116], the structure-property connection Monn and Kesari have identified in *Ta.* spicules falls in the entirely new category of buckling resistance. The work of this chapter is based on Monn and Kesari's results in [114]. Thus I will recap the results given by Monn and Kesari as a background of this work in Section 5.1.1 .

5.1.1 Structure-property connection of *Ta.* spicules by Monn and Kesari

In the paper by Monn and Kesari, they introduced and investigated the hypothesis that the *Ta.* spicules' taper is an adaptation aimed at enhancing their ability to provide stiffness to the sponge. This hypothesis is motivated by the observations of the sponge's skeletal anatomy (see Figure 1.6 (B) and (C)) and the theory of Euler buckling. For the sponge, mechanical stiffness is important for it to feed itself underwater. Based on the sponge's skeletal anatomy, *Ta.* spicules provides stiffness to sponges by sustaining compressive axial force. However, due to the slenderness of *Ta.* spicules, they will undergo abrupt buckling failure if the axial compressive force exceeds a critical amount, which is so called buckling strength or buckling resistance. According to the theory of Euler buckling, the buckling resistance of a slender structure can be increased by tapering it [43]. Therefore, Monn and Kesari proposed that the tapered shape of *Ta.* spicules will enhance their buckling resistance to better support the sponge.

They tested the hypothesis as follow. They performed flexural tests on *Ta.* spicules to characterize the deformation behavior and the stiffness of the spicules. The mechanical testing indicates that the spicules' mechanical behavior is linear elastic until failure. Then they performed finite element analysis (FEA) based computational mechanics calculations to identify the approximate loading scenario of the spicules. In their computational mechanics calculations, they used the information about the spicules' arrangement within the sponge and the stiffness of both the spongin and spicules. The results of the calculation indicates that the typical loading condition of the spicules is equivalent to a pin-ended column under compressive, axial forces. Combining the above two piece of information, they conclude that the spicules stiffening ability is limited by the Euler buckling instability. It has been proved that for a given length and volume, there exist an axisymmetric column with the greatest buckling strength. The correct solution of the optimal column profile was discovered in 1851 [117]

and an accessible proof that it is in fact optimal was given in 1962 [118]. This optimal profile, which they refer to as the Clausen profile, is also tapered on both end. The Clausen profile provide buckling strength enhancement of up to 33% over that of a cylinder.

Monn and Kesari compared spicules' profiles to the best fitted Clausen profile and several other prototypical best fitted profiles, such as a semiellipse, an isosceles triangle and a constant. They found that the Clausen profile describes the spicules' tapers the best out of the different profiles that they considered. They also used the structural mechanics model along with measurements of the spicules shape to directly estimate the load they can transmit before buckling. Compared to a cylinder with the same length and volume, they predicted that the spicules shape enhances this critical load by up to 30%, which is close to the enhancement of 33% provided by the Clausen column. Therefore, they conclude that the function of tapered shape of *Ta.* spicules is to enhance their buckling resistance to better support the sponge.

5.1.2 Tolerance of the Clausen profile

In the comparison between spicules' profiles and several prototypical profiles including Clausen profile, although Monn and Kesari found that Clausen profile describes the spicules' tapers the best out of the different profiles that they considered, around 0.0156% mean sum of squared residuals is measured between 31 *Ta.* spicules' profile and the Clausen profile.

The mathematically precise Clausen profile, of course, does not exist in nature. The precision with which *Ta.* can control the shape of the spicules is limited. This is evident through defects we observed, which include surface damage and step-like protrusions in a spicule's shape (see Figure 5.1). While the Clausen profile maximizes the buckling strength in our model for the spicules, it is possible that small deviations from this shape could result in disproportionately large decreases in buckling strength. That is, we have to make sure that the Clausen profile is not sensitive to geometry imperfections. In an equivalent way, the Clausen column should be tolerant to shape variations in order for the discussion in [18] to be solid.

We define a column's tolerance to shape variations as the extent to which perturbations in its profile decrease its buckling strength. A closely related concept to tolerance is sensitivity. We have

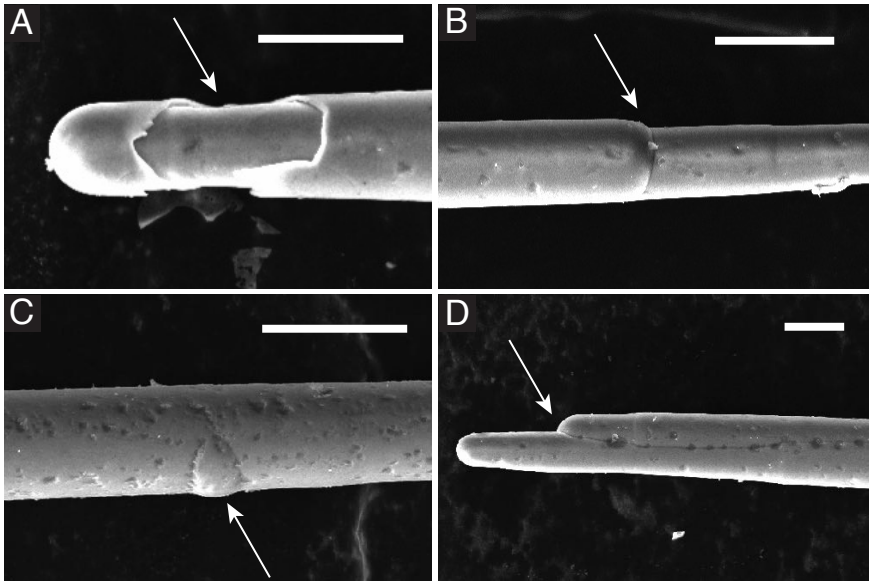

Figure 5.1: Representative SEM images of a few *Ta.* spicules with geometric imperfections, such as (A) damage, (B) steps, and (C),(D) protrusions. The scale bars in all subfigures are 25 μm.

a logical quantitative measure of the column's sensitivity to shape variations given in Section 5.3, where a smaller value indicates a smaller sensitivity, namely a greater tolerance. We derived the formulation of sensitivity for a given column through mathematical derivation that involves asymptotic analysis and calculus of variation. In order to validate the derivation, I performed numerical experiments using Rayleigh-Ritz method. The main result of our research is that the column with Clausen profile is not only the strongest column against buckling, but also the most tolerant column to shape variations. Both features of the Clausen profile make the structure-property connection between the spicules' shape and its ability to guard buckling instability more substantial.

The chapter is organized as follows: In §5.2 we introduce the mathematical setup of the buckling problem and perform perturbation to the problem. In §5.3 we derive the expression of buckling strength sensitivity through calculus of variation and apply to expression to both constant column and Clausen column. §5.4 presents the comparison of the theoretical result and numerical experimental result. §5.5 provides proof that Clausen column is the least sensitive column to shape variations The final section includes some discussions of the main conclusions.

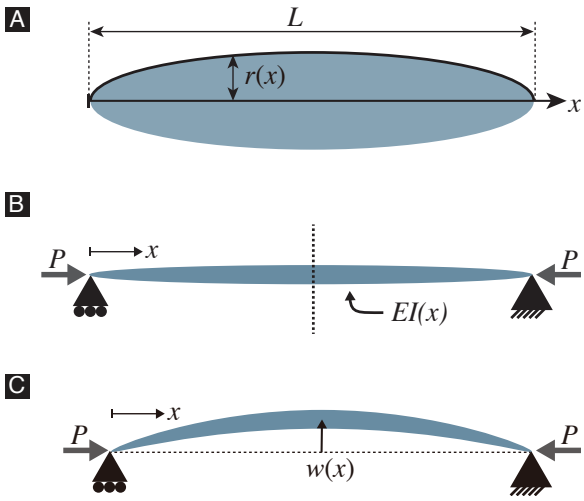

Figure 5.2: Schematics of a pin-ended non-uniform cross-sectional column under compressive axial loading. (A) A schematic of the profile of a tapered, circular cross-section column. We use the radius of the column's cross section, $r(x)$, to denote the shape of the column, where $x \in [0, L]$ is the distance along the column's length from its left end and L is the column's length. (B) The pin-ended column under compressive axial force P in reference configuration. Here E and $I(x)$ are the column's Young's modulus and second moment of area, respectively. (C) The column is in buckled configuration. Here $w(x)$ denote the column's transverse deflection.

5.2 Problem setup

We model the *Ta.* spicules as pin-ended slender columns under compressive axial loading. The failure mechanism of the spicules is governed by Euler buckling. However, unlike the usual Euler buckling problem in which the column has uniform cross-section, we focus on the cases where the column has variable radius along its neutral axis. It should be noted that Euler's buckling theory only applies for columns whose cross sections are either regular polygons or circular [43]. In our problem, we consider circular cross-section column and denote the radius of the cross sections as $r(x)$ where $x \in [0, L]$ is used to denote the coordinate along the column's neutral axis and L is the total length of the column. We refer $r(\cdot)$ as the column's profile. As we mentioned, the Clausen profile results in a column that is 33% stronger than a column with the same length and volume but for which the cross-sectional radius is constant.

In the rest of the chapter, we refer to columns with Clausen profile as Clausen columns. Similarly, we refer to columns with constant cross-sectional radius as constant columns.

5.2.1 Boundary value problem of non-uniform cross-sectional beam buckling

As we mentioned in section 5.1, we model the *Ta.* spicules as end-loaded columns under compressive axial loading. For a column whose profile is given by $r(\cdot)$, the second moment of inertia of the column is given by $I(x) = \pi r(x)^4/4$. As per Euler's buckling theory, the transverse deflection, $w(x)$, of the column's neutral axis satisfies the equations

$$E\,[I(x)w''(x)]'' + Pw''(x) = 0, \tag{5.1a}$$

$$I(x)w''(x)|_{x=0,\ L} = 0, \tag{5.1b}$$

$$w(x)|_{x=0,\ L} = 0, \tag{5.1c}$$

where E is the column's Young's modulus.

The buckling strength of a simply supported, end loaded column is the smallest force P for which there exists a solution to (5.1) other than $w(x) = 0$ for all $x \in [0, L]$.

By integrating (5.1a) twice from $x = 0$ to $x = L$ and using boundary conditions (5.1b) and (5.1c), we simplify the governing equations as

$$EI(x)w''(x) + Pw(x) = 0, \tag{5.2a}$$

$$w(0) = 0, \tag{5.2b}$$

$$w(L) = 0. \tag{5.2c}$$

In terms of the non-dimensional variables $\xi = x/L$, $\eta = w/L$, $\beta = P/(EL^2)$, $\hat{I} = I/L^4$, and $\rho = r/L$, we have

$$\hat{I}(\xi)\eta''(\xi) + \beta\eta(\xi) = 0, \tag{5.3a}$$

$$\eta(0) = 0, \tag{5.3b}$$

$$\eta(1) = 0, \tag{5.3c}$$

where

$$\hat{I}(\xi) = \frac{\pi}{4}\rho(\xi)^4. \tag{5.4}$$

5.2.2 Asymptotic expansion

When there are geometric variations on the spicules, the column's dimensionless profile will be changed to $\rho(\xi)$ from its original profile $\rho_0(\xi)$. We assume that the imperfect column is also axisymmetric, thus Euler's buckling theory still applies. The imperfection may not need to isovolumetric, i.e., it could change the volume of the original column. We seek to understand the relation between the perturbation in $\rho(\xi)$ and the resulting perturbation in β using the perturbation theory.

Let's assume that $\rho(\xi)$, $\hat{I}(\xi)$, $\eta(\xi)$ and β have the following asymptotic expansions,

$$\rho(\xi;\epsilon) = \rho_0(\xi) + \epsilon\rho_1(\xi) + O(\epsilon^2), \tag{5.5a}$$

$$\hat{I}(\xi;\epsilon) = \hat{I}_0(\xi) + \epsilon\hat{I}_1(\xi) + O(\epsilon^2), \tag{5.5b}$$

$$\eta(\xi;\epsilon) = \eta_0(\xi) + \epsilon\eta_1(\xi) + O(\epsilon^2), \tag{5.5c}$$

$$\beta(\epsilon) = \beta_0 + \epsilon\beta_1 + O(\epsilon^2). \tag{5.5d}$$

According to the relation (5.4), I have

$$\hat{I}_0(\xi) = \pi\rho_0(\xi)^4/4, \tag{5.6a}$$

$$\hat{I}_1(\xi) = \pi\rho_0(\xi)^3\rho_1(\xi). \tag{5.6b}$$

5.2.3 Solution to the initial problem

I substitute (5.5b)-(5.5d) into the dimensionless governing equation (5.3a) and collect terms involving ϵ. The resulting governing equations of order $O(1)$ is

$$\hat{I}_0(\xi)\eta_0(\xi)'' + \beta_0\eta_0(\xi) = 0, \tag{5.7a}$$

$$\eta_0(0) = 0, \tag{5.7b}$$

$$\eta_0(1) = 0. \tag{5.7c}$$

Since $\hat{I}_0(\xi)$ is nonzero in the interval $(0, 1)$, I multiply (5.7a) by $1/\hat{I}_0(\xi)$ and arrive at

$$\eta_0''(\xi) + \frac{\beta_0}{\hat{I}_0(\xi)}\eta_0(\xi) = 0, \tag{5.8}$$

I multiply equation (5.8) by $\eta_0(\xi)$ and integrate it from $\xi = 0$ to $\xi = 1$. Using the normalization condition

$$\int_0^1 \eta_0(\xi)^2 \hat{I}_0(\xi)^{-1} d\xi = 1, \tag{5.9}$$

the buckling strength of unperturbed column can be expressed as

$$\beta_0 = -\int_0^1 \eta_0(\xi)\eta_0''(\xi) d\xi. \tag{5.10}$$

5.2.4 Solution to the first-order problem

The resulting governing equations of order $O(\epsilon)$ is,

$$\hat{I}_0(\xi)\eta_1(\xi)'' + \beta_0\eta_1(\xi) = -\hat{I}_1(\xi)\eta_0(\xi)'' - \beta_1\eta_0(\xi), \tag{5.11a}$$

$$\eta_1(0) = 0, \tag{5.11b}$$

$$\eta_1(1) = 0. \tag{5.11c}$$

The above boundary value problem is not in standard Sturm-Liouville form. To convert the governing equation to be a Sturm-Liouville problem, I multiply (5.11a) by $1/\hat{I}_0(\xi)$ and arrive at

$$\eta_1''(\xi) + \frac{\beta_0}{\hat{I}_0(\xi)}\eta_1(\xi) = -\frac{\hat{I}_1(\xi)}{\hat{I}_0(\xi)}\eta_0''(\xi) - \frac{\beta_1}{\hat{I}_0(\xi)}\eta_0(\xi). \tag{5.12}$$

According to Sturm-Liouville theorem, the right hand side of (5.12) must be orthogonal to $\eta_0(\xi)$, which is the corresponding eigenfunction to the eigenvalue β_0. Thus I get the following condition

$$\int_0^1 \left(-\frac{\hat{I}_1(\xi)}{\hat{I}_0(\xi)}\eta_0''(\xi) - \frac{\beta_1}{\hat{I}_0(\xi)}\eta_0(\xi)\right)\eta_0(\xi) d\xi = 0. \tag{5.13}$$

Noting the normalization condition (5.9), the expression of β_1 is obtained as

$$\beta_1 = -\int_0^1 \hat{I}_1(\xi)\hat{I}_0(\xi)^{-1}\eta_0(\xi)\eta_0''(\xi)d\xi. \tag{5.14}$$

Recalling that (5.6a) and (5.6b), I can write β_1 as a functional of $\rho_1(\cdot)$ (parameterized by $\rho_0(\cdot)$):

$$\beta_1[\rho_1(\cdot);\rho_0(\cdot)] = -4\int_0^1 \rho_0(\xi)^{-1}\rho_1(\xi)\eta_0(\xi)\eta_0''(\xi)d\xi. \tag{5.15}$$

For a given column, eigenfunction $\eta_0(\xi)$ is fully determined by the column's profile $\rho_0(\xi)$. The expression for β_1 will be determined by $\rho_1(\xi)$, which is the first order perturbation of the column's profile. Using the notation $\rho_1(\xi)$ to describe the geometric imperfection of the spicule already implies our assumption that all variations are axisymmetric with respect to the spicules neutral axes. Although such assumption may sound restrictive in the field of biological material, it is quite reasonable in mechanical manufacturing and processing where rotating/revolving machinery are very common, especially when working on slender rod or column structures. For example, a Clausen column can be made by cutting the excess material off from a cylindrical column using a lathe machine. In practice, the lathed Clausen column specimen will deviate from the mathematical Clausen column because of the limited precision of the lathe machine. The deviation will be axisymmetric if it is not caused by eccentric turning of the lathe's center axis.

5.3 Buckling strength sensitivity to arbitrary axisymmetric perturbations

5.3.1 Admissible spaces

For a given column profile, in order to calculate the extreme value of the first order perturbation in buckling strength, β_1, the admissible spaces for $\rho_0(\cdot)$ and $\rho_1(\cdot)$ have to be clarified.

For the initial columns, I assume the volume of the columns to be a constant V_0. Therefore, the

space of admissible functions for $\rho_0(\cdot)$ is

$$\rho_0(\cdot) \in \mathcal{V}_0 := \left\{ \rho_0(\cdot) \in L^2([0,1]) \ : \ \rho_0(\xi) > 0, \forall \xi \in (0,1); \int_0^1 \pi \rho_0(\xi)^2 d\xi = \hat{V}_0, \right. \\ \left. \lim_{\xi \to 0} \frac{\xi^{3/8}}{\rho_0(\xi)} = \lim_{\xi \to 1} \frac{(\xi-1)^{3/8}}{\rho_0(\xi)} = 0 \right\}, \tag{5.16}$$

where $\hat{V}_0 = V_0/L^3$. In the definition of $\mathcal{V}_0$, the radius of the column's cross section has to be positive along the length of the column except for the both two ends. That is, the column can be tapered at both ends. However, $\rho_0(\xi)$ should converges to zero slower than $\xi^{3/8}$ as $\xi \to 0$ from above. Same constraint on the rate of $\rho_0(\xi)$ approaching zero exists for the right end $\xi \to 1$ from below. In other words, the two ends of the column cannot be too sharp in order to make the result (5.15) applicable. The derivation of the constraint involves the application of singular Sturm-Liouville theory. Please see Appendix B.1 for details. One immediate message we can get from the admissible space (5.16) is that our analysis applies to columns with constant and Clausen profiles, but not ellipse profiles.

The space of admissible functions for $\rho_1(\cdot)$ is related to $\rho_0(\cdot)$. The underlying principle is that the resulting column's profile $\rho(\xi;\epsilon) = \rho_0(\xi) + \epsilon\rho_1(\xi) + O(\epsilon^2)$ should satisfy the same constraints as $\rho_0(\cdot)$. In addition, the norm of $\rho_1(\cdot)$ is prescribed as

$$|\rho_1(\cdot)| := \left(\int_0^1 \rho_1^2(\xi) d\xi \right)^{1/2} = d. \tag{5.17}$$

Therefore, I have

$$\rho_1(\cdot) \in \mathcal{V}_d(\rho_0(\cdot)) := \left\{ \rho_1(\cdot) \in L^2([0,1]) \ : \ \rho(\xi;\epsilon) > 0, \forall \xi \in (0,1); |\rho_1(\cdot)| = d, \right. \\ \left. \lim_{\xi \to 0} \frac{\xi^{3/8}}{\rho(\xi;\epsilon)} = \lim_{\xi \to 1} \frac{(\xi-1)^{3/8}}{\rho(\xi;\epsilon)} = 0, \rho(\xi;\epsilon) = \rho_0(\xi) + \epsilon\rho_1(\xi) + O(\epsilon^2) \right\}. \tag{5.18}$$

5.3.2 Minimum value of the first order perturbation in buckling strength

In this section, I seek to calculate the extreme value of the first order reduction in buckling strength, β_1, for a given column profile for arbitrary $\rho_1(\cdot) \in \mathcal{V}_d(\rho_0(\cdot))$ given by (5.18). For columns with

profile $\rho_0(\cdot)$, I define the buckling strength sensitivity as

$$S[\rho_0(\cdot);\mathcal{V}_d] = -\lim_{d\to 0}\left(\min_{\rho_1(\cdot)\in\mathcal{V}_d(\rho_0(\cdot))}\frac{\beta_1[\rho_1(\cdot);\rho_0(\cdot)]}{\beta_0[\rho_0(\cdot)]d}\right). \tag{5.19}$$

The sensitivity definition makes sense only if the minimum value of β_1 exists and the limit operation converges. I will go ahead to derive the expression of the stationary point for which $\rho_1^*(\xi) = \arg\min_{\rho_1(\cdot)\in\mathcal{V}_d(\rho_0(\cdot))}\beta_1[\rho_1(\cdot);\rho_0(\cdot)]$. Then I will prove that the stationary point $\rho_1^*(\xi)$ I obtained is actually a global minimizer (see Appendix B.2 for details). Therefore the existence of minimum value of the first order perturbation in buckling strength, β_1^*, is guaranteed. Similarly, the existence of the limit as $d\to 0$ is evident when the expression β_1^*/β_0 is obtained.

By introducing the constraint (5.17) as a Lagrange multiplier, the Lagrangian function of $\beta_1[\rho_1(\cdot);\rho_0(\cdot)]$ is augmented as

$$\beta_1[\rho_1(\cdot);\rho_0(\cdot)] = \int_0^1 -4\rho_0(\xi)^{-1}\rho_1(\xi)\eta_0(\xi)\eta_0''(\xi)d\xi + \lambda\left[\int_0^1\rho_1(\xi)^2d\xi - d^2\right]. \tag{5.20}$$

Through variational method, for $\forall\ \delta\rho_1(\xi)\in\mathcal{TV}_d$,

$$\delta\beta_1[\rho_1(\cdot);\rho_0(\cdot)] = \int_0^1 -4\rho_0(\xi)^{-1}\eta_0(\xi)\eta_0''(\xi)\delta\rho_1(\xi)d\xi + 2\lambda\int_0^1\rho_1(\xi)\delta\rho_1(\xi)d\xi. \tag{5.21}$$

By enforcing $\delta\beta_1[\rho_1(\cdot);\rho_0(\cdot)] = 0$, I get the expression for a stationary point $\rho_1^*(\xi)$ as

$$\rho_1^*(\xi) = \frac{2\rho_0^{-1}(\xi)\eta_0(\xi)\eta_0''(\xi)}{\lambda}. \tag{5.22}$$

I proved that the stationary point $\rho_1^*(\xi)$ is actually a global minimizer. Please see Appendix B.2 for details of the proof.

I substitute $\rho_1^*(\xi)$ (5.22) into the constraint equation (5.17) and solve for λ,

$$\lambda = \frac{2}{d}\left[\int_0^1\rho_0^{-2}(\xi)\eta_0^2(\xi)\eta_0''^2(\xi)d\xi\right]^{1/2}. \tag{5.23}$$

The minimum value of $\beta_1[\rho_1(\cdot);\rho_0(\cdot)]$ is that

$$\beta_1^* = -4d\left[\int_0^1 \rho_0^{-2}(\xi)\eta_0^2(\xi)\eta_0''^2(\xi)d\xi\right]^{1/2}. \tag{5.24}$$

The relative change of the eigenvalue β_1^*/β_0 is a linear function of the norm of the perturbation d,

$$\frac{\beta_1^*}{\beta_0} = -\frac{4}{\beta_0}\left[\int_0^1 \rho_0^{-2}(\xi)\eta_0^2(\xi)\eta_0''^2(\xi)d\xi\right]^{1/2} d. \tag{5.25}$$

Here β_0, $\rho_0(\xi)$ and $\eta_0(\xi)$ are the dimensionless buckling strength, profile and normalized eigenfunction of the initial column, respectively.

According to the definition (5.19), the sensitivity is given by

$$S[\rho_0(\cdot);\mathcal{V}_d] = \frac{4}{\beta_0}\left[\int_0^1 \rho_0^{-2}(\xi)\eta_0^2(\xi)\eta_0''^2(\xi)d\xi\right]^{1/2}. \tag{5.26}$$

5.3.3 Application to constant profile column

With the expression of $S[\rho_0(\cdot);\mathcal{V}_d]$ given by (5.26), I can calculate the buckling strength sensitivity of arbitrary column whose profile, $\rho_0(\cdot)$, belongs to $\mathcal{V}_0$ (5.16). Let's first consider a constant profile column with dimensionless radius ρ_c and fixed volume $\hat{V}_0 = \pi\rho_c^2$. The second moment of inertia, according to (5.6a), is $\hat{I}_0(\xi) = \pi\rho_c^4/4$. For the initial unperturbed column, $\eta_0(\xi)$ is given as

$$\eta_0(\xi) = \alpha_c \sin(\pi\xi), \tag{5.27}$$

where α_c is an amplitude constant. Using the normalization condition (5.9), α_c can be determined as $\alpha_c = \rho_c^2\sqrt{\pi/2}$. Using expression (5.26), I can calculate the sensitivity as

$$S[\rho_0^{\text{Const}}(\cdot);\mathcal{V}_d] = \frac{2\sqrt{6}}{\rho_c}. \tag{5.28}$$

5.3.4 Application to Clausen column

For the Clausen column, the profile of the column is given in terms of a parameter θ varying from 0 to π:

$$\rho_0(\theta) = \rho_a \sin\theta, \tag{5.29a}$$

$$\xi(\theta) = \frac{1}{\pi}\left(\theta - \frac{1}{2}\sin 2\theta\right), \tag{5.29b}$$

where $\rho_a = \sqrt{4\hat{V}_0/(3\pi)}$. It can be deduced that the variable $\rho_a = \sqrt{4/3}\rho_c$ if the Clausen column has the same volume as the constant column.

The unperturbed eigenfunction is given by

$$\eta_0(\xi) = \alpha_a \sin^3\theta. \tag{5.30}$$

where α_a is an amplitude constant. Using the normalization condition (5.9), α_a can be determined as $\alpha_a^2 = -16\pi\rho_a^4/9$. Using expression (5.10), I calculate the unperturbed eigenvalue as

$$\beta_0 = \frac{\pi}{12}\hat{V}_0^2. \tag{5.31}$$

Finally, using expression (5.26), I calculate the sensitivity as

$$S[\rho_0^{\text{Clausen}}(\cdot); \mathcal{V}_d] = \frac{8}{\sqrt{3}\rho_a}. \tag{5.32}$$

5.4 Comparison with numerical experiments

To verify the theoretical results, I obtained in Section 5.3.3 and 5.3.4, I performed numerical experiments using Rayleigh-Ritz method and compared the numerical results with my theoretical prediction.

Taking the numerical experiments for the constant column as examples, I computed the buckling strengths of 10^6 different columns whose profiles are similar to the constant profile to quantify

the constant column's sensitivity to shape variations. I refer to these similar columns as perturbed columns. I model the perturbation of the column's profile, $\rho_1(\cdot)$ using random piecewise-constant functions. That is,

$$\rho_1(\xi) = a_i, \text{ for } \xi \in [\frac{i-1}{100}, \frac{i}{100}), \; i = 1, 2, \ldots, 100. \tag{5.33}$$

where a_i are random constants. I put constraints on a_i so that the resulting $\rho_1(\xi)$ is admissible. For example, the profile of the perturbed column cannot be negative anywhere along its length. Therefore, at the two ends of the Clausen column where $\rho_0(\cdot)$ is close to zero, a_i can only be positive. The profile of representative perturbed columns for constant/Clausen column are shown in Figure 5.3(A)/(B) along with the profiles of the original columns.

For each perturbed column, I calculate the norm of $\rho_1(\cdot)$ using equation (5.17). I then numerically computed the buckling strength, β_c, using the Rayleigh-Ritz method (see Appendix B.3). I define the relative change in buckling strength of the perturbed column as

$$\frac{\beta_c - \beta_0}{\beta_0} \approx \frac{\beta_1}{\beta_0}. \tag{5.34}$$

The numerical point $(d, \beta_1/\beta_0)$ is plotted in Figure 5.3(C) and (D). With 10^6 perturbed columns, all points are plotted as point cloud.

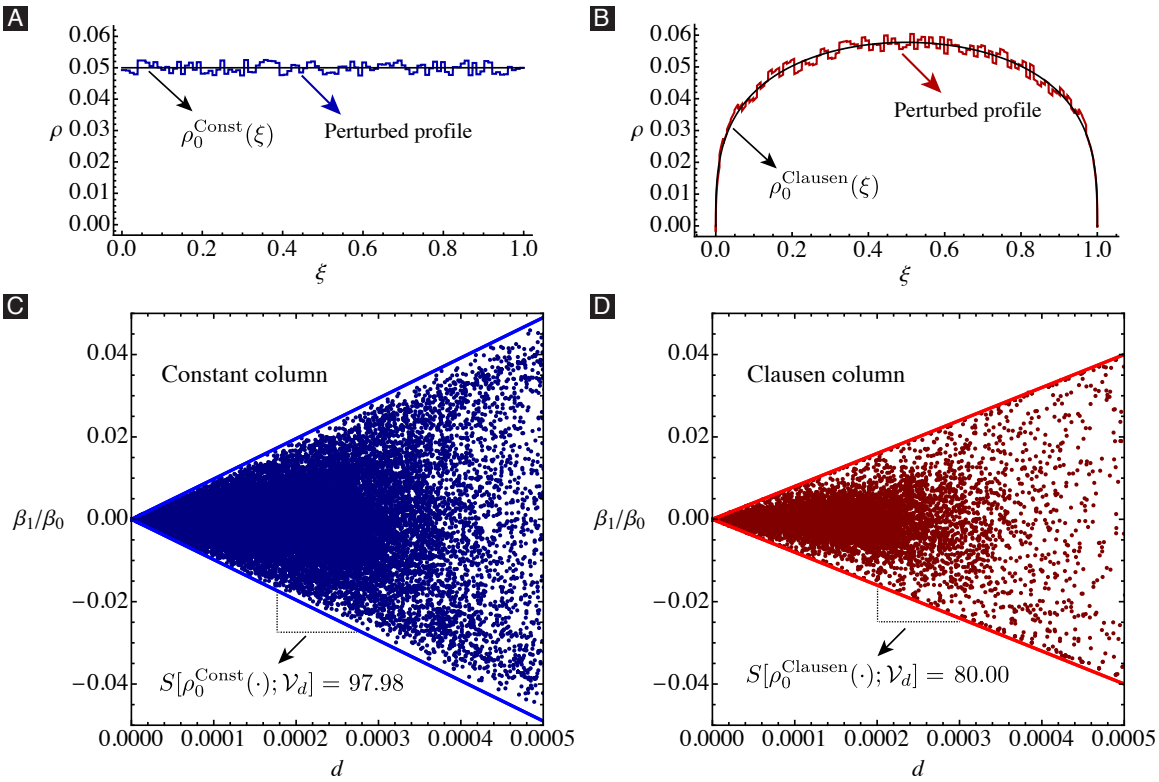

Figure 5.3: (A) Schematics of profiles of a constant column and a perturbed column. The radius of the column's cross-section is $\rho_c = 0.05$. (B) Schematics of profiles of a Clausen column and a perturbed column. The Clausen column shares the same volume as the constant column in (A). (C) Point clouds from numerical experiments for constant column along with theoretical predictions of upper and lower bounds. The sensitivity to small-scale geometric perturbation is $S[\rho_0^{\text{Const}}(\cdot);\mathcal{V}_d] = 97.98$. (D) Point clouds from numerical experiments for Clausen column along with theoretical predictions of upper and lower bounds. The sensitivity to small-scale geometric perturbation is $S[\rho_0^{\text{Clausen}}(\cdot);\mathcal{V}_d] = 80.00$.

I also plotted the upper and lower bounds from (5.28) and (5.32) in Figure 5.3(C) and (D) as straight lines. It can be shown that the theoretical prediction of the upper and lower bounds for β_1/β_0 match the numerical experimental results very well. Thus the sensitivity analysis is verified to be highly accurate.

The following table summarizes the main results for the two different types of columns.

Table 5.1: Comparison of two types of columns

Profile	Maximum radius	Buckling strength	Sensitivity
Constant	0.050	4.845×10^{-5}	97.98
Clausen	0.058	6.467×10^{-5}	80.00

From the above table, we can see that the Clausen column obtains the highest buckling strength. In addition, its buckling strength has smaller sensitivity to perturbation compared to the constant

column.

5.5 Optimal column profile that is least sensitive to shape variations

In Section 5.3, I derived the buckling strength sensitivity to shape variations for arbitrary column. A natural question to ask in the next step would be: what is the optimal column profile that is least sensitive to shape variations?

It has been shown that Clausen column is strongest against Euler buckling [114] and the resemblance of *Ta.* spicules to Clausen column implies a new structure-property connection created by nature. However, since it is inevitable that all biological structures have shape variations, the structure-property connection will be more substantial if Clausen column is least sensitive to shape variations. Therefore, in this section, I will prove that Clausen profile is the optimal column profile that is least sensitive to shape variations regarding Euler buckling.

The proof consists of three steps:

1. Derive the expression of sensitivity to isovolumetric perturbations for a given column profile;
2. Prove that the optimal column with most tolerance to arbitrary perturbations is same as the optimal column with most tolerance to isovolumetric perturbations;
3. Prove that the Clausen column is the optimal column with most tolerance to isovolumetric perturbations;

It follows from the above three steps that the Clausen column is indeed the optimal column with most tolerance to arbitrary perturbations. I will present the three steps in details in the following three subsections.

5.5.1 Sensitivity to isovolumetric axial-symmetric perturbations

In Section 5.3, I considered arbitrary perturbations that allow the volume change of the columns. When I try to derive the most insensitive column profile to shape variations, such assumption brings

difficulty. I will circumvent the difficulty by considering isovolumetric perturbations as a stepping stone.

The isovolumetric perturbations satisfy

$$\int_0^1 \pi\rho^2(\xi)d\xi = \int_0^1 \pi\left(\rho_0(\xi)+\epsilon\rho_1(\xi)\right)^2 d\xi = \hat{V}_0. \tag{5.35}$$

This is essentially

$$2\epsilon\int_0^1 \rho_0(\xi)\rho_1(\xi)d\xi + \epsilon^2\int_0^1 \rho_1^2(\xi)d\xi = 0. \tag{5.36}$$

I only keep the first order equation, which is

$$\int_0^1 \rho_0(\xi)\rho_1(\xi)d\xi = 0. \tag{5.37}$$

Therefore, the space of admissible space for $\rho_1(\cdot)$ is

$$\rho_1(\cdot) \in \mathcal{V}_d^{\mathrm{v}}(\rho_0(\cdot)) := \left\{\rho_1(\cdot) \in \mathcal{V}_d(\rho_0(\cdot)) \ : \ \int_0^1 \rho_0(\xi)\rho_1(\xi)d\xi = 0.\right\}. \tag{5.38}$$

By introducing an extra Lagrange multiplier λ_2 into the functional (5.20), we get

$$\beta_1[\rho_1(\cdot);\rho_0(\cdot)] = \int_0^1 -4\rho_0^{-1}(\xi)\rho_1(\xi)\eta_0(\xi)\eta_0''(\xi)d\xi + \lambda_1\left[\int_0^1 \rho_1^2(\xi)d\xi - d^2\right] + \lambda_2\left[\int_0^1 \rho_0(\xi)\rho_1(\xi)d\xi\right]. \tag{5.39}$$

Through variational method, for $\forall\ \delta\rho_1(\xi) \in \mathcal{TV}_d^{\mathrm{v}}$,

$$\begin{aligned}\delta\beta_1[\rho_1(\cdot);\rho_0(\cdot)] = &\int_0^1 -4\rho_0^{-1}(\xi)\eta_0(\xi)\eta_0''(\xi)\delta\rho_1(\xi)d\xi + 2\lambda_1\int_0^1 \rho_1(\xi)\delta\rho_1(\xi)d\xi \\ &+ \lambda_2\int_0^1 \rho_0(\xi)\delta\rho_1(\xi)d\xi.\end{aligned} \tag{5.40}$$

By enforcing $\delta\beta_1[\rho_1(\cdot);\rho_0(\cdot)] = 0$, I get the expression for the worst perturbation $\rho_1^*(\xi)$ as

$$\rho_1^*(\xi) = \frac{4\rho_0^{-1}(\xi)\eta_0(\xi)\eta_0''(\xi) - \rho_0(\xi)\lambda_2}{2\lambda_1}. \tag{5.41}$$

I substitute (5.41) into the constraint equations (5.17) and (5.37) and solve for λ_1 and λ_2 as,

$$\lambda_1 = \frac{2}{d}\left[\int_0^1 \rho_0^{-2}(\xi)\eta_0^2(\xi)\eta_0''^2(\xi)d\xi - \frac{\pi\beta_0^2}{\hat{V}_0}\right]^{1/2}, \tag{5.42}$$

$$\lambda_2 = -\frac{4\pi\beta_0}{\hat{V}_0}. \tag{5.43}$$

The minimum value of $\beta_1[\rho_1(\cdot);\rho_0(\cdot)]$ is obtained by inserting (5.42), (5.43) and (5.41) into (5.39)

$$\beta_1^* = -4d\left[\int_0^1 \rho_0^{-2}(\xi)\eta_0^2(\xi)\eta_0''^2(\xi)d\xi - \frac{\pi\beta_0^2}{\hat{V}_0}\right]^{1/2}. \tag{5.44}$$

The relative change of the eigenvalue β_1^*/β_0 is a linear function of the norm of the perturbation d,

$$\frac{\beta_1^*}{\beta_0} = -\frac{4}{\beta_0}\left[\int_0^1 \rho_0^{-2}(\xi)\eta_0^2(\xi)\eta_0''^2(\xi)d\xi - \frac{\pi\beta_0^2}{\hat{V}_0}\right]^{1/2} d. \tag{5.45}$$

The sensitivity $S[\rho_0(\cdot);\mathcal{V}_d^{\mathrm{v}}]$ caused by isovolumetric perturbations is

$$S[\rho_0(\cdot);\mathcal{V}_d^{\mathrm{v}}] = \frac{4}{\beta_0}\left[\int_0^1 \rho_0^{-2}(\xi)\eta_0^2(\xi)\eta_0''^2(\xi)d\xi - \frac{\pi\beta_0^2}{\hat{V}_0}\right]^{1/2}. \tag{5.46}$$

5.5.2 The equivalence of the optimal column with the most tolerance to isovolumetric perturbations to that of arbitrary perturbations

We introduce any subset of axisymmetric perturbations, scaling perturbations, in this section. For this type of perturbations, we impose $\rho_1(\cdot)$ to be $\rho_1(\cdot) = -\alpha\rho_0(\cdot)$, which is a scaling transformation of the original column's profile. We refer to the set of scaling perturbations as $\mathcal{V}_d^{\mathrm{s}}(\rho_0(\cdot))$

$$\rho_1(\cdot) \in \mathcal{V}_d^{\mathrm{s}}(\rho_0(\cdot)) := \left\{\rho_1(\cdot) \in L^2([0,1]) \ : \ \rho_1(\cdot) = -\alpha\rho_0(\cdot), \alpha \in \mathbb{R}, |\rho_1(\cdot)| = d\right\}. \tag{5.47}$$

The first order perturbation of the eigenvalue can be obtained from (5.15) as

$$\beta_1[-\alpha\rho_0(\cdot);\rho_0(\cdot)] = -4\alpha\beta_0. \tag{5.48}$$

Inserting $\rho_1(\cdot) = -\alpha\rho_0(\cdot)$ into (5.17), the norm of the perturbations is

$$d = \alpha\sqrt{\frac{\hat{V}_0}{\pi}}. \tag{5.49}$$

The sensitivity $S[\rho_0(\cdot); \mathcal{V}_d^{\mathrm{s}}]$ caused by scaling perturbations is

$$S[\rho_0(\cdot); \mathcal{V}_d^{\mathrm{s}}] = 4\sqrt{\frac{\pi}{\hat{V}_0}}. \tag{5.50}$$

Recall that we already derived the sensitivity to arbitrary perturbations, $S[\rho_0(\cdot); \mathcal{V}_d]$ (5.26), the sensitivity to isovolumetric perturbations, $S[\rho_0(\cdot); \mathcal{V}_d^{\mathrm{v}}]$ (5.46). The three sensitivities given by (5.26), (5.46) and (5.50) are related by the following equation

$$S[\rho_0(\cdot); \mathcal{V}_d]^2 = S[\rho_0(\cdot); \mathcal{V}_d^{\mathrm{v}}]^2 + S[\rho_0(\cdot); \mathcal{V}_d^{\mathrm{s}}]^2. \tag{5.51}$$

I take minimum operation on both sides of (5.51):

$$\min_{\rho_0(\cdot)\in\mathcal{V}_0} S[\rho_0(\cdot); \mathcal{V}_d]^2 = \min_{\rho_0(\cdot)\in\mathcal{V}_0} S[\rho_0(\cdot); \mathcal{V}_d^{\mathrm{v}}]^2 + \frac{16\pi}{\hat{V}_0}, \tag{5.52}$$

where the space of admissible functions $\mathcal{V}_0$ is given in (5.16).

The equation (5.52) shows that the minimizer for $S[\rho_0(\cdot); \mathcal{V}_d]^2$ is also the minimizer for $S[\rho_0(\cdot); \mathcal{V}_d^{\mathrm{v}}]^2$. Therefore, the optimal column with most tolerance to arbitrary perturbations is same as the optimal column with most tolerance to isovolumetric perturbations.

5.5.3 Proof of Clausen column as the optimal column in terms of tolerance to shape variations

For the Clausen column whose profile is given by (5.29), we already have the expressions for the unperturbed eigenfunction (5.30) and unperturbed eigenvalue (5.31) in Section 5.3.4. The Clausen column's sensitivity to isovolumetric perturbations can be calculated by inserting (5.29), (5.30) and

(5.31) into (5.46):

$$S[\rho_0^{\text{Clausen}}(\cdot);\mathcal{V}_d^{\text{v}}] = 0. \tag{5.53}$$

Since $S[\rho_0(\cdot);\mathcal{V}_d^{\text{v}}]^2 \geq 0$, $\forall\, \rho_0(\cdot) \in \mathcal{V}_0$, $\rho_0(\cdot) = \rho_0^{\text{Clausen}}(\cdot)$ is a minimizer of $S[\rho_0(\cdot);\mathcal{V}_d^{\text{v}}]^2$. That is

$$\min_{\rho_0(\cdot)\in\mathcal{V}_0} S[\rho_0(\cdot);\mathcal{V}_d^{\text{v}}]^2 = S[\rho_0^{\text{Clausen}}(\cdot);\mathcal{V}_d^{\text{v}}]^2 = 0, \tag{5.54a}$$

$$\arg\min_{\rho_0(\cdot)\in\mathcal{V}_0} S[\rho_0(\cdot);\mathcal{V}_d^{\text{v}}]^2 = \rho_0^{\text{Clausen}}(\cdot). \tag{5.54b}$$

However, the uniqueness is not guaranteed.

Recalling the relation between $S[\rho_0(\cdot);\mathcal{V}_d^{\text{v}}]^2$ and $S[\rho_0(\cdot);\mathcal{V}_d]^2$ given by (5.52), we have

$$\min_{\rho_0(\cdot)\in\mathcal{V}_0} S[\rho_0(\cdot);\mathcal{V}_d]^2 = \frac{16\pi}{\hat{V}_0}, \tag{5.55a}$$

$$\arg\min_{\rho_0(\cdot)\in\mathcal{V}_0} S[\rho_0(\cdot);\mathcal{V}_d]^2 = \arg\min_{\rho_0(\cdot)\in\mathcal{V}_0} S[\rho_0(\cdot);\mathcal{V}_d^{\text{v}}]^2 = \rho_0^{\text{Clausen}}(\cdot), \tag{5.55b}$$

which means that the Clausen column has least sensitivity to arbitrary perturbation comparing to any other columns whose profiles are given in $\mathcal{V}_0$.

5.6 Concluding remarks

1. As can be noted from Table 5.1 and Figure 5.3, for the worst case scenario, geometric imperfection of the same norm will cause different reduction in Clausen column and constant column's buckling strength. Clausen column is more tolerant to shape variations than constant column. In Section 5.5, we further proved that the Clausen profile is actually optimal in terms of tolerance to the shape variations. When the shape variations are isovolumetric, this result is a natural derivative of the fact that Clausen column is optimal in buckling strength with given length and volume. This reason is given as follows. According to calculus of variation, if we consider the buckling strength as a functional of the column's profile, the variation of the functional value vanishes when the column profile is optimal, i.e. Clausen profile. Any small variations of the column's profile won't make any change to the column's buckling strength.

This is equivalent to say that the Clausen column is tolerant to any small perturbations to shape variations. However, the admissible space of variations has been restricted to be isovolumetric. For arbitrary axisymmetric perturbations, we use the previously mentions result as a stepping stone and consider shape scaling perturbations as well to finally prove the result.

2. We deliberately avoid to use the term "imperfection sensitivity" in this study. The research object of "imperfection sensitivity" study is usually thin-walled shell structure. It is generally believed that buckling loads of pressure vessel components under various loading condition can be extremely sensitive to imperfection resulting in significant reduction of the load-carrying capacity [119]. However, in our case the spicules are solid and their sensitivity to imperfection is in general smaller than shell structures. Besides, the assumptions and approaches of this study are quite different from those in the studies of shell structures' imperfection sensitivity. We put forward these differences so that the audience should not compare this study with those imperfection sensitivity studies of shell structures.

3. As we have mentioned in Section 5.2.2, we assume that the norm of the geometric imperfections are asymptotically small and axisymmetric along the column's neutral axis. These two assumptions put some limitations to the range of applicability of the results. However, the results may hold even for larger perturbations as can be seen from 5.3 where the perturbations are not "asymptotically small". Besides, unlike thin-wall shell structures, solid columns are not very sensitive to geometric imperfections. With relatively large perturbations, the reduction in the buckling strength may still be small and linearly proportional to the norm of perturbations. The assumption of axisymmetric imperfection is quite reasonable even beyond the scope of spicules. For example, most of the columns or struts could be manufactured or processed by a rotating/revolving machinery that mainly produce axisymmetric defects. We hope our results can be useful in the buckling analysis of many artificial columns.

4. We proposed a admissible space for the column's profile in order for the buckling problem to be well-posed. For tapered column, this rate of the profile's radius approaching zero must lie in a specific range. The determination of the range involves singular Sturm-Liouville theory (see Appendix B.1 for details). It should be noted that our conditions are sufficient but not necessary. To the best of our knowledge, this is the first well-posedness discussion on tapered

column's buckling problem. One of the important insights that I got from the discussion is that, not all tapered columns have a well-defined buckling strength. For some tapered columns, e.g. ellipse-profile column and double-cone column, the buckling strength does not exist mathematically. This is also consistent with what I observed when I tried to calculate the buckling strength numerically for ellipse-profile column using Rayleigh-Ritz method. It is found that the numerical solution of buckling strength does not converge to a constant value as the number of basis function increases. However, without knowing the admissible space for the tapered column's profile, one may take a non-converged value from numerical computation as a tapered column's buckling strength by mistake, even when the buckling strength does not exist for this tapered column. Since the discussion of admissible space for the column's profile is not the main focus of this study, we did not put much effort in this topic. Further investigation on the well-posedness of buckling problem of tapered column is needed.

5. In our numerical experiments in Section 5.4, we model the perturbation of the column's profile using random piecewise-constant functions. Of course, the set of piecewise-constant functions is only a subset of the set of L^2 functions, which indicates that more points should be present in Figure 5.3(C) and (D). However, we do not expect the any new data point from general L^2 perturbations to lie outside the theoretical bounds. The fantastic match between the theoretical prediction and numerical point clouds implies that the set of piecewise-constant functions is a great representative of the set of L^2 functions. In the future, we will use a different subset of L^2 functions to model the perturbation of the column's profile to see if we will obtain a equally good match between the numerical experiments and our theoretical computations.

Chapter 6

Conclusions and outlook

Fundamental understanding of the mechanics of 1D continua is important and desirable due to its wide applications in many engineering and biological fields. In this dissertation, we investigated several critical problems related to the mechanics of 1D continua with particular application in the bio-inspired engineering. The main findings of this dissertation are summarized as follows:

1. In the three point bending experiments, if the stiffness of the specimen and the loading system is comparable, and the surface of the specimen is rough, then there is a chance to observe sawtooth patterns in the large deflection region of the force-deflection curve. A misinterpretation of the sawtooth pattern could lead to incorrect structure-property connections in the case of *Ea.* anchor spicules. Since three point bending test is prevalent in mechanical property characterization, it is worth pointing out this intrinsic pathology and providing a model to explain the underlying mechanism. The sawtooth pattern can be avoided by gluing the two ends of the specimen onto the test's supports as shown in Figure 2.2. In this case, the beam becomes fixed-fixed setup and the stretching deformation can be important in the deformed specimen.

2. We present an asymptotic analysis of bending stiffness of multilayered composite cylindrical structures with curvilinear orthotropy. The effective bending stiffness of multilayered hollow cylinders with alternatively arranged orthotropic materials and no slip interfacial conditions exceeds the bending stiffness of monolithic structure made of either material. What we can

learn from the result is that through alternatively oriented material arrangement, a multilayered composite beam can behave stiffer under bending without using intrinsic stiff material. In another example, the effective bending stiffness of multilayered hollow cylinders is reduced by cutting into multiple layers and assuming no friction interfacial conditions. The result provides an explanation about how lamellar architectures enhance the spicules' anchoring ability by reducing their effective bending stiffness.

3. Following classical kinematic hypothesis for plane beams and general three-dimensional continuum theory, we develop a geometrically nonlinear shear deformable beam theory in a rigorous and systematic way. The development of the beam theory utilizes Hellinger-Reissner variational principle, which looses the constitutive constraint and expands the solution space. It is also proved that under what conditions the solutions exist for the proposed beam model. We also provided a numerical scheme to solve for numerical solutions when analytical solutions are not available. Although the proposed model does not support our hypothesis for *Ea.* spicules' architecture, the development of the beam model itself is of significance. This work builds up a variationally consistent framework which can be used to systematically develop more complicated reduced-dimensional structural theories.

4. We investigated different axisymmetric beams' buckling strength and their tolerance to geometric variations. It is found that Clausen column is not only optimal in buckling strength with given length and volume, also optimal in tolerance to axisymmetric geometric variations. Our asymptotic analysis is consistent with numerical experiments based on Rayleigh-Ritz method. The result further support the structure-property connection in *Ta.* spicules—The tapered shape provides the *Ta.* spicules higher buckling strength against buckling failure and improves that overall structural strength of *Ta.* sponges.

It is important to note that the results in this dissertation is far from a confirmation that mechanical optimization is the only factor contributing to the spicule's design, including the lamellar architectures in *Ea.* anchor spicules and the tapered shape of *Ta.* spicules. Actually, many biological skeletal elements are inherently multi-functional and have evolved the ability to perform a variety of tasks in addition to their mechanical ones. In particular, it has been shown that *Ea.* anchor spicules have

exceptional fiber-optical properties [120, 121]. Currently, we cannot be certain that the *Ea.* spicule's internal architecture contributes solely to its mechanical function or whether it has additional (e.g., light transmission) benefits. In addition, it is also possible that the *Ea.* spicule's internal architecture is connected to a different metric of the spicule's mechanical efficiency, or the same mechanical metric through different mechanism. For example, the internal architectures in *Ea.* spicules are proved to optimize the stress distribution over the spicules' cross section [18]. This mechanism, although different from the mechanism in 3, is also correlated with the enhancement of the overall strength of each spicule. The two mechanisms can be combined together to better explain the load-bearing capacity of the spicules that benefits from the lamellar internal architecture.

Another common question regarding the structure-property connections in spicules is whether it is possible that the layered architecture is not for any mechanical benefits but just a result of growth process? It is known that some architectural features of biological structures are merely a consequence of the growth processes through which the structures are formed and have no obvious functional implications, e.g., growth rings in fish scales [122]. Despite previous efforts [123], knowledge regarding the detailed mechanisms underlying spicule formation is still incomplete and therefore, at this stage, it cannot be ruled out whether other factors, such as growth processes, are also responsible for the spicule's shape and architecture. However, whether the spicule's architecture is a simple outcome of its growth process or is specifically optimized for multi-functionality, it clearly offers the sponge skeleton an exceptional mechanical advantage. Therefore, even if the layered architecture in *Ea.* spicules is just a result of growth process, that does not call off the mechanical benefits in the spicules. And the structure-property connections have been supported independently by our theoretical model, which means the mechanical benefits are indeed related to the spicule's architecture. Even though the mechanical benefits may not be the evolution goal of the sponge, the theoretical model and the mechanics behind it is always effective and can be applied in engineering design and manufacture.

Despite the achieved advances in this dissertation, there are several potential research topics that could be explored in the future. Those topics include:

1. In order to further gauge the validity of applying the developed model to interpret the SS experiments, it would be ideal if $\mu(\cdot)$, the variation of the coefficient of friction between the

spicule and the trench when different cross-sections of the spicule are in contact with the trench, could be measured directly and independently of the SS experiments. In the future, we plan on characterizing $\mu(\cdot)$ using an Atomic Force Microscope [124, 60, 125]. Those experiments will provide alternate estimates for A and λ, which can then be, respectively, compared with the chosen values for them. That comparison would allow us to further gauge the validity of applying our model to the SS experiments.

2. The nonlinear bending-sliding model not only uncovers the mechanism behind the sawtooth patterns, but also provides a potential application of three point bending test: characterization of the frictional coefficient between a surface and a fillet edge. A potential setup could be a long, narrow plate-shape specimen slipping on a test stage with fillet supporting edges. The specimen is loaded by a cantilever on its midpoint and force-deflection response is recorded. Using the nonlinear bending-sliding model, the fractional coefficient between the specimen and the edge could be deduced inversely from the force-deflection response.

3. In the asymptotic analysis of the effective bending stiffness of multilayered composite cylinders with cylindrical orthotropy, we considered hollow cylinders and no slip/friction interfacial conditions. In order to model the *Ea.* anchor spicules, a more realistic model would be a multilayered cylinder with a solid core and elastic interfacial conditions. The change involves modifications on the innermost boundary condition given by (3.13a).

Appendix A

Supplementary Material: Effective bending stiffness of multilayered composite cylinders with cylindrical orthotropy

A.1 Material constants

The material constants m_i, g_i, Q_i, W_i and μ_i are dependent on elastic constants. We calculate m_i as

$$m_1 = \sqrt{\frac{-b + \sqrt{\mathsf{p}\,(b,2) - 4ac}}{2a}}, \tag{A.1a}$$

$$m_2 = \sqrt{\frac{-b - \sqrt{\mathsf{p}\,(b,2) - 4ac}}{2a}}, \tag{A.1b}$$

$$m_3 = -\sqrt{\frac{-b + \sqrt{\mathsf{p}\,(b,2) - 4ac}}{2a}}, \tag{A.1c}$$

$$m_4 = -\sqrt{\frac{-b - \sqrt{\mathsf{p}\,(b,2) - 4ac}}{2a}}, \tag{A.1d}$$

where

$$a := \beta_{22}\beta_{44} - \mathsf{p}\,(\beta_{24}, 2)\,, \tag{A.1e}$$

$$\begin{aligned} b := {} & \beta_{24}(2\beta_{14} + \beta_{24} + 2\beta_{56}) + \mathsf{p}\,(\beta_{14}, 2) \\ & - \beta_{44}(\beta_{11} + 2\beta_{12} + \beta_{22} + \beta_{66}) - \beta_{22}\beta_{55}, \end{aligned} \tag{A.1f}$$

$$c := \beta_{55}(\beta_{11} + 2\beta_{12} + \beta_{22} + \beta_{66}) - \mathsf{p}\,(\beta_{56}, 2)\,, \tag{A.1g}$$

and the reduced elastic constants β_{ij} are defined in terms of $s_{ij}^{(\hat{e})}$ as

$$\beta_{ij} := s_{ij}^{(\hat{e})} - \frac{s_{i3}^{(\hat{e})} s_{3j}^{(\hat{e})}}{s_{33}^{(\hat{e})}},\ i, j = 1, 2, \ldots, 6. \tag{A.2}$$

We calculate g_i, Q_i, W_i as

$$g_i = \frac{\beta_{24}\,\mathsf{p}\,(m_i, 2) + (\beta_{14} + \beta_{24})m_i - \beta_{56}}{\beta_{44}\,\mathsf{p}\,(m_i, 2) - \beta_{55}}, \tag{A.3a}$$

$$Q_i = \frac{1}{m_i}\left(\beta_{12}m_i + \beta_{22}m_i(m_i + 1) - \beta_{24}g_i\,\mathsf{p}\,(m_i, 2)\right), \tag{A.3b}$$

$$W_i = \frac{1}{m_i}\left(\beta_{55}g_i - \beta_{56}\right), \tag{A.3c}$$

for $i \in \mathcal{L} := (1, 2, 3, 4)$.

We calculate Q_5 and W_5 as

$$Q_5 = \mu_1(\beta_{12} + 3\beta_{22}) - 2\mu_2\beta_{24} + \frac{s_{23}^{(\hat{e})}}{s_{33}^{(\hat{e})}}, \tag{A.4a}$$

$$W_5 = \frac{1}{2}(\beta_{55}\mu_2 - \beta_{56}\mu_1), \tag{A.4b}$$

where

$$\begin{bmatrix} \mu_1 \\ \mu_2 \end{bmatrix} := \frac{1}{s_{33}^{(\hat{e})}}\,\mathrm{Inv}\left(\begin{bmatrix} -2\beta_{14} - 6\beta_{24} + \beta_{56} & 4\beta_{44} - \beta_{55} \\ -\beta_{11} - 2\beta_{12} + 3\beta_{22} - \beta_{66} & 2\beta_{14} - 2\beta_{24} + \beta_{56} \end{bmatrix}\right)\begin{bmatrix} 2s_{34}^{(\hat{e})} \\ s_{13}^{(\hat{e})} - s_{23}^{(\hat{e})} \end{bmatrix}. \tag{A.4c}$$

A.2 Expressions of P_i

The expressions of P_i in Eqn. (3.16) are given by

$$\begin{aligned} P_1 = -\frac{1}{q}\,&((g_2g_3(m_2-m_3)(m_4-2)+g_2g_4(m_4-m_2)(m_3-2)\\ &+g_3g_4(m_3-m_4)(m_2-2))\,\mu_1+(g_2(m_3-m_4)(m_2-2)\\ &+g_3(m_4-m_2)(m_3-2)+g_4(m_2-m_3)(m_4-2))\,\mu_2)\,, \end{aligned} \tag{A.5a}$$

$$\begin{aligned} P_2 = \frac{1}{q}\,&((g_1g_3(m_1-m_3)(m_4-2)+g_1g_4(m_4-m_1)(m_3-2)\\ &+g_3g_4(m_3-m_4)(m_1-2))\,\mu_1+(g_1(m_3-m_4)(m_1-2)\\ &+g_3(m_4-m_1)(m_3-2)+g_4(m_1-m_3)(m_4-2))\,\mu_2)\,, \end{aligned} \tag{A.5b}$$

$$\begin{aligned} P_3 = -\frac{1}{q}(&(g_1g_2(m_1-m_2)(m_4-2)+g_1g_4(m_4-m_1)(m_2-2)\\ &+g_2g_4(m_2-m_4)(m_1-2))\mu_1+(g_1(m_2-m_4)(m_1-2)\\ &+g_2(m_4-m_1)(m_2-2)+g_4(m_1-m_2)(m_4-2))\mu_2), \end{aligned} \tag{A.5c}$$

$$\begin{aligned} P_4 = \frac{1}{q}(&(g_1g_2(m_1-m_2)(m_3-2)+g_1g_3(m_3-m_1)(m_2-2)\\ &+g_2g_3(m_2-m_3)(m_1-2))\mu_1+(g_1(m_2-m_3)(m_1-2)\\ &+g_2(m_3-m_1)(m_2-2)+g_3(m_1-m_2)(m_3-2))\mu_2), \end{aligned} \tag{A.5d}$$

where

$$\begin{aligned} q :=&g_1(g_3-g_4)(m_1-m_3)(m_2-m_4)\\ &+g_2(g_3-g_4)(m_2-m_3)(m_4-m_1)\\ &-(g_1g_2+g_3g_4-g_1g_4-g_2g_4)(m_1-m_2)(m_3-m_4). \end{aligned} \tag{A.6}$$

A.3 Derivations in §3.3.3

A.3.1 Derivations of Eqn. (3.25)

To obtain Eqn. (3.25), let

$$
{}^{n}\tilde{\mathbf{A}} := \begin{bmatrix} 1 & 1 & 1 & 1 \\ {}^{n}g_1 & {}^{n}g_2 & {}^{n}g_3 & {}^{n}g_4 \\ {}^{n}Q_1 & {}^{n}Q_2 & {}^{n}Q_3 & {}^{n}Q_4 \\ {}^{n}W_1 & {}^{n}W_2 & {}^{n}W_3 & {}^{n}W_4 \end{bmatrix}, \tag{A.7a}
$$

$$
{}^{n}\tilde{\mathbf{B}} := \begin{bmatrix} 1 & 1 & 1 & 1 \\ {}^{n-1}g_1 & {}^{n-1}g_2 & {}^{n-1}g_3 & {}^{n-1}g_4 \\ {}^{n-1}Q_1 & {}^{n-1}Q_2 & {}^{n-1}Q_3 & {}^{n-1}Q_4 \\ {}^{n-1}W_1 & {}^{n-1}W_2 & {}^{n-1}W_3 & {}^{n-1}W_4 \end{bmatrix}, \tag{A.7b}
$$

$$
{}^{n}\mathbf{f}(r) := \begin{bmatrix} \mathsf{p}\,(r, {}^{n}m_1) & 0 & 0 & 0 \\ 0 & \mathsf{p}\,(r, {}^{n}m_2) & 0 & 0 \\ 0 & 0 & \mathsf{p}\,(r, {}^{n}m_3) & 0 \\ 0 & 0 & 0 & \mathsf{p}\,(r, {}^{n}m_4) \end{bmatrix}, \tag{A.7c}
$$

$$
{}^{n}\tilde{\mathbf{m}} := \begin{bmatrix} {}^{n}m_1 & 0 & 0 & 0 \\ 0 & {}^{n}m_2 & 0 & 0 \\ 0 & 0 & {}^{n}m_3 & 0 \\ 0 & 0 & 0 & {}^{n}m_4 \end{bmatrix}. \tag{A.7d}
$$

It is noted that ${}^{n}\tilde{\mathbf{A}}$, ${}^{n}\tilde{\mathbf{B}}$, and ${}^{n}\tilde{\mathbf{m}}$ are constant matrices. The coefficient matrices ${}^{n}\mathbf{A}$ and ${}^{n}\mathbf{B}$ in Eqn. (3.23a) can be written as

$$
{}^{n}\mathbf{A} = {}^{n}\tilde{\mathbf{A}}\,{}^{n}\mathbf{f}({}^{n-1}r), \quad {}^{n}\mathbf{B} = {}^{n}\tilde{\mathbf{B}}\,{}^{n-1}\mathbf{f}({}^{n-1}r). \tag{A.8}
$$

Approximating ${}^{n-1}\mathbf{A}$ and ${}^{n-1}\mathbf{B}$ to the first order of Δr around ${}^{n-1}r$, we have

$$ {}^{n-1}\mathbf{A} = {}^{n}\mathbf{B} - \delta\,{}^{n}\mathbf{B}\Delta r + O(\mathsf{p}\,(\Delta r, 2)), \tag{A.9a} $$

$$ {}^{n-1}\mathbf{B} = {}^{n}\mathbf{A} - \delta\,{}^{n}\mathbf{A}\Delta r + O(\mathsf{p}\,(\Delta r, 2)), \tag{A.9b} $$

where

$$ \delta\,{}^{n}\mathbf{A} = \frac{1}{{}^{n-1}r}\,{}^{n}\mathbf{A}\,{}^{n}\tilde{\mathbf{m}} = \frac{1}{{}^{n-1}r}\,{}^{n}\tilde{\mathbf{A}}\,{}^{n}\mathbf{f}({}^{n-1}r)\,{}^{n}\tilde{\mathbf{m}}, \tag{A.9c} $$

$$ \delta\,{}^{n}\mathbf{B} = \frac{1}{{}^{n-1}r}\,{}^{n}\mathbf{B}\,{}^{n-1}\tilde{\mathbf{m}} = \frac{1}{{}^{n-1}r}\,{}^{n}\tilde{\mathbf{B}}\,{}^{n-1}\mathbf{f}({}^{n-1}r)\,{}^{n-1}\tilde{\mathbf{m}}. \tag{A.9d} $$

Therefore, we derive the following relations by considering Eqns. (A.9) and approximating the resulting expression to the first order of Δr around ${}^{n-1}r$

$$ {}^{n}\mathbf{B}\,\mathrm{Inv}\left({}^{n-1}\mathbf{A}\right) = \mathbf{I}_{4\times4} + \frac{\Delta r}{{}^{n-1}r}\,{}^{n}\mathbf{B}\;{}^{n-1}\tilde{\mathbf{m}}\;\mathrm{Inv}\,({}^{n}\mathbf{B}) + O(\mathsf{p}\,(\Delta r, 2)), \tag{A.10a} $$

$$ {}^{n}\mathbf{B}\,\mathrm{Inv}\left({}^{n-1}\mathbf{A}\right)\;{}^{n-1}\mathbf{B} = {}^{n}\mathbf{A} + \frac{\Delta r}{{}^{n-1}r}\left({}^{n}\mathbf{B}\,{}^{n-1}\tilde{\mathbf{m}}\,\mathrm{Inv}\,({}^{n}\mathbf{B})\;{}^{n}\mathbf{A} - {}^{n}\mathbf{A}\,{}^{n}\tilde{\mathbf{m}}\right) + O(\mathsf{p}\,(\Delta r, 2)), \tag{A.10b} $$

$$ {}^{n}\mathbf{B}\,\mathrm{Inv}\left({}^{n-1}\mathbf{A}\right)\;{}^{n-1}\mathbf{D} + {}^{n}\mathbf{D} = \frac{\Delta r}{{}^{n-1}r}\left(2\,{}^{n}\mathbf{D} + {}^{n}\mathbf{B}\,{}^{n-1}\tilde{\mathbf{m}}\,\mathrm{Inv}\,({}^{n}\mathbf{B})\;{}^{n-1}\mathbf{D}\right) + O(\mathsf{p}\,(\Delta r, 2)). \tag{A.10c} $$

A.3.2 Derivation of ODE system given by (3.28) and (3.13)

Substituting Eqn. (3.27) into Eqn. (3.26), we obtain

$$ \begin{aligned} 2\,{}^{n-1}r\frac{d\,{}^{n}\bar{\mathbf{K}}(r)}{dr} = &\left(\mathrm{Inv}\,({}^{n}\mathbf{A})\;{}^{n}\mathbf{B}\,{}^{n-1}\tilde{\mathbf{m}}\,\mathrm{Inv}\,({}^{n}\mathbf{B})\;{}^{n}\mathbf{A} - {}^{n}\tilde{\mathbf{m}}\right)\;{}^{n}\bar{\mathbf{K}}(r) \\ &+ \mathrm{Inv}\,({}^{n}\mathbf{A})\left(2\,{}^{n}\mathbf{D} + {}^{n}\mathbf{B}\,{}^{n-1}\tilde{\mathbf{m}}\,\mathrm{Inv}\,({}^{n}\mathbf{B})\;{}^{n-1}\mathbf{D}\right) + O(\Delta r). \end{aligned} \tag{A.11} $$

Taking the zero order of approximation of Eqn. (A.11) around ${}^{n}r$ and noting that

$$ {}^{n}\mathbf{B}\,{}^{n-1}\tilde{\mathbf{m}}\,\mathrm{Inv}\,({}^{n}\mathbf{B}) = {}^{n}\tilde{\mathbf{B}}\,{}^{n-1}\tilde{\mathbf{m}}\,\mathrm{Inv}\left({}^{n}\tilde{\mathbf{B}}\right), \tag{A.12} $$

we have

$$ \begin{aligned} 2\,{}^{n}r\frac{d\,{}^{n}\bar{\mathbf{K}}(r)}{dr} = &\Big(\mathrm{Inv}\,({}^{n}\mathbf{f}({}^{n}r))\ \mathrm{Inv}\left({}^{n}\tilde{\mathbf{A}}\right)\ {}^{n}\tilde{\mathbf{B}}\,{}^{n-1}\tilde{\mathbf{m}}\,\mathrm{Inv}\left({}^{n}\tilde{\mathbf{B}}\right)\tilde{\mathbf{A}}_{n}\,{}^{n}\mathbf{f}({}^{n}r) - {}^{n}\tilde{\mathbf{m}}\Big)\ {}^{n}\bar{\mathbf{K}}(r) \\ &+ \mathsf{p}\,({}^{n}r,2)\ \mathrm{Inv}\,({}^{n}\mathbf{f}({}^{n}r))\ \mathrm{Inv}\left({}^{n}\tilde{\mathbf{A}}\right)\Big(-2\mathbf{I}_{4\times4} + {}^{n}\tilde{\mathbf{B}}\,{}^{n-1}\tilde{\mathbf{m}}\,\mathrm{Inv}\left({}^{n}\tilde{\mathbf{B}}\right)\Big)\ {}^{n}\tilde{\mathbf{D}} + O(\Delta r), \end{aligned} \tag{A.13} $$

where ${}^{n}\tilde{\mathbf{D}}$ is a constant vector

$$ {}^{n}\tilde{\mathbf{D}} := \begin{bmatrix} {}^{n}\mu_1 - {}^{n-1}\mu_1 \\ {}^{n}\mu_2 - {}^{n-1}\mu_2 \\ {}^{n}Q_5 - {}^{n-1}Q_5 \\ {}^{n}W_5 - {}^{n-1}W_5 \end{bmatrix}. \tag{A.14} $$

Let

$$ {}^{n}\tilde{\mathbf{M}} := \mathrm{Inv}\left({}^{n}\tilde{\mathbf{A}}\right)\ {}^{n}\tilde{\mathbf{B}}\,{}^{n-1}\tilde{\mathbf{m}}\,\mathrm{Inv}\left({}^{n}\tilde{\mathbf{B}}\right)\ {}^{n}\tilde{\mathbf{A}}, \tag{A.15a} $$

$$ {}^{n}\tilde{\mathbf{F}} := \mathrm{Inv}\left({}^{n}\tilde{\mathbf{A}}\right)\Big(-2\mathbf{I}_{4\times4} + {}^{n}\tilde{\mathbf{B}}\,{}^{n-1}\tilde{\mathbf{m}}\,\mathrm{Inv}\left({}^{n}\tilde{\mathbf{B}}\right)\Big)\ {}^{n}\tilde{\mathbf{D}}, \tag{A.15b} $$

We rewrite Eqn. (A.13) as

$$ 2\,{}^{n}r\frac{d\,{}^{n}\bar{\mathbf{K}}(r)}{dr} = \big(\mathrm{Inv}\,({}^{n}\mathbf{f}({}^{n}r))\ {}^{n}\tilde{\mathbf{M}}\,{}^{n}\mathbf{f}({}^{n}r) - {}^{n}\tilde{\mathbf{m}}\big)\,{}^{n}\bar{\mathbf{K}}(r) + \mathsf{p}\,({}^{n}r,2)\ \mathrm{Inv}\,({}^{n}\mathbf{f}({}^{n}r))\ {}^{n}\tilde{\mathbf{F}}. \tag{A.16} $$

For simplicity, we drop the left superscript in all variables in the following derivations when there is no confusion. We can rewrite Eqn. (A.16) as

$$ 2r\frac{d\bar{\mathbf{K}}(r)}{dr} = \big(\mathrm{Inv}\,(\mathbf{f}(r))\,\tilde{\mathbf{M}}\mathbf{f}(r) - \tilde{\mathbf{m}}\big)\,\bar{\mathbf{K}}(r) + \mathsf{p}\,(r,2)\ \mathrm{Inv}\,(\mathbf{f}(r))\,\tilde{\mathbf{F}}. \tag{A.17} $$

Then multiplying Eqn. (A.17) by $\mathbf{f}(r)$ on both sides, we obtain a linear ODE system of $\bar{\mathbf{K}}(r)$

$$ 2r\frac{d\left(\mathbf{f}(r)\bar{\mathbf{K}}(r)\right)}{dr} = \left(\tilde{\mathbf{M}} + \tilde{\mathbf{m}}\right)\left(\mathbf{f}(r)\bar{\mathbf{K}}(r)\right) + \mathsf{p}\,(r,2)\,\tilde{\mathbf{F}}, \tag{A.18} $$

with boundary conditions given by (3.13).

A.3.3 Solution procedures of ODE system given by (3.28) and (3.13)

The ODE system of ${}^{n}\bar{\mathbf{K}}(r)$ given by (3.28) and (3.13) is equivalent to

$$2r\frac{d\hat{\mathbf{K}}(r)}{dr} = \tilde{\mathbf{H}}\hat{\mathbf{K}}(r) + \mathsf{p}\,(r,2)\,\tilde{\mathbf{F}}, \tag{A.19}$$

where $\hat{\mathbf{K}}(r) := \mathbf{f}(r)\bar{\mathbf{K}}(r)$ and $\tilde{\mathbf{H}} := \tilde{\mathbf{M}} + \tilde{\mathbf{m}}$, with boundary conditions

$$\sum_{i\in\mathcal{L}} \hat{K}_i({}^{0}r)\,\mathsf{p}\left({}^{0}r,-2\right) = -\mu_1, \quad \sum_{i\in\mathcal{L}} \hat{K}_i({}^{0}r)g_i\,\mathsf{p}\left({}^{0}r,-2\right) = -\mu_2, \tag{A.20a}$$

$$\sum_{i\in\mathcal{L}} \hat{K}_i({}^{N}r)\,\mathsf{p}\left({}^{N}r,-2\right) = -\mu_1, \quad \sum_{i\in\mathcal{L}} \hat{K}_i({}^{N}r)g_i\,\mathsf{p}\left({}^{N}r,-2\right) = -\mu_2. \tag{A.20b}$$

Recall that the material properties of the multilayered material is alternately arranged, the constant coefficient matrix $\tilde{\mathbf{H}}$ and $\tilde{\mathbf{F}}$ are different for the odd and even layers. We denote $\tilde{\mathbf{H}}$ and $\tilde{\mathbf{F}}$ for the odd layers as ${}^{I}\tilde{\mathbf{H}}$ and ${}^{I}\tilde{\mathbf{F}}$ (for even layers, ${}^{II}\tilde{\mathbf{H}}$ and ${}^{II}\tilde{\mathbf{F}}$). The continuous functions $\hat{\mathbf{K}}(r)$ for the odd and even layers can be obtained by solving Eqn. (A.19) separately. We diagonalize the matrix $\tilde{\mathbf{H}}$ as

$$\tilde{\mathbf{H}} = \mathrm{Inv}\left(\tilde{\mathbf{Q}}\right)\tilde{\mathbf{\Lambda}}\tilde{\mathbf{Q}}, \tag{A.21}$$

where $\tilde{\mathbf{\Lambda}} := \mathrm{diag}(\tilde{\lambda}_1,\tilde{\lambda}_2,\tilde{\lambda}_3,\tilde{\lambda}_4)$ and $\tilde{\mathbf{Q}}$ are respectively the eigenvalue and eigenvector matrices of $\tilde{\mathbf{H}}$, $\tilde{\lambda}_i$ are eigenvalues. We denote $\mathbf{\Lambda} = \mathrm{diag}(\lambda_1,\lambda_2,\lambda_3,\lambda_4)$, where $\lambda_i = \tilde{\lambda}_i/2$ for $i \in \mathcal{L}$. Then it follows that $\mathbf{\Lambda} := \tilde{\mathbf{\Lambda}}/2$. Let

$$\mathbf{Y} := \tilde{\mathbf{Q}}\hat{\mathbf{K}}(r), \quad \mathbf{L} := \frac{1}{2}\tilde{\mathbf{Q}}\tilde{\mathbf{F}}, \tag{A.22}$$

then Eqn. (A.19) becomes

$$r\frac{d\mathbf{Y}}{dr} = \mathbf{\Lambda}\mathbf{Y} + \mathsf{p}\,(r,2)\,\mathbf{L}. \tag{A.23}$$

The solution of Eqn. (A.23) reads

$$\begin{bmatrix} Y_1 \\ Y_2 \\ Y_3 \\ Y_4 \end{bmatrix} = \begin{bmatrix} \frac{L_1}{2-\lambda_1} \\ \frac{L_2}{2-\lambda_2} \\ \frac{L_3}{2-\lambda_3} \\ \frac{L_4}{2-\lambda_4} \end{bmatrix} \mathsf{p}\,(r,2) + \begin{bmatrix} c_1\,\mathsf{p}\,(r,\lambda_1) \\ c_2\,\mathsf{p}\,(r,\lambda_2) \\ c_3\,\mathsf{p}\,(r,\lambda_3) \\ c_4\,\mathsf{p}\,(r,\lambda_4) \end{bmatrix}, \tag{A.24}$$

where c_i are the integration constants.

Therefore, $\hat{\mathbf{K}}(r)$ are given by

$$\hat{\mathbf{K}}(r) = \mathrm{Inv}\left(\tilde{\mathbf{Q}}\right)\mathbf{Y}, \tag{A.25}$$

where $\mathbf{Y}$ is given by Eqn. (A.24). The analytical expression of integration constants c_i can be obtained by solving the linear system given by inserting Eqns. (A.25) into the boundary conditions Eqns. (A.20). For the conciseness of the manuscript, we will not report the explicit analytical expression of c_i here.

Finally, we obtain $\bar{\mathbf{K}}(r)$ given by

$$\bar{\mathbf{K}}(r) = \mathrm{Inv}\left(\mathbf{f}(r)\right)\,\mathrm{Inv}\left(\tilde{\mathbf{Q}}\right)\mathbf{Y}. \tag{A.26}$$

Substituting Eqns. (A.7c) and (A.24) into Eqn. (A.26), we obtain a general discrete expression of ${}^{n}\mathbf{K}$ in component form as

$${}^{n}K_i = \mathsf{p}\,({}^{n}r, -{}^{n}m_i)\left({}^{n}G_{i0}\,{}^{n}\mathsf{p}\,(r,2) + \sum_{j\in\mathcal{L}} {}^{n}G_{ij}\,\mathsf{p}\left({}^{n}r, {}^{n}\lambda_j\right)\right), \quad \text{for } i \in \mathcal{L}, \tag{A.27}$$

where ${}^{n}G_{ij}$ are constants given by

$${}^{n}G_{i0} := \sum_{k\in\mathcal{L}} \mathrm{Inv}\left({}^{n}\tilde{\mathbf{Q}}\right)_{ik} \frac{{}^{n}L_k}{2-{}^{n}\lambda_k}, \tag{A.28a}$$

$${}^{n}G_{ij} := \mathrm{Inv}\left({}^{n}\tilde{\mathbf{Q}}\right)_{ij} {}^{n}c_j, \quad \text{for } j \in \mathcal{L}. \tag{A.28b}$$

Appendix B

Supplementary Material: Asymptotic analysis of sponge spicules' tolerance to geometric variations regarding buckling instability

B.1 Admissible space for the initial column's profile

In this section, I will explain the development of the admissible space $\mathcal{V}_0$ for the initial column's profle $\rho_0(\cdot)$. The derivation involves singular Sturm-Liouville theory and will be explained in detail.

B.1.1 Definition and notation

In order to explain the singular Sturm-Liouville theory, I first introduce some necessary definitions and notations from the chapter *A Catalogue of Sturm-Liouville Differential Equations* by W. Norrie Everitt [126] of the book *Sturm-Liouville Theory: Past and Present* [127].

(1) $L^1(I)$: **Lebesgue integration space** of complex-valued functions defined on the interval I

(2) $L^1_{\text{loc}}(I)$: **Local integration space**, the set of all complex-valued functions on I which are

Lebesgue integrable on all compact sub-intervals $[a, b] \subseteq I$.

(3) AC : **Absolute continuity**, with respect to Lebesgue measure

(4) $AC_{\mathrm{loc}}(I)$: The space of all complex-valued functions defined on I which are absolutely continuous on all compact sub-intervals of I

B.1.2 Sturm-Liouville differential equation

Consider the following boundary value problem

$$-(p(x)y'(x))' = \lambda y(x), \quad \forall x \in (0,1), \tag{B.1.1a}$$

$$p(0)y'(0) = 0, \tag{B.1.1b}$$

$$y(1) = 0. \tag{B.1.1c}$$

The coefficient function $p(x)$ is continuous in $[0, 1]$, $p(x) > 0$ for $0 < x \leq 1$ and $p(0) \geq 0$.

This is a special case of the general Sturm-Liouville differential equation

$$-(p(x)y'(x))' + q(x)y(x) = \lambda w(x)y(x), \quad \forall x \in (a,b), \tag{B.1.2}$$

where $\lambda \in \mathbb{C}$ is a complex-valued spectral parameter. The set of Sturm-Liouville coefficients $\{p, q, w\}$ has to satisfy the minimal conditions

(1) $p,\ q,\ w\ : (a,b) \to \mathbb{R}$,

(2) $p^{-1},\ q,\ w \in L^1_{\mathrm{loc}}(a,b)$,

(3) w is a weight function on (a, b), which means that $w(x) : (a, b) \to \mathbb{R}$ is a Lebesgue measurable function and $w(x) > 0$ for almost all $x \in (a, b)$.

For the problem (B.1.1), all of the above three minimal conditions are satisfied.

B.1.3 Endpoints classification

I introduce the endpoints classification given in [126] by W. Norrie Everitt.

Suppose given the interval (a, b) and the set of coefficients $\{p, q, w\}$.

(1) The endpoint a is **regular** if

(I) $a > -\infty$, and

(II) $p^{-1},\ q,\ w \in L^1(a, c],\ \forall\ c \in (a, b)$.

(2) The endpoint a is **singular** if it is not regular, *i.e.*,

(I) either $a = -\infty$,

(II) or $a > -\infty$ but $\int_a^c \left(|p(x)|^{-1} + |q(x)| + |w(x)|\right) dx = +\infty,\ \forall\ c \in (a, b)$.

If a is a singular endpoint, there are two classification subcases as follows:

(1) It is **limit-point** if for some $\lambda \in \mathbb{C}$, at least one solution $y(\cdot, \lambda)$ of the differential equation (B.1.1) satisfies

$$\int_a^c w(x)|y(x, \lambda)|^2 dx = +\infty,\ \forall\ c \in (a, b). \tag{B.1.3}$$

(2) It is **limit-circle** if for some $\lambda \in \mathbb{C}$, all solutions $y(\cdot, \lambda)$ of the differential equation (B.1.1) satisfy

$$\int_a^c w(x)|y(x, \lambda)|^2 dx < +\infty,\ \forall\ c \in (a, b). \tag{B.1.4}$$

According to above classification, for our problem (B.1.1), $x = 1$ is a regular endpoint. The singularity of the endpoint $x = 0$ depends on the behavior of $1/p(x)$ as $x \to 0$. Taking the leading order term x^α from the series expansion of $p(x)$, I have the following discussion:

(1) If $\alpha \leq 0$, which means $p(0) \neq 0$, the endpoint $x = 0$ is **regular**.

(2) If $0 < \alpha < 1$, which means $p(0) = 0$ but $\int_0^c 1/p(t)dt < +\infty,\ \forall\ c \in (0, 1)$, the endpoint $x = 0$ is still **regular**.

(3) If $\alpha \geq 1$, which means $p(0) = 0$ and $\int_0^c 1/p(t)dt = +\infty,\ \forall\ c \in (0, 1)$, the endpoint $x = 0$ is **singular**.

Therefore, if the singularity of $1/p(x)$ is moderate ($0 < \alpha < 1$), the problem (B.1.1) is regular and all the results of regular Sturm-Liouville theory hold (see [128] by Boyce and Di Prima).

However, if the singularity of $1/p(x)$ is substantial ($\alpha \geq 1$), problem (B.1.1) becomes a singular Strum-Liouville problem. For example, in the context of Euler buckling, the problem is singular if the column has **ellipse** or **Clausen** profile (see Section B.1.5). I will further explore whether the following results still hold in a singular Strum-Liouville problem:

(1) The self-adjoint relation holds.

(2) The problem consists only a discrete set of eigenvalues.

(3) All the eigenvalues are real.

(4) The corresponding eigenfunctions form a complete, orthogonal set in the Hilbert function space.

(5) The expansion of a given continuous function f in terms of a series of eigenfunctions is convergent.

Taking $\lambda = 0$, the differential equation (B.1.1a) becomes $-(p(x)y'(x))' = 0$. Approximating $p(x)$ by its leading order term x^α, $\alpha \geq 1$, I get the non-trivial solution of $y(x)$ as

$$y(x) \sim C_1 \frac{x^{1-\alpha}}{1-\alpha} + C_2, \tag{B.1.5}$$

where C_1 and C_2 are integration constants. For $c \in (0, 1)$, the L^2 norm of $y(x)$ can be estimated

$$\int_0^c |y(x)|^2 dx \sim \lim_{x\to 0} \left[\frac{C_1^2}{(1-\alpha)^2(3-2\alpha)} x^{3-2\alpha} + \frac{C_1 C_2}{(1-\alpha)(2-\alpha)} x^{2-\alpha} + C_2^2 x \right]. \tag{B.1.6}$$

For $\alpha < \frac{3}{2}$, $\int_0^c |y(x)|^2 dx < +\infty$, the endpoint $x = 0$ is **limit-circle**; for $\alpha \geq \frac{3}{2}$, $\int_0^c |y(x)|^2 dx = +\infty$, the endpoint $x = 0$ is **limit-point**.

B.1.4 Spectrum properties

Since the endpoint $x = 1$ is **regular**, the spectrum property of the problem (B.1.1) depends on the classification of endpoint $x = 0$. For the spectrum properties of endpoints in different classification, we have the following discussion (see [129] by Bailey *et al.* for reference)

(1) If $x = 0$ is **regular** or **limit-circle**, then the spectrum is always *discrete*, *simple* and *bounded below*.

(2) If $x = 0$ is **limit-point**, then the spectrum is always *simple* but may or may not be *discrete*, and may or may not be *bounded below*.

Thus, to make sure that the buckling problem given by (B.1.1) to be valid, the endpoint $x = 0$ must be **regular** or **limit-circle**. That is, for $p(x) \sim x^\alpha$, $\alpha < \frac{3}{2}$ must be satisfied. This condition is sufficient but not necessary.

B.1.5 Application to buckling of constant, Clausen, ellipsoidal columns

For arbitrary axisymmetric pin-ended, non-uniform cross-section column, one can identify a critical point in the buckled configuration where the tangential angle at that point is zero. If the geometry of the column is symmetric with respect to the midpoint of the column, the critical point is the midpoint of the column. In general, the critical point will divide the column into two pieces with uneven length. We focus on one of the pieces. By introducing $\zeta(\xi) = \eta'(\xi)$ as the tangential angle of the column's neutral axis, we have the governing equations of the Euler buckling problem for a non-uniform column with hinged left end and built-in right end given by

$$(\hat{I}(\xi)\zeta'(\xi))' + \beta\zeta(\xi) = 0, \quad \forall \xi \in (0,1), \tag{B.1.7a}$$

$$\hat{I}(\xi)\zeta'(\xi)\big|_{\xi=0} = 0, \tag{B.1.7b}$$

$$\zeta(\xi)\big|_{\xi=1} = 0. \tag{B.1.7c}$$

At the end $\xi = 0$, the beam is hinged so the bending moment $\hat{I}(0)\zeta'(0)$ vanishes. The end $\xi = 1$ is the critical point of the original column where no rotation is observed. The coefficient function $\hat{I}(\xi)$ is non-zero at $\xi = 1$ and may vanish at $\xi = 0$. If we replace the variables $\hat{I}(\xi)$, $\zeta(\xi)$, ξ, β by $p(x)$, $y(x)$, x, λ, respectively, the above problem is equivalent to the standard Sturm-Liouville problem as given by (B.1.1).

I apply the results in the above sections to constant, ellipsoidal and Clausen column profiles.

The mathematical description for the three types of columns' profiles are given by

$$\rho_{\square}(\xi) = \rho_0, \tag{B.1.8a}$$

$$\rho_{\bigcirc}(\xi) = C_1 \xi^{1/2}(1-\xi)^{1/2}, \tag{B.1.8b}$$

$$\rho_{\text{Clausen}}(\theta) = C_2 \sin\theta, \quad \xi(\theta) = \frac{1}{\pi}\left(\theta - \frac{1}{2}\sin 2\theta\right). \tag{B.1.8c}$$

Noting that $p(x) \sim \hat{I}(\xi) \sim \rho(\xi)^4$, it is straightforward that for the constant profile, $p(x) \sim x^0$, and for the ellipse profile, $p(x) \sim x^2$ at the endpoint $x = 0$. For the Clausen profile, using series expansion I found that $p(x) \sim x^{4/3}$. For columns with constant ($\alpha = 0$) and Clausen profile ($\alpha = 4/3$), the endpoint $x = 0$ is regular and limit-circle, respectively. For columns with ellipse profile ($\alpha = 2$), the endpoint $x = 0$ is limit-point. Therefore, the buckling analysis applies for constant and Clausen profile columns, but may not apply for ellipsoidal columns.

B.2 Proof that the stationary point is a global minimizer

In this section, I provide a simple proof that the stationary point that I obtained in Section 5.3.2 is a global minimizer for the following problem:

$$\min_{\rho_1(\cdot)\in\mathcal{V}_1(\rho_0(\cdot))} \beta_1[\rho_1(\cdot);\rho_0(\cdot)], \tag{B.2.1}$$

where

$$\beta_1[\rho_1(\cdot);\rho_0(\cdot)] = -4\int_0^1 \rho_0(\xi)^{-1}\rho_1(\xi)\eta_0(\xi)\eta_0''(\xi)d\xi. \tag{B.2.2}$$

According to Cauchy-Schwarz inequality

$$\left(\int_0^1 -4\rho_0^{-1}(\xi)\rho_1(\xi)\eta_0(\xi)\eta_0''(\xi)d\xi\right)^2 \le \int_0^1 \left(-4\rho_0^{-1}(\xi)\eta_0(\xi)\eta_0''(\xi)d\xi\right)^2 d\xi \cdot \int_0^1 \rho_1^2(\xi)d\xi, \tag{B.2.3}$$

which gives the range for $\beta_1[\rho_1(\cdot);\rho_0(\cdot)]$:

$$-4d\left[\int_0^1 \rho_0^{-2}(\xi)\eta_0^2(\xi)\eta_0''^2(\xi)d\xi\right]^{1/2} \leq \beta_1[\rho_1(\cdot);\rho_0(\cdot)] \leq 4d\left[\int_0^1 \rho_0^{-2}(\xi)\eta_0^2(\xi)\eta_0''^2(\xi)d\xi\right]^{1/2}. \tag{B.2.4}$$

When I take $\rho_1^*(\xi)$ given by (5.22) as $\rho_1(\xi)$, the minimum value $-4d\left[\int_0^1 \rho_0^{-2}(\xi)\eta_0^2(\xi)\eta_0''^2(\xi)d\xi\right]^{1/2}$ is arrived. Thus I proved that the stationary point that I obtained in Section 5.3.2 is indeed a global minimizer.

B.3 Computation of the critical buckling load for perturbed columns using Rayleigh-Ritz method

Consider the boundary value problem (BVP) in (5.1a). In terms of the non-dimensional variables, we have

$$(\hat{I}(\xi)\eta''(\xi))'' + \beta\eta''(\xi) = 0, \tag{B.3.1a}$$

$$\hat{I}(\xi)\eta''(\xi)\big|_{\xi=0,\,1} = 0, \tag{B.3.1b}$$

$$\eta(\xi)|_{\xi=0,\,1} = 0, \tag{B.3.1c}$$

where $\hat{I}(\xi)$ is given by (5.4). In order to find the buckling strength numerically, I cast the above BVP in the form of a variational problem. It can be shown that the BVP, Eqns. (B.3.1a), is equivalent to the following variational problem. Find $\eta(\xi) \in \mathcal{V}_\eta$, where

$$\mathcal{V}_\eta = \{\eta \in C^2(0,1) \mid \eta(0) = \eta(1) = 0.\}$$

so that the functional

$$\Pi[\eta(\cdot)] = \frac{1}{2}\int_0^1 \left[\hat{I}(\xi)\eta''(\xi)^2 - \beta\eta'(\xi)^2\right]\, d\xi, \tag{B.3.2}$$

attains its minimum value.

We use the Rayleigh-Ritz method [130] to find an approximate solution to this variational problem. The approximation to the minimizer $\eta_*(\cdot)$ is $\eta_*^h(\cdot)$, which is the minimizer of $\hat{\Pi}$ over the

finite dimensional space $\mathcal{V}_\eta^h$, where

$$\mathcal{V}_\eta^h = \left\{ \sum_{i=1}^{N_{\max}} B_i \phi_i(\cdot) \ : \ B_i \in \mathbb{R} \text{ and } \phi_i(\cdot) \in C^2(0,1) \text{ for } i = 1, 2, \ldots, N_{\max}, \phi_i(0) = \phi_i(1) = 0. \right\}, \tag{B.3.3}$$

$$\eta^h(\cdot) = \sum_{i=1}^{N_{\max}} B_i \phi_i(\cdot), \qquad (\eta^h)'(\cdot) = \sum_{i=1}^{N_{\max}} B_i \phi_i'(\cdot), \qquad (\eta^h)''(\cdot) = \sum_{i=1}^{N_{\max}} B_i \phi_i''(\cdot), \tag{B.3.4}$$

Using the above expansions in Eqn. (B.3.2), we get

$$\Pi[\eta^h(\cdot)] = \frac{1}{2} \int_0^1 \left[\hat{I}(\xi) \left(\sum_{i=1}^{N_{\max}} B_i \phi_i''(\xi) \right)^2 - \beta \left(\sum_{i=1}^{N_{\max}} B_i \phi_i'(\xi) \right)^2 \right] d\xi. \tag{B.3.5}$$

Setting $\partial \Pi / \partial B_j = 0$ we get that

$$\sum_{j=1}^{N_{\max}} K_{ij}^M B_j = \beta \sum_{j=1}^{N_{\max}} K_{ij}^G B_j, \tag{B.3.6}$$

where

$$K_{ij}^M = \int_0^1 \hat{I}(\xi) \phi_i''(\xi) \phi_j''(\xi) \, d\xi, \tag{B.3.7}$$

$$K_{ij}^G = \int_0^1 \phi_i'(\xi) \phi_j'(\xi) \, d\xi. \tag{B.3.8}$$

In matrix notion, it reads

$$\left(\mathbf{K^G} \right)^{-1} \mathbf{K^M B} = \beta \mathbf{B}. \tag{B.3.9}$$

In the numerical experiments, I choose $\phi_i = \sin(i\pi\zeta)$ with $N_{\max} = 50$. Thus, the dimensionless buckling strength, β_c, is the lowest eigenvalue of the matrix $\mathbf{K} = \left(\mathbf{K^G} \right)^{-1} \mathbf{K^M}$.

Bibliography

[1] A. H. Nayfeh and P. F. Pai. Linear and nonlinear structural mechanics. Wiley series in nonlinear science. Wiley-Interscience, Hoboken, N.J, 2004.

[2] S. Timoshenko. On the correction for shear of the differential equation for transverse vibrations of prismatic bars. The London, Edinburgh, and Dublin Philosophical Magazine and Journal of Science, 41(245):744–746, May 1921.

[3] S. Timoshenko. X. On the transverse vibrations of bars of uniform cross-section. The London, Edinburgh, and Dublin Philosophical Magazine and Journal of Science, 43(253):125–131, January 1922.

[4] A. A. V. KRISHN. Vibrations of short beams. AIAA Journal, 8(1):34–38, 1970.

[5] P. R. Heyliger and J. N. Reddy. A higher order beam finite element for bending and vibration problems. Journal of Sound and Vibration, 126(2):309–326, October 1988.

[6] A. E. H. Love. A treatise on the mathematical theory of elasticity. Dover classics of science and mathematics. Dover Publ, New York, 4. ed., unabridged and unaltered republ. of the 4. (1927) ed edition, 1990.

[7] S. Timoshenko and J. M. Gere. Theory of elastic stability. Dover Publications, Mineola, 2009.

[8] E. Reissner. On one-dimensional finite-strain beam theory: The plane problem. Zeitschrift für angewandte Mathematik und Physik ZAMP, 23(5):795–804, September 1972.

[9] J. C. Simo. A finite strain beam formulation. The three-dimensional dynamic problem. Part I. Computer Methods in Applied Mechanics and Engineering, 49(1):55–70, May 1985.

[10] L. Euler. Methodus inveniendi lineas curvas maximi minimive proprietate gaudentes (appendix, de curvis elasticis). Lausanne und Genf, 1744, 1774.

[11] F. Engesser. Ober die knickfestigkeit gerader stabe (on the buckling strength of straight struts) zeitschrift fur architektur und ingenieurwesen, 1889.

[12] F. Engesser. Über knickfragen. Schweizerische Bauzeitung, 26(4):24, 1895.

[13] F. Shanley. The column paradox. Journal of the Aeronautical Sciences, 13(12):678–678, 1946.

[14] S. Leelavanichkul and A. Cherkaev. Why the grain in tree trunks spirals: a mechanical perspective. Structural and Multidisciplinary Optimization, 28(2):127–135, 2004.

[15] U. G. K. Wegst, H. Bai, E. Saiz, A. P. Tomsia, and R. O. Ritchie. Bioinspired structural materials. Nature Materials, 14(1):23–36, January 2015.

[16] J. Aizenberg, J. C. Weaver, M. S. Thanawala, V. C. Sundar, D. E. Morse, and P. Fratzl. Skeleton of Euplectella sp.: Structural hierarchy from the nanoscale to the macroscale. Science, 309(5732):275–278, 2005.

[17] A. P. Jackson, J. F. V. Vincent, and R. M. Turner. The mechanical design of nacre. Proc. R. Soc. Lond. B, 234(1277):415–440, September 1988.

[18] M. A. Monn, J. C. Weaver, T. Zhang, J. Aizenberg, and H. Kesari. New functional insights into the internal architecture of the laminated anchor spicules of Euplectella aspergillum. Proceedings of the National Academy of Sciences, 112(16):4976–4981, April 2015.

[19] J. D. Currey. Mechanical properties of mother of pearl in tension. Proceedings of the Royal Society B: Biological Sciences, 196:443–463, 1977.

[20] M. A. Meyers, P.-Y. Chen, A. Y.-M. Lin, and Y. Seki. Biological materials: Structure and mechanical properties. Progress in Materials Science, 53(1):1–206, 2008.

[21] H. D. Espinosa, A. L. Juster, F. J. Latourte, O. Y. Loh, D. Gregoire, and P. D. Zavattieri. Tablet-level origin of toughening in abalone shells and translation to synthetic composite materials. Nature Communications, 2:173, 2011.

[22] T. Zhang, Y. Ma, K. Chen, M. Kunz, N. Tamura, M. Qiang, J. Xu, and L. Qi. Structure and mechanical properties of a pteropod shell consisting of interlocked helical aragonite nanofibers. Angewandte Chemie, 123(44):10545–10549, 2011.

[23] L. Li, J. C. Weaver, and C. Ortiz. Hierarchical structural design for fracture resistance in the shell of the pteropod Clio pyramidata. Nature Communications, 6:1–10, 2015.

[24] O. Kolednik, J. Predan, F. D. Fischer, and P. Fratzl. Bioinspired design criteria for damage-resistant materials with periodically varying microstructure. Advanced Functional Materials, 21(19):3634–3641, 2011.

[25] J. C. Weaver, J. Aizenberg, G. E. Fantner, D. Kisailus, A. Woesz, P. Allen, K. Fields, M. J. Porter, F. W. Zok, P. K. Hansma, P. Fratzl, and D. E. Morse. Hierarchical assembly of the siliceous skeletal lattice of the hexactinellid sponge Euplectella aspergillum. Journal of Structural Biology, 158(1):93–106, April 2007.

[26] G. Mayer. Rigid biological systems as models for synthetic composites. Science, 310(5751):1144–1147, 2005.

[27] G. Mayer. New toughening concepts for ceramic composites from rigid natural materials. Journal of the mechanical behavior of biomedical materials, 4(5):670–681, 2011.

[28] S. Walter, B. Flinn, and G. Mayer. Mechanisms of toughening of a natural rigid composite. Materials Science and Engineering: C, 27(3):570–574, 2007.

[29] M. A. Monn and H. Kesari. Enhanced bending failure strain in biological glass fibers due to internal lamellar architecture. Journal of the Mechanical Behavior of Biomedical Materials, 76:69–75, December 2017.

[30] M. A. Monn, K. Vijaykumar, S. Kochiyama, and H. Kesari. Lamellar architectures in stiff biomaterials may not always be templates for enhancing toughness in composites. Nature Communications, 11:373, 2020.

[31] S. Kochiyama, W. Fang, M. A. Monn, and H. Kesari. Sawtooth patterns in flexural force curves of structural biological materials are not signatures of toughness enhancement. Journal of the Mechanical Behavior of Biomedical Materials, page 104362, 2021.

[32] J. C. Weaver, G. W. Milliron, P. Allen, A. Miserez, A. Rawal, J. Garay, P. J. Thurner, J. Seto, B. Mayzel, L. J. Friesen, B. F. Chmelka, P. Fratzl, J. Aizenberg, Y. Dauphin, D. Kisailus, and D. E. Morse. Unifying Design Strategies in Demosponge and Hexactinellid Skeletal Systems. The Journal of Adhesion, 86(1):72–95, January 2010.

[33] J. Aizenberg, J. C. Weaver, M. S. Thanawala, V. C. Sundar, D. E. Morse, and P. Fratzl. Skeleton of Euplectella sp.: Structural Hierarchy from the Nanoscale to the Macroscale. Science, 309(5732):275–278, July 2005.

[34] M. Sarikaya, H. Fong, N. Sunderland, B. Flinn, G. Mayer, A. Mescher, and E. Gaino. Biomimetic model of a sponge-spicular optical fiber—mechanical properties and structure. Journal of Materials Research, 16:1420–1428, 2001.

[35] C. Levi, J. Barton, C. Guillemet, E. Le Bras, and P. Lehuede. A remarkably strong natural glassy rod: the anchoring spicule of the Monorhaphis sponge. Journal of Materials Science Letters, 8:337–339, 1989.

[36] R. Rabiei, S. Bekah, and F. Barthelat. Nacre from mollusk shells: inspiration for high-performance nanocomposites. Natural Polymers, 2:113–149, 2012.

[37] W. Clegg, K. Kendall, N. M. Alford, T. Button, and J. Birchall. A simple way to make tough ceramics. Nature, 347:455–457, 1990.

[38] M. A. Monn, J. Ferreira, J. Yang, and H. Kesari. A millimeter scale flexural testing system for measuring the mechanical properties of marine sponge spicules. J. of Visualized Experiments, page e56571, 2017.

[39] M. A. Monn and H. Kesari. A new structure-property connection in the skeletal elements of the marine sponge Tethya aurantia that guards against buckling instability. Scientific Reports, 7, January 2017.

[40] C. Jolicoeur and A. Cardou. Analytical solution for bending of coaxial orthotropic cylinders. Journal of Engineering Mechanics, 120(12):2556–2574, 1994.

[41] M. Nickel, E. Bullinger, and F. Beckmann. Functional morphology of tethya species (porifera): 2. three-dimensional morphometrics on spicules and skeleton superstructures of t. minuta. Zoomorphology, 125(4):225–239, 2006.

[42] G. Bavestrello, B. Calcinai, L. Ceccati, C. Cerrano, and M. Sarà. Skeletal development in two species of tethya (porifera, demospongiae). Italian Journal of Zoology, 67(3):241–244, 2000.

[43] B. K. Lee and S. J. Oh. Elastica and buckling load of simple tapered columns with constant volume. International Journal of Solids and Structures, 37(18):2507–2518, 2000.

[44] M. Sarikaya. An introduction to biomimetics: a structural viewpoint. Microscopy Research and Technique, 27(5):360–375, 1994.

[45] R. Menig, M. Meyers, M. Meyers, and K. Vecchio. Quasi-static and dynamic mechanical response of Haliotis rufescens (abalone) shells. Acta Materialia, 48(9):2383–2398, 2000.

[46] K. J. Koester, J. Ager, and R. Ritchie. The true toughness of human cortical bone measured with realistically short cracks. Nature Materials, 7(8):672–677, 2008.

[47] Cook J., Gordon J. E., Evans C. C., Gordon J. E., Marsh D. M., and Bowden Frank Philip. A mechanism for the control of crack propagation in all-brittle systems. Proceedings of the Royal Society of London A, 282:508–520, 1964.

[48] H. Ming-Yuan and J. W. Hutchinson. Crack deflection at an interface between dissimilar elastic materials. International Journal of Solids and Structures, 25(9):1053–1067, 1989.

[49] M. M. Rahaman, W. Fang, A. L. Fawzi, Y. Wan, and H. Kesari. An accelerometer-only algorithm for determining the acceleration field of a rigid body, with application in studying the mechanics of mild traumatic brain injury. Journal of the Mechanics and Physics of Solids, page 104014, 2020.

[50] W. Deng and H. Kesari. Angle-independent optimal adhesion in plane peeling of thin elastic films at large surface roughnesses. Journal of the Mechanics and Physics of Solids, 148:104270, 2021.

[51] A. R. Forsyth. Lectures on the differential geometry of curves and surfaces. University Press, 1912.

[52] L. Euler. Methodus inveniendi lineas curvas maximi minimive proprietate gaudentes sive solutio problematis isoperimetrici latissimo sensu accepti, volume 1. Springer Science & Business Media, 1952.

[53] V. L. Popov. Coulomb's law of friction. In Contact Mechanics and Friction, pages 151–172. Springer, 2017.

[54] S. Goldstein. Modern developments in fluid dynamics: an account of theory and experiment relating to boundary layers, turbulent motion and wakes. Number V.1 in Modern Developments in Fluid Dynamics. Clarendon Press, 1938.

[55] M. S. Klamkin. On the transformation of a class of boundary value problems into initial value problems for ordinary differential equations. SIAM Review, 4(1):43–47, 1962.

[56] L. Euler. De novo genere oscillationum. Commentarii Academiæ Scientiarum Petropolitanæ, pages 128–149, 1750.

[57] E. T. Whittaker. A treatise on the analytical dynamics of particles and rigid bodies. CUP Archive, 1937.

[58] A. Beléndez, C. Pascual, D. Méndez, T. Beléndez, and C. Neipp. Exact solution for the nonlinear pendulum. Revista Brasileira de Ensino de Física, 29(4):645–648, 2007.

[59] W. Deng and H. Kesari. Effect of machine stiffness on interpreting contact force–indentation depth curves in adhesive elastic contact experiments. Journal of the Mechanics and Physics of Solids, 131:404–423, 2019.

[60] H. Kesari and A. J. Lew. Effective macroscopic adhesive contact behavior induced by small surface roughness. Journal of the Mechanics and Physics of Solids, 12:2488–2510, 2011.

[61] G. Tomlinson. CVI. A molecular theory of friction. The London, Edinburgh, and Dublin Philosophical Magazine and Journal of Science, 7(46):905–939, 1929.

[62] W. Beare and F. P. Bowden. Physical properties of surfaces i-kinetic friction. Philosophical Transactions of the Royal Society of London. Series A, Mathematical and Physical Sciences, 234(741):329–354, 1935.

[63] E. A. Deulin, V. Mikhailov, Y. V. Panfilov, and R. Nevshupa. Mechanics and physics of precise vacuum mechanisms, volume 91. Springer, 2010.

[64] A. Marsal, F. Ansart, V. Turq, J.-P. Bonino, J.-M. Sobrino, Y. M. Chen, and J. Garcia. Mechanical properties and tribological behavior of a silica or/and alumina coating prepared by sol-gel route on stainless steel. Surface and Coatings Technology, 237:234–240, 2013.

[65] E. Rabinowicz and R. Tanner. Friction and wear of materials. Journal of Applied Mechanics, 33(2):479, 1966.

[66] P. Mora and D. Place. Simulation of the frictional stick-slip instability. Pure and Applied Geophysics, 143(1):61–87, 1994.

[67] A. D. Berman, W. A. Ducker, and J. N. Israelachvili. Origin and characterization of different stick-slip friction mechanisms. Langmuir, 12(19):4559–4563, 1996.

[68] H. Gao. Application of fracture mechanics concepts to hierarchical biomechanics of bone and bone-like materials. International Journal of Fracture, 138(1-4):101–137, 2006.

[69] B. Ji and H. Gao. Mechanical principles of biological nanocomposites. Annual Review of Materials Research, 40:77–100, 2010.

[70] K. Bertoldi, D. Bigoni, and W. Drugan. Nacre: an orthotropic and bimodular elastic material. Composites Science and Technology, 68(6):1363–1375, 2008.

[71] J. E. Rim, P. Zavattieri, A. Juster, and H. D. Espinosa. Dimensional analysis and parametric studies for designing artificial nacre. Journal of the Mechanical Behavior of Biomedical Materials, 4(2):190–211, February 2011.

[72] M. R. Begley, N. R. Philips, B. G. Compton, D. V. Wilbrink, R. O. Ritchie, and M. Utz. Micromechanical models to guide the development of synthetic 'brick and mortar' composites. Journal of the Mechanics and Physics of Solids, 60(8):1545–1560, 2012.

[73] Y. Shao, H.-P. Zhao, X.-Q. Feng, and H. Gao. Discontinuous crack-bridging model for fracture toughness analysis of nacre. Journal of the Mechanics and Physics of Solids, 60(8):1400–1419, 2012.

[74] M. C. Kingsley and M. A. Ramsay. The spiral in the tusk of the narwhal. Arctic, pages 236–238, 1988.

[75] T. C. Gasser, R. W. Ogden, and G. A. Holzapfel. Hyperelastic modelling of arterial layers with distributed collagen fibre orientations. Journal of the Royal Society Interface, 3(6):15–35, 2006.

[76] P. Fratzl and R. Weinkamer. Nature's hierarchical materials. Progress in Materials Science, 52(8):1263 – 1334, 2007.

[77] J. Buckwalter, M. Glimcher, R. Cooper, and R. Recker. Bone biology. Part I: Structure, blood supply, cells, matrix, and mineralization. Journal of Bone and Joint Surgery - Series A, 77(8):1256–1275, 1995.

[78] J. L. Delgado, M. Á. Herranz, and N. Martin. The nano-forms of carbon. Journal of Materials Chemistry, 18(13):1417–1426, 2008.

[79] S. G. Lekhnitskii. Theory of the elasticity of anisotropic bodies. Mir Publishers, 1981.

[80] T. C. T. Ting. Anisotropic elasticity : theory and applications. Oxford University Press, USA, 1996.

[81] L. Kollár and G. S. Springer. Stress analysis of anisotropic laminated cylinders and cylindrical segments. International Journal of Solids and Structures, 29(12):1499–1517, 1992.

[82] L. Kollár, J. M. Patterson, and G. S. Springer. Composite cylinders subjected to hygrothermal and mechanical loads. International Journal of Solids and Structures, 29(12):1519–1534, 1992.

[83] T. Ting. Pressuring, shearing, torsion and extension of a circular tube or bar of cylindrically anisotropic material. Proceedings of the Royal Society of London A: Mathematical, Physical and Engineering Sciences, 452(1954):2397–2421, 1996.

[84] T. Chen, C.-T. Chung, and W.-L. Lin. A revisit of a cylindrically anisotropic tube subjected to pressuring, shearing, torsion, extension and a uniform temperature change. International Journal of Solids and Structures, 37(37):5143–5159, 2000.

[85] J.-Q. Tarn and Y.-M. Wang. Laminated composite tubes under extension, torsion, bending, shearing and pressuring: a state space approach. International Journal of Solids and Structures, 38(50):9053–9075, 2001.

[86] C. Huang and S. Dong. Analysis of laminated circular cylinders of materials with the most general form of cylindrical anisotropy.: I. Axially symmetric deformations. International Journal of Solids and Structures, 38(34):6163–6182, 2001.

[87] M. Xia, H. Takayanagi, and K. Kemmochi. Bending behavior of filament-wound fiber-reinforced sandwich pipes. Composite Structures, 56(2):201–210, 2002.

[88] J. Crossley, A. Spencer, and A. England. Analytical solutions for bending and flexure of helically reinforced cylinders. International Journal of Solids and Structures, 40(4):777–806, 2003.

[89] I. Tsukrov and B. Drach. Elastic deformation of composite cylinders with cylindrically orthotropic layers. International Journal of Solids and Structures, 47(1):25–33, 2010.

[90] D. Gnoli, S. Babamohammadi, and N. Fantuzzi. Homogenization and equivalent beam model for fiber-reinforced tubular profiles. Materials, 13(9):2069, 2020.

[91] G. Chatzigeorgiou, N. Charalambakis, and F. Murat. Homogenization problems of a hollow cylinder made of elastic materials with discontinuous properties. International Journal of Solids and Structures, 45(18):5165–5180, 2008.

[92] G. Chatzigeorgiou, Y. Efendiev, N. Charalambakis, and D. C. Lagoudas. Effective thermoelastic properties of composites with periodicity in cylindrical coordinates. International Journal of Solids and Structures, 49(18):2590–2603, 2012.

[93] X. Sun, Y. Chen, V. Tan, R. Jaiman, and T. Tay. Homogenization and stress analysis of multi-layered composite offshore production risers. Journal of Applied Mechanics, 81(3):031003, 2014.

[94] X. Sun, V. Tan, Y. Chen, L. Tan, R. Jaiman, and T. Tay. Stress analysis of multi-layered hollow anisotropic composite cylindrical structures using the homogenization method. Acta Mechanica, 225(6):1649–1672, 2014.

[95] M. M. Rahaman, W. Fang, A. L. Fawzi, Y. Wan, and H. Kesari. An accelerometer-only algorithm for determining the acceleration field of a rigid body, with application in studying the mechanics of mild traumatic brain injury. Journal of the Mechanics and Physics of Solids, 143:104014, 2020.

[96] W. Deng and H. Kesari. Angle-independent optimal adhesion in plane peeling of thin elastic films at large surface roughnesses. Journal of the Mechanics and Physics of Solids, 148:104270, 2021.

[97] J. C. Simo, K. D. Hjelmstad, and R. L. Taylor. Numerical formulations of elasto-viscoplastic response of beams accounting for the effect of shear. Computer Methods in Applied Mechanics and Engineering, 42(3):301–330, March 1984.

[98] J. C. Simo and L. Vu-Quoc. A three-dimensional finite-strain rod model. part II: Computational aspects. Computer Methods in Applied Mechanics and Engineering, 58(1):79–116, October 1986.

[99] G. Yoshiaki, Y. Tomoo, and O. Makoto. Elliptic integral solutions of plane elastica with axial and shear deformations. International Journal of Solids and Structures, 26(4):375–390, January 1990.

[100] E. Reissner. On One-Dimensional Large-Displacement Finite-Strain Beam Theory. Studies in Applied Mathematics, 52(2):87–95, June 1973.

[101] T. Iwakuma and S. Kuranishi. How much contribution does the shear deformation have in a beam theory? Doboku Gakkai Ronbunshu, (344):141–151, 1984.

[102] T. Chaisomphob, F. Nishino, A. Hasegawa, and A.-S. Alygamalaly. An elastic finite displacement analysis of plane beams with and without shear deformation. Doboku Gakkai Ronbunshu, (368):169–177, 1986.

[103] L. Liu and N. Lu. Variational formulations, instabilities and critical loadings of space curved beams. International Journal of Solids and Structures, 87:48–60, June 2016.

[104] C. L. Dym and I. H. Shames. Solid Mechanics. Springer New York, New York, NY, 2013.

[105] E. Reissner. On a Variational Theorem in Elasticity. Journal of Mathematics and Physics, 29(1-4):90–95, April 1950.

[106] P. G. Ciarlet. Mathematical elasticity. Number v. 20, 27, 29 in Studies in mathematics and its applications. North-Holland ; Sole distributors for the U.S.A. and Canada, Elsevier Science Pub. Co, Amsterdam ; New York : New York, N.Y., U.S.A, 1988.

[107] B. Dacorogna. Direct methods in the calculus of variations. Number v. 78 in Applied mathematical sciences. Springer, New York, NY, 2nd ed edition, 2008.

[108] L. C. Evans. Partial differential equations. Number v. 19 in Graduate studies in mathematics. American Mathematical Society, 2nd ed edition, 2010.

[109] T. J. R. Hughes. The Finite Element Method: Linear Static and Dynamic Finite Element Analysis. Courier Corporation, May 2012.

[110] K. F. Riley, M. P. Hobson, and S. J. Bence. Mathematical methods for physics and engineering. Cambridge Univ. Press, Cambridge, 2006.

[111] P. E. Gill, W. Murray, and M. H. Wright. Practical optimization. Elsevier Acad. Press, Amsterdam, 14. print edition, 2004.

[112] J. Nocedal and S. J. Wright. Numerical optimization. Springer series in operations research. Springer, New York, 2nd ed edition, 2006.

[113] M. Sarà and E. Manara. Cortical structure and adaptation in the genus tethya (porifera, demospongiae). In Fossil and recent sponges, pages 306–312. Springer, 1991.

[114] M. A. Monn and H. Kesari. A new structure-property connection in the skeletal elements of the marine sponge tethya aurantia that guards against buckling instability. Scientific reports, 7(1):1–10, 2017.

[115] M. Launey, E. Munch, D. Alsem, H. Barth, E. Saiz, A. Tomsia, and R. Ritchie. Designing highly toughened hybrid composites through nature-inspired hierarchical complexity. Acta Materialia, 57(10):2919–2932, 2009.

[116] M. Mirkhalaf, A. K. Dastjerdi, and F. Barthelat. Overcoming the brittleness of glass through bio-inspiration and micro-architecture. Nature Communications, 5, 2014.

[117] T. Clausen. Über die form architektonischer säulen. Bull cl, Physico Math Acad St Pétersbourg, 9:369–380, 1851.

[118] I. Tadjbakhsh and J. Keller. Strongest columns and isoperimetric inequalities for eigenvalues. Journal of Applied Mechanics, 29(1):159–164, 1962.

[119] W. Wunderlich and U. Albertin. Analysis and load carrying behaviour of imperfection sensitive shells. International journal for numerical methods in engineering, 47(1-3):255–273, 2000.

[120] V. C. Sundar, A. D. Yablon, J. L. Grazul, M. Ilan, and J. Aizenberg. Fibre-optical features of a glass sponge. Nature, 424(6951):899–900, 2003.

[121] J. Aizenberg, V. C. Sundar, A. D. Yablon, J. C. Weaver, and G. Chen. Biological glass fibers: Correlation between optical and structural properties. Proceedings of the National Academy of Sciences, 101(10):3358–3363, March 2004.

[122] D. Thompson. On Growth and Form., chapter On form and mechanical efficiency, pages 976–982. Cambridge Univ. Press, 1942.

[123] S. Leys. Comparative study of spiculogenesis in demosponge and hexactinellid larvae. Microscopy Research and Technique, 62(4):300–311, November 2003.

[124] H. Kesari, J. C. Doll, B. L. Pruitt, W. Cai, and A. J. Lew. Role of surface roughness in hysteresis during adhesive elastic contact. Philosophical Magazine & Philosophical Magazine Letters, 90(12):891–902, 2010.

[125] W. Deng and H. Kesari. Depth-dependent hysteresis in adhesive elastic contacts at large surface roughness. Scientific Reports, 9:1–12, 2019.

[126] W. N. Everitt. A catalogue of sturm-liouville differential equations. In Sturm-Liouville Theory, pages 271–331. Birkhäuser Basel, 2005.

[127] W. O. Amrein, A. M. Hinz, and D. P. Pearson, editors. Sturm-Liouville theory: past and present. Birkhäuser, Basel ; Boston, 2005.

[128] W. E. Boyce and R. C. DiPrima. Elementary differential equations and boundary value problems. Wiley, Hoboken, NJ, tenth edition edition, 2012.

[129] P. B. Bailey, W. N. Everitt, and A. Zettl. Algorithm 810: The sleign2 sturm-liouville code. ACM Trans. Math. Softw., 27(2):143–192, June 2001.

[130] K. D. Hjelmstad. Fundamentals of structural mechanics, chapter The planar buckling of beams, pages 415–417. Springer Science & Business Media, 2007.